

Multifunctional Composite Frameworks for Advanced Lithium-Sulfur Batteries

Luke Hencz

BSc. (Hons.)

School of Environment and Science

Griffith University

Submitted in fulfilment of the requirements of the degree of Doctor of
Philosophy



August 2021

Statement of Originality

This work has not previously been submitted for a degree or diploma in any university. To the best of my knowledge and belief, the thesis contains no material previously published or written by another person except where due reference is made in the thesis itself.

Signature of Candidate

Luke Hencz

Acknowledgements

First and foremost, I would like to extend my sincerest thanks to my supervisor, Prof. Shanqing Zhang. Since meeting Eddie during my undergraduate studies, he has advised me not only through research but also through all aspects of academia. I have thoroughly enjoyed our discussions and will always be grateful for what Eddie taught me during my studies.

Secondly, I have to thank A.Prof. Xingxing Gu. Gary took me under his wing and guided me through all the intricacies of battery assembly and research. I especially appreciate his time since it was given to me during such a busy period during his PhD. I could not have completed this thesis without him.

Next, I would like to extend my gratitude to Dr Hao Chen, Dr Michael Ling, Dr Yazhou Wang, Dr David Adekoya, Dr Meng Zu, Zhenzhen Wu, Zhong Su, Shangshu Qian, Yuhui Tian, Meng Li, Mengting Zheng and all other members all the members of Eddie's research group who helped me along the way. I have always felt that I am welcome and a part of the team.

I would also like to sincerely thank my associate supervisor, Prof. Huijun Zhao and all members of C.C.C.E, including Dr Porun Liu, Dr M-Al Mamun, and Christina Perry, for providing, maintaining, and managing the facilities where I conducted the majority of my research. Additionally, I give my warmest thanks to both Abdulaziz Bati and Su Chen for their help with XPS analysis and mechanical testing, respectively.

Next, I would like to thank Dr William Wen, Dr Andrew Pearson, and Prof. Richard John for allowing me to gain experience in undergraduate chemistry education during my PhD. I thoroughly enjoyed teaching chemistry in both the School of Environment and Science and the School of Pharmacy and Medical Science.

I would like to acknowledge how fortunate I am for being born and raised in Australia. I am fortunate to be a citizen of a country willing to support its students and provide a pathway to education for people of all backgrounds. The support I received through Austudy and the RTP stipend was crucial for my success.

Finally, I extend my love and thanks to my friends and family. I want to thank Darren Holland, James Baxter, Brody Gospel, and Nick Malart for our friendships during my studies. Thanks to my brothers, Tim and Mike, for being sources of inspiration and pride. Thanks to my mother, Christine, for always being loving and supporting. Most of all, thanks to my

fiancé Kate. I am in no way exaggerating when I say I could not have completed my PhD without Kate's support. Kate has helped me in more ways than I can express in words.

I dedicate this thesis to my father, who is no longer with us but will always live on in our hearts.

Table of Contents

Statement of Originality	i
Acknowledgements	iii
Table of Contents	v
Acronyms	vii
Publications	x
Abstract.....	xv
Chapter 1: Introduction.....	1
1.1 Significance of the Project.....	2
1.2 Research Objectives	4
1.3 Thesis Outline.....	5
1.4 References.....	7
Chapter 2: Housing Sulfur in Polymer Composite Frameworks for Li–S Batteries.....	9
2.1 Statement of Contribution.....	10
2.2 Abstract.....	11
2.3 Introduction	12
2.4 Polymeric Binders in LIBs.....	13
2.5 Working Mechanisms and Challenges of Li–S Batteries.....	16
2.6 Sulfur Host-Based Polymeric Composite Frameworks.....	20
2.7 Sulfur Host-Free Polymeric Composite Frameworks	32
2.8 Multifunctional Polymer Composite Frameworks	60
2.9 Conclusions	69
2.10 References	71
Chapter 3: Poly(thiourea triethylene glycol) as a Multifunctional Binder for Enhanced Performance in Lithium-Sulfur Batteries	88
3.1 Statement of Contribution.....	89
3.2 Abstract.....	90
3.3 Introduction	92

3.4	<i>Experimental Section</i>	93
3.5	<i>Results and Discussion</i>	96
3.6	<i>Conclusion</i>	111
3.7	<i>Acknowledgments</i>	112
3.8	<i>References</i>	113
Chapter 4: Multifunctional Cation-Vacancy-Rich ZnCo₂O₄ Polysulfide-Blocking Layer for Ultrahigh-Loading Li-S Battery		118
4.1	<i>Abstract</i>	119
4.2	<i>Introduction</i>	120
4.3	<i>Experimental Section</i>	122
4.4	<i>Results and Discussion</i>	126
4.5	<i>Conclusion</i>	147
4.6	<i>References</i>	148
Chapter 5: Environmentally Benign and Highly-Branched Amylopectin (HBA) Binder for Enhanced Longevity in Sulfur Cathodes		157
5.1	<i>Abstract</i>	158
5.2	<i>Introduction</i>	160
5.3	<i>Experimental Section</i>	163
5.4	<i>Results and Discussion</i>	165
5.5	<i>Conclusion</i>	179
5.6	<i>References</i>	181
Chapter 6: Oxygen-Rich Hierarchical Porous Carbon Host (HPCH) for Li-S Cathodes		186
6.1	<i>Abstract</i>	187
6.2	<i>Introduction</i>	189
6.3	<i>Experimental Section</i>	190
6.4	<i>Results and Discussion</i>	192
6.5	<i>Conclusion</i>	207
6.6	<i>References</i>	208
Chapter 7: Conclusion and Future Work		213
7.1	<i>General Conclusions</i>	214
7.2	<i>Future Work</i>	217

Acronyms

σ_W : Warburg factor

A.M.U.: Atomic mass unit

BE: Binding energy

BET: Brunauer, Emmett, and Teller

CE: Coulombic efficiency

CV: Cyclic voltammetry

DFT: Density functional theory

D_{Li} : Lithium-ion diffusion

E/S: Electrolyte/Sulfur

EDS: Energy dispersive X-ray spectroscopy

EIS: Electrochemical impedance spectroscopy

EPR: Electron paramagnetic resonance

EV: Electric vehicle

FTIR: Fourier Transform Infrared

FWHM: Full width half maximum

GGA: Generalized gradient approximation

GITT: Galvanostatic intermittent titration technique

HR: High resolution

ICP-OES: Inductively coupled plasma-optical emission spectroscopy

IEP: Isoelectric point

I_P : Peak current

LIB: Lithium-ion battery

LiPS: Lithium polysulfide

Li-S: Lithium-Sulfur

LSB: Lithium-sulfur battery

M_w : Molecular weight

NIR: Near-infrared

NLDFT: Non-local density functional theory

NMR: Nuclear resonance spectroscopy

OCV: Open circuit voltage

PAW: Projector-augmented-wave

PBE: Perdew–Burke–Ernzerhof

PCF: Polymer composite framework

PTTG: Poly(thiourea triethylene glycol)

PVDF: Poly(vinylidene fluoride)

R_{ct} : Charge transfer resistance

R_e : Ohmic resistance

R_{int} : Interphase contact resistance

RT: Room temperature

S.H.E.: Standard hydrogen electrode

SAED: Selected area diffraction

SEI: Solid electrolyte interface

SEM: Scanning electron microscope

SPM: Scanning Probe Microscopy

SSA: Specific surface area

TEM: Transmission electron microscopy

TGA: Thermogravimetric analysis

UV: Ultraviolet

VASP: Vienna ab initio simulation package

W_o : Warburg resistance

XAS: X-ray absorption spectroscopy

XPS: X-ray photoelectron spectroscopy

XRD: X-ray diffraction

ν : Scan rate

Publications

Acknowledgement of Papers included in this Thesis

Section 9.1 of the Griffith University Code for the Responsible Conduct of Research (“Criteria for Authorship”), in accordance with Section 5 of the Australian Code for the Responsible Conduct of Research, states:

To be named as an author, a researcher must have made a substantial scholarly contribution to the creative or scholarly work that constitutes the research output, and be able to take public responsibility for at least that part of the work they contributed. Attribution of authorship depends to some extent on the discipline and publisher policies, but in all cases, authorship must be based on substantial contributions in a combination of one or more of:

- conception and design of the research project
- analysis and interpretation of research data
- drafting or making significant parts of the creative or scholarly work or critically revising it so as to contribute significantly to the final output.

Section 9.3 of the Griffith University Code (“Responsibilities of Researchers”), in accordance with Section 5 of the Australian Code, states:

Researchers are expected to:

- Offer authorship to all people, including research trainees, who meet the criteria for authorship listed above, but only those people.
- accept or decline offers of authorship promptly in writing.
- Include in the list of authors only those who have accepted authorship
- Appoint one author to be the executive author to record authorship and manage correspondence about the work with the publisher and other interested parties.
- Acknowledge all those who have contributed to the research, facilities or materials but who do not qualify as authors, such as research assistants, technical staff, and advisors on cultural or community knowledge. Obtain written consent to name individuals.

Included in this thesis are papers in Chapters 2 to 6, which are co-authored with other researchers. The bibliographic details of the published works and the status for the prepared manuscripts for these papers including all authors, are:

Chapter 2:

Hencz, L., Chen, H., Ling, H. Y., Wang, Y., Lai, C., Zhao, H. & Zhang, S. (2019). Housing Sulfur in Polymer Composite Frameworks for Li-S batteries. *Nano-Micro Letters*, 11(1), 1-44. (DOI: 10.1007/s40820-019-0249-1)

Chapter 3:

Hencz, L., Chen, H., Wu, Z., Gu, X., Li, M., Tian, Y., Chen, S., Cheng, Y., Bati, A., Shapter, J., Kiefel, M., Li, D-S. & Zhang, S. (2021). Poly (thiourea triethylene glycol) as a Multifunctional Binder for Enhanced Performance in Lithium-Sulfur Batteries. *Green Energy & Environment*, In Press. (DOI: 10.1016/j.gee.2021.01.014)

Chapter 4:

Li, Z. *, Zhang, Q. *, **Hencz, L.** *, Liu, J., Kaghazchi, P., Han, J., Wang, L & Zhang, S. (2021). Multifunctional Cation-Vacancy-Rich ZnCo_2O_4 Polysulfide-Blocking Layer for Ultrahigh-Loading Li-S Battery. *Nano Energy*, 89(A), 106331. (DOI: 10.1016/j.nanoen.2021.106331)

* These authors contributed equally

Chapter 5:

Hencz, L., Chen, H., Qian, S., Chen, S., Yan, C. & Zhang, S. Environmentally Benign and Highly-Branched Amylopectin (HBA) Binder for Enhanced Longevity in Sulfur Cathodes

Chapter 6:

Hencz, L., Zheng, M., Chen, H., Bat-Erdene, M., Su, Z., Gu, X. & Zhang, S. Oxygen-Rich Hierarchical Porous Carbon Host (HPCH) for Li-S Cathodes

Appropriate acknowledgements of those who contributed to the research but did not qualify as authors are included in each manuscript.

(Signed) _____ (Date) 27/08/2021

Luke Hencz

(Countersigned) _____ (Date) 27/08/2021

Supervisor: Prof. Shanqing Zhang

Additional Relevant Publications

In addition to the published works that formed the research chapters of this thesis, there are several other co-authored publications that are directly relevant but did not form part of the thesis itself.

Chen, H., Wu, Z., Su, Z., **Hencz, L.**, Chen, S., Yan, C. & Zhang, S. (2021). A Hydrophilic Poly(methyl vinyl ether-alt-maleic acid) Polymer as a Green, Universal, and Dual-Functional Binder for High-Performance Silicon Anode and Sulfur Cathode. *Journal of Energy Chemistry*, 62, 127-135. (DOI: 10.1016/j.jechem.2021.03.015)

Ling, H.Y., **Hencz, L.**, Chen, H., Wu, Z., Su, Z., Chen, S., Yan, C., Lai, C., Liu, X. & Zhang, S. (2021). Sustainable Okra Gum for Silicon Anode in Lithium-Ion Batteries. *Sustainable Materials and Technologies*, 28, e00283. (DOI: 10.1016/j.susmat.2021.e00283)

Ling, H.Y., Chen, H., Zhang, S., Wu, Z., **Hencz, L.**, Qian, S., Liu, X., Liu, T. & Zhang, S. (2021). Sustainable Bio-Derived Materials for Addressing Critical Problems of Next-Generation High-Capacity Lithium Ion Batteries. *Materials Chemistry Frontiers*. (DOI: 10.1039/D1QM00255D)

Chen, H., Adekoya, D., **Hencz, L.**, Ma, J., Chen, S., Yan, C., Zhao, H. Cui, G. & Zhang, S. (2020). Stable Seamless Interfaces and Rapid Ionic Conductivity of Ca-CeO₂/LiTFSI/PEO Composite Electrolyte for High-Rate and High-Voltage All-Solid-State Battery. *Advanced Energy Materials*, 10(21), 2000049. (DOI: 10.1002/aenm.202000049)

Wang, C., Zhang, L., Dou, Y., **Hencz, L.**, Jiang, L., Al-Mamun, M., Liu, P., Zhang, S. & Zhao, H. (2020). Transition Metal (Fe, Co, Mn) Boosting the Lithium Storage of the Multishelled NiO Anode. *Energy Technology*, 8(5), 2000008. (DOI: 10.1002/ente.202000008)

Yuan, D., Dou, Y., Xu, L., Yu, L., Cheng, N., Xia, Q., **Hencz, L.**, Ma, J., Dou, S-X. & Zhang, S. (2020). Atomically Thin Mesoporous NiCo₂O₄ Grown on Holey Graphene for Enhanced Pseudocapacitive Energy Storage. *Journal of Materials Chemistry A*, 8(27), 13443-13451. (DOI: 10.1039/D0TA03007D)

Ling, H.Y., Su, Z., Chen, H., **Hencz, L.**, Zhang, M., Tang, Y. & Zhang, S. (2019). Biomass-Derived Poly (Furfuryl Alcohol)-Protected Aluminum Anode for Lithium-Ion Batteries. *Energy Technology*, 7(8), 1800995. (DOI: 10.1002/ente.201800995)

Chen, H., Ling, M., **Hencz, L.**, Ling, H.Y., Li, G., Lin, Z., Liu, G. & Zhang, S. (2018). Exploring Chemical, Mechanical, and Electrical Functionalities of Binders for Advanced Energy-Storage Devices. *Chemical Reviews*, 118(18), 8936-8982. (DOI: 10.1021/acs.chemrev.8b00241)

Abstract

Rechargeable batteries have recently solidified their role in society's transition toward a cleaner energy future through the emergence of electric vehicles and grid-scale energy storage. The deployment of electrochemical energy storage near electricity generators and at home has increased the reliability of renewable energy, thus easing renewable energy's emergence into power grids worldwide. Similarly, electric vehicles have continued to increase their implementation into global transportation networks, which reduces the reliance on fossil fuel-based vehicles and helps mitigate CO₂ emissions.

At present, lithium-ion batteries (LIBs) dominate the portable electronics market due to their superior energy density. However, as lithium-ion batteries are late in their development cycle, the limitations of the technology are becoming apparent, and researchers have turned to new battery chemistries to enhance the energy density, reduce the cost, and mitigate the environmental impacts of current-generation batteries.

Lithium-sulfur batteries (Li-S) are an excellent example of next-generation batteries, and can deliver higher energy densities, reduce costs, and minimise environmental impacts over current-generation LIBs. However, Li-S batteries have technical limitations associated with their chemistry. The most troublesome limitation of the Li-S cell is the dubbed the polysulfide shuttle and refers to the dissolution and migration of soluble discharge intermediates which results in rapid capacity fading. Other limitations revolve around the limited conductivity of sulfur cathodes, volume expansion of electroactive materials, and poor performance at high current densities. Researchers have focused on various cell components to address the limitations, with substantial research on the cathode, anode, and electrolyte. This thesis employs strategies targeted at the composite sulfur cathode in lithium-sulfur cells.

In the first work of this thesis, poly(thiourea triethylene glycol) is synthesised and applied as a multifunctional binder so that a composite sulfur cathode can be constructed. The abundant lone-pair rich thiourea and ether functional groups provide ample chemical bonding to retain soluble polysulfides to reduce the shuttle effect. Additionally, the robust adhesive properties of the polymer maintain the composite cathode's conductive network after cycling to enhance the electrochemical performance of the lithium-sulfur batteries.

The second work develops a zinc defective zinc cobalt oxide (ZDZCO) material and applies it in constructing a conductive composite blocking layer at the cathode's surface in lithium-sulfur

batteries. The ZDZCO has a high affinity towards the soluble polysulfide reaction intermediates and prevents their migration through the separator, thus delivering a long cycle-life Li-S battery. What's more, the catalytic properties of the ZDZCO-based blocking layer promotes fast polysulfide conversion enabling cycling at extremely high current densities. These synergistic effects allow the ZDZCO-composite to facilitate the stable cycling of a sulfur cathode with an extremely high sulfur loading.

Following this, a highly-branched amylopectin (HBA) binder is extracted from sticky rice and used in the sulfur cathode. The HBA improved the performance in Li-S batteries via two mechanisms. First, the HBA binder can chemically retain soluble polysulfides at the cathode via coordinate and C-S bonds for strong adsorption, reducing capacity fading due to the shuttle effect. Secondly, the highly-branched structure of the HBA delivers excellent mechanical and adhesive properties. Compared with a mixed lowly-branched polysaccharide (LBP), the HBA maintained a robust composite framework throughout the sulfur cathode which contributed to the improved performance of the cell.

Lastly, a hierarchical porous carbon host (HPCCH) is produced and used in sulfur composite cathodes as a bi-functional sulfur host. The HPCCH was found to have an extremely high specific surface area with a desirable pore size distribution which was achieved through the novel porogen/solvent system during synthesis. The HPCCH was also functionalised with abundant carbonyl and hydroxyl groups during fabrication, which allowed for chemical polysulfide retention via the formation of coordinate bonds with the lone-pair rich oxygen groups, enhancing cycle stability and capacity retention. The carbon framework also enhanced electronic and ionic conductivity throughout the cathode composite, which enabled the cells based on this host to possess superb reaction kinetics. Compared with the composite cathode based on carbon black alone, the HPCCH-based electrode delivered substantially improved electrochemical performances while being produced from a scalable and environmentally friendly synthesis method.

Overall, each work in this thesis aims to chemically trap the soluble polysulfides at the cathode to reduce the capacity fading in Li-S cells. Additionally, each work aims to improve the reaction kinetics in the Li-S battery by rationally designing composite cathode so that the electronic and ionic conductivity can be improved.

Chapter 1:

Introduction

1.1 Significance of the Project

Global population growth, economic development, and technological advancement are intimately linked to CO₂ emissions due to the worldwide reliance on fossil fuel-based energy and transportation [1-2]. To avoid a climate disaster and move towards a carbon-neutral future, CO₂ emissions from fossil fuel combustion must be addressed [3]. Two means to address these concerns is the broader uptake of renewable energy and electric vehicles (EVs) into global markets [4-5].

Renewable energy, that is, energy production that does not generate CO₂ emissions, can displace energy production technologies such as coal and gas-fired power stations, which are known to contribute a substantial portion of global CO₂ emissions [6]. Renewable energy generation, including solar and wind, has already significantly infiltrated global energy infrastructure [7]. However, increased uptake of these technologies is still required, mainly because fossil fuel-based power stations continue to be built in the developing world [6]. Renewable energy technologies must become cheaper and more reliable to reduce the domination of fossil fuel-based energy. Technological advances have enabled renewable technologies to become considerably cheaper [8], but despite this, the intermittent nature of renewable energy continues to hinder its uptake at a broader scale [9].

A promising solution to the intermittent nature of renewable energy is through rechargeable batteries, both at the grid and residential scale [10]. These grid-scale applications, along with the widespread uptake of in-home energy storage, have cemented rechargeable batteries' niche in the future carbon-neutral energy grid. Similarly, the role that rechargeable batteries have played in the successful emergence of EVs into global transportation markets cannot be ignored [11].

Rechargeable batteries' success in energy storage and EV applications is strictly owed to the dominance of the lithium-ion battery (LIB) [12]. Since its introduction by Sony in the 1990s, LIBs have revolutionised the portable electronic markets due to their superior energy density compared with the battery technologies available at the time [13]. However, LIBs are late in their development life cycle, and the limitations of this now mature technology must be addressed. One such limitation of the LIB is the reliance on sporadically distributed and expensive transition metals required to fabricate the transition metal cathodes upon which LIBs rely [14]. These transition metal cathodes provide an improved energy density over obsolete

technologies but are not sufficient for future requirements, such as allowing an EV to travel the same distance as a fossil-fuel-based vehicle on a single charge [15].

To address these concerns, researchers are looking towards rechargeable battery technologies that are cheaper in cost, larger in energy capacity, increased in power density, and cleaner to the environment. One such promising technology is batteries based on the lithium-sulfur (Li-S) cell [16]. Lithium-sulfur batteries (LSBs) have a theoretical energy density up to 5 times greater than current-generation LIBs while also avoiding the reliance on transition metal materials in the cathode [17]. However, LSBs are plagued by technical limitations, which are hindering their widespread application [18]. The technical challenges associated with LSBs are the focus of researchers in the field. Both the technical limitations and methods to address these concerns are thoroughly outlined in the next section. This thesis aims to address some of the technical limitations of the Li-S cell through the investigation and application of multifunctional composites in sulfur cathodes for advanced Li-S batteries

If their associated limitations can be addressed, LSBs can cause a paradigm shift in global rechargeable battery markets, which could help further to increase the infiltration of EVs into transportation markets. In addition to this, the negative aspects of renewable energy sources could be mitigated, thus also improving their infiltration into energy grids worldwide. Both of these applications could have severe ramifications in the pursuit of a carbon-neutral future.

1.2 Research Objectives

The ultimate goal of this thesis is to improve the electrochemical performance of the Li–S cell by rationally designing and applying multi-functional cathodic composites. More specifically, the precise aims of this thesis are as follows;

1. Explore materials that can trap the soluble polysulfides, either via physical or chemical means, at the cathode matrix so that the polysulfide dissolution and shuttling during cycling is hindered so that the cycle life of the Li–S cell can be improved.
2. Rationally design composite cathodes that can maintain the electronic conducting networks throughout the cathode matrix, which can help to overcome the insulating nature of sulfur and the discharge products ($\text{Li}_2\text{S}_2/\text{Li}_2\text{S}$).
3. Implement specially designed materials that can enhance the ionic conducting channels within the composite cathodes so that the sluggish reaction kinetics and poor rate performance of the Li–S cell can be improved
4. Where possible, look towards synthesis methods that are environmentally friendly, cheap, and scalable so that the chances of commercial Li–S battery implementation can be improved whilst minimising harm to the environment

1.3 Thesis Outline

This thesis aims to investigate multifunctional composites to be applied at the cathode of the Li–S battery in the hopes of addressing the rapid capacity fading due to the polysulfide shuttling phenomenon, the sluggish electrochemical reaction kinetics, the high cost, and the environmental concerns associated with these cells.

The framework of this thesis and the aims of each chapter are as follows:

- Chapter 1: Provide a broad overview of the problems this thesis aims to address and provide the structure of the thesis
- Chapter 2: Outline the technical challenges as well as the current methods to address the shortfalls of the Li–S cell and provide a literature review of the research to date
- Chapter 3: Investigate the role of the polymer poly(thiourea triethylene glycol) (PTTG) as a multifunctional binder in Li–S cathode composites to chemically trap soluble polysulfides at the lone-pair rich thiourea and ether groups. The chemical retention of soluble polysulfides should enhance the cycle life and reduce the capacity fading in the LSBs.
- Chapter 4: Apply a Zinc defective Zinc Cobalt Oxide (ZDZCO) polysulfide blocking composite at the surface of the Li–S cathode, which can chemically retain polysulfides at the bi-metallic oxide's surface and facilitate the rapid electrochemical conversion of reaction intermediates. The electrochemical performance of the LSBs could be enhanced through chemical polysulfide retention. In addition, the rapid electrochemical conversion of polysulfides facilitated by the ZDZCO composite should improve the electrochemical performance of the LSBs, especially under fast charge/discharge scenarios.
- Chapter 5: Extract and apply an environmentally friendly highly-branched amylopectin (HBA) binder derived from sticky rice in the construction of composite Li–S cathodes to chemically retain soluble polysulfides through coordinate and C–S bonds to mitigate the polysulfide shuttling. The HBA inherently contains the necessary chemical functionality to trap polysulfides at the cathode, reducing capacity fading and improving electrochemical performance, while reducing the environmental impacts of the LSBs fabrication due to its biological origins

- Chapter 6: Develop a scalable and environmentally friendly synthesis method for a hierarchical porous carbon host (HPCH) and apply the material in composite cathodes of Li–S batteries to trap soluble polysulfides in the microporous network and via the abundant lone-pair rich carbonyl and hydroxyl functional groups contained on the host. The physical and chemical retention of the soluble polysulfides should enhance the longevity and electrochemical performance of the LSBs.
- Chapter 7: Summarise the work included in this thesis and provide a general outlook and future works

1.4 References

1. Guillebaud, J. and P. Hayes, *Population growth and climate change*. BMJ, 2008. **337**: p. a576.
2. Fankhauser, S. and R. S.J. Tol, *On climate change and economic growth*. Resource and Energy Economics, 2005. **27**(1): p. 1-17.
3. Quadrelli, R. and S. Peterson, *The energy–climate challenge: Recent trends in CO₂ emissions from fuel combustion*. Energy Policy, 2007. **35**(11): p. 5938-5952.
4. Owusu, P.A. and S. Asumadu-Sarkodie, *A review of renewable energy sources, sustainability issues and climate change mitigation*. Cogent Engineering, 2016. **3**(1): p. 1167990.
5. Li, C., et al., *Hidden Benefits of Electric Vehicles for Addressing Climate Change*. Scientific Reports, 2015. **5**(1): p. 9213.
6. Sims, R.E.H., *Renewable energy: a response to climate change*. Solar Energy, 2004. **76**(1): p. 9-17.
7. Liserre, M., T. Sauter, and J.Y. Hung, *Future Energy Systems: Integrating Renewable Energy Sources into the Smart Power Grid Through Industrial Electronics*. IEEE Industrial Electronics Magazine, 2010. **4**(1): p. 18-37.
8. Lund, P.D., *Boosting new renewable technologies towards grid parity – Economic and policy aspects*. Renewable Energy, 2011. **36**(11): p. 2776-2784.
9. Barton, J.P. and D.G. Infield, *Energy storage and its use with intermittent renewable energy*. IEEE Transactions on Energy Conversion, 2004. **19**(2): p. 441-448.
10. Yang, Z., et al., *Electrochemical Energy Storage for Green Grid*. Chemical Reviews, 2011. **111**(5): p. 3577-3613.
11. Cairns, E.J. and P. Albertus, *Batteries for Electric and Hybrid-Electric Vehicles*. Annual Review of Chemical and Biomolecular Engineering, 2010. **1**(1): p. 299-320.
12. Tarascon, J.M. and M. Armand, *Issues and challenges facing rechargeable lithium batteries*, in *Materials for Sustainable Energy*. 2010, Co-Published with Macmillan Publishers Ltd, UK. p. 171-179.

13. Blomgren, G.E., *The Development and Future of Lithium Ion Batteries*. Journal of The Electrochemical Society, 2016. **164**(1): p. A5019-A5025.
14. Simon, B., S. Ziemann, and M. Weil, *Potential metal requirement of active materials in lithium-ion battery cells of electric vehicles and its impact on reserves: Focus on Europe*. Resources, Conservation and Recycling, 2015. **104**: p. 300-310.
15. Fotouhi, A., et al., *A review on electric vehicle battery modelling: From Lithium-ion toward Lithium–Sulphur*. Renewable and Sustainable Energy Reviews, 2016. **56**: p. 1008-1021.
16. Wild, M., et al., *Lithium sulfur batteries, a mechanistic review*. Energy & Environmental Science, 2015. **8**(12): p. 3477-3494.
17. Kang, W., et al., *A review of recent developments in rechargeable lithium–sulfur batteries*. Nanoscale, 2016. **8**(37): p. 16541-16588.
18. Wang, Y., et al., *Sulfur Hosts against the Shuttle Effect*. Small Methods, 2018.

Chapter 2:
Housing Sulfur in Polymer Composite
Frameworks for Li–S Batteries

2.1 Statement of Contribution

The bibliographic details of the manuscript included in this chapter are as follows:

Hencz, L., Chen, H., Ling, H. Y., Wang, Y., Lai, C., Zhao, H., & Zhang, S. (2019). Housing Sulfur in Polymer Composite Frameworks for Li–S Batteries. *Nano-Micro Letters*, 11(1), 1-44. DOI: 10.1007/s40820-019-0249-1

My contribution to the involved manuscript:

The conceptualisation of the idea; collect, read, and review the included references; write the review manuscript; prepare the manuscript for submission to *Nano-Micro Letters* and address reviewers comments.

(Signed) _____ (Date) 27/08/2021

Name of Student: Luke Hencz

(Countersigned) _____ (Date) 27/08/2021

The corresponding author of the paper: Prof. Shanqing Zhang

(Countersigned) _____ (Date) 27/08/2021

Supervisor: Prof. Shanqing Zhang

2.2 Abstract

Extensive efforts have been devoted to designing micro-, nano-, or molecular structures of sulfur hosts to address the challenges of lithium-sulfur (Li-S) batteries, yet comparatively, little research has been carried out on the binders in Li-S batteries. Herein, we systematically review the polymer composite frameworks that confine the sulfur within the sulfur electrode, taking the roles of sulfur hosts and functions of binders into consideration. In particular, we investigate the binding mechanism between the binder and sulfur host (such as mechanical interlocking and interfacial interactions), the chemical interactions between the polymer binder and sulfur (such as covalent bonding, electrostatic bonding, etc.), as well as the beneficial functions that polymer binders can impart on Li-S cathodes, such as conductive binders, electrolyte intake, adhesion strength etc. This work could provide a more comprehensive strategy in designing sulfur electrodes for long-life, large-capacity, and high-rate Li-S batteries.

Highlights

- The roles of binders in both sulfur host-based and sulfur host-free systems are considered for polymer composite frameworks in lithium-sulfur batteries.
- The applications of the existing and potential multifunctional polymer composite frameworks are summarized for manufacturing lithium-sulfur batteries.

2.3 Introduction

The recent increases in global population and worldwide development continue to put upward pressure on the demand for energy [1]. As most energy is still produced through the combustion of fossil fuels, this increased demand for energy continues to raise global greenhouse gas emissions, which is the driving force behind climate change [2]. A transition away from fossil fuel-based energy to more renewable sources must be realized to reduce the environmental impacts of society's energy demands. Solar and wind power have made inroads into global energy infrastructure concerning grid-scale energy generation but are hindered by their intermittent energy supply [3]. Further uptake of electric vehicles (EVs) could also put downward pressure on emissions from fossil fuel combustion for transportation. However, for this to be realized on a larger scale, the travel range of EVs must be improved [4]. Current generation lithium-ion batteries (LIBs) have been successfully applied in both grid-scale energy storage and EVs, but the limitations of this mature technology are beginning to show. The high cost of LIBs is limiting their widespread application as grid-scale storage devices, and their limited energy densities cap the travel range of EVs [5]. To counteract these shortfalls, researchers in the field are investigating more cost-effective and energy-dense rechargeable batteries. Lithium-sulfur (Li-S) batteries are a promising alternative to current generation LIBs, as their associated electrochemistry delivers an energy density up to 5 times higher than current cells [6].

Additionally, the active materials in Li-S cells are cheaper and more abundant than their traditional LIB counterparts. However, Li-S cells have hindrances in their commercial application due to their limited conductivity, volume expansion, and rapid capacity fading [7]. The most common method to address these concerns is through the rational design and implementation of nanostructured sulfur hosts, toward which a great deal of research has been focused [8]. In comparison, the design and implementation of novel polymeric binders have been largely overlooked in Li-S cells [9] and has only recently started to capture the attention of researchers, as shown in recent reviews [10-12], yet approaches investigating the entire cathode structure are lacking. This review investigates the role of polymeric binders in constructing polymer composite frameworks (PCFs) to consolidate the current research in the field and provide future research directions. To begin with, we summarize the general binding mechanism in LIBs and then introduce the current challenges and solutions in Li-S batteries. Finally, we investigate the role of polymeric binders in host-based PCFs, followed by a

discussion on the role of binders in host-free PCFs, and finish with a review of multifunctional binders in PCFs, as shown in **Fig. 2.1**.

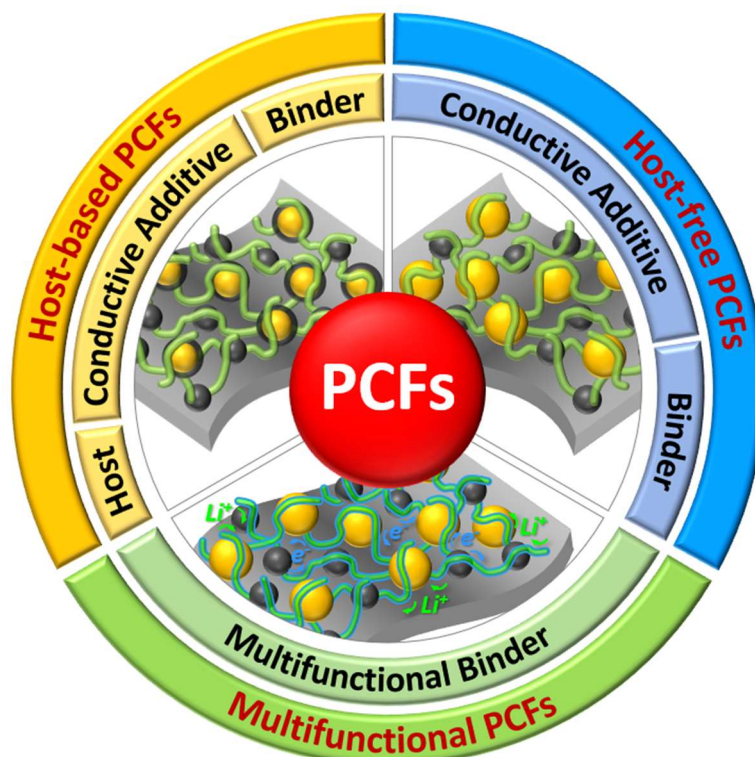


Figure 2.1: Three polymer composite frameworks (PCFs) in Li–S batteries; sulfur host-based PCFs, sulfur host-free PCFs, and multifunctional PCFs for sulfur cathodes in Li–S Batteries

2.4 Polymeric Binders in LIBs

2.4.1 General Binding Mechanism

As the electrodes in LIBs are composite electrodes containing the active material and conductive additives, polymeric binders are employed to ensure intimate contact between the electrode components and the current collector is maintained over extended cycling. Before an in-depth review of binders in Li–S batteries is carried out, a summary of the adhesion mechanism is provided. An electrode slurry can be fabricated by combining a binder solution and the desired active materials. During this step, the solution can thoroughly wet the surface pores of the particles. Once the slurry is coated and dried, adhesion throughout the polymer composite framework is achieved. This adhesion can be thought to arise via two mechanisms, mechanical interlocking and interfacial forces, as shown in **Fig. 2.2** [13].

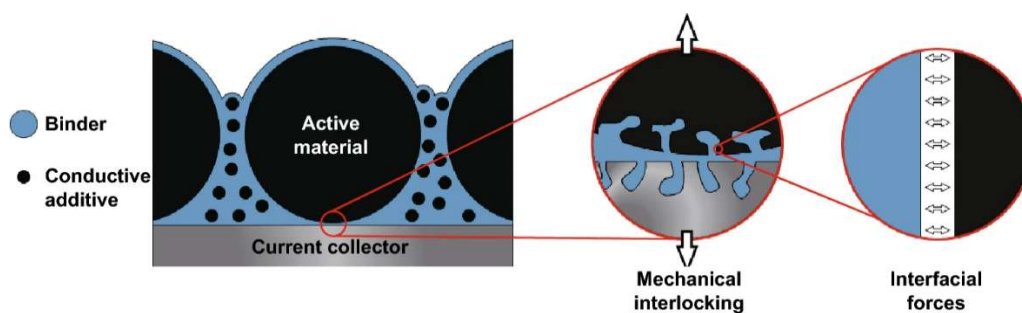


Figure 2.2: The roles of polymeric binders in a typical LIB

2.4.1.1 Mechanical Interlocking

D.E. Packham has provided a fascinating history into the role of mechanical interlocking in adhesion theory [14]. Mechanical interlocking arises when a binder solution penetrates the pores of a particular surface (or surfaces) and is subsequently hardened. As the binder solution solidifies in situ, a solid, embedded film remains in the material's pores, leading to adhesion. The surface roughness influences the adhesion strength, which allows for a higher area for bonding [15] and the nature of the adhesive itself [16].

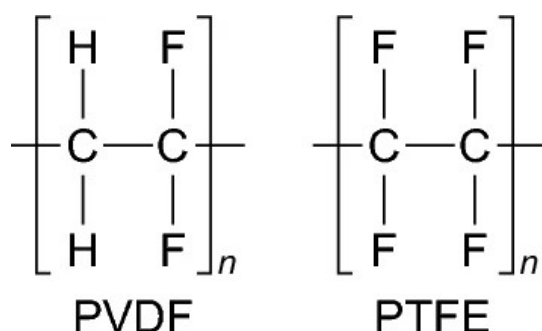
2.4.1.2 Interfacial Interactions

Various adhesive mechanisms which occur at the interface between the adhesive and the active material surface have been proposed [17]. The mechanisms most commonly encountered in LIBs adhesion include intermolecular forces, electrostatic forces, and covalent bonding, which occur at the binder/surface interface. In the case of intermolecular forces, the adhesive strength between two materials can be improved if the ever-present Van der Waals forces are supplemented by hydrogen bonding between the binder and substrate [18]. Similarly, the adhesive strength can be improved if either electrostatic [19] or covalent bonds [20] occur at the interface. For a more comprehensive introduction to the forces that occur both at the interface and within a binder itself, we refer readers to our recent review, which thoroughly investigates the matter [13].

2.4.2 Challenges of Traditional Binders

Fluorine containing polymers have experienced remarkable success when applied in energy storage devices such as batteries [13], supercapacitors [21], and fuel cells [22] and are the current status quo for binders in energy storage devices. Poly(vinylidene fluoride) or poly(vinylidene difluoride) (PVDF) (**Scheme 2.1**) is mainly produced by emulsion or suspension polymerization [11] and is the most widely used binder in battery electrodes due to its relative chemical inertness and stability over a wide voltage window [23].

Poly(Tetrafluoroethylene) (PTFE) (**Scheme 2.1**), another fluoro-polymer, has also found success in energy storage devices, particularly in supercapacitors due to its more superior tolerance to alkaline conditions compared with PVDF [24]. However, its inferior mechanical/adhesive properties have led to the dominance of the PVDF binder in battery systems. As PVDF is the most common binder in batteries, its limitations are the most relevant and are briefly discussed below.



Scheme 2.1: The molecular structures of the PVDF and PTFE

2.4.2.1 Chemical Stability

Although wildly successful and chemically stable under various conditions, PVDF still causes operational concerns due to its chemistry. PVDF can react with lithium metal (or lithiated graphite) during high-temperature operation to form LiF [25]. Furthermore, under “abuse-conditions” such as over-charge/discharging or short circuits, unwanted reactions with PVDF can cause thermal runaway, which leads to safety concerns [26]. Finally, PVDF has been shown to cause accelerated degradation of active materials at contact points under elevated temperatures [27].

2.4.2.2 Adhesion Strength

The polymer backbone of PVDF consists of alternating CH₂ and CF₂ species, which, according to the aforementioned binding theory, delivers adhesion through mechanical interlocking and Van der Waals forces. Although the C-F bond in PVDF is highly polar due to fluorine’s electronegativity, the polymer arranges itself so that the dipole moments cancel each other out [28]. Therefore, PVDF cannot produce strong interfacial interactions (i.e., hydrogen bonding, electrostatic interactions, or covalent bonds) toward the active materials or current collector. As a result, the more robust bonding mechanisms mentioned previously do not present themselves in PVDF-based electrodes. What is more, PVDF is prone to swelling in common LIB electrolytes, which can lead to the migration of the electrolyte between the binder/substrate interface [29], which reduces the intimate contact between electrode components required for

tight bonding. Thus, it proves difficult for the PVDF binder to maintain a stable electrode structure over extended cycling.

2.4.2.3 Environmental, Health and Cost Concerns

PVDF is a rather costly synthetic polymer that is only soluble in volatile and toxic organic solvents, with the most commonly used solvent being N-methyl pyrrolidine (NMP) [30]. A shift toward aqueous-soluble binders could not only lower costs but could also reduce the associated health hazards and environmental impact associated with the manufacturing and recycling of secondary cells.

2.5 Working Mechanisms and Challenges of Li–S Batteries

2.5.1 Li–S Battery Working Mechanism

A typical Li–S cell contains a composite sulfur cathode (containing sulfur, a conductive additive, and a binder), lithium metal anode, separator, and organic electrolyte. As discharge begins, Li^+ ions migrate from the anode to the cathode so that the reduction of elemental sulfur can begin. A multi-step electrochemical reaction occurs with two associated voltage plateaus, as shown in **Fig. 2.3** [31].

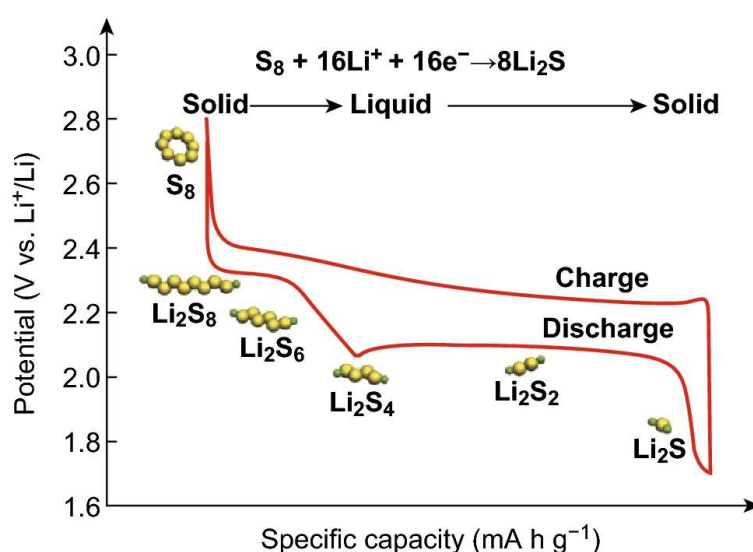


Figure 2.3: A typical charge/discharge profile for a Li–S battery. Reproduced with permission from Ref. [31]. Copyright 2017 John Wiley and Sons

The voltage plateau at 2.4 - 2.15 V corresponds to the formation of long-chain polysulfides (Li_2S_x ; $x = 4 - 8$). As the long-chain polysulfides are soluble in organic electrolytes, this portion of the electrochemical reaction involves a solid to liquid phase conversion of the active material and supplies $\approx 418 \text{ mAh} \cdot \text{g}^{-1}$ toward the total discharge capacity [8]. Upon further lithiation, the

long-chain polysulfides are converted to short-chain polysulfides (Li_2S_x ; $x = 1 - 2$), which are insoluble in the electrolyte and precipitate at the cathode surface, providing the remaining $\approx 1254 \text{ mAh}\cdot\text{g}^{-1}$ for a total of $1672 \text{ mAh}\cdot\text{g}^{-1}$ specific capacity which roughly corresponds to an energy density of $2600 \text{ Wh}\cdot\text{kg}^{-1}$ (based upon the complete formation of Li_2S) [31].

2.5.2 Challenges and Strategies of Li–S Batteries

The limitations of conventional LIBs have led researchers to investigate higher energy density storage options [6]. Li–S batteries, one of the most promising options, have received well-deserved attention, with over 1000 research papers published on this topic since 2015 [9]. Such devoted attention to this system aims to solve the inherent problems with the Li–S cell, which are briefly introduced below.

2.5.2.1 Low Electronic and Ionic Conductivity of Sulfur

It is well established that sulfur cathodes suffer from low electron and ion transportation due to the insulating nature of both sulfur and its discharge product, Li_2S , which results in poor rate kinetics and low sulfur utilization [32]. What's more, upon discharge, a passivating layer of Li_2S can form on the cathode surface, further reducing the cell's capacity [33]. In Li–S cells, the low conductivities are typically addressed by implementing conductive sulfur hosts within the cathode [34, 35]. Additionally, to gain a better theoretical understanding of the ionic transport mechanisms within battery components, researchers have turned to density functional theory (DFT) calculations [36].

2.5.2.2 Volume Expansion of Sulfur

Another challenge in Li–S cells pertains to the volume expansion experienced by the active materials during discharge [37]. Upon complete lithiation, the elemental sulfur undergoes a volume expansion of $\approx 70\%$ [38], which can cause internal stresses within the electrode and results in electrode pulverization and capacity decay [39]. The volume fluctuations of the active materials are typically combated by the rational design and implementation of nanostructured sulfur hosts in the Li–S cathode [5].

2.5.2.3 The Shuttle Effect of Polysulfides

The most significant challenge relating to Li–S batteries is dubbed the “shuttle effect” (or shuttle phenomenon) [40]. This issue arises from the phase transformation of the active material during discharge, wherein the solid elemental sulfur is reduced to long-chain polysulfides (PSs), which are highly soluble in the common organic electrolytes found in Li–S cells. This formation of soluble long-chain polysulfides causes a concentration gradient to

arise, which promotes the migration of these species toward the anode, where they can undergo parasitic reactions, causing a severe reduction in the discharge capacity and efficiency of the battery [41].

Initial attempts to curtail the PS shuttle involved the restriction of PSs through physical means, including surface coatings and the loading of sulfur into porous materials at the cathode, but more recent solutions include the chemical restriction of PSs [42]. DFT calculations have been utilized to investigate mechanisms by which PSs can be chemically anchored within the Li-S battery, including through the lithium bond [43], heteroatom doping (particularly N and O doping) [44], and transition metal sulfide bonding [45].

A wide variety of materials have recently been investigated which aim to suppress the PS shuttle by various means, as summarized in the recent reviews on polar materials [46], metal oxide/sulfides [7, 47], organosulfur polymers [48], porous organic polymers [49], redox mediators [50], and flexible materials [51] for Li-S batteries. These chemical PS anchors are commonly applied in the cathode of Li-S batteries, which significantly improve Li-S performance [52-62]. Another successful approach to anchor the PSs and prevent their migration to the anode is the application of functionalized interlayers and separators [34, 35, 49, 63-67]. Overall, anchoring the PS at either the cathode or the separator has dramatically improved the capacity retention of Li-S cells over extended cycles.

2.5.2.4 Low Sulfur Loading and High Electrolyte/Sulfur (E/S) Ratio

There are two key considerations which must be addressed concerning the sulfur loading in Li-S cells. The first relates to the sulfur weight fraction in the composite electrode and the second relates to the areal sulfur loading. Fang et al. [31] suggest a sulfur weight fraction of over 70% in the active materials and an areal loading of over $5 \text{ mg}\cdot\text{cm}^{-2}$ for a reliable Li-S cell. Over the last few years, significant improvements have been made concerning the composite's sulphur loading and the areal sulfur loading [34].

The electrolyte is another crucial component of the Li-S cell. The go-to solution for electrolytes in Li-S batteries has been liquid organic electrolytes [68], but recently researchers have turned their attention to solid electrolytes [69]. However, regardless of the electrolyte system chosen, another challenge with the Li-S cell is the excessive amount of electrolyte used in the cells reported in the literature, resulting in a high electrolyte to sulfur (E/S) ratio reported in test cells. Often, an E/S ratio greater than $7 \text{ }\mu\text{L}$ of electrolyte to 1 mg of sulfur is used to obtain a high sulfur utilization; however, an E/S ratio of less than 4:1 is required so that the

energy density of the Li-S cell can reach suitable levels [70]. Fang et al. [31] have shown that among the literature that reports the E/S ratio of Li-S cells (which is already the minority of literature), over half use an E/S ratio of greater than 10:1, with only 3 achieving a ratio of 4:1 or lower. Liu et al. [34] have shown that little has changed concerning the E/S ratio of Li-S cells in the literature over the past few years. More recently, however, researchers are beginning to work on this problem [71].

2.5.2.5 Unstable Lithium Metal Anode

As mentioned earlier, the Li-S cell relies on a lithium metal anode, which is an attractive candidate for high-energy-density batteries due to its remarkable theoretical capacity of $\approx 3860 \text{ mAh}\cdot\text{g}^{-1}$ and low electrochemical potential of -3.040 V versus the standard hydrogen electrode (SHE) [72]. However, the Li metal anode suffers from a practically infinite volume expansion, parasitic reactions with the organic electrolyte and PSs, as well as dendrite formation during cycling, resulting in an unstable solid electrolyte interphase (SEI) layer, electrolyte depletion, and a decreased cycling efficiency [73, 74]. Attempts to rectify the problems caused by the lithium metal anode include polymer protecting layers and artificial SEI layers applied either ex-situ or formed in situ through electrolyte additives [75]. Additional approaches include the fabrication of 3D host materials to house lithium metal [34, 35].

2.5.2.6 Safety of the Li-S Cell

In addition to the challenges regarding the performance of the Li-S cell, some significant safety concerns must be overcome for successful Li-S commercialization. In addition to reducing cell efficiency, dendrite growth in Li metal anodes can pierce the separator and cause short circuits within the cell, resulting in thermal runaway and explosions [73]. Additionally, LiNO_3 is commonly used as an electrolyte additive to passivate the Li anode and inhibit PS shuttling; however, it is prone to excessive gassing in pouch cells [70], causing an increase in internal pressure resulting in a risk of explosion [34, 69]. Recent approaches, which aim to increase the safety of Li-S cells, include the application of specially tailored liquid and solid electrolytes [69] and the inclusion of flame retardant materials within the cell [76, 77].

2.5.2.7 Polymer Composite Frameworks in Li-S Batteries

As mentioned earlier, a significant amount of research on the Li-S system has been focused on the cathode host materials; however, the polymer binder, a crucial component of a high-performance cathode, is comparatively under-researched [9]. In order to review the research progress in this area, we first classify the type of PCF based on the components present in the

cathode. For the sake of this review, we define a host-based PCF as a cathode constructed using sulfur, a sulfur host, conductive additives, and a polymeric binder. First, we discuss the role of the binders in host-based PCFs. Another PCF forgoes the traditional sulfur-host entirely and sulfur cathodes are fabricated simply through the combination of sulfur, conductive additives, and a binder. In this review, we dub these cathodes as host-free PCFs. The role of polymeric binders in host-free PCFs are reviewed in the next section. Finally, researchers have turned to multifunctional binders to impart additional features into the Li-S cathode, which we review in the final section.

2.6 Sulfur Host-Based Polymeric Composite Frameworks

2.6.1 Sulfur Hosts and Interlayers in Li-S Batteries

A plethora of research into sulfur host-based cathodes in Li-S batteries (LSBs) has shown that the application of these materials can enhance the electrochemical performance of LSBs in a multitude of ways. Typical sulfur host materials include hierarchical porous carbons [78], heteroatom-doped carbon [79], and transition metal oxides/sulfides [47]. The success of sulfur hosts in LSBs stems from their unique ability to simultaneously alleviate many of the technical limitations of the chemistry in LSBs [8].

As mentioned in the previous section, the commercialization of LSBs is hindered by the insulating nature of sulfur and its discharge products (Li_2S_2 and Li_2S). Early attempts to improve the electrochemical performance of the LSBs relied on the addition of a simple conductive additive, for example, Carbon Black, into the composite cathode so that the electronic conductivity of the cathode could be improved [80]. By improving the electronic conductivity of the composite, electronic pathways between the current collector (and thus, the external circuit) and the electroactive sulfur species can be enhanced so that more of the electronically insulating species can participate in the electrochemical processes [81]. Since this development, the conductive additives have been modified further to enhance the Li-S cathode in a multifunctional capacity.

The first step in the transition between traditional conductive additives and multifunctional sulfur hosts was the realisation that a porous and conductive structure can house the sulfur within the material, rather than simply distributing the sulfur and conductive additive throughout the cathode, as shown by Nazar et al. [82]. This development gave rise to the class of materials now known as sulfur hosts. The incorporation of the sulfur in the porous host matrix improves the electrochemical performance of the LSBs by reducing the agglomeration

and particle size of the sulfur material throughout the cathode, which in turn shortens electronic pathways and improves the sulfur utilization in the cathode [83].

However, in contrast to traditional conductive additives, sulfur hosts can enhance the performance of the LSBs due to their multifunctional nature [84]. In addition to shortening the electronic pathways, porous host materials also provide an ample void structure that can house the sulfur. Traditionally, the expansion of the sulfur species during discharge causes electrode pulverisation, which reduces the electrochemically active regions of the cathode and causes rapid capacity fading [85]. When the ample void structure is provided by the porous hosts, the material expansion is buffered and the electrode damage can be avoided, which enhances the longevity of the LSBs. The void structure of the host material also allows for a sufficiently high sulfur loading in the cathode, which helps to address the concerns related to insufficient sulfur content in the electrode [86].

The most important feature of the recently developed sulfur hosts relates to their polysulfide retention ability [87]. Early works into this phenomenon investigated various conductive porous carbon materials, which were shown to physically trap the soluble polysulfides in the micropores thereby reducing the polysulfide shuttling phenomenon and enhancing the capacity retention in LSBs [88]. Although initially effective, over extended cycling, physical trapping of polysulfides becomes ineffective and the capacity fading associated with the shuttle effect persists [89].

In response to this, researchers began investigating porous sulfur host materials with tailored chemical functionality, which enables the chemical trapping of soluble polysulfides at the cathode surface [90]. The chemical retardation of soluble polysulfides was vastly superior to previous attempts based on physical trapping, and led to an astounding amount of literature on the topic.

Finally, multifunctional sulfur hosts can enhance the electrochemical performance in the LSBs by catalysing the conversion of polysulfide intermediates in the cell and work reducing the energy barriers associated with the complex multi-step conversion of polysulfides, which is especially beneficial in fast charge/discharge settings [91-93].

The success of the multifunctional sulfur host has been thoroughly reinforced in recent literature, with the mechanisms of action thoroughly investigated. Since the exploratory studies into these materials have been conducted, researchers can now shift their attention to the scalability, environmental impact, and costs of sulfur hosts going forward.

Another common approach to enhance the electrochemical performance of the LSBs is achieved through the application of multifunctional interlayers [63]. Interlayers can be applied as free-standing components [94], cathode surface coatings [95], or as a coating applied at the separator of the cell [96]. The materials used in the fabrication of multifunctional interlayers closely mirror those used as sulfur hosts in LSBs, with investigations into carbon [97], metal oxides [98], and metal sulfide-based interlayers [99] being produced from a wide range of researchers.

Not only are the materials that are used for Li-S interlayers similar to those used for sulfur hosts, but so too are the mechanisms by which the performance is improved in the LSBs. Carbon-based interlayers enhance the electronic conductivity of the cathode composite by acting as an upper current collector, which can reduce the electrochemically inaccessible sections of the cathode, thus enhancing sulfur utilisation and improving electrochemical performance under fast charging/discharging conditions [100]. Additionally, similar to carbon-based sulfur hosts, the carbon-based interlayer can physically trap the soluble polysulfides at the cathode side of the LSBs, reducing the polysulfide shuttling phenomenon and improving the longevity of the cell [101].

Polar heteroatom-doped carbons, metal oxides, and metal sulfides applied at the interlayer of the LSBs, similar to their sulfur host-based counterparts, also provide chemical polysulfide retention. Again, this retention ensures the soluble polysulfides are trapped at the cathode side of the cell, which reduces the troublesome effects of the shuttle effect [102]. Catalytic materials applied at the interlayer also facilitate the rapid conversion of reaction intermediates in the LSBs [103].

Although the multifunctional sulfur hosts and interlayer materials share many similarities, a significant difference between the two materials can be observed. Due to the fact that the interlayer material is applied only at the surface of the cathode, not throughout the entire cathode as is the case for sulfur host-based composite, less of the material is required to elicit a similar effect, which has significant ramifications on the total mass, and thus the energy density, of the entire cell [104].

Regardless of whether the multifunctional material is applied as a sulfur-host or as an interlayer, the interactions between the material and the polymer binder must be thoroughly considered. These considerations are detailed thoroughly in the subsequent sections.

2.6.2 Mechanical Interlocking Between Binders and Sulfur Host

A selection of hosts and binders in host-based Li–S batteries are listed in **Table 2.1**. It can be seen that the most commonly used binders are PVDF and PTFE. Due to the inertness of the polymers, the interaction between these polymers and sulfur is weak; however, because the polymer can penetrate and interlock the pores of the sulfur host, a relatively stable structure is obtained, and the electrode can still deliver acceptable electrochemical performance in Li–S batteries [105, 106].

As mentioned earlier, a vast array of sulfur hosts has been investigated for use in sulfur cathodes. Of these, the carbonaceous host materials are generally porous so that the binder can mechanically interlock the sulfur host, while the host can provide an efficient confining structure for sulfur. Morphologies of the host can include hollow carbon spheres [102], carbon nanotubes [129], graphene [130], and hierarchical porous carbons [131]. For example, Zhao et al. synthesized a tube-in-tube carbon nanotube structure as a host for Li–S batteries while using PVDF as a binder to fabricate a host-based PCF structure, as shown in **Fig. 2.4** [130]. The Li–S battery exhibited excellent electrochemical performance due to the porous carbon layers' good electrical conductivity and large pore volume. The specific capacity remained at $918 \text{ mAh}\cdot\text{g}^{-1}$ at $500 \text{ mA}\cdot\text{g}^{-1}$ after 50 cycles and $647 \text{ mAh}\cdot\text{g}^{-1}$ at $2 \text{ A}\cdot\text{g}^{-1}$ after 200 cycles. It also delivered high capacity at high current density ($550 \text{ mAh}\cdot\text{g}^{-1}$ at $6 \text{ A}\cdot\text{g}^{-1}$).

Table 2.1: PCFs via the interlocking binding mechanism for Li–S batteries

Binder	Sulfur Host	Reference(s)
PVDF	Nitrogen-doped porous carbon	[105]
	Flower-shaped porous carbon	[107]
	Monolithic carbon	[108]
	Nitrogen-doped carbon nanofiber	[109]
	Hollow carbon nanofiber	[110]
	Carbon nanocube	[111]
	Nitrogen-doped porous carbon	[112]
	Porous carbon layer	[113]
	Mesoporous carbon	[114-118]
	PPy	[119]
	Carbon nanotube	[120, 121]
	Ti ₄ O ₇	[122]
	MnO ₂	[123]
	Co ₉ S ₈	[124]
	Porous carbon aerogel	[125]
PTFE	Li ₂ S/TiO ₂ -impregnated hollow CNF	[126]
	Ti ₂ C	[127]
	Porous carbon nanosheets	[106]
	Carbon sphere	[128]

Similarly, structured metal oxides [122], metal sulfides [124], and metal carbides [127] can provide sites for binder mechanical interlocking while simultaneously housing the sulfur active materials. Many researchers have already provided in-depth reviews on the design of sulfur hosts, which we direct readers to for further information [7, 34, 35, 46-51, 133-137].

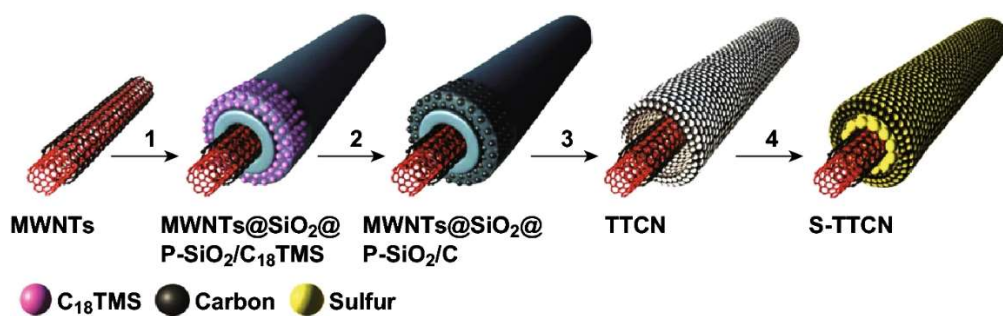


Figure 2.4: Schematic illustration for the formation of S-TTCN composite: (1) Uniform coating a solid SiO₂ layer and a porous SiO₂ layer embedded with C₁₈TMS molecules on MWNTs; (2) formation of porous carbon nanotube by carbonization of C₁₈TMS; (3) etching SiO₂ layers to obtain tube-in-tube carbon nanostructure (TTCN) with MWNTs encapsulated within hollow porous carbon nanotube; (4) sulfur infused into TTCN to fabricate S-TTCN composite. Reproduced with permission from Ref. [130]. Copyright 2014 John Wiley and

Sons

2.6.3 Combined Interfacial Forces in Polymer Composite Frameworks

In some cases, a host-based PCF based on PVDF/PTFE can still deliver suitable electrochemical performance due to the functionality provided by the sulfur host, while these binders maintain electrode integrity through weak adhesive interactions. However, to further improve the stability of the electrode, binders with functional groups have been explored for Li-S batteries, especially for high sulfur loading cathodes where PVDF/PTFE binders become insufficient. The binders poly(acrylic acid) (PAA), carboxymethyl cellulose (CMC)/styrene butadiene rubber (SBR), and sodium alginate (SA) contain abundant hydroxyl or carboxylate groups that can provide strong binding forces for the electrodes [13]. The interaction between binders and hosts should be further enhanced to obtain prolonged cycles for high-loading electrodes. As shown in **Table 2.2**, many novel binders have been designed to work with the hosts synergistically.

Table 2.2: PCFs composed of binders and sulfur hosts with additional interfacial binding forces in Li–S batteries

Binder	Sulfur Host	Reference
CMC/SBR	Meso@microporous carbon	[138]
CMC/SBR	PPy warped mesoporous carbon	[139]
CMC/SBR	CNF	[140]
CMC/SBR	CNF	[141]
CMC/SBR	Co ₉ S ₈	[124]
CMC	PAN	[142]
CMC	Hollow porous carbon sphere	[143]
SA	Hollow carbon nanorod	[144]
SA	Microporous carbon	[145]
LA132	Nitrogen-doped carbon sphere	[146]
LA133	Core-shell carbon sphere	[147]
PAA	S-CPAN	[148]
PMMA	FeS ₂	[149]
PVP/PEO	CNF	[150]
Nafion/PVP	Porous carbon sphere	[151]
Nafion	Nickel sulfide/hollow carbon spheres	[152]
PVP	Porous carbon sheets	[153]
PES	CNT	[153]
PEB-1	Nitrogen-doped mesoporous carbon	[154]
D11	Porous carbon sheets	[152]
PDAT	Porous carbon sheets	[152]
PANi	CNF/S	[152]
GG	PAN	[155]
Carbonyl β -cyclodextrin	PAN	[156]

Binder	Sulfur Host	Reference
Polycation β -cyclodextrin	PANi	[157]
Double-chain polymer	Carbon material	[158]

For example, a PVDF binder was sufficient to maintain electrode integrity and obtain stable cycle performance when using a Co_9S_8 host with a sulfur loading below $2.5 \text{ mg}\cdot\text{cm}^{-2}$. However, when the electrodes were fabricated with higher sulfur loadings ($2.5\text{-}4.5 \text{ mg}\cdot\text{cm}^{-2}$), the use of a CMC/SBR binder was required to maintain the high capacity and stable cycles [124]. Another example is that Kim et al. [159] investigated PAA as a binder in host-based PCF Li-S cathodes. The group combined sulfurized carbonized poly(acrylonitrile) (S-CPAN) as a sulfur host and PAA as a binder to form the framework. The PAA-based electrode delivered a higher specific capacity upon cycling than the PVDF-based electrode while also delivering a higher Coulombic efficiency (CE) (**Fig. 2.5a and b**). After 100 cycles, post-mortem analysis of the electrode cross-section under SEM revealed severe delamination in the PVDF-based framework (**Fig. 2.5c**); however, there was still intimate contact between the electrode film and current collector when PAA was used as the binder (**Fig. 2.5e**). The surface of the PVDF-based electrode displayed large cracks, whereas the PAA-based electrode maintained its integrity. The group suggested that the structural integrity was maintained in the cathode due to hydrogen bonding occurring between the carboxylate groups of the PAA and the OH groups found on the carbonized PAN and current collector. This hydrogen bonding displayed high elasticity and maintained intimate contact between electrode components during the volume expansion/contraction of the S-CPAN upon cycling. Following this, an FEC additive was used to stabilize the lithium metal anode in the alkyl carbonate electrolyte, which enabled a 98.5 % capacity retention ($\approx 1500 \text{ mAh}\cdot\text{g}^{-1}$) after 100 cycles at 0.5C.

Rao et al. [141] used a chemical deposition method to prepare a CNF-S composite. From there, they fabricated host-based PCF cathodes using PVDF in NMP, poly(ethylene oxide) (PEO) in acetonitrile, and CMC/SBR (2:3) in water as binders, respectively. By observing the discharge profiles (**Fig. 2.6**), it was seen that the CMC/SBR and PEO-based frameworks displayed a lower voltage plateau of around 2.0 V, compared with the PVDF-based framework's lower voltage plateau of 1.95 V, which suggests a greater degree of polarization in the PVDF-based cell. Upon extended cycling, the discharge capacities were 586, 420, and 350 $\text{mAh}\cdot\text{g}^{-1}$ for the CMC/SBR, PEO, and PVDF-based batteries, respectively, highlighting the superior capacity retention when CMC/SBR is used as a binder.

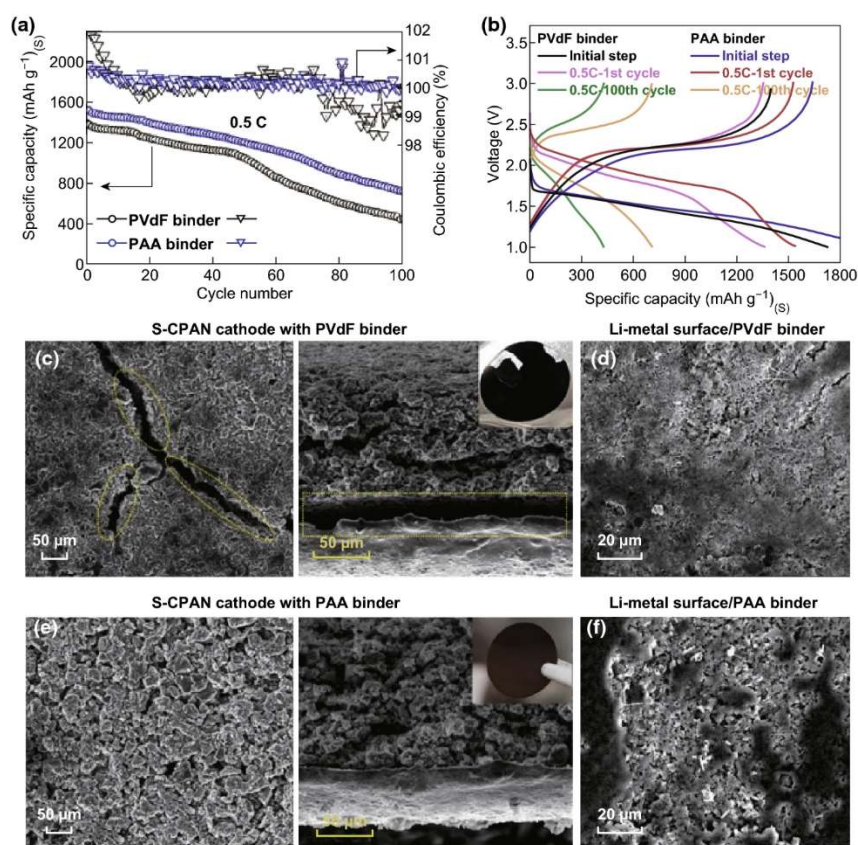


Figure 2.5: (a) Cycle retention graph and (b) charge-discharge curve graph of S-CPAN cells with PVdF and PAA binders. SEM images of (c) surface and cross section of S-CPAN with PVdF binder electrode, (d) lithium metal surface of S-CPAN cell with PVdF binder, (e) surface and cross section of S-CPAN with PAA binder electrode, and (f) lithium metal surface of S-CPAN with PAA binder after 100 cycles. Reproduced with permissions from Ref. [159]. Copyright 2017 American Chemical Society

Lacey et al. investigated the effects of binders and hosts in Li–S batteries. They fabricated an acceptably high sulfur loading cathode using their optimized poly(vinylpyrrolidone) (PVP):PEO binder [149]. They found that with a small addition of CNFs into the cathode, the homogeneity of the electrode film was vastly improved (**Fig. 2.7**), which allowed for increased sulfur loading up to 5 mg·cm⁻² without delamination of the electrode film.

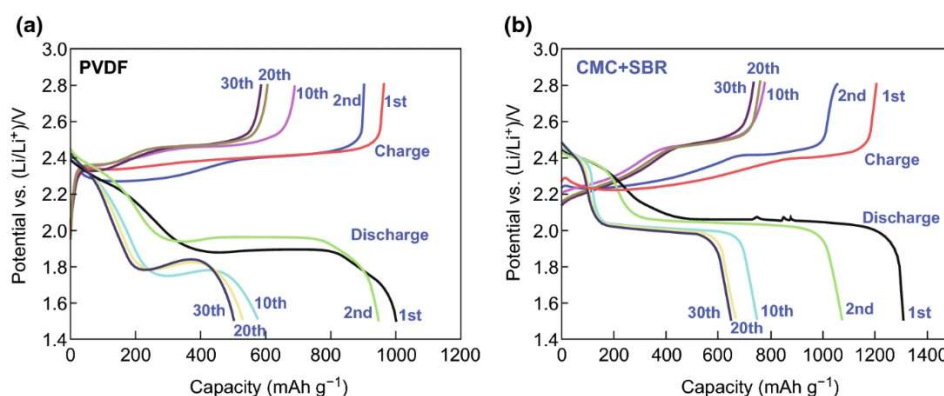


Figure 2.6: Charge and discharge curves of (a) lithium/sulfur cell with a PVDF binder and (b) CMC + SBR binder at 0.05C. Reproduced with permission from Ref. [141]. Copyright 2012 Elsevier

Oppositely charged binders can also enhance the mechanical properties of the electrodes. Soft-pack Li-S batteries with an ultra-low binder content of 0.5 wt% were fabricated by Wang et al. [150]. The group used an innovative layer-by-layer air spray method to synthesize a Nafion/PVP (N/P)-based Li-S electrode (**Fig. 2.8**). The adhesion of the electrode film was examined via a peel test, which revealed the N/P binder delivered a stronger adhesion with 0.5 wt% than the PVDF film with 10 wt% loading owing to the electrostatic interaction between the positively charged PVP and negatively charged Nafion. The as-fabricated pouch cells delivered a higher initial capacity and a slower capacity decay than the PVDF batteries, even with the ultra-low binder loading.

Besides the solid binding forces, the binders are also expected to be multifunctional. Considering that, various functional binders have been explored for host-based sulfur electrodes, such as electronically and ionically conductive binders [142, 158]. For example, a poly(pyrrole) (PPy)-based double-chain polymer binder was developed by Liu et al. [158]. 4,4'-Biphenyl disulfonic acid (BSA) was capped with pyrrole before polymerising on a CMC matrix. The incorporation of 6.4 wt% of the BSA/PPy into the CMC matrix reduced the resistance of the composite, in turn vastly increasing the conductivity of the cathodes fabricated using this binder while simultaneously providing anchoring sites for PS retention. A thick electrode with a sulfur loading of $9.8 \text{ mg}\cdot\text{cm}^{-2}$ was fabricated and delivered a high areal capacity of $9.2 \text{ mAh}\cdot\text{cm}^{-2}$ even with a low electrolyte to sulfur ratio of 5:1 ($\mu\text{L}:\text{mg}$).

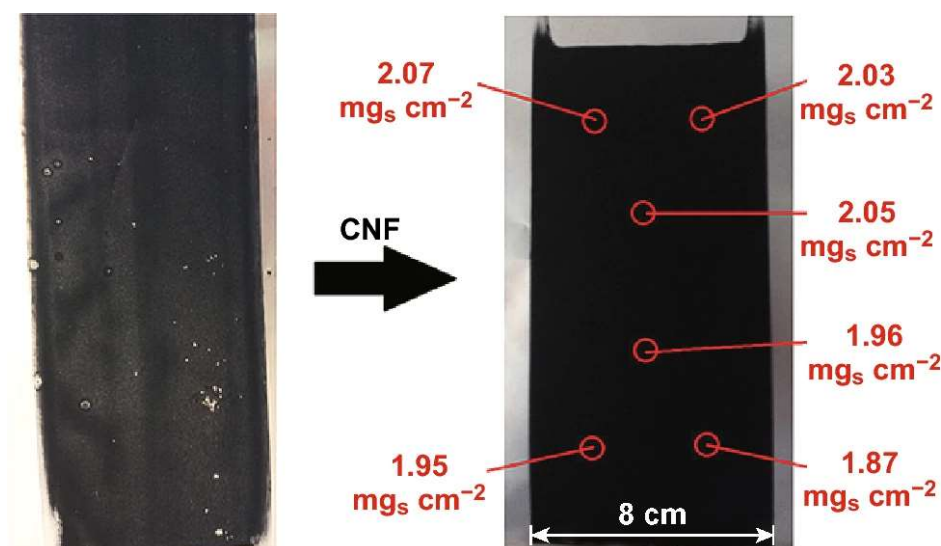


Figure 2.7: Photographs comparing the effect of a 3.5% w/w addition of carbon nanofibers to water-based slurries employing a PVP:PEO binder. Uniformity of sulfur loading is indicated for the coating with CNF. Reproduced with permission from Ref. [122]. Copyright 2017 Wiley-VCH Verlag GmbH & Co. KGaA, Weinheim

Binders can also facilitate ion transport across the electrolyte-host interface. Li et al. [154] introduced a polyelectrolyte binder—poly[(N,N-diallyl-N,N-dimethylammonium) bis(trifluoromethanesulfonyl)imide] (PEB-1) to sulfur cathodes with nitrogen-doped mesoporous carbon (N-MC) hosts, as shown in **Fig. 2.9**. Due to the high ionic conductivity of PEB-1, sulphur utilisation could be enhanced even in the depths of the mesoporous carbon. The Li–S batteries with high sulfur loading could deliver high capacities at a fast rate ($1004 \text{ mAh} \cdot \text{g}^{-1}$ at 0.2 C with a high mass loading of $8.1 \text{ mg} \cdot \text{cm}^{-2}$) and exhibit long cycle life, which is attributed to the sizeable N-doped surface area of the N-MC and facile Li^+ ion transport in the electrode as aided by PEB-1.

To further improve the design of hosts for sulfur cathodes, free-standing structures can be realized. A free-standing CNF/S/poly(aniline) (PANi) cathode was introduced by Zhu et al. [160]. A S/ CS_2 solution was first used to impregnate a carbon nanofiber mat with sulfur before a coating of PANi was applied through an in situ polymerization process. The resultant electrode delivered a reversible discharge capacity of $953 \text{ mAh} \cdot \text{g}^{-1}$ after 300 cycles at 0.2 C, owing to the ability of the 3D architecture to accommodate the sulfur volume expansion/contraction during cycling. The energy density of the entire electrode was improved through the reduction in unnecessary electrode components.

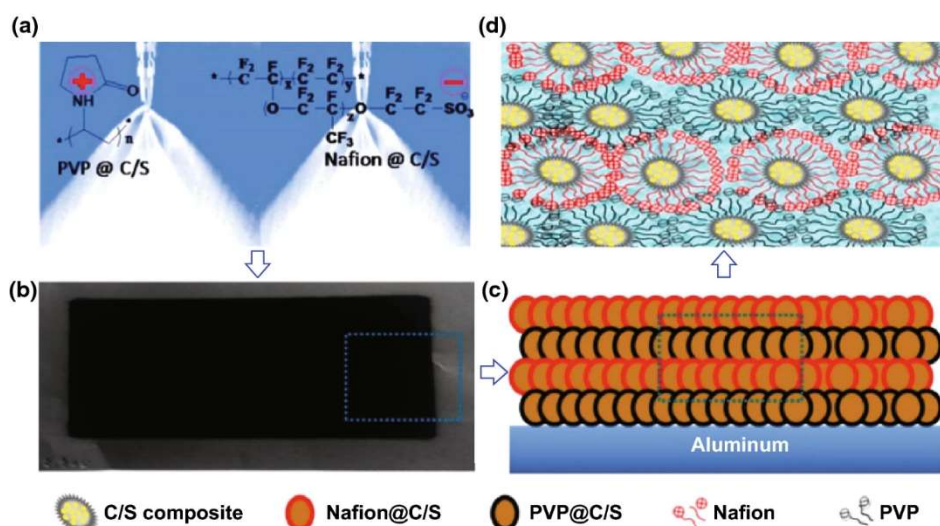


Figure 2.8: Illustration of (a) the air spray process of cathode, (b) the sprayed cathode, (c) the layer-by-layer C/S composite, (d) the cross-link between Nafion and PVP. Reproduced with permission from Ref. [123]. Copyright 2015 American Chemical Society

Overall, the implementation of rationally designed sulfur hosts has made great strides in overcoming the technical challenges associated with Li-S cells. However, there has been comparatively little research into the combined effects realized by sulfur hosts and novel binders. Future progress could be made by further investigating the combination of sulfur hosts and novel multifunctional binders.

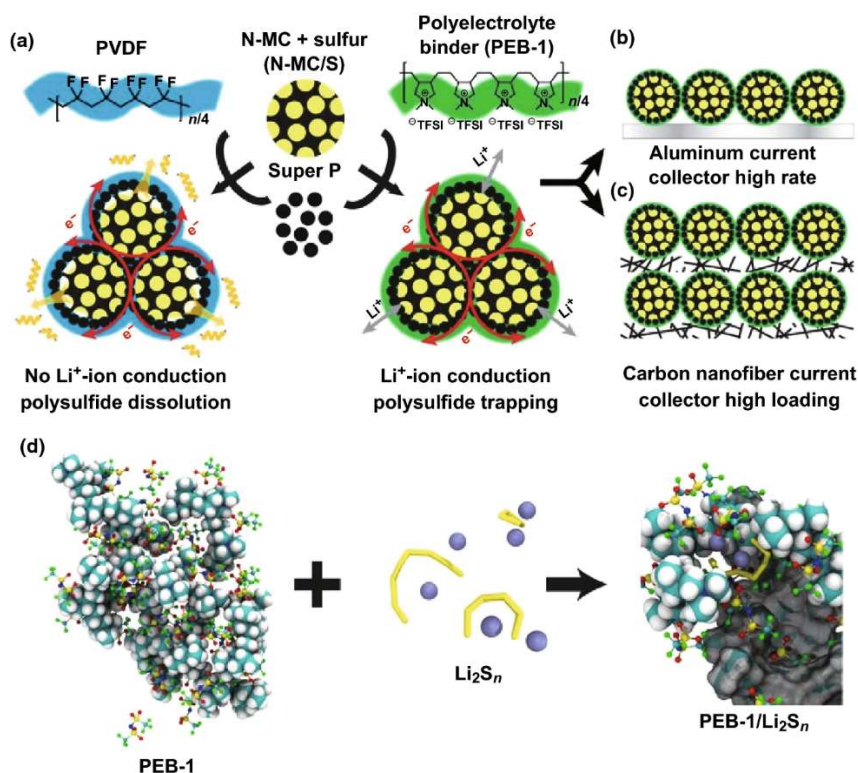


Figure 2.9: Illustration of the fabrication of sulfur electrodes with PVDF or PEB-1 binder.

(a) The cathode is comprised of sulfur-active materials loaded into N-doped mesoporous carbon (N-MC) hosts, “Super-P” as the conductive additive, and a polymer binder (PEB-1 or PVDF). (b) A conventional sulfur cathode cast onto an aluminum current collector. (c) A highly loaded sulfur cathode cast onto a carbon nanofiber current collector. (d) Schematic illustrating the formation of complex ion clusters via anion metathesis, when PEB-1 encounters soluble polysulfides during Li–S cell cycling. Reproduced with permissions from Ref. [154]

2.7 Sulfur Host-Free Polymeric Composite Frameworks

Sulfur-host-free PCFs are fabricated without the use of traditional sulfur hosts. As there is no sulfur host present, the polymeric binders' responsibility in host-free PCFs is to provide a stable electrode structure. This section reviews the research progress on host-free PCFs in Li–S batteries. A table overviewing the performances of host-free PCFs and their respective binders is provided in **Table 2.3**.

Table 2.3: Binders and their electrochemical performance in host-free PCFs

Binder	Discharge capacity @ nth cycle	C-rate	Reference(s)
<i>Natural polymers</i>			
Gelatin	544 mAh·g ⁻¹ @ 50 cycles	≈ 0.1 C	[161]
SA	508 mAh·g ⁻¹ @ 50 cycles	≈ 0.2 C	[162]
CMC/SBR (1:1)	580 mAh·g ⁻¹ @ 60 cycles	≈ 0.05 C	[163]
Chitosan	≈ 950 mAh·g ⁻¹ @ 20 cycles	0.1 C (1st 3 cycles), 0.5 C remaining cycles	[164]
GA	841 mAh·g ⁻¹ @ 500 cycles	0.5 C	[165]
GG	≈ 600 mAh·g ⁻¹ @ 400 cycles	1 C	[166]
Carrageenan	≈ 700 mAh·g ⁻¹ @ 100 cycles	0.05 C	[167]
Starch	≈ 500 mAh·g ⁻¹ @ 200 cycles	0.2 C	[168]
<i>Synthetic polymers</i>			
PVP	≈ 1000 mAh·g ⁻¹ @ 100 cycles	0.2 C	[169]
PEO	≈ 650 mAh·g ⁻¹ @ 50 cycles	0.2 C	[170]
AMAC	652 mAh·g ⁻¹ @ 100 cycles	≈ 0.05 C (1st 6 cycles), ≈ 1 C remaining cycles	[171]
PAA	325 mAh·g ⁻¹ @ 50 cycles	0.2 C	[172]
LA132	470 mAh·g ⁻¹ @ 100 cycles	0.5 C	[173]

Binder	Discharge capacity @ nth cycle	C-rate	Reference(s)
PAMAM	$\approx 640 \text{ mAh}\cdot\text{g}^{-1}$ @ 100 cycles	0.05 C (1st 2 cycles), 0.2 C remaining cycles	[174]
PEI	$744.2 \text{ mAh}\cdot\text{g}^{-1}$ @ 50 cycles	0.05 C	[175]
PQ	$885.1 \text{ mAh}\cdot\text{g}^{-1}$ @ 50 cycles	0.05 C	[176]
PDAT	$\approx 700 \text{ mAh}\cdot\text{g}^{-1}$ @ 50 cycles	0.1 C	[152]
PIL-5	$446 \text{ mAh}\cdot\text{g}^{-1}$ @ 500 cycles	0.2 C	[177]
Thiokol	$501 \text{ mAh}\cdot\text{g}^{-1}$ @ 200 cycles	0.1 C	[178]
APP	$530 \text{ mAh}\cdot\text{g}^{-1}$ @ 200 cycles	0.5C	[179]
<i>Composite binders</i>			
PVP:PEO (1:4)	$\approx 1000 \text{ mAh}\cdot\text{g}^{-1}$ @ 50 cycles	0.2 C	[180]
PEI:PVP	$\approx 580 \text{ mAh}\cdot\text{g}^{-1}$ @ 50 cycles	0.1 C charge, 0.25 C	[181]
PEI:Gelatin	$871.3 \text{ mAh}\cdot\text{g}^{-1}$ @ 100 cycles	0.5C	[182]
<i>Cross-linked binders</i>			
SA/Cu ²⁺	$758 \text{ mAh}\cdot\text{g}^{-1}$ @ 250 cycles	0.2 C (1st cycle), 1 C remaining	[183]
XG/GG	$724 \text{ mAh}\cdot\text{g}^{-1}$ @ 150 cycles	0.5 C	[184]
Amino functional group binder	$\approx 400 \text{ mAh}\cdot\text{g}^{-1}$ @ 600 cycles	2 C	[185]
PEI/PEGDGE	$430 \text{ mAh}\cdot\text{g}^{-1}$ @ 400 cycles	1.5 C	[186]

Binder	Discharge capacity @ nth cycle	C-rate	Reference(s)
PEI/ER	829 mAh·g ⁻¹ @ 1000 cycles	0.5 C	[1879]

2.7.1 Natural Polymers

Natural polymers have been a staple in binder research since Kovalenko et al. [187] used alginate to fabricate high-performance silicon anodes in LIBs. Natural polymers are abundant, environmentally friendly, aqueous-soluble, and are endowed with a high degree of functionality via their inherent functional groups. As such, natural polymers are an attractive option when fabricating host-free sulfur cathodes.

2.7.1.1 Gelatin

Gelatin is a water-soluble biological macromolecule, and in an aqueous solution, it delivers a sufficient viscosity to function as a binder in rechargeable battery electrodes [188]. Huang et al. [189] applied gelatin derived from bovine bones to form a bio-derived host-free cathode in Li–S batteries. When compared with an electrode fabricated with PEO, it was observed that the gelatin-based cathode displayed superior homogeneity of the sulfur and acetylene black conductive additive. The –COOH and –NH₂ functional groups contained in gelatin allowed for a high adhesion among the electrode components and current collector. Furthermore, as these functional groups are highly hydrophilic, the resultant polymeric framework was substantially insoluble in the organic electrolyte, which resulted in superior performance of the gelatin-based cathode [188].

Wang et al. [190] characterized a gelatin-based sulfur cathode at different discharge stages via SEM and XRD analysis. SEM images were taken before first discharge (**Fig. 2.10a**) and reveal a homogeneous distribution of sulfur, carbon, and pores throughout the polymeric framework. **Fig. 2.10b** reveals the reduction in pore volume as elemental sulfur is reduced to long-chain polysulfides, with **Fig. 2.10c** revealing a further reduction in pore volume as the long-chain polysulfides are further reduced to the insoluble short-chain polysulfides. Upon full discharge (**Fig. 2.10d**), the Li₂S layer becomes denser with a further reduction in porosity across the electrode. After a full charge, the Li₂S layer is fully oxidized, and the framework's porous structure returns (**Fig. 2.10e**). The gelatin-based cathode obtained a capacity of 1235 mAh·g⁻¹ at the first discharge and retained a capacity of 626 mAh·g⁻¹ after 50 cycles at a discharge

current density of $0.4 \text{ mA} \cdot \text{cm}^{-2}$, which the group attributed to the framework's ability to retain a stable void structure after PS dissolution.

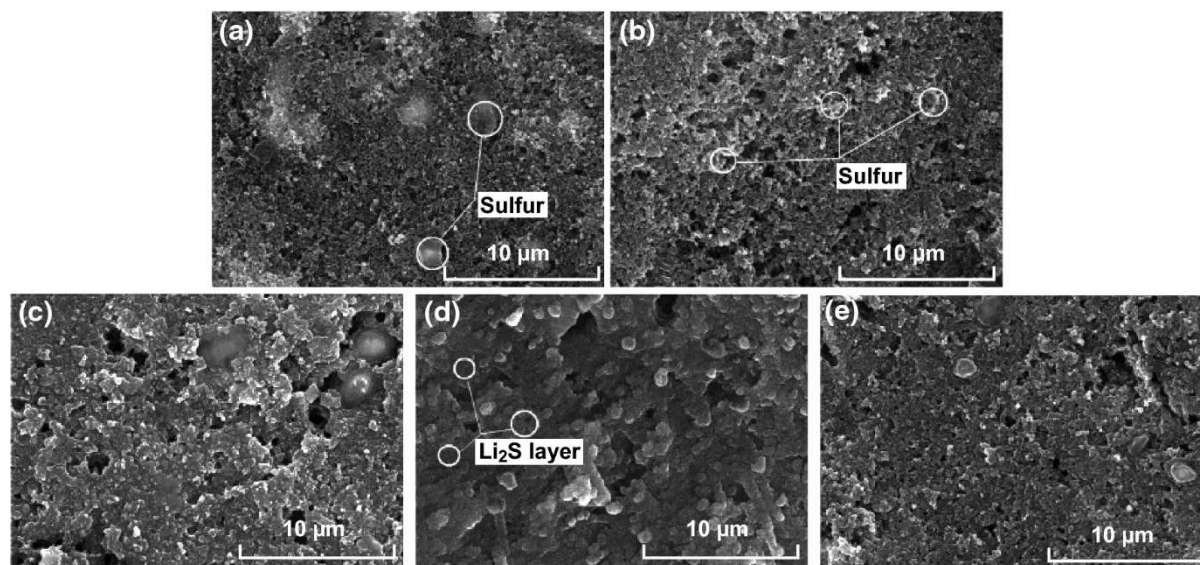


Figure 2.10: SEM images of the porous sulfur cathodes during the discharge-charge process at the (a) original, (b) 6% discharge, (c) 36% discharge, (d) full discharge and (e) first charge.

Reproduced with permission from Ref. [190]. Copyright 2009 Elsevier

Following this, the group observed the electrochemical behaviour of both the gelatin-based (SGA) and PEO-based (SPA) cathodes, as shown in **Fig. 2.11** [161]. They observed that, for the gelatin-based cathode (**Fig. 2.11a**), the two distinct plateaus are present on the discharge profile even at a high current density of $1600 \text{ mA} \cdot \text{g}^{-1}$, whereas for the PEO-based cathodes, the distinct plateaus disappear at current densities greater than $800 \text{ mA} \cdot \text{g}^{-1}$ (**Fig. 2.11b**), which suggests two different discharge mechanisms for the two cells. X-ray diffraction (XRD) analysis of both cells pre- and post-discharge supported this hypothesis by revealing that in the gelatin-based cell, no elemental sulfur remained in the XRD pattern, suggesting that all of the sulfur participated in the reaction, which they accredited to the excellent dispersion properties of the gelatin-based composite conductive binding framework. Although the gelatin-based cathode retained both of the characteristic discharge plateaus at high current densities, the specific capacity for the entire discharge was only 29% of the expected theoretical capacity. The group postulated as the first discharge region was relatively unchanged that only a part of the dissolved long-chain PS could be fully reduced on the cathode surface due to already precipitated Li_2S restricting ionic transport for the remaining active material. A freeze-drying method was employed to increase the porosity in the gelatin-based framework to provide more reaction sites for complete PS reduction to counteract this phenomenon. SEM analysis revealed

an increased porosity of the as-fabricated electrode with a corresponding specific capacity increase to $733 \text{ mAh} \cdot \text{g}^{-1}$ when discharged at $1600 \text{ mA} \cdot \text{g}^{-1}$.

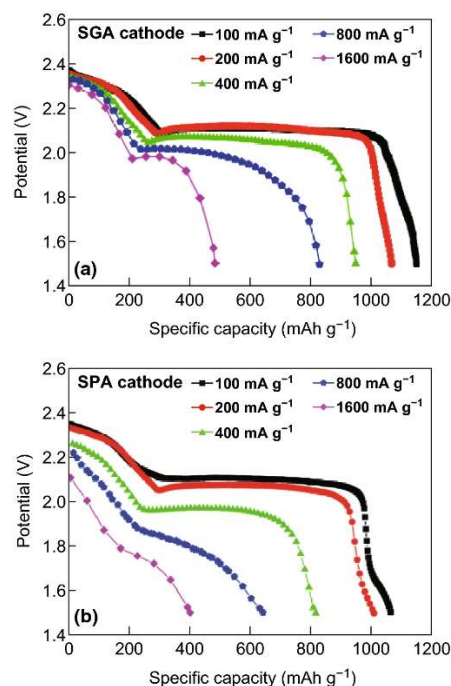


Figure 2.11: Initial discharge curves of Li-S batteries using SGA (gelatin-based) cathode (a) and SPA (PEO-based) cathode (b) at different current densities. Reproduced with permission from Ref. [161]. Copyright 2011 The Electrochemical Society

Zhang et al. [191] further investigated the dispersion properties of gelatin-based host-free cathodes by controlling the pH of the aqueous electrode slurry to observe the influence on the homogeneity of the resultant electrode. The group found that the cathode prepared at pH 10 resulted in a more even dispersion of sulfur and conductive additives across the framework when compared to the cathodes prepared at pH 8 and 5. They hypothesized that the origin of this increase in dispersion in the framework was due to gelatin's tendency to shift its conformation in solution when the pH is far from the isoelectric point (IEP). This increase in homogeneity resulted in superior performance from the cathode fabricated at pH 10, which delivered an initial discharge capacity of $1137 \text{ mAh} \cdot \text{g}^{-1}$, compared with the $1024 \text{ mAh} \cdot \text{g}^{-1}$ delivered by the pH 8 cathode and $1034 \text{ mAh} \cdot \text{g}^{-1}$ delivered by the pH 5 cathode. The pH 10 cathode mediated the active sulfur's more complete redox reaction, as evidenced by the strong re-emergence of the sulfur peak on the XRD pattern after the first discharge/charge.

Jiang et al. [192] further improved the dispersion, adhesion, and electrochemistry of gelatin-based host-free cathodes by introducing l-cysteine onto the gelatin biopolymer framework.

Incorporating l-cysteine into this framework helped reduce the polarization of the as-fabricated cathode, as evidenced by CV taken on the 1st and 10th cycle (**Fig. 2.12a**). EIS analysis also revealed a reduced charge-transfer resistance for the l-cysteine modified electrode (**Fig. 2.12b**), which the group attributed to the enhanced electronic network formed by the superior dispersion properties of the fabricated binding framework.

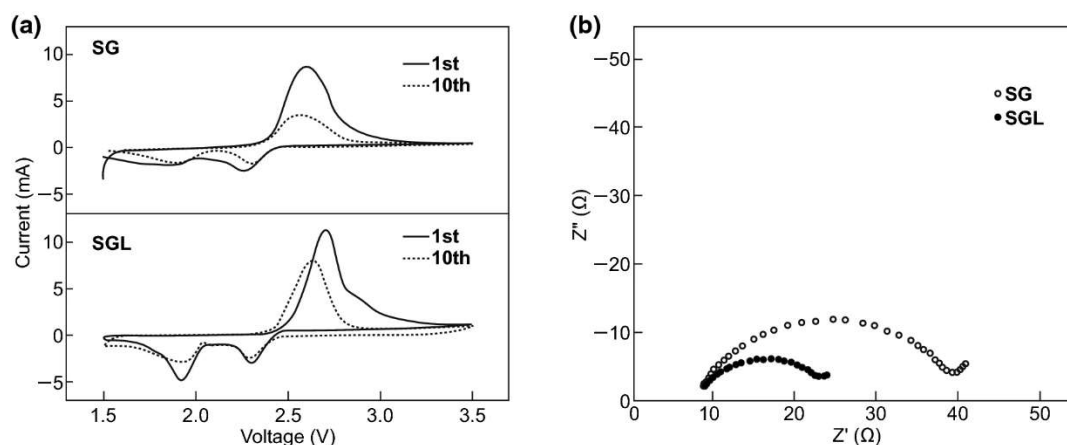


Figure 2.12: (a) CV of gelatin (SG) and l-cysteine gelatin (SGL) cathodes after 1st and 10th discharge with scan rate of $0.5 \text{ mV} \cdot \text{s}^{-1}$ and (b) impedance plots for Li-S cells with SG and SGL after 1st discharge in the frequency range of (100 kHz-100 mHz). Reproduced with permission from Ref. [192]. Copyright 2012 Taylor and Francis

2.7.1.2 Sodium Alginate (SA)

Na-alginate's adhesion and dispersion properties are well established; however, Bao et al. [162] found that polymeric frameworks based on Na-alginate can also initiate chemical interactions with the active sulfur material. The group used the relative decrease in the obtained Fourier Transform Infrared (FTIR) spectrum to confirm the interaction between the alginate and sulfur, which they postulate is the reason for the improved discharge capacity and capacity retention compared with the sulfur cathode fabricated with PVDF.

2.7.1.3 Carboxymethyl Cellulose (CMC)

CMC, derived from cellulose, is a low-cost, water-soluble, and commercially available polysaccharide, which has found uses in medical applications, pharmaceuticals, cosmetics, and, most relevantly, as a thickener, dispersion aid, stabilizer, and binder in a variety of applications [193]. CMC can be used directly as a binder in the electrode manufacturing process but, due to its crystallinity, the electrodes fabricated in this matter are stiff and rigid and prone to cracking. As such, CMC is typically combined with styrene butadiene rubber (SBR) to increase the elasticity of the composite. The CMC/SBR blend is an attractive

alternative to the conventional PVDF binder and is already finding commercial success in manufacturing graphite anodes for LIBs [23]. He et al. [163] applied a 1:1 blend of CMC/SBR to form a host-free PCF for Li-S batteries. The dispersion morphology of the electrode slurry was investigated via optical microscopy, as shown in **Fig. 2.13**. A superior dispersion was obtained for the aqueous-based CMC/SBR (**Fig. 2.13a1**) slurry compared to the PVDF-based slurry in NMP (**Fig. 2.13b1**). The group supposed that the addition of CMC into the slurry allowed the carbon black to be dispersed effectively as the carboxylate groups of the CMC can give rise to an adequate surface charge on the carbon black, stabilizing the dispersion through an electrostatic double-layer repulsion effect. They further analysed the dispersion properties by measuring the zeta potentials of the electrode components and verified the strong electrostatic repulsive force. Following this, the group suggested that this homogeneous dispersion of the CMC/SBR could result in a more effective conductive framework supported by the low internal and charge-transfer resistance of the CMC/SBR-based composite determined by EIS analysis. As a result, the CMC/SBR-based cathode delivered a reversible capacity of $580 \text{ mAh}\cdot\text{g}^{-1}$ after 60 cycles at $100 \text{ mA}\cdot\text{g}^{-1}$ current density, far surpassing the reference electrode based on a PVDF binder.

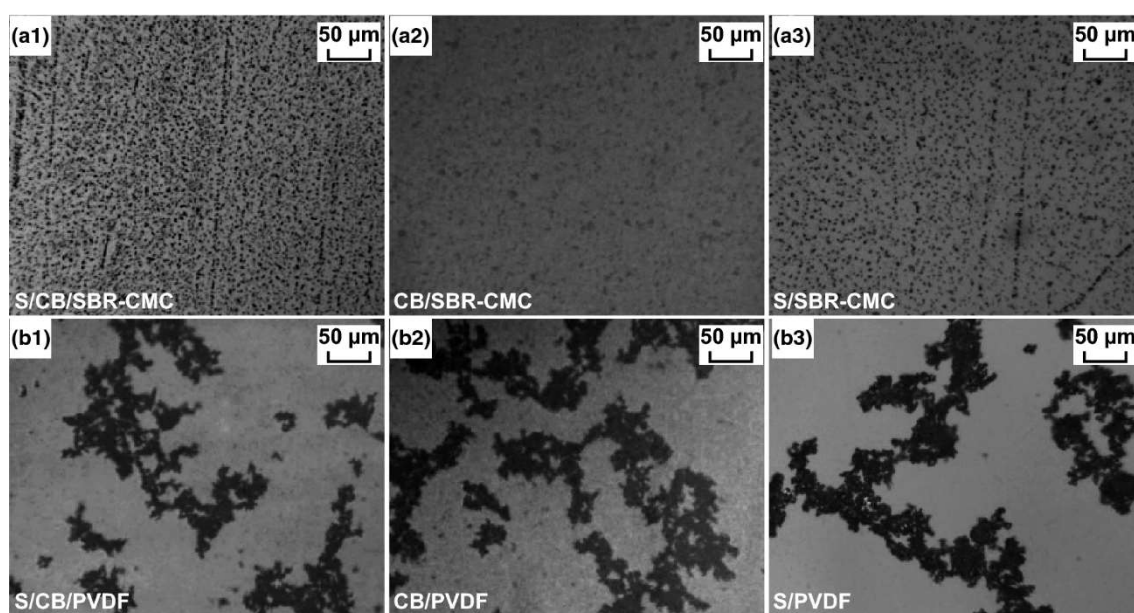


Figure 2.13: Dispersion morphology of (a1) S/CB/SBR-CMC, (a2) CB/SBR-CMC, (a3) S/SBR-CMC, (b1) S/CB/PVDF, (b2) CB/PVDF, and (b3) S/PVDF. Reproduced with permission from Ref. [163]. Copyright 2011 American Chemical Society

2.7.1.4 Chitosan

Chitosan is an attractive natural polymer with a high nitrogen and hydroxyl content commonly sourced from crab and shrimp shells [194]. Chen et al. [164] applied chitosan as a chemical polysulfide anchor combined with acetylene black to form a host-free framework for Li-S batteries. Considerable improvements in the sulfur redox reversibility and cycling performance were achieved using this binder, as evidenced by the higher reversible capacity displayed after cycling compared with the gelatin-based cathode (**Fig. 2.14**). The authors attributed the chitosan-based electrode's higher upper plateau discharge capacities to its polysulfide anchoring effect (**Fig. 2.14c**).

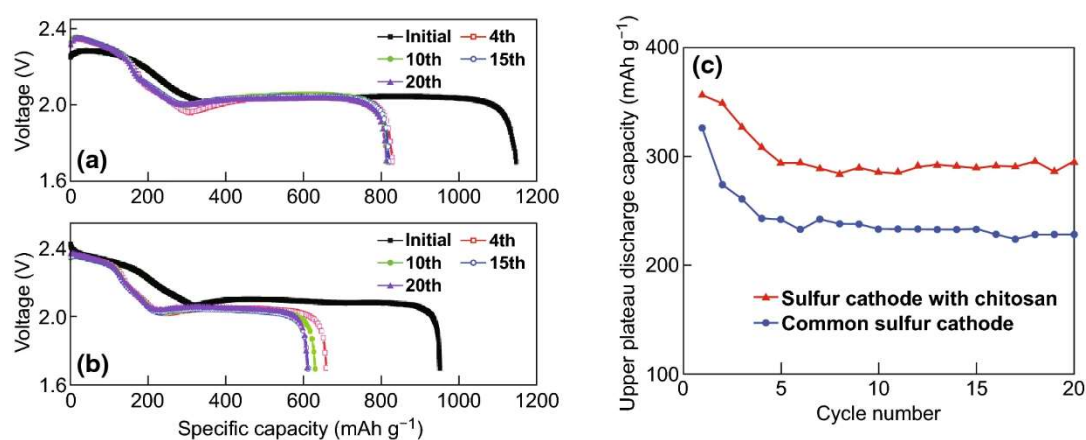


Figure 2.14: Discharge curves of batteries: (a) sulfur cathode with chitosan, (b) sulfur cathode with gelatin, and (c) the upper plateau discharge capacities of batteries with different sulfur cathodes. Reproduced with permission from Ref. [164]. Copyright 2015 Royal Society of Chemistry

2.7.1.5 Gum Arabic (GA)

Gum Arabic (GA) is a tree gum exudate that has been utilized for over 5000 years in various applications, including as an adhesive for paint and during the ancient Egyptian embalming process [195]. More recently, GA has been used as a thickening and stabilizing agent [196]. It is a branched, complex polysaccharide polymer, consisting of a leading chain of β -D-galactopyranosyl and side chains endowed with abundant carbonyl and nitrogen-containing functional groups [196]. Li et al. [165] adopted GA as a low-cost water-soluble binder to fabricate a host-free framework. The GA allowed the electrode slurry to possess a good dispersion of active materials, resulting in a homogeneous electrode with reduced electrochemical impedance. The as-fabricated electrode delivered a high capacity of 841 mAh·g⁻¹ over 500 cycles at 0.5 C with a high sulfur loading of 4.4 mg·cm⁻². Nano-indentation

analysis revealed that the GA displayed superior flexibility when compared with the gelatin and PVDF-based electrodes, which allowed for better delamination tolerance. X-ray absorption spectroscopy (XAS) was used to verify the chemical bonding between the GA and sulfur, while FTIR was used to verify bonding between GA and PS (**Fig. 2.15**). This analysis revealed that not only can the GA firmly hold sulfur through the host-free framework, it can also retain PS, which can prevent migration and parasitic reactions at the lithium metal anode.

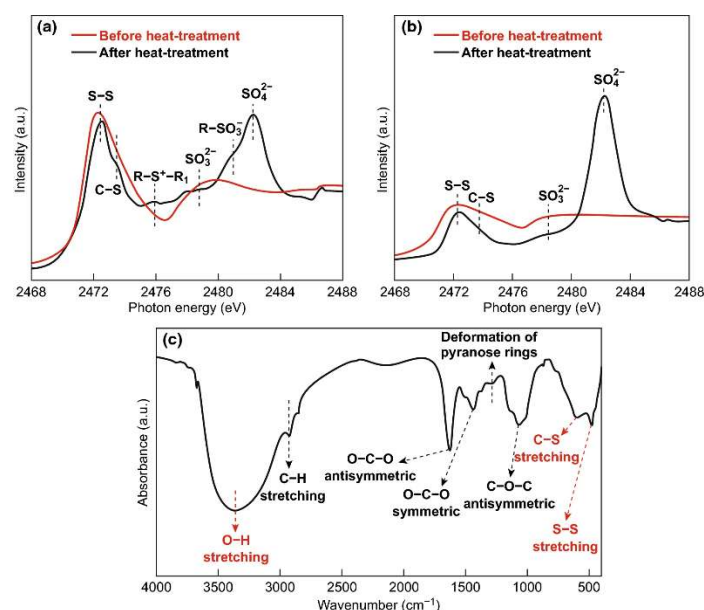


Figure 2.15: Characterization of chemical bonds between GA and S. (a) TEY XAS and (b) TFY XAS spectra for the mixture of GA and S before and after the thermal treatment at 80 °C. (c) FTIR spectroscopy of the mixture of GA and polysulfides (Li_2S_x , $x = 8$). Reproduced with permission from Ref. [165]. Copyright 2015 John Wiley and Sons

2.7.1.6 Guar Gum

Guar gum (GG) is yet another commonly used and widely available biopolymer [197]. GG can also fabricate host-free frameworks for sulfur cathodes, as evidenced by Lu et al. [166]. When cycled at 1 C, the resultant Li-S batteries delivered a reversible capacity of $\approx 600 \text{ mAh} \cdot \text{g}^{-1}$ over 400 cycles. To explain the improved performance over the reference PVDF-based electrode, the group investigated the chemical and mechanical properties of the GG. FTIR analysis revealed that the polar OH groups of the GG interact with both the sulfur and polysulfide species, which could have inhibited the shuttling effect, increasing electrode stability and cell performance. The material's behaviour toward the electrolyte was observed for both GG and PVDF. It was found that the GG displayed minor swelling in the electrolyte, whereas PVDF was quickly swollen, which the group supposed to lead to the degradation of the bonding and

conductive pathways in the PVDF framework. Furthermore, the GG sample displayed better viscosity (when measured in a 1 wt% solution) and hardness than the PVDF sample, all of which were suspected reasons for the superior performance of the GG framework in Li–S cells.

Following this, Cheng et al. [198] conducted a thorough investigation into how the rheological behaviour of GG solutions changed with time and the effects of these observations on the resultant dispersions of the electrode slurries. The group found that when an aqueous solution of GG was made, a gelatinous slurry (g-GG) was obtained; however, after 48 h, the viscosity of the solution decreases, and a better fluidity is obtained in a process called retrogradation (r-GG). FTIR spectroscopy was used to investigate this phenomenon, which revealed that the g-GG solution exhibited strong hydrogen bonding between the polymer and aqueous solvent; however, the r-GG solution preferred hydrogen bonding toward itself. Electrode slurries were constructed with both forms of GG, and rheological analysis was conducted. The g-GG-based slurry exhibited shear-thinning behaviour, which suggested powder agglomerates were present; conversely, the r-GG slurry was more homogeneous. Consequently, electrodes fabricated from the r-GG slurry displayed better homogeneity and reduced agglomeration, as revealed by SEM analysis, which resulted in increased electrochemical performance.

2.7.1.7 Carrageenan

Ling et al. [167] investigated a new method to achieve PS retention in Li–S batteries. A strong polysulfide anchoring effect was realised by taking advantage of a nucleophilic substitution reaction between the polymer binder and polysulfides. By considering the reaction mechanism, the group determined that a sulfate group could serve as a suitable leaving group; therefore poly(vinyl sulfate) potassium salt (PVS) polymer was initially tried as a nucleophilic substitution binder for Li–S batteries. Although a strong PS anchoring effect was observed in the time-lapse ultraviolet (UV)-Vis spectra and C–S bonds formed between the binder and PS, the insufficient mechanical properties left room for improvement in cycling stability, which led the group to investigate carrageenan as a nucleophilic substitution binder for Li–S batteries. Carrageenan is an aqueous-soluble natural product polymer with abundant sulfate groups and has a high amount of hydroxyl groups which provides enhanced adhesive capabilities. As with the PVS polymer, the carrageenan binder strongly adsorbed PS through the formation of a C–S bond, as determined by XAS and XPS analysis. The carrageenan binder allowed for a sulfur cathode with a high sulfur loading of $24.6 \text{ mg} \cdot \text{cm}^{-2}$, which delivered an areal capacity of $33.7 \text{ mAh} \cdot \text{cm}^{-2}$. The polysulfide retention was also demonstrated during cell operation using operando XAS measurements (**Fig. 2.16**). The cells were discharged at 0.2 C between 2.6 and

1.8 V, while the fluorescence spectra were observed. As shown in **Fig. 2.16b**, the polysulfide concentration (purple peak) quickly increases and plateaus as the discharge proceeds; however, the polysulfide dissolution in the carrageenan-based electrode remains low (**Fig. 2.16c**), highlighting successful PS shuttling mitigation.

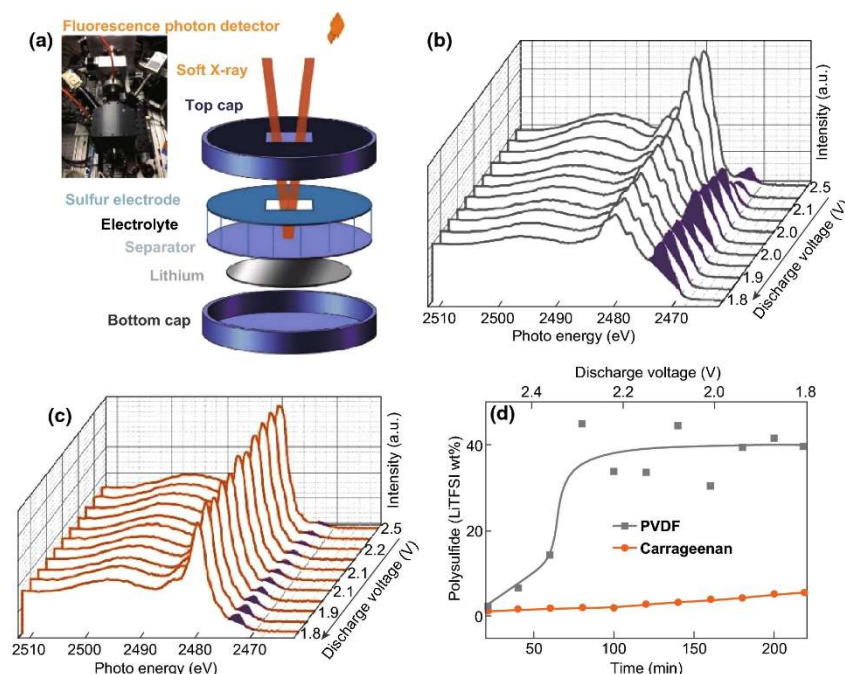


Figure 2.16: Operando XAS measurements of Li-S cell. (a) Schematic of the in situ XAS measurement set-up. The inset photo is the actual customer build instrumentation for this experiment. (b), (c) The S K-edge XAS spectra evolution of the electrolyte with voltage scan. The purple highlighted peaks are polysulfide adsorption peaks, which evolve during first discharge. PVDF binder-based Li-S cell shows the dramatic increase of polysulfide concentration in the electrolyte during the first lithiation process. The carrageenan binder-based Li-S cell shows much slow concentration built up of polysulfide. (d) The relative polysulfide concentration changes with discharge shows the superiority of carrageenan binder in immobilizing polysulfide. Reproduced with permission from Ref. [167]. Copyright 2017 Elsevier

2.7.1.8 Starch

Starch is also a natural biopolymer also with good mechanical properties. Duan et al. [168] subjected starch to a gelatinization process before using the product to fabricate a host-free framework using only Super-P and commercial sulfur powder. The as-fabricated framework delivered a $\approx 90\%$ capacity retention at 0.2 C after 200 cycles, corresponding to a capacity decay of only 0.05 % per cycle. SEM analysis revealed that before cycling, the starch-based

framework displayed a rather severe degree of agglomeration. The authors ascribed this to the greater wettability of Super-P and sulfur particles compared with the starch, however after 100 cycles, the framework's integrity remained intact.

Conversely, the PVDF framework displayed cracks throughout the composite, resulting in electronically isolated electrode sections. The authors attributed this stability to the minimal swelling of the gelatinized starch framework when the framework was exposed to the electrolyte. This resistance to swelling allowed the structure to avoid the exfoliation of sections of the electrode. In short, natural polymers often display the necessary viscosity in solutions to form suitable binders and are often naturally endowed with specialized functional groups conducive to good host-free sulfur cathode function.

Overall, natural polymers have many inherent benefits. The aqueous-soluble and cheap natural polymers could be combined with sulfur hosts synthesized through cheap and green chemical methods to reduce the environmental impact of Li-S cell fabrication while still obtaining high electrochemical performance. A relatively small amount of research has been carried out with multifunctional sulfur hosts combined with natural polymers, which may be a fruitful future research direction.

2.7.2 Synthetic Polymers

The wide range of available synthetic polymers have the advantage of being highly tailorable so that favourable mechanical properties and a strong binding force in host-free PCFs can be achieved.

2.7.2.1 Poly(Vinylpyrrolidone) (PVP)

The crucial work by Seh et al. [169] provided the theoretical insight into achieving a robust chemical bonding mechanism between binders and polysulfides. The group used *Ab initio* simulations in the framework of DFT to evaluate the interactions between various functional groups (R) and Li₂S on a vinyl polymer $[-(\text{CH}_2\text{CHR})_n-]$ framework (**Fig. 2.17**). They found that a lithium atom in Li₂S can form coordination-like bonds with electron-rich groups containing lone pairs of electrons on oxygen, nitrogen, and halogens. The most robust interaction was determined to be between Li₂S and carbonyl ($>\text{C}=\text{O}$) groups, found in esters, ketones, and amides, as shown in **Fig. 2.17a**. The group attributed this tight binding to the hard-acid properties of Li⁺, which can interact with the hard oxygen donor atoms in the carbonyl groups to form a strong lithium-oxygen bond (Li–O). Conversely, the interaction between fluoroalkane groups and Li₂S is much weaker, which explains why the PVDF binder cannot

act as a polysulfide anchor. Considering this, the group selected PVP to act as a multifunctional binder to construct a polymeric framework using Li_2S as an active material. Evidence of the strong interaction between the active material and the binder was provided by observing the high degree of dispersion in the electrode slurry, which the authors attributed to the strong adsorption of PVP onto the Li_2S particles, which stabilized the dispersion. Upon cycling at 0.2 C, the as-fabricated batteries retained 69% of their original capacity, corresponding to a low 0.062% capacity loss per cycle attributed to a strong PS retention effect. The group quantified the PS anchoring effect by conducting inductively coupled plasma-optical emission spectroscopy (ICP-OES) analysis on the electrolyte after discharge. The PVP-based electrode consistently showed reduced sulfur amounts in the electrolyte after 1, 5, 10, and 20 cycles.

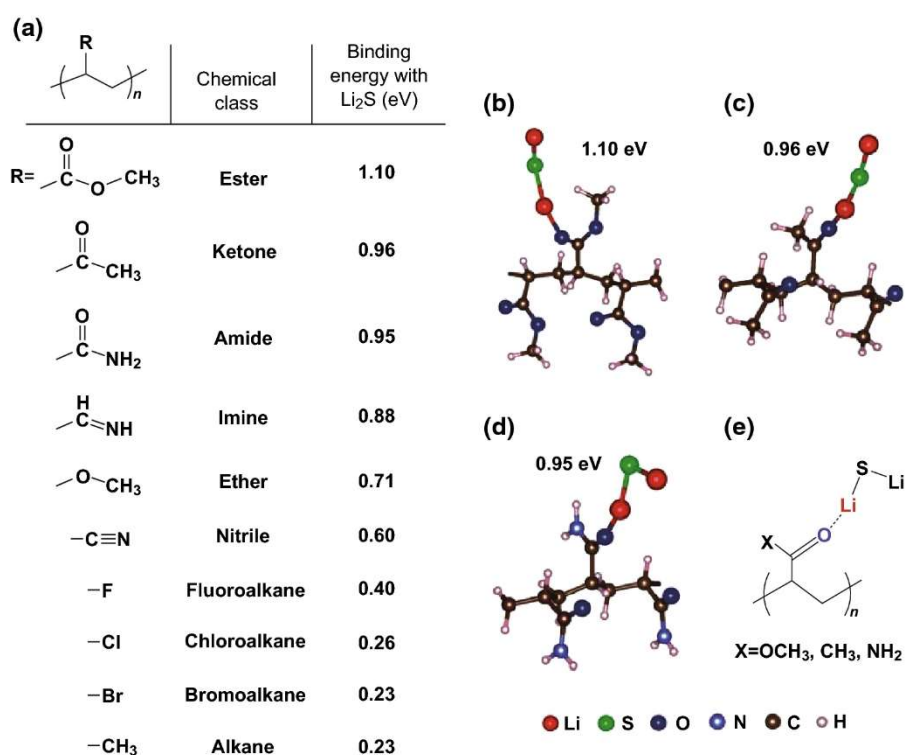


Figure 2.17: (a) Table showing the calculated binding energy of Li_2S with various functional groups (R) based on the framework of vinyl polymers $-(\text{CH}_2-\text{CHR})_n-$. (b-d) Ab initio simulations showing the most stable configuration and calculated binding energy of Li_2S with (b) ester, (c) ketone and (d) amide R groups in vinyl polymers. (e) General schematic representing the Li-O interaction between Li_2S and $>\text{C}=\text{O}$ groups as shown in (b-d). Reproduced with permission from Ref. [169]. Copyright 2013 Royal Society of Chemistry

An interesting phenomenon regarding the solvent effects on slurry dispersions was investigated by Fu et al. [199]. The group found that by using acetic acid (AA) as a co-solvent, the dispersion properties of aqueous PVP and PAA slurries were substantially increased due to a chain

opening effect. The co-solvent-based slurries displayed an increased viscosity, with a correspondingly enhanced porosity, uniformity, and mechanical properties of the electrodes fabricated by this approach. The PVP-based host-free cathode fabricated using the AA co-solvent approach delivered an initial discharge capacity improvement of $220 \text{ mAh}\cdot\text{g}^{-1}$ over the PVP-based framework cast from a pure water slurry. The long-term cycling performance of the AA co-solvent approach was also improved, delivering a reversible capacity of $530 \text{ mAh}\cdot\text{g}^{-1}$ after 100 cycles at $0.3 \text{ A}\cdot\text{g}^{-1}$.

2.7.2.2 Poly(Ethylene Oxide) (PEO)

One of the primary considerations when fabricating host-free PCFs with traditional binders, which swell or dissolve in the organic electrolyte, is that the void structure required to house the sulfur is lost during sulfur dissolution. The interaction between the binder and the electrolyte in host-free cathodes is a critical consideration, as elucidated through investigating PEO as a binder in host-free frameworks [200, 201]. Lacey et al. [170] investigated the mechanisms by which PEO binders can improve sulfur cathode performance. As lower molecular weight polymers (i.e., PEG-20000) are soluble, and higher molecular weight PEO ($M_w \leq 4,000,000$) swell in common liquid electrolytes, they considered it unlikely that PEO coatings can physically retard dissolved polysulfides during cycling. Upon observing the voltage profile for the first cycle (**Fig. 2.18a**), they observed that the voltage peak at the beginning of the charge cycle, attributed to cell polarization due to insoluble discharge product deposition, is removed when PEO is used as a binder. After 50 cycles, the PEO-based composite conductive framework enables high capacity retention with distinct upper and lower voltage plateaus during discharge (**Fig. 2.18b**). They concluded that the PEO binder improved electrochemical reversibility and suppression of passivation on the sulfur cathode due to the nature of PEO dissolution (or swelling), which modified the electrolyte system.

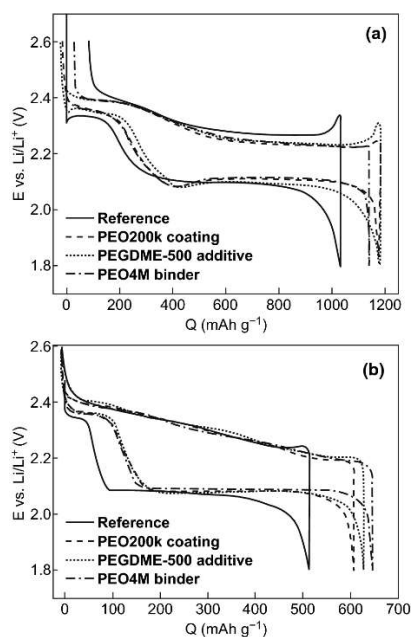


Figure 2.18: Voltage profiles for the reference and PEG/PEO-modified cells at C/5 for (a) the 1st cycle and (b) 50th cycle. Reproduced with permission from Ref. [170]. Copyright 2013 Royal Society of Chemistry

Further investigation into the swelling/dissolution phenomenon of PEO binders was conducted by Zhang [171], who argued that polymeric frameworks which are based on polymer binders that dissolve or swell in common liquid electrolytes could not maintain a stable void structure during sulfur dissolution and are thus unsuitable for Li-S cells with a long cycle life (**Fig. 2.19**).

2.7.2.3 Poly(Acrylamide-co-diallyldimethylammonium Chloride) (AMAC)

In response to this swelling/dissolution phenomenon observed with PEO binders, S.S. Zhang introduced a cationic polyelectrolyte named poly(acrylamide-co-diallyldimethylammonium chloride) (AMAC) which is substantially insoluble in organic electrolytes but highly soluble in water [171].

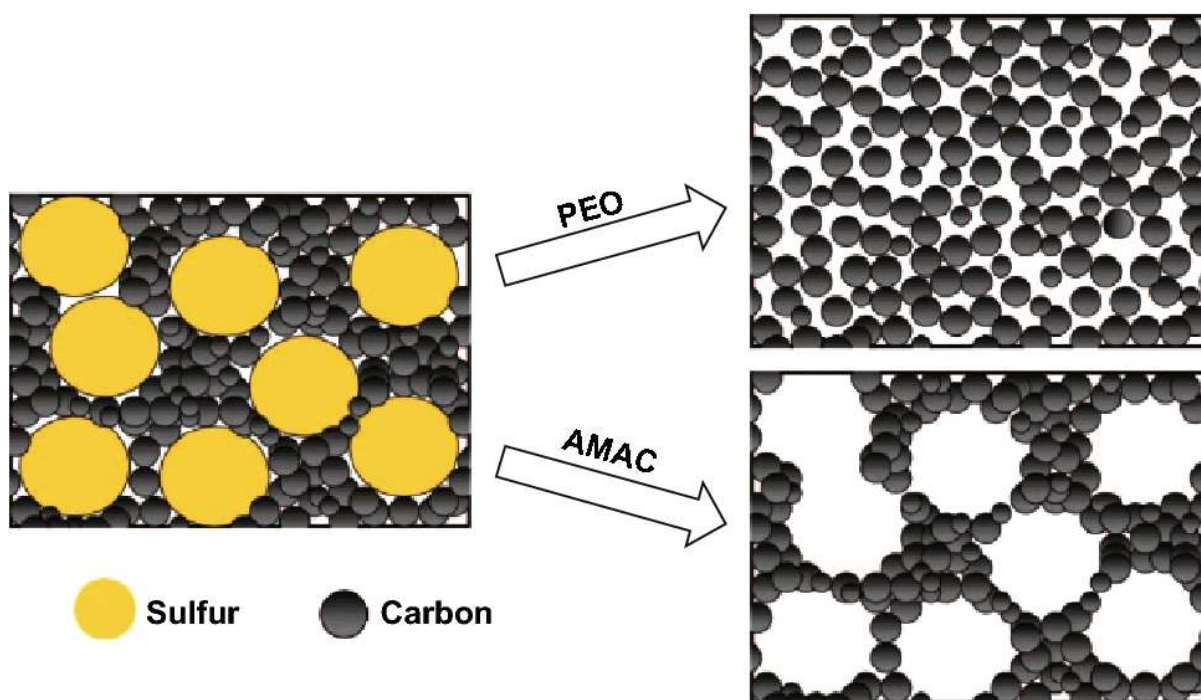


Figure 2.19: Schematic structure of the sulfur cathode before and after PS dissolution.

Reproduced with permission from Ref. [171]. Copyright 2012 The Electrochemical Society

The author attributed the enlarged second discharge plateau to the retained pore structure after sulfur dissolution, allowing for easy deposition of Li_2S_2 and Li_2S . To further illustrate this effect, the group partially discharged the PEO and AMAC-based cathodes to $300 \text{ mAh} \cdot \text{g}^{-1}$ to achieve a total conversion of solid sulfur to soluble PS to observe the composite behaviour conductive binding framework after PS dissolution. The partially discharged cells were disassembled and washed with electrolyte before being stored in triglyme. Due to the gelation of the PEO-based cathode, many of the electrode components were stuck to the separator after disassembly. In contrast, the AMAC-based cathode maintained its structural integrity, as shown in **Fig. 2.20**.

Furthermore, the AMAC-based cathode could withstand storage in the triglyme solvent for 48 h at 60°C , which was not the case for the PEO-based electrode. These results revealed that the AMAC-based composite conductive binding framework delivers greater structural integrity and void structure compared to PEO-based composites. Electrochemical results reinforced this claim, with the AMAC-based cathode delivering a reversible capacity of $652 \text{ mAh} \cdot \text{g}^{-1}$ after 100 cycles compared with $384 \text{ mAh} \cdot \text{g}^{-1}$ for the PEO-based cathode. This work highlights the importance of the interaction between the electrolyte and binder, especially during the fabrication of host-free sulfur cathodes.

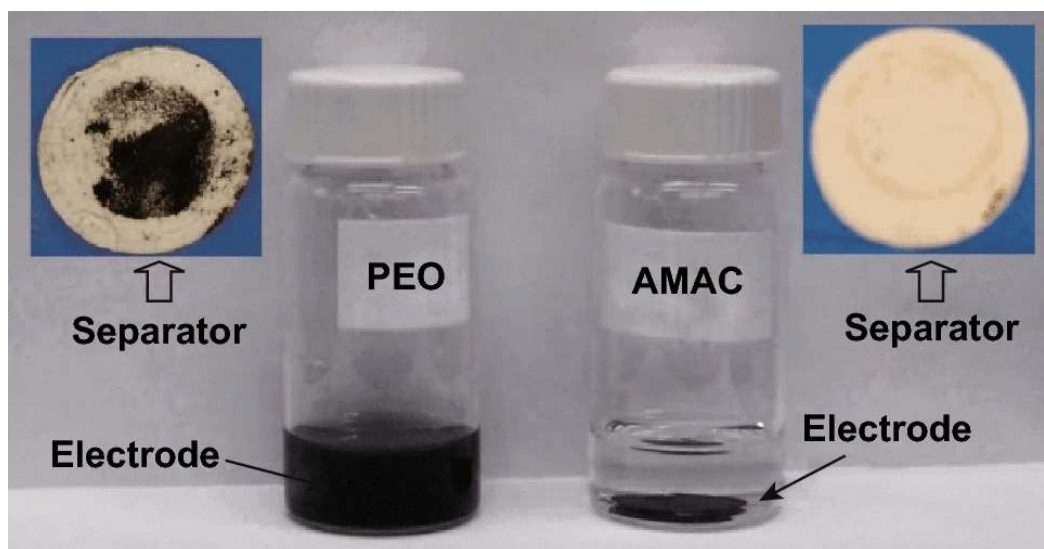


Figure 2.20: Visual pictures of separator and sulfur cathode after the Li-S cell was discharged to $300 \text{ mAh} \cdot \text{g}^{-1}$ sulfur and the cathode was stored in triglyme at 60°C for 48 h. Reproduced with permission from Ref. [171]. Copyright 2012 The Electrochemical Society

2.7.2.4 Poly(Acrylic Acid) (PAA)

PAA, a mechanically robust, water-soluble polymer was first investigated by Zhang et al. [172] as a polymeric binder in Li-S batteries. The PAA-based cathode delivered a higher discharge capacity than the PVDF-based cell, and it also displayed an almost twofold increase in the reduction current and a threefold increase in the oxidation current when observing the CV (**Fig. 2.21**), which suggests better reaction kinetics within the PAA electrode. The group suggested that the binding strength helped stabilize the electrode framework, restrain polysulfides, and prevent electrode delamination.

2.7.2.5 LA132

LA132, a flexible, water-soluble, highly adhesive copolymer containing acrylonitrile, acrylate, and acrylamide, was investigated as a binder in Li-S batteries by Hong et al. [202]. The dispersions of electrode slurries using SA, CMC, and LA132 were compared (**Fig. 2.22**), and it was found that the LA132-based slurry provided the best dispersion after being left overnight. The better dispersion corresponded to a more homogenous and stable cathode, which allowed for a higher discharge capacity over 50 cycles. Pan et al. [173] demonstrated that a cathode fabricated with a 5 wt% loading of LA132 binder could even outperform a cathode using 10 wt% of PVDF.

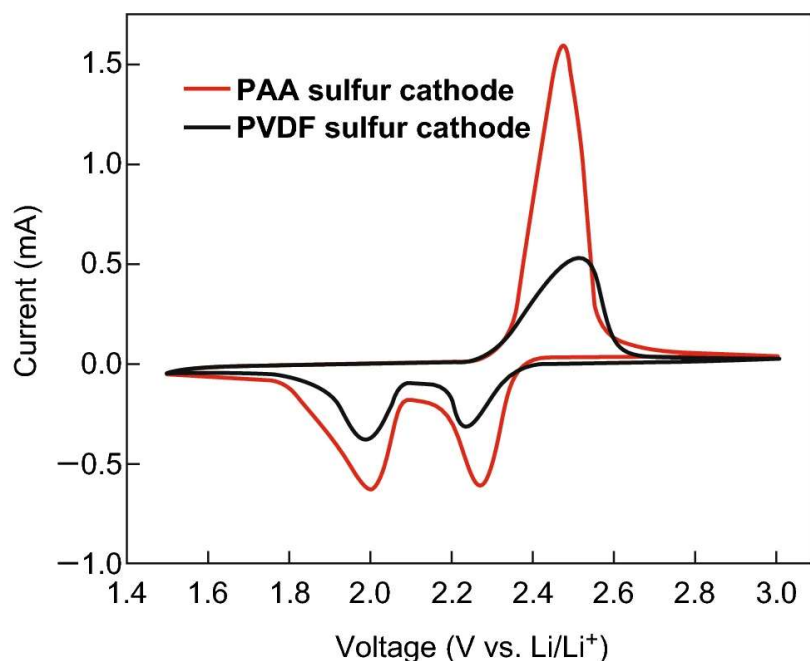


Figure 2.21: Cyclic voltammogram curves of the Li–S cells with PAA sulfur cathode and PVDF sulfur cathode at a scan rate of $0.1 \text{ mV} \cdot \text{s}^{-1}$. Reproduced with permission from Ref. [172]. Copyright 2012 The Electrochemical Society

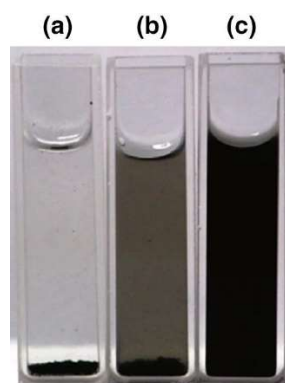


Figure 2.22: Suspensions of $1 \text{ mg} \cdot \text{mL}^{-1}$ sulfur composites dispersed in a SA; b CMC; c LA132 after an overnight settlement. Reproduced with permission from Ref. [202].

Copyright 2016 Elsevier

2.7.2.6 Poly(Amidoamine) (PAMAM)

Poly(amidoamine) (PAMAM) is a highly branched synthetic polymer referred to as a dendrimer, which possesses a central core, repeating interior branch cells, and terminal functional groups [203]. Bhattacharya et al. [174] compared various PAMAM dendrimers with different functional groups as aqueous-soluble binders for Li–S batteries. Most importantly, the cathodes based on PAMAM dendrimers with hydroxyl (G4OH), 4-carboxymethylpyrrolidone (G4CMP), and carboxylate (G4COONa) functionality enabled a

high sulfur loading above $4 \text{ mg}\cdot\text{cm}^{-2}$, comparatively greater than the reference CMC/SBR-based cathodes ($2.34 \text{ mg}\cdot\text{cm}^{-2}$). As predicted by Seh et al.'s work [169], the previously mentioned PAMAM dendrimers with carbonyl functional groups enabled chemical anchoring of PSs within the cathode framework, as evidenced by XPS analysis. Not only that, but the dendrimers also display an internal porous structure in the range of 2 nm, which could physically trap PS, resulting in a dual-approach PS restriction at the cathode. The PAMAM dendrimer framework enabled a high sulfur loading in the composite ($> 68 \text{ wt}\%$), a high areal capacity ($4.32 \text{ mAh}\cdot\text{cm}^{-2}$), and a capacity retention of $\approx 640 \text{ mAh}\cdot\text{g}^{-1}$ after 100 cycles.

2.7.2.7 Poly(Ethylenimine) (PEI)

Poly(Ethylenimine) is an amine-containing polymer used as a chemical PS trap in Li-S batteries [204]. Zhang et al. [175] used PEI as a binder and PS anchor to form a host-free framework. A high sulfur loading of $8.6 \text{ mg}\cdot\text{cm}^{-2}$ was achieved throughout the composite, which delivered a reversible capacity of $744.2 \text{ mAh}\cdot\text{g}^{-1}$ after 50 cycles. UV-Vis and XAS analysis revealed direct evidence of electrostatic interaction between the amino groups in the PEI with PS intermediates, resulting in a reduction in PS shuttling and a subsequent improvement in the electrochemical performance. Wang et al. [205] subsequently modified PEI polymer with methyl iodide (CH_3I), which resulted in an even greater PS anchoring ability; thus, a further improved electrochemical performance was obtained.

2.7.2.8 Polycationic Binders

Electrostatic confinement of polysulfide intermediates was realized by using a cationic polymer binder by Ling et al. [176]. The poly[bis(2-chloroethyl) ether-alt-1,3-bis[3(dimethylamino) propyl]urea] quaternized (PQ) binder, endowed with quaternary ammonium cations (**Fig. 2.23**), binds with the soluble polysulfide (Li_2S_6) with an energy of 1.89 eV, but is lower than the covalent bonding energy thus providing an electrostatic interaction. The retention abilities of the PQ binder were evaluated experimentally through time-lapse UV-Vis spectroscopy, which found that the PQ binder can reduce the amount of polysulfides in the solution through electrostatic interaction whereas the concentration in the PVDF experiment remains unchanged. Electrochemical characterization revealed the PQ displayed good separation of discharge plateaus and delivered a high areal capacity of $9 \text{ mAh}\cdot\text{cm}^{-2}$ with a sulfur loading of $7.5 \text{ mg}\cdot\text{cm}^{-2}$.

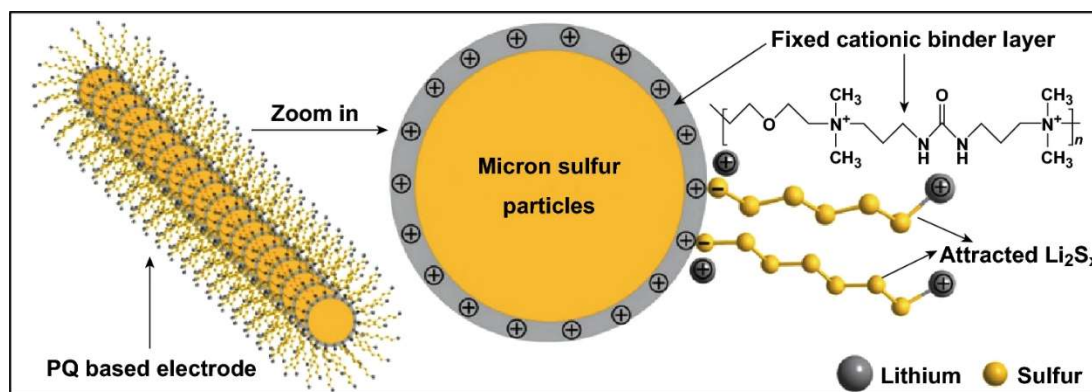


Figure 2.23: Polysulfides confinement through cationic polymer. The electrostatic attraction between the PQ quaternary ammonium cations and polysulfide anions. Reproduced with permission from Ref. [176]. Copyright 2017 American Chemical Society

Two representative cationic binders for Li–S batteries were investigated by Su et al. [152]. The group used poly[(2-ethyltrimethylammonioethyl methacrylate ethyl sulfate)-co-(1-vinylpyrrolidone)] (D11) and poly(diallyldimethylammonium triflate) (PDAT), synthesized through an anion exchange reaction between poly(diallyldimethyl ammonium chloride) and silver triflate ($\text{CF}_3\text{SO}_3\text{Ag}$) as shown in **Fig. 2.24**, and compared the electrochemical performance with a PVP-based Li–S cell. D11 and PDAT were chosen due to their positively charged nitrogen atom, while PVP contains uncharged nitrogen, and were chosen so that the role of a positively charged nitrogen in PS anchoring could be investigated. Both the D11- and PDAT-based Li–S cells delivered an improved cycling performance compared with the PVP-based cell. Although the D11-based cell delivered a similar initial discharge capacity to the PVP, its capacity retention over 50 cycles improved. The PDAT binder-based electrode delivered an increased initial discharge capacity and improved capacity retention over both the PVP and D11-based electrodes; thus, the PDAT binder was further examined. Short duration polysulfide adsorption tests (i.e., <1 min) revealed that the PDAT binder composite displays a superior anchoring effect, as confirmed by UV-Vis spectroscopy. Furthermore, XPS analysis of the lithiated electrodes revealed a superior sulfur utilization for the PDAT-based electrode. The group concluded that polycation containing binders could mediate a stronger PS sequestration.

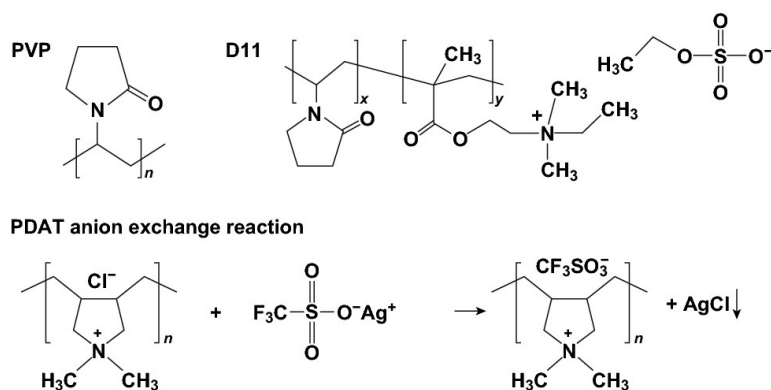


Figure 2.24: Molecular structures of polyvinylpyrrolidone (PVP) and poly[(2-ethyl-2-(dimethylammonioethyl) methacrylate ethyl sulfate)-co-(1-vinylpyrrolidone)] (D11) and the synthesis of poly(diallyldimethylammonium triflate) (PDAT) via anion exchange. Reproduced with permission from Ref. [152]. Copyright 2017 American Chemical Society

Liao et al. [206] investigated the effect of the chosen counter anions on poly(diallyldimethylammonium) (PDADMA)-based binders for Li-S batteries. The chosen counter anions in this case were: Cl^- , PF_6^- , BF_4^- , and TFSI $^-$. The group found that the PDADMA with the latter 3 counter anions could successfully anchor PS, whereas the PDADMA with a Cl^- counter anion was ineffective at PS trapping. The TFSI $^-$ anion-based binder delivered the lowest capacity decay and lowest polarization while maintaining the best cycling stability.

2.7.2.9 Polymeric Ionic Liquid (PIL) Binders

Five different polymer ionic liquids (PILs) were investigated as cathode binders in Li-S batteries by Vizintin et al. [177]. PIL4 (**Fig. 2.25**) was of particular interest, which enabled a discharge capacity of $1015 \text{ mAh}\cdot\text{g}^{-1}$ after 3 cycles, $657 \text{ mAh}\cdot\text{g}^{-1}$ after 200 cycles, and $446 \text{ mAh}\cdot\text{g}^{-1}$ after 500 cycles. The group found that between the 50th and the 200th cycle, the ratio between the upper voltage discharge plateau (Q_{high}) and the total discharge capacity (Q_{total}) increased, which they related to a more efficient reduction of sulfur to Li_2S_4 during prolonged discharge-charge cycling. Post-mortem SEM analysis was carried out to obtain possible reasons for the increased cycling performance. The PVDF and PIL electrodes in the discharged state displayed a different morphology, which the authors suggested was due to increased uptake of ionic compounds by the PIL binder, thus mediating a more uniform mixing and retention of sulfide species within the PIL binding framework. This was supported by submerging the PIL4 in a PS solution, which noticeably swelled and formed a white gel. Overall, the authors attributed the increased cycling performance of the PIL4 to its ability to provide sufficient adhesion, improve sulfur redox and dispersion, and trap polysulfide during

swelling/deswelling cycles thus reducing volume change-induced stress throughout the framework.

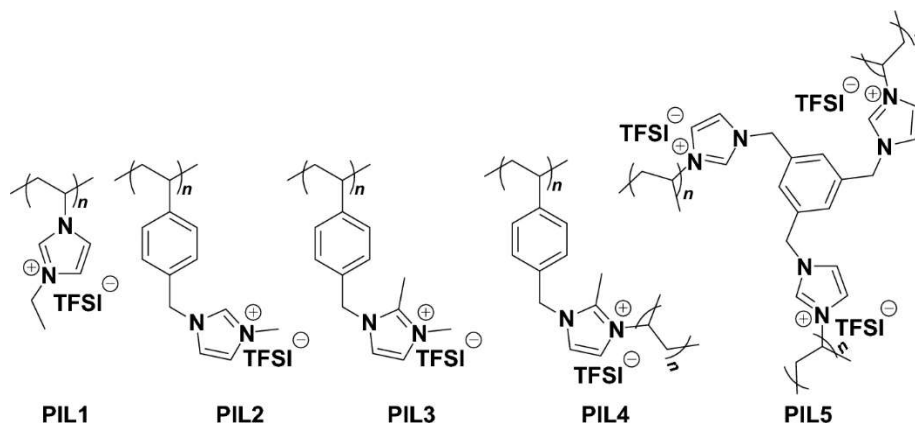


Figure 2.25: PIL binders examined for use in Li–S systems. Reproduced with permission from Ref. [177]. Copyright 2018 American Chemical Society

2.7.2.10 Thiokol

Thiokol, a type of synthetic polysulfide rubber, was also adopted as a functional binder for restricted polysulfide shuttling in Li–S batteries by Liu et al. [178]. The group proposed that the Thiokol could act as a kind of polysulfide scissor, reducing the amount of long-chain PS, thereby reducing the PS shuttle. A similar mechanism was also reported when dithiothreitol was used as an electrolyte additive [207]. The thiokol-based binder is insoluble in the electrolyte, which, as mentioned earlier, results in a stable structure during cycling [171]. As a result, the thiokol-based cathode delivered an initial discharge capacity of $819 \text{ mAh} \cdot \text{g}^{-1}$ at 0.1 C and achieved a capacity retention of 61.1 % after 200 cycles.

2.7.2.11 Ammonium Polyphosphate (APP)

The binder materials reviewed thus far have been based on organic polymer backbones; however, the work by Zhou et al. [77] demonstrates this does not necessarily have to be the case. The group used the inorganic polymer ammonium polyphosphate (APP), a commercially available food additive, emulsifier, and fertilizer, as a multifunctional binder in Li–S cathodes. In contrast to traditional polymers based on an organic C–C backbone (which cannot mediate PS anchoring), the backbone of the APP polymer can indeed initiate polysulfide trapping due to its polar nature. Evidence of the PS retention by the APP binder was provided by way of adsorption experiments and UV-Vis spectroscopy, which revealed a substantial decrease in polysulfide concentration when exposed to APP polymer. DFT calculations were conducted using a range of polysulfide species (Li_2S_x where $x = 1, 2, 4$, and 8), which showed that the

APP binder delivered binding energies in the range of 2.16 to 2.30 eV, much higher than the PVDF binder can achieve (0.58 to 0.74 eV).

Further evidence for the APPs superior polysulfide retention was given by the open circuit voltage (OCV) stability over 30 days. The voltage of the APP binder-based Li–S cell showed almost no decrease in OCV, whereas the PVDF-based cell’s voltage dropped from 2.42 to 2.29 V, suggesting the reduction of sulfur to PS had begun. When electrochemical testing was carried out, the APP binder allowed for an active material loading of $5.6 \text{ mg}\cdot\text{cm}^{-2}$ to be achieved, which delivered a reversible discharge capacity of $530 \text{ mAh}\cdot\text{g}^{-1}$ after 200 cycles at 0.5 C. The group also carried out burning time tests that showed the APP binder's flame-retardant properties could increase the safety of Li–S cells, as shown in **Fig. 2.26**.

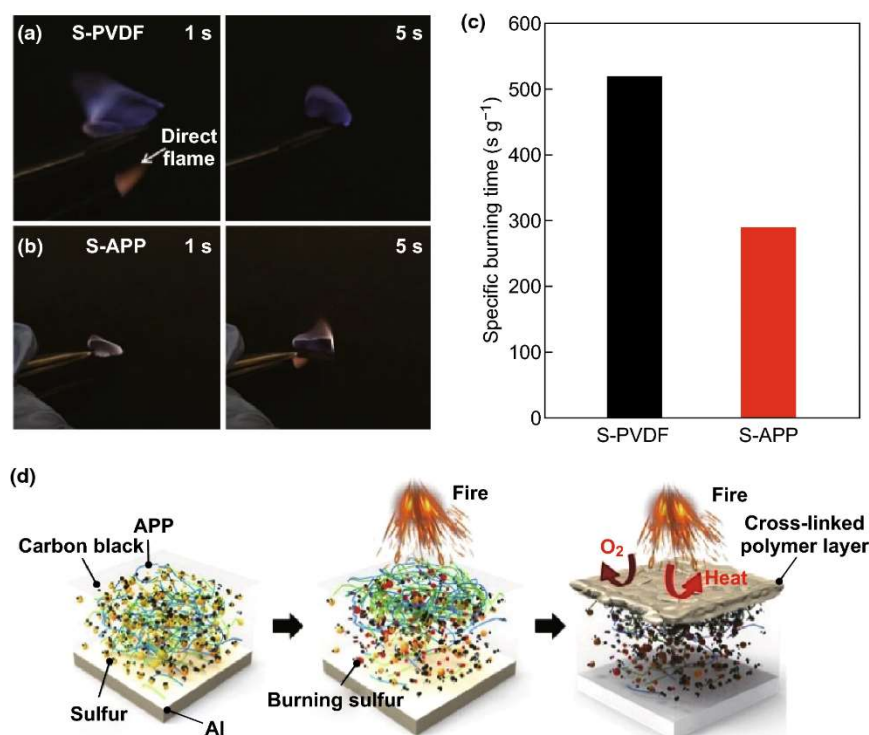


Figure 2.26: Flame-retardant properties. The specific burning time test of sulfur electrodes with (a) S-PVDF electrode and (b) S-APP electrode. The times indicated in the pictures are counted as soon as the electrodes are exposed to the direct flame from a lighter (indicated by the white arrow in panel a). (c) The specific burning time of the sulfur cathodes with APP and PVDF binders. (d) Schematic showing the flame-retardant mechanism of the APP binder-based sulfur electrode. Reproduced with permission from Ref. [77]. Copyright 2018

American Chemical Society

In summary, synthetic polymers have remarkably improved the mechanical properties, sulfur loading, and PS anchoring abilities in PCFs. Future works with synthetic polymers could aim to improve the E/S ratio of Li–S cells and improve safety through the inclusion of flame-retardant materials.

2.7.3 Composite Binders

Composite binders can be synthesized by combining two different polymers, resulting in a synergistic performance greater than the sum of their parts. For example, Lacey et al. [179] investigated a combination of PVP and PEO as a binder for Li–S cathodes. The group found that a 1:4 mixture of PVP:PEO delivered the highest capacity after 50 cycles at 0.2 C, outperforming both pure PEO- and pure PVP-based electrodes as well as a 2:3 CMC/SBR-based electrode.

Jung et al. [180] utilized a small amount of poly(ethyleneimine) (PEI) to form a PVP-based composite binder. The PEI functions as a cationic dispersant that can stabilize aqueous dispersions and increase the adhesion of paints, inks, and pigments on different surfaces. The work showed that by increasing the PEI loading in the electrode slurry from 0.25 to 2.5%, the resultant viscosity of the 5% PVP solution increased from 14 to 120 cP, providing a suitable slurry for electrode coating while also increasing the stability of the framework in the electrolyte. These characteristics allowed the PVP/PEI composite binder to deliver higher electrochemical performance than a framework based on PVP alone.

Ahktar et al. [181] fabricated a composite binder (GPC) by combining PEI and gelatin. Gelatin was chosen due to its established dispersion and adhesion properties, and PEI was utilized for its PS trapping ability. Interestingly, when subjected to a PS solution, the GPC binder displayed better PS trapping than either of the individual components of the composite, as verified by UV-Vis spectroscopy. Owing to the adhesion, strong dispersion, and PS anchoring, the GPC-based electrode delivered a reversible capacity of $871.3 \text{ mAh}\cdot\text{g}^{-1}$ at 0.2 C after 100 cycles.

Kim et al. [208] investigated the effect that different binders had on the resultant porosity of Li–S cathodes. The group fabricated composite binders using CMC:PTFE, PVA:PTFE, and various M_w PVP before conducting BET measurements on the product. The average pore diameters in different cathodes were found to be around 20 and $0.05 \mu\text{m}$, regardless of the type of binder; however, the electrodes with PTFE binders displayed a high specific surface area (SSA). Upon electrochemical investigation, the group found that the PTFE:CMC-based framework delivered a higher operating voltage and a sulfur utilization approaching 70%,

which they suspected was due to the lower interfacial resistance related to the increased surface area.

2.7.4 Cross-Linked Binders

Further improvements in the mechanical properties of binders can be realized through a cross-linking mechanism. Liu et al. [182] fabricated a robust network binder through an ionic cross-linking effect using SA and Cu^{2+} ions. As mentioned previously, the oxygen-rich groups on polymeric binders can mediate coordination like interactions toward the Li^+ ions in polysulfides; however, this work found that a more efficient PS anchoring effect can be realized through direct interaction between the polysulfide anions and cations in the polymer binder (i.e., Cu^{2+}). DFT calculations showed that the most substantial polysulfide constraint is obtained when synergistic electronegative and electropositive anchoring is achieved (**Fig. 2.27**). Adsorption tests along with UV-Vis spectroscopy confirmed the strong anchoring effect of the SA/ Cu^{2+} binder, which corresponded to an increase in electrochemical performance. The Li-S cell based on the SA/ Cu^{2+} framework delivered an 83 % capacity retention over 100 cycles, a discharge capacity of $758 \text{ mAh}\cdot\text{g}^{-1}$ after 250 cycles at 1 C, and when the rate performance was evaluated, the cell delivered an outstanding capacity of $586 \text{ mAh}\cdot\text{g}^{-1}$ at 6 C. This work shows the electropositive/electronegative approach toward polysulfide anchoring can show favourable retention.

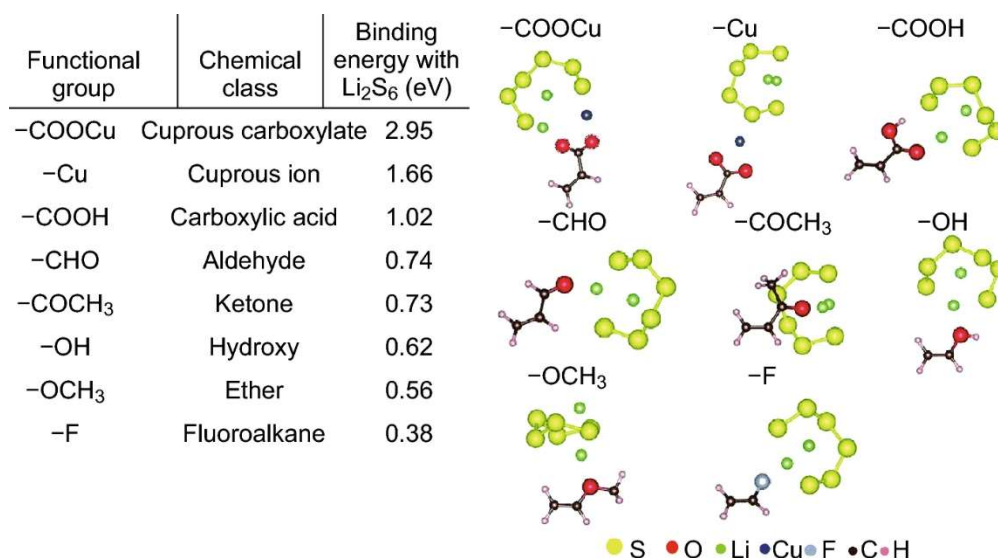


Figure 2.27: Binding energies of Li_2S_6 with various functional groups. Reproduced with permission from Ref. [182]. Copyright 2018 Royal Society of Chemistry

A mechanically robust composite guar gum and xanthan gum (XG) binder was developed by Liu et al. [183], as shown in **Fig. 2.28**. Xanthan gum, similar to guar gum, is a natural

polysaccharide biopolymer; however, the side chains in the XG polymer contain acetic and pyruvic acid residues (**Fig. 2.28b**) [209]. Hydrogen bonding occurs between the XG polymer and “smooth” regions (i.e., areas along the polymer backbone with no galactose residues) of the GG polymer, and as a result, a mechanically robust biopolymer network is synthesized (**Fig. 2.28c**). The group examined the intermolecular interactions of the network through FTIR spectroscopy (**Fig. 2.28e**), which indicated the interaction had occurred, with the optimal ratio between the GG and XG determined to be 3:1 (GG:XG). The mechanically robust binding framework, with abundant functional groups from both polymers, allowed for an ultra-high sulfur loading of $19.8 \text{ mg}\cdot\text{cm}^{-2}$ to be achieved, which delivered an areal capacity of $26.4 \text{ mAh}\cdot\text{cm}^{-2}$.

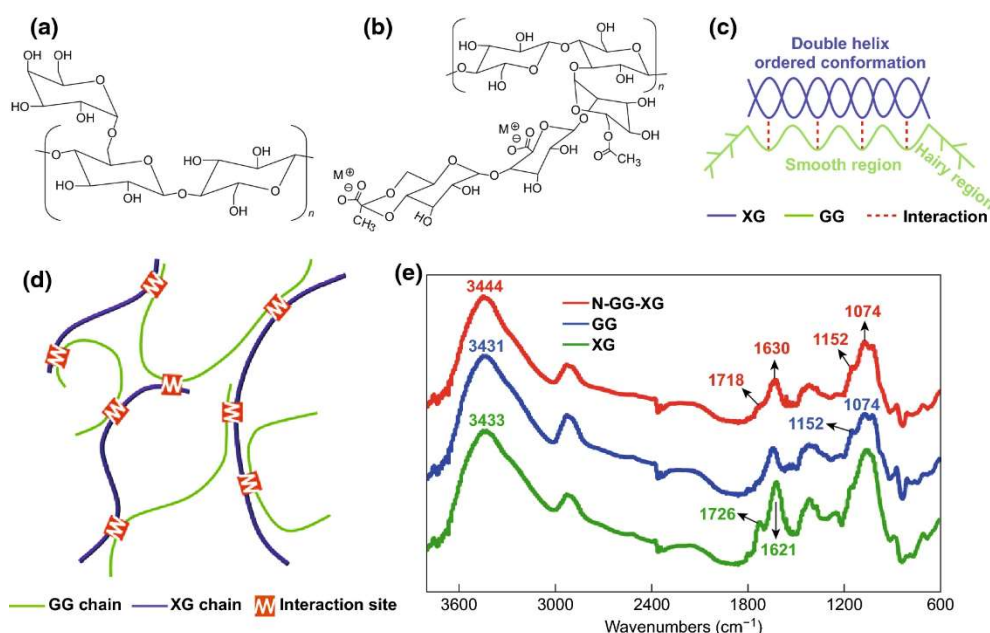


Figure 2.28: Chemical structures of (a) GG and (b) XG; (c) schematic of the intermolecular binding effect between GG and XG; (d) schematic of the polymer network formed by the intermolecular binding effect; and (e) FTIR spectra of GG, XG, and N-GG-XG. Reproduced with permission from Ref. [183]. Copyright 2017 Royal Society of Chemistry

Chen et al. [184] created a 3D hyperbranched polymer network through the copolymerization of PEI and hexamethylene diisocyanate (HDI) to form the amino functional group (AFG) binder (**Fig. 2.29**). The covalent bonding between the PEI and HDI was verified through ^{13}C nuclear magnetic resonance (NMR) spectroscopy and XPS analysis. This covalent network enabled the AFG binder to be stretched $>70\%$ without damage (**Fig. 2.29d**). Electrodes fabricated using the AFG binder delivered a 91.3 % capacity retention over 600 cycles at 2 C. Following this, the group conducted a series of experiments to explain the low capacity fading.

In situ UV-vis spectroscopy was used to monitor the discharge products qualitatively and found that the polysulfides were released from the PVDF-based electrode far faster than from the AFG-based cell. DFT analysis was also carried out, revealing considerable binding between the amino groups in the AFG backbone.

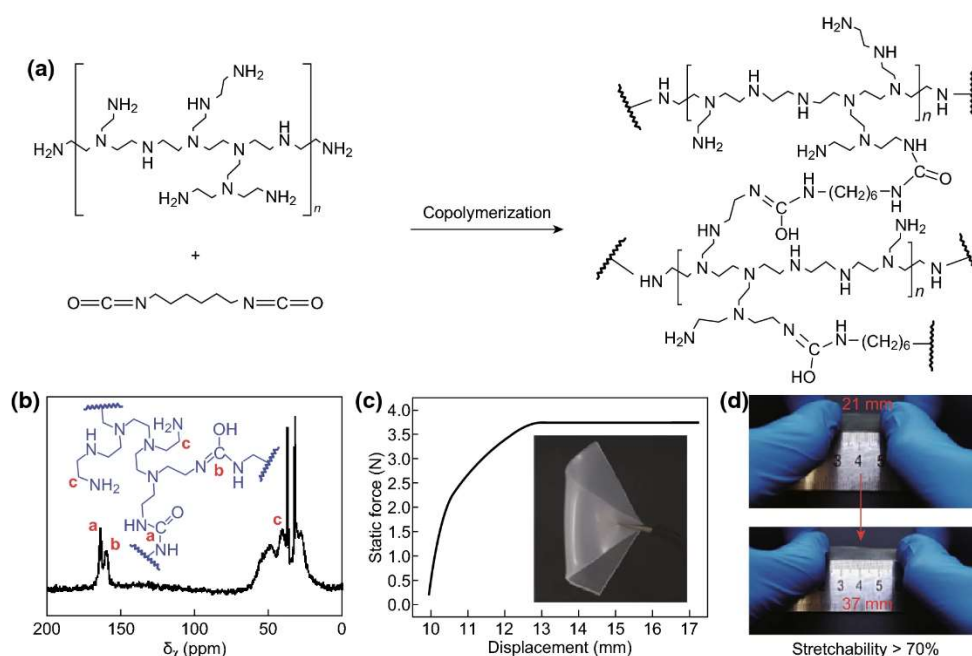


Figure 2.29: (a) Synthesis scheme of AFG binder by copolymerization of PEI with HDI in DMF solution. (b) ¹³C NMR spectrum of AFG, and the resonance amide signal at 163.58 ppm (red a, N-CH=O) with 159.45 ppm (red b, N=C-OH) and amine group signal at 40.09 ppm (red c, C-C- NH₂) were detected. (c) Tensile property test of the AFG binder, which reveals the flexibility of the AFG binder polymer. (d) Digital photographs show the AFG copolymer with excellent stretchability. Reproduced with permission from Ref. [184].

Copyright 2017 John Wiley and Sons

Although it possessed interesting physical and electrochemical properties, the AFG binder was insoluble in common solvents used in electrode slurries. This prompted Chen et al. [185] to develop a cross-linked PEI and poly(ethylene glycol) diglycidyl ether (PEGDGE) composite binder, named PPA, which was hydrophilic and thus water-soluble. The PPA binder displayed excellent adhesion strength and was strong enough to support up to a 100 g weight, unlike PVDF, which could not support any weight. As a result of its excellent adhesion and chemical polysulfide anchoring, the Li-S batteries based on this cross-linked binder delivered outstanding electrochemical performances.

Yan et al. [186] introduced a robust network structure based on PEI and epoxy resin (ER). The group tailored the ratio between the framework components and found that a PEI:ER ratio between 1:1 and 1:4 delivered a binder with unnoticeable deformation toward the electrolyte after 7 days of submersion. UV-Vis spectroscopy was carried out to observe the binder's polysulfide anchoring ability, with the peak relating to polysulfides approaching zero. The mechanical properties of the PEI/ER binder with different component ratios were also examined. A 1:1 ratio delivered a relatively low tensile strength of 1.5 MPa, which the author's attributed to insufficient cross-linking, however when the ratio was increased to 1:2 a tensile strength of 22.3 MPa was obtained, which increased to 27.5 and 29.6 MPa for 1:3 and 1:4 based composites, respectively. Electrochemical testing revealed that the PEI/ER1:2 binder delivered a discharge capacity of 829 mAh·g⁻¹ after 1000 cycles at 0.5 C, which was increased to 937 mAh·g⁻¹ after 1000 cycles with the inclusion of a PEI/ER/Super-P interlayer.

Composite and cross-linked binders excel when two or more outstanding properties of individual materials are synergistically utilized. Further improvements in the overall performance, loadings, electrolyte content, and safety of Li-S cells could be realized through the rational combination of composite/cross-linked binders and a relevant sulfur host.

2.8 Multifunctional Polymer Composite Frameworks

The research reviewed thus far typically utilizes polymeric binders to form robust networks which can retain the sulfur and electrode components. However, multifunctional binders can fulfil more than one role in the composite. For example, electronically conductive binders can fill the role of both binder and conductive additive. Though some of the papers in this section mention multifunctional polymers in host-based PCFs, the research into multifunctional binders in host-free PCFs is emphasized in this section. A table containing the electrochemical performances of multifunctional PCFs is included in **Table 2.4**.

Table 2.4: Binders and their electrochemical performance in multifunctional PCFs

Binder	Discharge capacity @ n th cycle	C-rate	Reference
<i>Electronically conductive binders</i>			
PAA/PEDOT:PSS	833 mAh·g ⁻¹ @ 80 cycles	0.5 C	[210]
PEDOT:PSS/Mg ²⁺	≈ 810 mAh·g ⁻¹ @ 250 cycles	0.5 C	[211]
PANi	439 mAh·g ⁻¹ @ 50 cycles	≈ 0.07 C	[212]
PPy/PU	≈ 1000 mAh·g ⁻¹ @ 100 cycles	0.33 C	[213]
PFM	≈ 800 mAh·g ⁻¹ @ 150 cycles	0.1 C	[214]
<i>Ionically conductive binders</i>			
Li-Nafion	≈ 540 mAh·g ⁻¹ @ 100 cycles	0.2 C	[142]
Li-Nafion/PVP/nano silica	≈ 800 mAh·g ⁻¹ @ 350 cycles	1 C	[215]
SPEEK	≈ 300 mAh·g ⁻¹ @ 300 cycles	≈ 0.6 C	[216]
PEO/TA	476.7 mAh·g ⁻¹ @ 1000 cycles	0.2 C	[217]
<i>Redox-active binders</i>			
π-Stacked PBI	600 mAh·g ⁻¹ @ 150 cycles	1 C	[218]
Naphthalene-polyether	≈ 910 mAh·g ⁻¹ @ 30 cycles	0.2 C	[219]

2.8.1 Electronically Conductive Binders

It is a well-established fact that sulfur and the insoluble PS discharge products are electronic and ionic insulators, which leads to the utilization of conductive carbon hosts and additives to promote conductivity across Li–S cathodes. Therefore, it is unavoidable that the capacity according to the mass of the entire cathode is reduced, as some of the composite mass goes toward promoting conductivity, while another portion is devoted to the adhesion and structural stability of the electrode (i.e., the binder). If both the conductivity and adhesion could be provided by one electrode component, the mass loading of components, which do not contribute to the capacity of the electrode, can be reduced; thus, a higher capacity according to the mass of the entire electrode could be realized. Conductive polymers may be able to fill this requirement with the works toward this aim reviewed below.

Poly(3,4-ethylenedioxythiophene) (PEDOT) can either be used directly, or more generally, as a composite polymer with poly(styrene sulfonate) (PEDOT:PSS), as shown in **Fig. 2.30**, PEDOT:PSS consists of conjugated PEDOT with a positive charge and a negatively charged saturated PSS. PEDOT:PSS is the most successful conductive polymer in practical application and has found uses in many electrochemical applications [220]. Recently, researchers focusing on Li-S batteries have applied PEDOT and PEDOT:PSS to Li-S cathodes to produce electronically conductive polymeric binding frameworks.

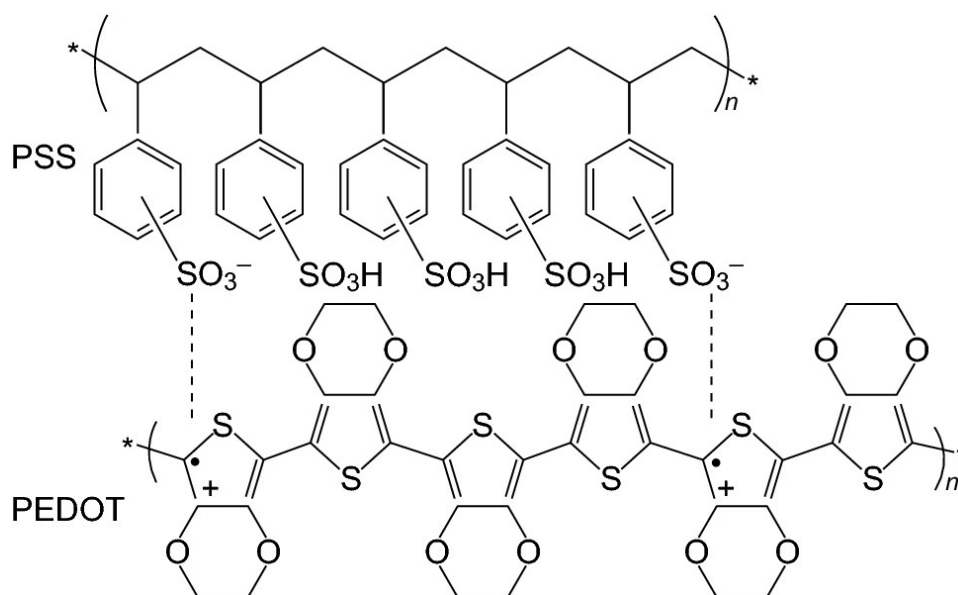


Figure 2.30: Chemical structure of PEDOT:PSS. Reproduced with permission from Ref. [220]. Copyright 2015 Springer Nature

Wang et al. [221] first investigated PEDOT as a binder for sulfur cathodes in Li-S batteries. The group examined the electrochemical performance derived from this binder when commercial micrometric sulfur and prepared nanometric sulfur were used as active materials in two electrolyte systems (1,3-dioxolane(DOL):1,2-dimethoxyethane (DME) and poly(ethylene glycol) dimethoxyethane (PEGDME)) and compared the performance obtained with a PVDF binder. The best electrochemical performance was obtained when the cathode framework was synthesized with the commercial micrometric sulfur power and PEDOT binder in a PEGDME electrolyte. The group ascribed this to a reduced polysulfide dissolution and more viscous electrolyte, reducing particle mobility.

Pan et al. [210] investigated a water-soluble PAA/PEDOT:PSS composite binder for Li-S batteries which delivered synergistic functions in high-performance Li-S cells. The PAA binder modified the electrolyte-electrode interface, which improved reaction kinetics and

provided electrode adhesion, while the PEDOT:PSS provided chemical anchoring for PS retention and allowed for good electronic and ionic conductivity. The group varied the ratio between the multifunctional binder components and found that a ratio of 2:3 (PAA to PEDOT:PSS) delivered the optimum performance. As a result, the polymeric conductive binding framework enabled an initial discharge capacity of $1121 \text{ mAh}\cdot\text{g}^{-1}$ and a reversible capacity of $833 \text{ mAh}\cdot\text{g}^{-1}$ after 80 cycles at 0.5 C .

Later, an ionically cross-linked PEDOT:PSS/ Mg^{2+} network binder was developed by Yan et al. [211]. The Mg^{2+} ions interacted with the free SO_2OH groups on the PSS backbone, which enabled a robust and conductive 3-D network that could better withstand the volume expansion-related stresses that the framework is exposed to during cycling. As a result, the PEDOT:PSS/ Mg^{2+} network binder enabled an initial discharge capacity of $1097 \text{ mAh}\cdot\text{g}^{-1}$ with a 74 % capacity retention after 250 cycles at 0.5 C .

PANi, in its acid-doped form, is an electronically conductive polymer. However, the brittle PANi chain can hardly accommodate the stresses associated with the volume variation during cycling. In response to this, extended conducting PANi with good electrical conductivity was developed by Gao et al. [212] through an anion doping strategy. Sulfuric acid was employed to coordinate with the PANi chain in an m-cresol solvent to form the extended chain structure, which subsequently enabled a “cobweb” structure that efficiently bonded the active materials with sufficient space for electrolyte swelling and channels for ion transfer, even under an intriguingly low binder dose of 2 wt%. Additionally, the positively charged conductive matrix and the heteroatoms also help to electrostatically and chemically adsorb polysulfides for inhibited shuttling behaviour. Owing to these merits, a sulfur electrode based on cobweb PANi binder displayed a reduced internal resistance and faster reaction kinetics, corresponding to a ca. 104 % and 74 % increase in the specific capacity at a current density of 122 and $610 \text{ mA}\cdot\text{g}^{-1}$, respectively, when compared to the PVDF-based cathode.

PPy is another conductive polymer that has been successfully applied to other LIB systems but has struggled to be implemented in Li–S cells due to its brittleness, making its direct use difficult. Milroy et al. fabricated a conductive, electroactive, and elastic PPy/poly(urethane) (PU) multifunctional binder for a free-standing and flexible Li–S cathode to circumvent this [213]. The PPyPU binder delivered dual benefits; an electronically conductive network deriving from the PPy and mechanical pliability from the PU that can help to accommodate the severe volume change characteristic of sulfur cathodes. A high reversible discharge capacity

of ca. 1000 mAh·g⁻¹ was delivered after 100 cycles at 3 C rate owing to the prevention of premature electrode degradation by the PPyPU binder.

Poly(9,9-dioctylfluorene-co-fluorenone-co-methylbenzoic ester) (PFM) binder (**Fig. 2.31a**) is a specifically designed polymer with both carbonyl groups for chemical sulfur anchoring and an enhanced electronic conductivity developed by Ai et al. [214]. The group chose representative polymer binders with specific functionality to compare with the PFM binder in their study. PEDOT:PSS was chosen as an example binder that displays electronic conductivity, PVP was chosen for its chemical PS anchoring ability, and PVDF was chosen as it has neither functionality. Upon investigating the obtained electrochemical performances, it can be noted that between the PEDOT:PSS and PVP-based electrode, the PEDOT:PSS electrode displays a comparatively higher initial discharge capacity but a faster capacity fading upon cycling, whereas the opposite is true for the PVP binder (i.e. a comparatively lower initial capacity but better capacity retention). The group supposed that PEDOT:PSS's electronic conductivity allowed for a greater degree of initial sulfur utilization, whereas the chemical bonding mediated by the PVP binder resulted in improved capacity retention. The PFM binder combines both of these traits and, as a result, delivers the best electrochemical performance. Post-mortem SEM analysis of the top and bottom of the PFM electrodes revealed that in the fully charged state, the PFM binder enables the long-chain PS to be precipitated as elemental sulfur homogeneously throughout the entire electrode due to the combined effects of the carbonyl functional groups and the conductivity of the binder. Complete Li₂S precipitation is also mediated by the PFM binder owing to the strong affinity between the carbonyl groups and Li₂S and an increased amount of reaction sites for Li₂S precipitation, owing to the enhanced conductive surface of the multifunctional PFM binding framework.

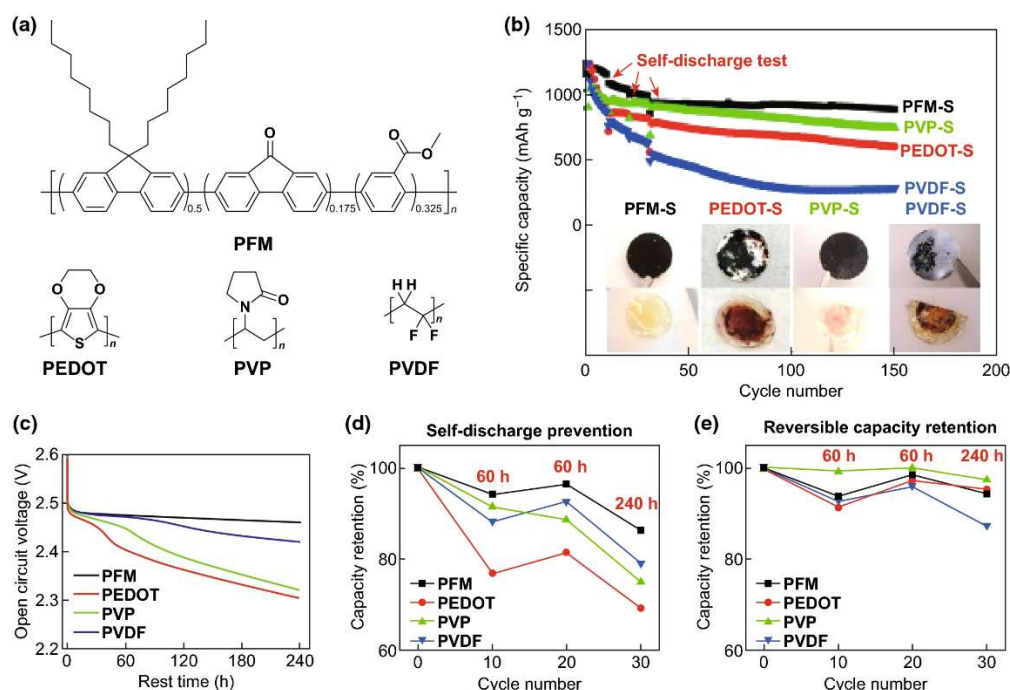


Figure 2.31: (a) Chemical structures of the four different binders: PFM, PEDOT, PVP, and PVDF. (b) Cycling performance at C/10 and self-discharge performance of cathodes with different binders. (c) The open-circuit voltage change versus rest time during the third self-discharge rest of 240 h for the PFM-S, PEDOT-S, PVP-S, and PVDF-S cathodes. The self-discharge capacity prevention ratio (d) and reversible capacity retention ratio (e) for cathodes with different binders during the self-discharge test. Reproduced with permission from Ref. [214]. Copyright 2015 Elsevier

2.8.2 Ionically Conductive Binders

Ionically conductive binders can help overcome the low ionic conductivity of sulfur and Li₂S, so sulfur utilization and mass transport can be improved within the electrode. The work using ionically conductive binders is reviewed below.

One such example is Nafion, a perfluorosulfonate ionomer (ionic polymer) that is most commonly used in proton exchange membranes [222]. The ion-conducting properties of Nafion can be altered through cation exchange, as evidenced by Schneider et al. [142]. The group treated the commercial Nafion polymer with LiOH to carry out a cation exchange and examined the material as a binder for Li-S batteries (**Fig. 2.32**). Electrodes were fabricated using the Li-Nafion as a binder with an additional Li-Nafion layer spray-coated on the surface. The resultant batteries displayed an improved initial discharge capacity when compared to CMC and PTFE-based cells, which indicates an improved sulfur utilization owing to the improved ionic conductivity of the Li-Nafion-based cell.

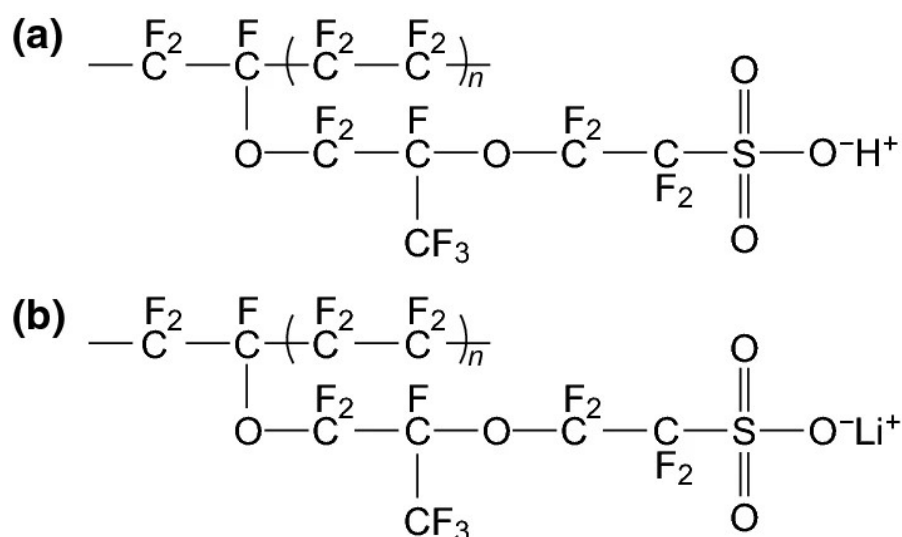


Figure 2.32: Chemical structures of H-Nafion (a) and Li-Nafion (b). Reproduced with permission from Ref. [223]. Copyright 2018 Elsevier

Following this, Li et al. combined Li-Nafion, PVP and nano-silica as a multifunctional binder for high-performance Li-S batteries [215]. Each component of the binder contributed to improved cell performance. The Li-Nafion improved Li^+ supply for sulfur redox reactions. The PVP provided PS anchoring for a reduced shuttle effect, improved the mechanical properties of the composite, and enabled a good dispersion of active materials within the sulfur electrode. The impregnated nano-silica could further inhibit the shuttle effect due to the strong affinity toward its polar surface and polysulfides while introducing abundant interfaces within the electrode for improved electrolyte wetting. Attributed to these favourable functionalities, the sulfur electrode based on the composite binder achieved a high sulfur utilization with an initial discharge capacity of $1373 \text{ mAh}\cdot\text{g}^{-1}$ at 0.2 C, excellent sulfur redox kinetics with a high reversible capacity of $470 \text{ mAh}\cdot\text{g}^{-1}$ at a high current rate up to 5 C, and superb cycling stability over 300 cycles at 1 C. More recently, Gao et al. used a Li-Nafion resin as the binder and solid electrolyte in Li-S cells [223]. An optimized loading of 40% Li-Nafion and 10% conductive additive allowed for a balance of ionic and electronic conductivity in the cathode, which delivered a reversible capacity of $895 \text{ mAh}\cdot\text{g}^{-1}$ at 1 C with an 89 % capacity retention after 100 cycles.

Cheng et al. developed a sulfonated poly(ether ether ketone) (SPEEK) polymer as a functional binder for sulfur electrodes [216]. The ether and benzene rings endowed the SPEEK with an appropriate combination of flexibility and stiffness, leading to good adhesion for active electrode materials, while the abundant carbonyl, sulfonyl, and benzene ring groups

contributed to a strong electronegativity that repelled the dissolution and diffusion of polysulfide anions, thus facilitating the inhibition on polysulfide shuttling. As a result, the SPEEK-based Li-S cell delivered a more stable performance after 300 cycles at a current density of $1000 \text{ mA} \cdot \text{g}^{-1}$ than the PVDF-based cell.

As mentioned earlier, the mechanical strength and adhesive properties of PEO frameworks suffer from swelling/dissolution in organic electrolytes. Zhang et al. attempted to rectify this phenomenon by creating a 3D-cross-linked tannic acid (TA)/PEO binder with enhanced ionic conductivity for Li-S cells [217]. The formation of the 3D network was realized through hydrogen bonding interactions between the TA and the PEO, which could enable the TA/PEO framework to provide strong adhesion even after submersion in the electrolyte. Electrochemical investigation revealed that the TA/PEO framework delivered a stable discharge capacity of $476.7 \text{ mAh} \cdot \text{g}^{-1}$ after an outstanding 1000 cycles, owing to the composite network binder's PS anchoring ability and mechanical properties. Post-mortem SEM analysis of the cathodes revealed that the PEO and PVDF-based electrodes displayed a thick Li_2S layer deposited on the surface. In contrast, the TA/PEO electrode had a relatively uniform distribution of discharge products, which the authors suggest was due to a facile diffusion of lithium ions throughout the framework.

2.8.3 Redox-Active Binders

A straightforward strategy to achieve a reactive binder is incorporating active sulfur into the binder structure, contributing additional capacity while maintaining good electrode integrity. Trofimov et al. [224] prepared bis-[3-(vinylxyethoxy)-2-hydroxypropyl-] polysulfides (BVPS) by reacting ethylene glycol vinyl glycidyl ether (EGVGE) with Na_2S_4 in the presence of NaHCO_3 and a phase transfer catalyst triethylbenzylammonium chloride. The obtained BVPS contained 24.5% sulfur ($n = 2, 3$, where n represents the length of the polysulfide chain in the BVPS molecule) bridging the symmetric organic moieties, which was further copolymerized with elemental sulfur at 130°C for 1 h to yield a polymer containing up to 32.6% sulfur ($n = 4$). The polymerization leads to cross-linked polymers, which were used as the active binder for Li-S batteries. The obtained binder exhibited strong adhesion that could retain a robust electrode even under low binder content of 5%. Meanwhile, the binder also contributed additional capacity due to the redox reactivity of the sulfur incorporated in the binder structure.

Imide-based organic compounds have recently been investigated as redox-active mediators in Li-S systems by Frischmann et al. [225]. The group then implemented π -stacked perylene bisimide (PBI) as redox-active supramolecular polymer binders to overcome the ionic and electronic bottlenecks in sulfur cathodes [218]. The PBI binder offered self-healing properties to reduce structural damage from the active material volume expansion upon cycling. By fabricating a PBI/PVDF composite binder, the over-potential of the electrodes during discharge was minimized, as evidenced by a galvanostatic intermittent titration technique (GITT). The group then further investigated a lithiated, redox-active, aqueous-soluble PBI binder which showed further electrochemical improvements [226].

Hernández et al. [219] investigated three polyimide-polyether composite redox-active binders for Li-S batteries (**Fig. 2.33**). Among the pyromellitic, naphthalene, and perylene polyimides, the cell based on the naphthalene-polyether composite binder showed a higher sulfur utilization and a lower polarization and thus delivered the best electrochemical performance for a few reasons. The redox potential of the naphthalene-polyether coincided best with the sulfur redox potential and, as a result, successfully facilitated charge transfer across the binding framework and sulfur interfaces, improving active mass utilization. The incorporation of PEO within the composite increased the solubility of the copolymer, making electrode fabrication easier, and during cycling enabled an improved mass transport across the electrode while simultaneously limiting PS diffusion from the cathode. The resultant naphthalene-polyether based electrodes delivered an initial capacity of $1300 \text{ mAh} \cdot \text{g}^{-1}$ with a 70 % capacity retention after 30 cycles at 0.2 C.

Overall, multifunctional PCFs can increase the performance of a sulfur cathode relative to its entire mass by endowing a cell component that would have otherwise not contributed to a cell's electrochemical function (beyond providing structural stability) with such abilities as electronic and ionic conductivity or redox activity. Further improvements could be achieved by combining these multifunctional binders with relevant sulfur hosts for increased performance.

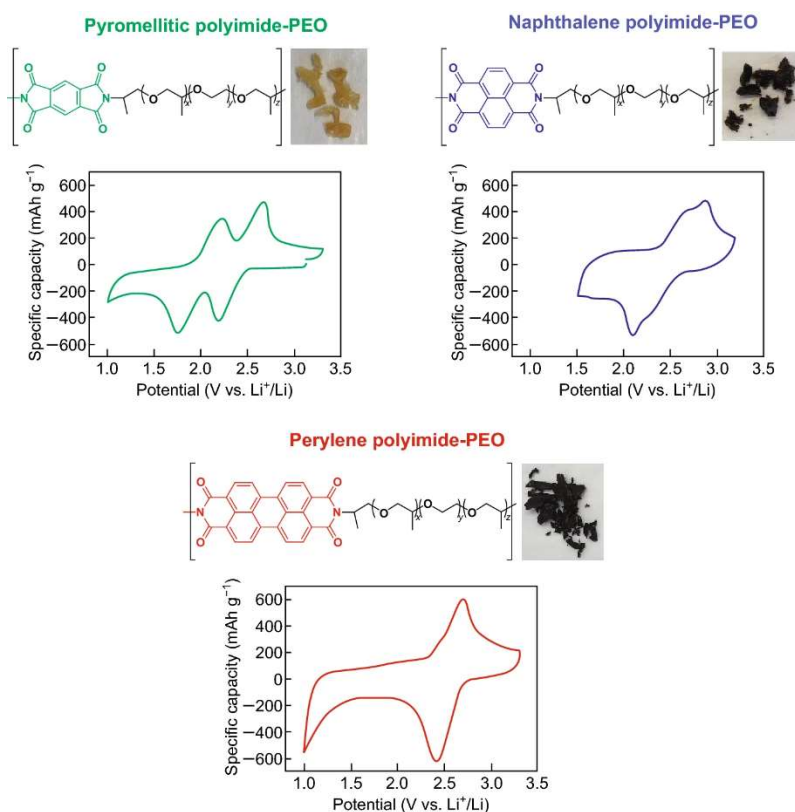


Figure 2.33: Chemical structure, physical aspect and cyclic voltammogram of polyimide-polyether copolymers. Reproduced with permission from Ref. [219]. Copyright 2017 Elsevier

2.9 Conclusions

Thus far, most efforts to address the inherent challenges of Li-S batteries have been focused on the design of micro-, nano-, or molecular structured sulfur hosts. The function of binders and the widespread availability of multifunctional binders have been neglected. Recently, sulfur host-based cathodes that utilize the traditional PVDF binder have been the dominant research direction; however, the role of novel binders in these cathodes is beginning to be explored. Briefly, by the careful selection of multifunctional binders and sulfur hosts, the following benefits could be realized:

1. By combining natural polymers with hosts synthesized via green chemical routes, the overall environmental impact of Li-S cell fabrication could be reduced.
2. By combining synthetic binders, cross-linked binders, or composite binders with a suitable sulfur host, further improvements in sulfur loading, sulfur utilization, E/S ratio, and safety of the Li-S system could be achieved.

3. By using relevant multifunctional binders, the specific capacity of the Li–S cathode could be improved by reducing the amount of electrochemically inactive components.

These relatively new research directions could provide vast improvements in the future. However, in the case of host-free PCFs, special attention must be paid to assure that the polymeric binder can not only initiate strong adhesive forces between the electrode components, it must also be able to retain a stable void structure during sulfur dissolution. In short, binder research in Li–S batteries is an under-explored and fruitful research direction.

Acknowledgments

This work was financially supported by the Australian Research Council Future Fellowship and Discovery Projects, RTP, and GUPRS Scholarships.

2.10 References

1. Pachauri, R.K., et al., Climate change 2014: synthesis report. Contribution of Working Groups I, II and III to the fifth assessment report of the Intergovernmental Panel on Climate Change. 2014: IPCC.
2. Yang, Z., et al., *Electrochemical Energy Storage for Green Grid*. Chemical Reviews, 2011. **111**(5): p. 3577-3613.
3. Budischak, C., et al., Cost-minimized combinations of wind power, solar power and electrochemical storage, powering the grid up to 99.9% of the time. Journal of Power Sources, 2013. **225**: p. 60-74.
4. Bruce, P.G., et al., *Li-O₂ and Li-S batteries with high energy storage*. Nature materials, 2012. **11**(1): p. 19.
5. Yang, Y., G. Zheng, and Y. Cui, *Nanostructured sulfur cathodes*. Chemical Society Reviews, 2013. **42**(7): p. 3018-3032.
6. Yin, Y.X., et al., *Lithium-sulfur batteries: electrochemistry, materials, and prospects*. Angewandte Chemie International Edition, 2013. **52**(50): p. 13186-13200.
7. Gu, X. and C. Lai, Recent development of metal compound applications in lithium-sulphur batteries. Journal of Materials Research, 2018. **33**(1): p. 16-31.
8. Wang, Y., et al., Sulfur Hosts against the Shuttle Effect. Small Methods, 2018.
9. Cleaver, T., et al., *Perspective—Commercializing Lithium Sulfur Batteries: Are We Doing the Right Research?* Journal of The Electrochemical Society, 2018. **165**(1): p. A6029-A6033.
10. Yuan, H., et al., *A Review of Functional Binders in Lithium-Sulfur Batteries*. Advanced Energy Materials. **0**(0): p. 1802107.
11. Ma, Y., J. Ma, and G. Cui, Small things make big deal: Powerful binders of lithium batteries and post-lithium batteries. Energy Storage Materials, 2018.
12. Zhu, J., et al., Recent progress in polymer materials for advanced lithium-sulfur batteries. Progress in Polymer Science, 2018.
13. Chen, H., et al., Exploring Chemical, Mechanical, and Electrical Functionalities of Binders for Advanced Energy-Storage Devices. Chemical Reviews, 2018.
14. Packham, D., *The Mechanical Theory of Adhesion—Changing Perceptions 1925-1991*. the Journal of Adhesion, 1992. **39**(2-3): p. 137-144.

15. Gent, A.N. and C.W. Lin, Model Studies of the Effect of Surface Roughness and Mechanical Interlocking on Adhesion. *The Journal of Adhesion*, 1990. **32**(2-3): p. 113-125.
16. Nunes, S.L.S., et al., Comparative Failure Assessment of Single and Double Lap Joints with Varying Adhesive Systems. *The Journal of Adhesion*, 2016. **92**(7-9): p. 610-634.
17. Gardner, D.J., et al., *Adhesion theories in wood adhesive bonding*. Progress in Adhesion and Adhesives; John Wiley & Sons, Inc.: San Francisco, CA, USA, 2015: p. 125-168.
18. Magasinski, A., et al., *Toward Efficient Binders for Li-Ion Battery Si-Based Anodes: Polyacrylic Acid*. *ACS Applied Materials & Interfaces*, 2010. **2**(11): p. 3004-3010.
19. Derjaguin, B.V., I.N. Alenikova, and Y.P. Toporov, *On the role of electrostatic forces in the adhesion of polymer particles to solid surfaces*. *Powder Technology*, 1969. **2**(3): p. 154-158.
20. Song, J., et al., Interpenetrated Gel Polymer Binder for High-Performance Silicon Anodes in Lithium-ion Batteries. *Advanced Functional Materials*, 2014. **24**(37): p. 5904-5910.
21. Zhong, C., et al., A review of electrolyte materials and compositions for electrochemical supercapacitors. *Chemical Society Reviews*, 2015. **44**(21): p. 7484-7539.
22. Smitha, B., S. Sridhar, and A. Khan, *Solid polymer electrolyte membranes for fuel cell applications—a review*. *Journal of membrane science*, 2005. **259**(1-2): p. 10-26.
23. Yoshio, M., R.J. Brodd, and A. Kozawa, *Lithium-ion batteries*. Vol. 1. 2009: Springer.
24. Zhu, Z., et al., *Effects of various binders on supercapacitor performances*. *Int J Electrochem Sci*, 2016. **11**(10): p. 8270-8279.
25. Zhang, S.S. and T.R. Jow, Study of poly(acrylonitrile-methyl methacrylate) as binder for graphite anode and LiMn₂O₄ cathode of Li-ion batteries. *Journal of Power Sources*, 2002. **109**(2): p. 422-426.
26. Maleki, H., et al., *Thermal Stability Studies of Li-Ion Cells and Components*. *Journal of The Electrochemical Society*, 1999. **146**(9): p. 3224-3229.
27. Markevich, E., G. Salitra, and D. Aurbach, *Influence of the PVdF binder on the stability of LiCoO₂ electrodes*. *Electrochemistry Communications*, 2005. **7**(12): p. 1298-1304.
28. Kasap, S. and P. Capper, *Springer handbook of electronic and photonic materials*. 2017: Springer.
29. Liu, W.-R., et al., Enhanced Cycle Life of Si Anode for Li-Ion Batteries by Using Modified Elastomeric Binder. *Electrochemical and Solid-State Letters*, 2005. **8**(2): p. A100-A103.

30. Lux, S.F., et al., *Low Cost, Environmentally Benign Binders for Lithium-Ion Batteries*. Journal of The Electrochemical Society, 2010. **157**(3): p. A320-A325.
31. Fang, R., et al., More Reliable Lithium-Sulfur Batteries: Status, Solutions and Prospects. Advanced Materials, 2017. **29**(48): p. 1606823.
32. Zhou, G., et al., *Catalytic oxidation of Li₂S on the surface of metal sulfides for Li–S batteries*. Proceedings of the National Academy of Sciences, 2017. **114**(5): p. 840-845.
33. Han, K., et al., Free-Standing Nitrogen-doped Graphene Paper as Electrodes for High-Performance Lithium/Dissolved Polysulfide Batteries. ChemSusChem, 2014. **7**(9): p. 2545-2553.
34. Liu, B., et al., Revisiting Scientific Issues for Industrial Applications of Lithium–Sulfur Batteries. ENERGY & ENVIRONMENTAL MATERIALS, 2018. **1**(4): p. 196-208.
35. He, Y., et al., *Effective strategies for long-cycle life lithium–sulfur batteries*. Journal of Materials Chemistry A, 2018. **6**(15): p. 6155-6182.
36. Yoon, G., et al., Using First-Principles Calculations for the Advancement of Materials for Rechargeable Batteries. Advanced Functional Materials, 2017. **27**(40): p. 1702887.
37. Nazar, L.F., M. Cuisinier, and Q. Pang, *Lithium-sulfur batteries*. MRS Bulletin, 2014. **39**(5): p. 436-442.
38. Peng, H.-J., et al., *Review on High-Loading and High-Energy Lithium–Sulfur Batteries*. Advanced Energy Materials, 2017. **7**(24): p. 1700260.
39. Li, C., et al., Chemical Immobilization Effect on Lithium Polysulfides for Lithium–Sulfur Batteries. Small, 2018. **14**(4): p. 1701986.
40. Lin, Z. and C. Liang, *Lithium–sulfur batteries: from liquid to solid cells*. Journal of Materials Chemistry A, 2015. **3**(3): p. 936-958.
41. Song, M.-K., E.J. Cairns, and Y. Zhang, Lithium/sulfur batteries with high specific energy: old challenges and new opportunities. Nanoscale, 2013. **5**(6): p. 2186-2204.
42. Li, S.-Y., et al., Recent progress on confinement of polysulfides through physical and chemical methods. Journal of Energy Chemistry, 2018. **27**(6): p. 1555-1565.
43. Hou, T.-Z., et al., *Lithium Bond Chemistry in Lithium–Sulfur Batteries*. Angewandte Chemie International Edition, 2017. **56**(28): p. 8178-8182.
44. Hou, T.-Z., et al., Design Principles for Heteroatom-Doped Nanocarbon to Achieve Strong Anchoring of Polysulfides for Lithium–Sulfur Batteries. Small, 2016. **12**(24): p. 3283-3291.

45. Chen, X., et al., An Analogous Periodic Law for Strong Anchoring of Polysulfides on Polar Hosts in Lithium Sulfur Batteries: S- or Li-Binding on First-Row Transition-Metal Sulfides? *ACS Energy Letters*, 2017. **2**(4): p. 795-801.
46. Wang, H., et al., *Advances in Polar Materials for Lithium–Sulfur Batteries*. *Advanced Functional Materials*, 2018. **28**(38): p. 1707520.
47. Liu, X., et al., Nanostructured Metal Oxides and Sulfides for Lithium–Sulfur Batteries. *Advanced Materials*, 2017. **29**(20): p. 1601759.
48. Liu, J., et al., Progress and perspective of organosulfur polymers as cathode materials for advanced lithium-sulfur batteries. *Energy Storage Materials*, 2018. **15**: p. 53-64.
49. Cheng, Z., et al., Porous Organic Polymers for Polysulfide Trapping in Lithium–Sulfur Batteries. *Advanced Functional Materials*, 2018. **28**(38): p. 1707597.
50. Zhang, Z.-W., et al., Heterogeneous/Homogeneous Mediators for High-Energy-Density Lithium–Sulfur Batteries: Progress and Prospects. *Advanced Functional Materials*, 2018. **28**(38): p. 1707536.
51. Peng, H.-J., J.-Q. Huang, and Q. Zhang, A review of flexible lithium–sulfur and analogous alkali metal–chalcogen rechargeable batteries. *Chemical Society Reviews*, 2017. **46**(17): p. 5237-5288.
52. Chen, C.-Y., et al., A Quinonoid-Imine-Enriched Nanostructured Polymer Mediator for Lithium–Sulfur Batteries. *Advanced Materials*, 2017. **29**(23): p. 1606802.
53. Xiao, Z., et al., Covalent organic frameworks with lithiophilic and sulfiphilic dual linkages for cooperative affinity to polysulfides in lithium-sulfur batteries. *Energy Storage Materials*, 2018. **12**: p. 252-259.
54. Li, B.-Q., et al., Porphyrin Organic Framework Hollow Spheres and Their Applications in Lithium–Sulfur Batteries. *Advanced Materials*, 2018. **30**(23): p. 1707483.
55. Liu, J., et al., Molecularly Imprinted Polymer Enables High-Efficiency Recognition and Trapping Lithium Polysulfides for Stable Lithium Sulfur Battery. *Nano Letters*, 2017. **17**(8): p. 5064-5070.
56. Shi, J.-L., et al., Effective exposure of nitrogen heteroatoms in 3D porous graphene framework for oxygen reduction reaction and lithium–sulfur batteries. *Journal of Energy Chemistry*, 2018. **27**(1): p. 167-175.
57. Hu, G., et al., A Sulfur-Rich Copolymer@CNT Hybrid Cathode with Dual-Confinement of Polysulfides for High-Performance Lithium–Sulfur Batteries. *Advanced Materials*, 2017. **29**(11): p. 1603835.

58. Yang, W., et al., A polypyrrole-coated acetylene black/sulfur composite cathode material for lithium–sulfur batteries. *Journal of Energy Chemistry*, 2018. **27**(3): p. 813-819.
59. Zhang, H., et al., Nitrogen-doped hierarchical porous carbon derived from metal–organic aerogel for high performance lithium–sulfur batteries. *Journal of Energy Chemistry*, 2017. **26**(6): p. 1282-1290.
60. Tao, X., et al., Balancing surface adsorption and diffusion of lithium-polysulfides on nonconductive oxides for lithium–sulfur battery design. *Nature Communications*, 2016. **7**: p. 11203.
61. Chen, W., et al., Atomic Interlamellar Ion Path in High Sulfur Content Lithium-Montmorillonite Host Enables High-Rate and Stable Lithium–Sulfur Battery. *Advanced Materials*, 2018. **30**(40): p. 1804084.
62. Lei, T., et al., Multi-Functional Layered WS₂ Nanosheets for Enhancing the Performance of Lithium–Sulfur Batteries. *Advanced Energy Materials*, 2017. **7**(4): p. 1601843.
63. Huang, J.-Q., Q. Zhang, and F. Wei, Multi-functional separator/interlayer system for high-stable lithium-sulfur batteries: Progress and prospects. *Energy Storage Materials*, 2015. **1**: p. 127-145.
64. Lei, T., et al., Inhibiting Polysulfide Shuttling with a Graphene Composite Separator for Highly Robust Lithium-Sulfur Batteries. *Joule*, 2018. **2**(10): p. 2091-2104.
65. Fu, X., et al., A polymeric nanocomposite interlayer as ion-transport-regulator for trapping polysulfides and stabilizing lithium metal. *Energy Storage Materials*, 2018. **15**: p. 447-457.
66. Tu, S., et al., A Polysulfide-Immobilizing Polymer Retards the Shuttling of Polysulfide Intermediates in Lithium–Sulfur Batteries. *Advanced Materials*, 2018. **30**(45): p. 1804581.
67. Huang, J.-Q., et al., *Ionic shield for polysulfides towards highly-stable lithium–sulfur batteries*. *Energy & Environmental Science*, 2014. **7**(1): p. 347-353.
68. Scheers, J., S. Fantini, and P. Johansson, *A review of electrolytes for lithium–sulphur batteries*. *Journal of Power Sources*, 2014. **255**: p. 204-218.
69. Chen, W., et al., Designing Safe Electrolyte Systems for a High-Stability Lithium–Sulfur Battery. *Advanced Energy Materials*, 2018. **8**(10): p. 1702348.
70. Hagen, M., et al., Lithium–Sulfur Cells: The Gap between the State-of-the-Art and the Requirements for High Energy Battery Cells. *Advanced Energy Materials*, 2015. **5**(16): p. 1401986.

71. Chung, S.-H. and A. Manthiram, *Designing Lithium–Sulfur Batteries with High-Loading Cathodes at a Lean Electrolyte Condition*. ACS Applied Materials & Interfaces, 2018. **10**(50): p. 43749-43759.
72. Xu, W., et al., *Lithium metal anodes for rechargeable batteries*. Energy & Environmental Science, 2014. **7**(2): p. 513-537.
73. Lin, D., Y. Liu, and Y. Cui, *Reviving the lithium metal anode for high-energy batteries*. Nature Nanotechnology, 2017. **12**: p. 194.
74. Manthiram, A., et al., *Rechargeable lithium–sulfur batteries*. Chemical reviews, 2014. **114**(23): p. 11751-11787.
75. Dai, H., et al., Cationic Surfactant-Based Electrolyte Additives for Uniform Lithium Deposition via Lithiophobic Repulsion Mechanisms. Journal of the American Chemical Society, 2018. **140**(50): p. 17515-17521.
76. Lei, T., et al., A Nonflammable and Thermotolerant Separator Suppresses Polysulfide Dissolution for Safe and Long-Cycle Lithium-Sulfur Batteries. Advanced Energy Materials, 2018. **8**(32): p. 1802441.
77. Zhou, G., et al., An Aqueous Inorganic Polymer Binder for High Performance Lithium–Sulfur Batteries with Flame-Retardant Properties. ACS central science, 2018. **4**(2): p. 260-267.
78. Gu, X., L. Hencz, and S. Zhang, Recent development of carbonaceous materials for lithium–sulphur batteries. Batteries, 2016. **2**(4): p. 33.
79. Wang, J. and W.-Q. Han, *A Review of Heteroatom Doped Materials for Advanced Lithium–Sulfur Batteries*. Advanced Functional Materials, 2021. **n/a**(n/a): p. 2107166.
80. Choi, Y.S., et al., Effect of cathode component on the energy density of lithium–sulfur battery. Electrochimica Acta, 2004. **50**(2): p. 833-835.
81. Evers, S. and L.F. Nazar, *New Approaches for High Energy Density Lithium–Sulfur Battery Cathodes*. Accounts of Chemical Research, 2013. **46**(5): p. 1135-1143.
82. He, G., et al., Tailoring Porosity in Carbon Nanospheres for Lithium–Sulfur Battery Cathodes. ACS Nano, 2013. **7**(12): p. 10920-10930.
83. Wang, M., et al., *Porous Carbon Hosts for Lithium–Sulfur Batteries*. Chemistry – A European Journal, 2019. **25**(15): p. 3710-3725.
84. Pang, Q., et al., Advances in lithium–sulfur batteries based on multifunctional cathodes and electrolytes. Nature Energy, 2016. **1**(9): p. 16132.

85. McNulty, D., V. Landgraf, and S. Trabesinger, *The importance of sulfur host structural preservation for lithium–sulfur battery performance*. Journal of Materials Chemistry A, 2020. **8**(48): p. 26085-26097.
86. Hu, Y., et al., *Strategies toward High-Loading Lithium–Sulfur Battery*. Advanced Energy Materials, 2020. **10**(17): p. 2000082.
87. Chen, M., et al., Suppressing the Polysulfide Shuttle Effect by Heteroatom-Doping for High-Performance Lithium–Sulfur Batteries. ACS Sustainable Chemistry & Engineering, 2018. **6**(6): p. 7545-7557.
88. Ji, X. and L.F. Nazar, *Advances in Li–S batteries*. Journal of Materials Chemistry, 2010. **20**(44): p. 9821-9826.
89. Chiochan, P., et al., Chemical Adsorption and Physical Confinement of Polysulfides with the Janus-faced Interlayer for High-performance Lithium-Sulfur Batteries. Scientific Reports, 2017. **7**(1): p. 17703.
90. Ren, W., et al., Recent advances in shuttle effect inhibition for lithium sulfur batteries. Energy Storage Materials, 2019. **23**: p. 707-732.
91. Liu, Y.-T., et al., High Volumetric Energy Density Sulfur Cathode with Heavy and Catalytic Metal Oxide Host for Lithium–Sulfur Battery. Advanced Science, 2020. **7**(12): p. 1903693.
92. Shi, Z., et al., Catalytic cobalt phosphide Co₂P/carbon nanotube nanocomposite as host material for high performance lithium-sulfur battery cathode. Journal of Alloys and Compounds, 2021. **851**: p. 156289.
93. Li, Y., et al., A heterostructured Co₃S₄/MnS nanotube array as a catalytic sulfur host for lithium–sulfur batteries. Electrochimica Acta, 2020. **330**: p. 135311.
94. Singhal, R., et al., A free-standing carbon nanofiber interlayer for high-performance lithium–sulfur batteries. Journal of Materials Chemistry A, 2015. **3**(8): p. 4530-4538.
95. Peng, Y., et al., Directly Coating a Multifunctional Interlayer on the Cathode via Electrospinning for Advanced Lithium–Sulfur Batteries. ACS Applied Materials & Interfaces, 2017. **9**(35): p. 29804-29811.
96. Sun, J., et al., Entrapment of Polysulfides by a Black-Phosphorus-Modified Separator for Lithium–Sulfur Batteries. Advanced Materials, 2016. **28**(44): p. 9797-9803.
97. Su, Y.-S. and A. Manthiram, A new approach to improve cycle performance of rechargeable lithium–sulfur batteries by inserting a free-standing MWCNT interlayer. Chemical Communications, 2012. **48**(70): p. 8817-8819.

98. Tang, H., et al., In-situ synthesis of carbon@Ti₄O₇ non-woven fabric as a multi-functional interlayer for excellent lithium-sulfur battery. *Electrochimica Acta*, 2018. **263**: p. 158-167.
99. Huang, Y., et al., Co-Fe bimetallic sulfide with robust chemical adsorption and catalytic activity for polysulfides in lithium-sulfur batteries. *Chemical Engineering Journal*, 2020. **387**: p. 124122.
100. Su, Y.-S. and A. Manthiram, Lithium-sulphur batteries with a microporous carbon paper as a bifunctional interlayer. *Nature Communications*, 2012. **3**(1): p. 1166.
101. Yin, L., et al., A functional interlayer as a polysulfides blocking layer for high-performance lithium-sulfur batteries. *New Journal of Chemistry*, 2018. **42**(2): p. 1431-1436.
102. Manthiram, A., Y. Fu, and Y.-S. Su, *Challenges and Prospects of Lithium-Sulfur Batteries*. *Accounts of Chemical Research*, 2013. **46**(5): p. 1125-1134.
103. Lin, H., et al., A Cathode-Integrated Sulfur-Deficient Co₉S₈ Catalytic Interlayer for the Reutilization of “Lost” Polysulfides in Lithium-Sulfur Batteries. *ACS Nano*, 2019. **13**(6): p. 7073-7082.
104. Li, Z., et al., Multifunctional cation-vacancy-rich ZnCo₂O₄ polysulfide-blocking layer for ultrahigh-loading Li-S battery. *Nano Energy*, 2021. **89**: p. 106331.
105. Yang, J., et al., Novel nitrogen-doped hierarchically porous coralloid carbon materials as host matrixes for lithium-sulfur batteries. *Electrochimica Acta*, 2015. **159**: p. 8-15.
106. Rehman, S., et al., 3D Vertically Aligned and Interconnected Porous Carbon Nanosheets as Sulfur Immobilizers for High Performance Lithium-Sulfur Batteries. *Advanced Energy Materials*, 2016. **6**(12): p. 1502518.
107. Zhou, L., T. Huang, and A. Yu, Three-Dimensional Flower-Shaped Activated Porous Carbon/Sulfur Composites as Cathode Materials for Lithium-Sulfur Batteries. *ACS Sustainable Chemistry & Engineering*, 2014. **2**(10): p. 2442-2447.
108. He, B., et al., Incorporating sulfur inside the pores of carbons for advanced lithium-sulfur batteries: An electrolysis approach. *ACS nano*, 2016. **10**(1): p. 1633-1639.
109. Zhou, L., et al., Nitrogen-doped porous carbon nanofiber webs/sulfur composites as cathode materials for lithium-sulfur batteries. *Electrochimica Acta*, 2014. **116**: p. 210-216.
110. Li, Q., et al., A simple synthesis of hollow carbon nanofiber-sulfur composite via mixed-solvent process for lithium-sulfur batteries. *Journal of Power Sources*, 2014. **256**: p. 137-144.

111. Chen, S., et al., Multi-chambered micro/mesoporous carbon nanocubes as new polysulfides reservoirs for lithium–sulfur batteries with long cycle life. *Nano Energy*, 2015. **16**: p. 268-280.
112. Xiao, S., et al., Polyurethane-derived N-doped porous carbon with interconnected sheet-like structure as polysulfide reservoir for lithium–sulfur batteries. *Journal of Power Sources*, 2015. **293**: p. 119-126.
113. Niu, S., et al., A carbon sandwich electrode with graphene filling coated by N-doped porous carbon layers for lithium–sulfur batteries. *Journal of Materials Chemistry A*, 2015. **3**(40): p. 20218-20224.
114. Werner, J.G., et al., Carbon–Sulfur Composites from Cylindrical and Gyroidal Mesoporous Carbons with Tunable Properties in Lithium–Sulfur Batteries. *Chemistry of Materials*, 2015. **27**(9): p. 3349-3357.
115. Schuster, J., et al., Spherical Ordered Mesoporous Carbon Nanoparticles with High Porosity for Lithium–Sulfur Batteries. *Angewandte Chemie*, 2012. **124**(15): p. 3651-3655.
116. Li, X., et al., Optimization of mesoporous carbon structures for lithium–sulfur battery applications. *Journal of Materials Chemistry*, 2011. **21**(41): p. 16603-16610.
117. He, G., X. Ji, and L. Nazar, *High “C” rate Li-S cathodes: sulfur imbibed bimodal porous carbons*. *Energy & Environmental Science*, 2011. **4**(8): p. 2878-2883.
118. Ji, X., K.T. Lee, and L.F. Nazar, A highly ordered nanostructured carbon–sulphur cathode for lithium–sulphur batteries. *Nature materials*, 2009. **8**(6): p. 500.
119. Wang, J., et al., Sulphur-polypyrrole composite positive electrode materials for rechargeable lithium batteries. *Electrochimica Acta*, 2006. **51**(22): p. 4634-4638.
120. Yang, C.-P., et al., Electrochemical (de) lithiation of 1D sulfur chains in Li–S batteries: a model system study. *Journal of the American Chemical Society*, 2015. **137**(6): p. 2215-2218.
121. Xin, S., et al., *Smaller sulfur molecules promise better lithium–sulfur batteries*. *Journal of the American Chemical Society*, 2012. **134**(45): p. 18510-18513.
122. Tao, X., et al., Strong Sulfur Binding with Conducting Magnéli-Phase TiO_{2n-1} Nanomaterials for Improving Lithium–Sulfur Batteries. *Nano Letters*, 2014. **14**(9): p. 5288-5294.
123. Liang, X., et al., A highly efficient polysulfide mediator for lithium–sulfur batteries. *Nature Communications*, 2015. **6**: p. 5682.

124. Pang, Q., D. Kundu, and L.F. Nazar, A graphene-like metallic cathode host for long-life and high-loading lithium–sulfur batteries. *Materials Horizons*, 2016. **3**(2): p. 130-136.
125. Zhang, Z., et al., 3D Interconnected Porous Carbon Aerogels as Sulfur Immobilizers for Sulfur Impregnation for Lithium-Sulfur Batteries with High Rate Capability and Cycling Stability. *Advanced Functional Materials*, 2014. **24**(17): p. 2500-2509.
126. Wang, X., et al., High-Rate and Long-Term Cycle Stability of Li–S Batteries Enabled by Li₂S/TiO₂-Impregnated Hollow Carbon Nanofiber Cathodes. *ACS Applied Materials & Interfaces*, 2018. **10**(19): p. 16552-16560.
127. Liang, X., A. Garsuch, and L.F. Nazar, Sulfur Cathodes Based on Conductive MXene Nanosheets for High-Performance Lithium–Sulfur Batteries. *Angewandte Chemie*, 2015. **127**(13): p. 3979-3983.
128. Zhang, B., et al., Enhancement of long stability of sulfur cathode by encapsulating sulfur into micropores of carbon spheres. *Energy & Environmental Science*, 2010. **3**(10): p. 1531-1537.
129. Qu, Y., et al., A simple SDS-assisted self-assembly method for the synthesis of hollow carbon nanospheres to encapsulate sulfur for advanced lithium–sulfur batteries. *Journal of Materials Chemistry A*, 2013. **1**(45): p. 14306-14310.
130. Zhao, Y., et al., Encapsulating MWNTs into Hollow Porous Carbon Nanotubes: A Tube-in-Tube Carbon Nanostructure for High-Performance Lithium-Sulfur Batteries. *Advanced Materials*, 2014. **26**(30): p. 5113-5118.
131. Wang, H., et al., Graphene-Wrapped Sulfur Particles as a Rechargeable Lithium–Sulfur Battery Cathode Material with High Capacity and Cycling Stability. *Nano Letters*, 2011. **11**(7): p. 2644-2647.
132. Luo, C., et al., Dual-functional hard template directed one-step formation of a hierarchical porous carbon–carbon nanotube hybrid for lithium–sulfur batteries. *Chemical Communications*, 2016. **52**(82): p. 12143-12146.
133. Wang, Y., et al., *Sulfur Hosts against the Shuttle Effect*. *Small Methods*, 2018. **2**(6): p. 1700345.
134. Wang, D.-W., et al., *Carbon–sulfur composites for Li–S batteries: status and prospects*. *Journal of Materials Chemistry A*, 2013. **1**(33): p. 9382-9394.
135. Shi, H., et al., Functional Carbons Remedy the Shuttling of Polysulfides in Lithium–Sulfur Batteries: Confining, Trapping, Blocking, and Breaking up. *Advanced Functional Materials*, 2018. **28**(38): p. 1800508.

136. Ould Ely, T., et al., *Lithium–Sulfur Batteries: State of the Art and Future Directions*. ACS Applied Energy Materials, 2018. **1**(5): p. 1783-1814.
137. Hencz, L., et al., Highly porous nitrogen-doped seaweed carbon for high-performance lithium–sulfur batteries. *Journal of Materials Science*, 2017. **52**(20): p. 12336-12347.
138. Li, Z., et al., A Highly Ordered Meso@Microporous Carbon-Supported Sulfur@Smaller Sulfur Core–Shell Structured Cathode for Li–S Batteries. *ACS Nano*, 2014. **8**(9): p. 9295-9303.
139. Ma, G., et al., Enhanced performance of lithium sulfur battery with polypyrrole warped mesoporous carbon/sulfur composite. *Journal of Power Sources*, 2014. **254**: p. 353-359.
140. Li, Z., J. Zhang, and X.W. Lou, Hollow Carbon Nanofibers Filled with MnO₂ Nanosheets as Efficient Sulfur Hosts for Lithium–Sulfur Batteries. *Angewandte Chemie International Edition*, 2015. **54**(44): p. 12886-12890.
141. Rao, M., et al., Carbon nanofiber–sulfur composite cathode materials with different binders for secondary Li/S cells. *Electrochimica Acta*, 2012. **65**: p. 228-233.
142. Schneider, H., et al., Influence of different electrode compositions and binder materials on the performance of lithium–sulfur batteries. *Journal of Power Sources*, 2012. **205**: p. 420-425.
143. Li, M., et al., Gas Pickering Emulsion Templated Hollow Carbon for High Rate Performance Lithium Sulfur Batteries. *Advanced Functional Materials*, 2016. **26**(46): p. 8408-8417.
144. Chen, S., et al., 3D Hyperbranched Hollow Carbon Nanorod Architectures for High-Performance Lithium-Sulfur Batteries. *Advanced Energy Materials*, 2014. **4**(8): p. 1301761.
145. Xu, Y., et al., Confined sulfur in microporous carbon renders superior cycling stability in Li/S batteries. *Advanced Functional Materials*, 2015. **25**(27): p. 4312-4320.
146. Li, Z. and L. Yin, Nitrogen-doped MOF-derived micropores carbon as immobilizer for small sulfur molecules as a cathode for lithium sulfur batteries with excellent electrochemical performance. *ACS applied materials & interfaces*, 2015. **7**(7): p. 4029-4038.
147. Sun, Q., et al., Engineering of Hollow Core–Shell Interlinked Carbon Spheres for Highly Stable Lithium–Sulfur Batteries. *ACS Nano*, 2015. **9**(8): p. 8504-8513.

148. Zhang, S.S. and D.T. Tran, Pyrite FeS₂ as an efficient adsorbent of lithium polysulphide for improved lithium–sulphur batteries. *Journal of Materials Chemistry A*, 2016. **4**(12): p. 4371-4374.
149. Lacey, M.J., et al., A Robust, Water-Based, Functional Binder Framework for High-Energy Lithium–Sulfur Batteries. *ChemSusChem*, 2017. **10**(13): p. 2758-2766.
150. Wang, Q., et al., Layer-by-layer assembled C/S cathode with trace binder for Li–S battery application. *ACS applied materials & interfaces*, 2015. **7**(45): p. 25002-25006.
151. Ye, C., et al., A 3D Hybrid of Chemically Coupled Nickel Sulfide and Hollow Carbon Spheres for High Performance Lithium–Sulfur Batteries. *Advanced Functional Materials*, 2017. **27**(33): p. 1702524.
152. Su, H., et al., Polycation Binders: An Effective Approach toward Lithium Polysulfide Sequestration in Li–S Batteries. *ACS Energy Letters*, 2017. **2**(11): p. 2591-2597.
153. Wahyudi, W., et al., Phase Inversion Strategy to Flexible Freestanding Electrode: Critical Coupling of Binders and Electrolytes for High Performance Li–S Battery. *Advanced Functional Materials*, 2018: p. 1802244.
154. Li, L., et al., Molecular understanding of polyelectrolyte binders that actively regulate ion transport in sulfur cathodes. *Nature communications*, 2017. **8**(1): p. 2277.
155. Li, Q., et al., Guar gum as a novel binder for sulfur composite cathodes in rechargeable lithium batteries. *Chemical Communications*, 2016. **52**(92): p. 13479-13482.
156. Wang, J., et al., Carbonyl- β -Cyclodextrin as a Novel Binder for Sulfur Composite Cathodes in Rechargeable Lithium Batteries. *Advanced Functional Materials*, 2013. **23**(9): p. 1194-1201.
157. Zeng, F., et al., Multidimensional polycation β -cyclodextrin polymer as an effective aqueous binder for high sulfur loading cathode in lithium–sulfur batteries. *ACS applied materials & interfaces*, 2015. **7**(47): p. 26257-26265.
158. Liu, X., et al., Greatly Improved Conductivity of Double-Chain Polymer Network Binder for High Sulfur Loading Lithium–Sulfur Batteries with a Low Electrolyte/Sulfur Ratio. *Small*, 2018. **14**(33): p. 1801536.
159. Kim, H.M., et al., Electrochemical properties of sulfurized-polyacrylonitrile cathode for lithium–sulfur batteries: effect of polyacrylic acid binder and fluoroethylene carbonate additive. *The Journal of Physical Chemistry Letters*, 2017. **8**(21): p. 5331-5337.
160. Zhu, P., et al., In Situ Polymerization of Nanostructured Conductive Polymer on 3D Sulfur/Carbon Nanofiber Composite Network as Cathode for High-Performance Lithium–Sulfur Batteries. *Advanced Materials Interfaces*, 2018. **5**(10): p. 1701598.

161. Wang, Q., et al., *Improve rate capability of the sulfur cathode using a gelatin binder*. Journal of The Electrochemical Society, 2011. **158**(6): p. A775-A779.
162. Bao, W., et al., *Enhanced cyclability of sulfur cathodes in lithium-sulfur batteries with Na-alginate as a binder*. Journal of Energy Chemistry, 2013. **22**(5): p. 790-794.
163. He, M., et al., *Enhanced cyclability for sulfur cathode achieved by a water-soluble binder*. The Journal of Physical Chemistry C, 2011. **115**(31): p. 15703-15709.
164. Chen, Y., et al., *Chitosan as a functional additive for high-performance lithium-sulfur batteries*. Journal of Materials Chemistry A, 2015. **3**(29): p. 15235-15240.
165. Li, G., et al., *Acacia Senegal-inspired bifunctional binder for longevity of lithium-sulfur batteries*. Advanced Energy Materials, 2015. **5**(21).
166. Lu, Y.-Q., et al., *Achieving high capacity retention in lithium-sulfur batteries with an aqueous binder*. Electrochemistry Communications, 2016. **72**: p. 79-82.
167. Ling, M., et al., *Nucleophilic substitution between polysulfides and binders unexpectedly stabilizing lithium sulfur battery*. Nano Energy, 2017. **38**: p. 82-90.
168. Duan, X., et al., *Improved capacity retention of low cost sulfur cathodes enabled by a novel starch binder derived from food*. Rsc Advances, 2014. **4**(105): p. 60995-61000.
169. Seh, Z.W., et al., *Stable cycling of lithium sulfide cathodes through strong affinity with a bifunctional binder*. Chemical Science, 2013. **4**(9): p. 3673-3677.
170. Lacey, M.J., et al., *Why PEO as a binder or polymer coating increases capacity in the Li-S system*. Chemical Communications, 2013. **49**(76): p. 8531-8533.
171. Zhang, S.S., *Binder based on polyelectrolyte for high capacity density lithium/sulfur battery*. Journal of The Electrochemical Society, 2012. **159**(8): p. A1226-A1229.
172. Zhang, Z., et al., *Water-soluble polyacrylic acid as a binder for sulfur cathode in lithium-sulfur battery*. ECS Electrochemistry Letters, 2012. **1**(2): p. A34-A37.
173. Pan, J., et al., *Enhanced electrochemical performance of sulfur cathodes with a water-soluble binder*. RSC Advances, 2015. **5**(18): p. 13709-13714.
174. Bhattacharya, P., et al., *Polyamidoamine dendrimer-based binders for high-loading lithium-sulfur battery cathodes*. Nano Energy, 2016. **19**: p. 176-186.
175. Zhang, L., et al., *Effective electrostatic confinement of polysulfides in lithium/sulfur batteries by a functional binder*. Nano Energy, 2017. **40**: p. 559-565.
176. Ling, M., et al., *Electrostatic Polysulfides Confinement to Inhibit Redox Shuttle Process in the Lithium Sulfur Batteries*. ACS applied materials & interfaces, 2017. **9**(37): p. 31741-31745.

177. Vizintin, A., et al., Linear and Crosslinked Ionic Liquid Polymers as Binders in Lithium-Sulfur Battery. *Chemistry of Materials*, 2018.
178. ThiokoLiu, B., et al., Thiokol with Excellent Restriction on the Shuttle Effect in Lithium-Sulfur Batteries. *Applied Sciences*, 2018. **8**(1): p. 79.
179. Lacey, M.J., et al., Functional, water-soluble binders for improved capacity and stability of lithium-sulfur batteries. *Journal of Power Sources*, 2014. **264**: p. 8-14.
180. Jung, Y. and S. Kim, *New approaches to improve cycle life characteristics of lithium-sulfur cells*. *Electrochemistry Communications*, 2007. **9**(2): p. 249-254.
181. Akhtar, N., et al., Gelatin-polyethylenimine composite as a functional binder for highly stable lithium-sulfur batteries. *Electrochimica Acta*, 2018.
182. Liu, J., et al., A robust network binder with dual functions of Cu ²⁺ ions as ionic crosslinking and chemical binding agents for highly stable Li-S batteries. *Journal of Materials Chemistry A*, 2018. **6**(17): p. 7382-7388.
183. Liu, J., et al., Exploiting a robust biopolymer network binder for an ultrahigh-area-capacity Li-S battery. *Energy & Environmental Science*, 2017. **10**(3): p. 750-755.
184. Chen, W., et al., A new type of multifunctional polar binder: toward practical application of high energy lithium sulfur batteries. *Advanced Materials*, 2017. **29**(12): p. 1605160.
185. Chen, W., et al., A New Hydrophilic Binder Enabling Strongly Anchoring Polysulfides for High-Performance Sulfur Electrodes in Lithium-Sulfur Battery. *Advanced Energy Materials*, 2018. **8**(12): p. 1702889.
186. Yan, L., et al., A novel epoxy resin-based cathode binder for low cost, long cycling life, and high-energy lithium-sulfur batteries. *Journal of Materials Chemistry A*, 2018.
187. Kovalenko, I., et al., A major constituent of brown algae for use in high-capacity Li-ion batteries. *Science*, 2011: p. 1209150.
188. Sun, J., et al., Application of gelatin as a binder for the sulfur cathode in lithium-sulfur batteries. *Electrochimica acta*, 2008. **53**(24): p. 7084-7088.
189. Huang, Y., et al., *Discharge process of the sulfur cathode with a gelatin binder*. *Journal of The Electrochemical Society*, 2008. **155**(10): p. A764-A767.
190. Wang, Y., et al., Structural change of the porous sulfur cathode using gelatin as a binder during discharge and charge. *Electrochimica Acta*, 2009. **54**(16): p. 4062-4066.
191. Zhang, W., et al., *Influence of pH of gelatin solution on cycle performance of the sulfur cathode*. *Journal of the Electrochemical Society*, 2010. **157**(4): p. A443-A446.

192. Jiang, S., et al., *Enhanced performance of the sulfur cathode with L-cysteine-modified gelatin binder*. Journal of Adhesion Science and Technology, 2013. **27**(9): p. 1006-1011.
193. Kamel, S., et al., *Pharmaceutical significance of cellulose: a review*. Express Polym Lett, 2008. **2**(11): p. 758-778.
194. Kumar, M.N.R., *A review of chitin and chitosan applications*. Reactive and functional polymers, 2000. **46**(1): p. 1-27.
195. Islam, A., et al., *A review of recent developments on the regulatory, structural and functional aspects of gum arabic*. Food Hydrocolloids, 1997. **11**(4): p. 493-505.
196. Renard, D., et al., *Acacia senegal gum: continuum of molecular species differing by their protein to sugar ratio, molecular weight, and charges*. Biomacromolecules, 2006. **7**(9): p. 2637-2649.
197. Mudgil, D., S. Barak, and B.S. Khatkar, *Guar gum: processing, properties and food applications—a review*. Journal of food science and technology, 2014. **51**(3): p. 409-418.
198. Cheng, W.-J., C.-S. Cho, and C.-C. Li, *Communication—Gelatinization of Guar Gum and Its Effects on the Dispersion and Electrochemistry of Lithium-Sulfur Batteries*. Journal of The Electrochemical Society, 2018. **165**(10): p. A2058-A2060.
199. Fu, X., et al., *Small Molecules Make a Big Difference: A Solvent-Controlled Strategy for Building Robust Conductive Network Structures in High-Capacity Electrode*. ACS Nano, 2018. **12**(10): p. 10006-10016.
200. Chen, S., et al., *Enhanced performance of lithium-sulfur cathodes with poly (ethylene oxide) binder for performance of rechargeable lithium sulfur batteries*. Journal of the Electrochemical Society, 2002. **149**(11): p. A1437-A1441.
201. Shim, J., K.A. Striebel, and E.J. Cairns, *The lithium/sulfur rechargeable cell effects of electrode composition and solvent on cell performance*. Journal of the Electrochemical Society, 2002. **149**(10): p. A1321-A1325.
202. Hong, X., et al., *On the dispersion of lithium-sulfur battery cathode materials effected by electrostatic and stereo-chemical factors of binders*. Journal of Power Sources, 2016. **324**: p. 455-461.
203. Bhattacharya, P., et al., *Exploiting the physicochemical properties of dendritic polymers for environmental and biological applications*. Physical Chemistry Chemical Physics, 2013. **15**(13): p. 4477-4490.
204. Ma, L., et al., *Enhanced Li-S batteries using amine-functionalized carbon nanotubes in the cathode*. ACS nano, 2015. **10**(1): p. 1050-1059.

205. Wang, H., et al., Cationic polymer binder inhibit shuttle effects through electrostatic confinement in lithium sulfur batteries. *Journal of Materials Chemistry A*, 2018. **6**(16): p. 6959-6966.
206. Liao, J. and Z. Ye, Quaternary ammonium cationic polymer as a superior bifunctional binder for lithium–sulfur batteries and effects of counter anion. *Electrochimica Acta*, 2018. **259**: p. 626-636.
207. Hua, W., et al., Polysulfide-Scission reagents for the suppression of the shuttle effect in lithium–sulfur batteries. *ACS nano*, 2017. **11**(2): p. 2209-2218.
208. Kim, N.-I., et al., Correlation between positive-electrode morphology and sulfur utilization in lithium–sulfur battery. *Journal of power sources*, 2004. **132**(1-2): p. 209-212.
209. García-Ochoa, F., et al., *Xanthan gum: production, recovery, and properties*. *Biotechnology advances*, 2000. **18**(7): p. 549-579.
210. Pan, J., et al., PAA/PEDOT: PSS as a multifunctional, water-soluble binder to improve the capacity and stability of lithium–sulfur batteries. *RSC Advances*, 2016. **6**(47): p. 40650-40655.
211. Yan, L., et al., Ionically cross-linked PEDOT: PSS as a multi-functional conductive binder for high-performance lithium–sulfur batteries. *Sustainable Energy & Fuels*, 2018.
212. Gao, H., et al., Significantly Raising the Cell Performance of Lithium Sulfur Battery via the Multifunctional Polyaniline Binder. *Electrochimica Acta*, 2017. **232**: p. 414-421.
213. Milroy, C. and A. Manthiram, An elastic, conductive, electroactive nanocomposite binder for flexible sulfur cathodes in lithium–sulfur batteries. *Advanced Materials*, 2016. **28**(44): p. 9744-9751.
214. Ai, G., et al., Investigation of surface effects through the application of the functional binders in lithium sulfur batteries. *Nano Energy*, 2015. **16**: p. 28-37.
215. Li, G., et al., A multi functional binder with lithium ion conductive polymer and polysulfide absorbents to improve cycleability of lithium–sulfur batteries. *Journal of Power Sources*, 2015. **294**: p. 187-192.
216. Cheng, M., et al., A functional binder–sulfonated poly (ether ether ketone) for sulfur cathode of Li–S batteries. *RSC Advances*, 2016. **6**(81): p. 77937-77943.
217. Zhang, H., et al., 3D-crosslinked tannic acid/poly (ethylene oxide) complex as a three-in-one multifunctional binder for high-sulfur-loading and high-stability cathodes in lithium-sulfur batteries. *Energy Storage Materials*, 2018.

218. Frischmann, P.D., et al., Redox-active supramolecular polymer binders for lithium–sulfur batteries that adapt their transport properties in operando. *Chemistry of Materials*, 2016. **28**(20): p. 7414-7421.
219. Hernández, G., et al., Polyimide-polyether binders—diminishing the carbon content in lithium sulfur batteries. *Materials Today Energy*, 2017. **6**: p. 264-270.
220. Sun, K., et al., *Review on application of PEDOTs and PEDOT: PSS in energy conversion and storage devices*. *Journal of Materials Science: Materials in Electronics*, 2015. **26**(7): p. 4438-4462.
221. Wang, Z., et al., Improving the performance of lithium–sulfur batteries using conductive polymer and micrometric sulfur powder. *Journal of Materials Research*, 2014. **29**(9): p. 1027-1033.
222. Mauritz, K.A. and R.B. Moore, *State of understanding of Nafion*. *Chemical reviews*, 2004. **104**(10): p. 4535-4586.
223. Yang, Z., R. Li, and Z. Deng, Polyelectrolyte Binder for Sulfur Cathode To Improve the Cycle Performance and Discharge Property of Lithium–Sulfur Battery. *ACS applied materials & interfaces*, 2018. **10**(16): p. 13519-13527.
224. Trofimov, B., et al., Vinyl ethers with polysulfide and hydroxyl functions and polymers therefrom as binders for lithium–sulfur batteries. *Journal of applied polymer science*, 2006. **101**(6): p. 4051-4055.
225. Frischmann, P.D., et al., Supramolecular perylene bisimide-polysulfide gel networks as nanostructured redox mediators in dissolved polysulfide lithium–sulfur batteries. *Chemistry of Materials*, 2015. **27**(19): p. 6765-6770.
226. Hwa, Y., et al., Aqueous-Processable Redox-Active Supramolecular Polymer Binders for Advanced Lithium/Sulfur Cells. *Chemistry of Materials*, 2018.

Chapter 3:
Poly(thiourea triethylene glycol) as a
Multifunctional Binder for Enhanced
Performance in Lithium-Sulfur Batteries

3.1 Statement of Contribution

The bibliographic details of the manuscript included in this chapter are as follows:

Hencz, L., Chen, H., Wu, Z., Gu, X., Li, M., Tian, Y., Chen, S., Yan, C., Bati, A., Shapter, J., Kiefel, M., Li, D.S., Zhang, S. (2021). Poly (thiourea triethylene glycol) as a Multifunctional Binder for Enhanced Performance in Lithium-Sulfur Batteries. Green Energy & Environment, In Press. DOI: 10.1016/j.gee.2021.01.014

My contribution to the involved manuscript:

Polymer synthesis; experimentation; data collection and analysis; preparation of manuscript; response to reviewers comments.

(Signed) _____ (Date) 27/08/2021

Name of Student: Luke Hencz

(Countersigned) _____ (Date) 27/08/2021

The corresponding author of the paper: Prof. Shanqing Zhang

(Countersigned) _____ (Date) 27/08/2021

Supervisor: Prof. Shanqing Zhang

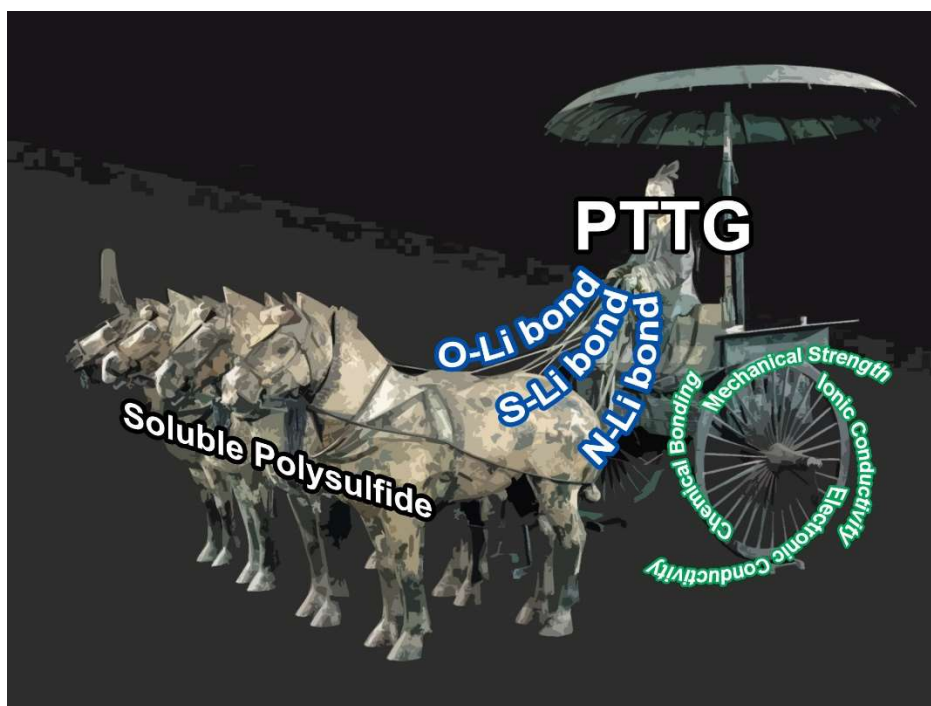
3.2 Abstract

A mechanically strong binder with polar functional groups could overcome the dilemma of the significant volume change during charge/discharge processes and poor cyclability of lithium-sulfur batteries (LSBs). In this work, for the first time, we report the use of poly(thiourea triethylene glycol) (PTTG) as a multifunctional binder for sulfur cathodes to enhance the performance of LSBs. As expected, the PTTG binder facilitates the high performance and stability delivered by the Sulfur-PTTG cathode, including a higher reversible capacity of 825 mAh·g⁻¹ at 0.2 C after 80 cycles, a lower capacity fading (0.123 % per cycle) over 350 cycles at 0.5 C, a higher areal capacity of 2.5 mAh·cm⁻² at 0.25 mA·cm⁻², and better rate capability of 587 mAh·g⁻¹ at 2 C. Such superior electrochemical performances could be attributed to PTTG's strong chemical adsorption towards polysulfides, which may avoid the lithium polysulfide shuttle effect and excellent mechanical characteristics that prevent electrode collapse during cycling and allow the Sulfur-PTTG electrode to maintain robust electron and ion migration pathways for accelerated redox reaction kinetics.

Highlights

- A multifunctional PTTG binder is used to fabricate lithium-sulfur batteries for the first time.
- PTTG binder illustrates higher mechanical strength compared to the PVDF binder.
- PTTG binder demonstrates an excellent ability to inhibit polysulfides from shuttling via strong chemical adsorption.
- The Sulfur-PTTG electrode displays improved electron and ion transportation.
- The Sulfur-PTTG cathode delivers improved electrochemical performance and outstanding stability.

Graphical Abstract



Graphical Abstract 3-1: Poly(thiourea triethylene glycol) PTTG polymer used as a lithium-sulfur battery (LSB) binder shows strong chemical interaction with soluble polysulfides. Sulfur-PTTG cathodes possess high electronic and ionic conductivity as well as robust mechanical properties to provide excellent LSB performance.

Keywords

Lithium-sulfur battery; Polymer binder; Chemical adsorption; DFT; Poly(thiourea triethylene glycol)

3.3 Introduction

Li-ion batteries (LIBs) dominate the portable electronics market, but the limits of this mature technology are beginning to become apparent, especially where higher energy densities are required, namely for electric vehicle (EV) applications [1]. As such, novel battery chemistries that can deliver increased energy densities are being explored [2]. One prominent example is the lithium-sulfur battery (LSB), based on a metallic lithium anode and a sulfur composite cathode [3]. The primary appeal of the LSB is its high theoretical capacity and energy density (ca. $1670 \text{ mAh}\cdot\text{g}^{-1}$ and $2500 \text{ Wh}\cdot\text{kg}^{-1}$, respectively) delivered by electrochemical reduction of elemental sulfur to Li_2S , which dwarfs the energy density delivered by current generation LIBs [4, 5]. Additional appeals of the LSB are the natural abundance, low cost, and environmental benignity of sulfur [6].

Despite their appeal, LSBs are plagued with inherent problems that researchers are working to address. Perhaps the most severe problem with the LSB is dubbed the lithium polysulfide (LiPS) shuttle phenomenon, which arises from the soluble nature of the discharge intermediates and causes loss of active material, low Coulombic efficiency (CE), capacity fading, and self-discharge [7]. Additionally, sulfur, along with its discharge product Li_2S , suffers from low electronic conductivity [8] and undergoes a significant volume expansion upon conversion [9]. Last but not least, the use of a lithium metal anode causes further technical challenges by way of dendrite formation during the repeated charge/discharge process, leading to an additional reduction in CE along with safety concerns arising from short circuits [10]. Research into alleviating the concerns mentioned above is multi-faceted, with the focus typically being directed towards particular battery components, including the cathode [5, 11, 12], interlayer/separator [13], anode [14], liquid electrolytes [15], and even all-solid-state LSBs [16, 17].

Moreover, research into polymeric binders, a critical cathode component, has also received increased attention [18-25]. The requirement for advanced binders in LSBs stems from the fact that the most commonly used binder, polyvinylidene difluoride (PVDF), cannot withstand the volume change of the active materials or prevent the loss of soluble LiPSs during cycling [20]. Therefore, battery researchers have devoted much effort to developing binders with strong mechanical adhesion to the electrode components and chemical adsorption to LiPSs to develop practical LSBs [19]. Additionally, electronically conductive binders, ionically conductive

binders, and redox-active binders could also help deliver improved electrochemical performance and stability of LSBs [23, 24].

Inspired by these strategies, we synthesized a novel polymer binder, poly(thiourea triethylene glycol) (PTTG) to fabricate Sulfur-PTTG cathodes. The electrochemical performance of the resultant LSBs has been significantly enhanced due to PTTG's multifunctional properties, i.e., abundant polar functional groups to chemically hinder LiPS shuttling, and excellent mechanical properties to withstand mechanical damage during the charge/discharge process while maintaining robust electron and ion migration pathways to accelerate redox reaction kinetics.

3.4 Experimental Section

3.4.1 Materials Synthesis

Unless stated otherwise, all chemicals were purchased from Sigma Aldrich, stored in an Argon filled glovebox (MBraun, Germany), and used directly with no further purification. The synthesis of poly(thiourea triethylene glycol) (PTTG) was carried out following the method reported by Yanagisawa et al. [26]. Briefly, 1,1'-thiocarbonyldiimidazole (5.7 g) was added to a solution of 4.9 g of 1,2-bis(2-aminoethoxy)ethane and 16 mL DMF and was stirred for 24 h at 24 °C. After stirring, ca. 30 mL of chloroform was added to the reaction vessel before the solution was poured into cold diethyl ether (ca. 500 mL). The supernatant solution was removed, and the precipitate was collected before it was redissolved in chloroform and added to methanol. The precipitate was collected by centrifugation, redissolved in chloroform, added to methanol, and centrifuged again. The product was dried at 80 °C for 48 h in a vacuum oven to yield the PTTG polymer.

3.4.2 Materials Characterisation

^1H and ^{13}C NMR spectra were obtained using a Bruker 400 MHz spectrometer at 400 and 100 MHz, respectively. Signals are reported in terms of their chemical shift (δ in ppm) relative to the deuterated solvent used to obtain that spectrum. The ^1H and ^{13}C chemical shifts were referenced to the residual $\text{d}_6\text{-DMSO}$ (Cambridge isotope Laboratory, Inc.) solvent peaks, δ_{H} 2.50 and δ_{C} 39.52 respectively, and processed using the MnovaTM software suite. 500 mg of PVDF and PTTG samples were exposed to a ca. 1 M solution of Li_2S_6 in 1,2-dimethoxyethane (DME) and allowed to rest for 24 h to observe the LiPS adsorption ability of the PTTG polymer. Fourier transform infrared (FTIR) spectra of the pristine PTTG polymer and the PTTG polymer after LiPS exposure were obtained on a Bruker Alpha (Bruker, USA) in transmission mode.

The supernatant solutions from the LiPS adsorption experiment were diluted 20:1 and UV-Vis spectra were obtained on a Cary Series UV-Vis-NIR Spectrophotometer (Agilent Technologies, USA). For X-ray photoelectron spectroscopic (XPS) analysis, 40 mg of the PTTG polymer was exposed to 40 mL of 0.1 M solution of Li_2S_4 in DME for 2 h. Afterwards, the supernatant solution was removed, and the remaining solid was transferred to a silicon wafer. XPS data was acquired using a Kratos Axis ULTRA X-ray Photoelectron Spectrometer incorporating a 165 mm hemispherical electron energy analyser. The incident radiation was Monochromatic Al $K\alpha$ X-rays (1486.6 eV) at 225 W (15 kV, 15 mA). Survey (wide) scans were taken at an analyser pass energy of 160 eV and multiplex (narrow) high-resolution scans at 40 eV. Survey scans were carried out over 1200 - 0 eV binding energy range with 1.0 eV steps and a dwell time of 100 ms. Narrow high-resolution scans were run with 0.05 eV steps and 250 ms dwell time. The base pressure in the analysis chamber was 1.0×10^{-9} torr and 1.0×10^{-8} torr during sample analysis. Peak fitting of the high-resolution data was carried out using the CasaXPS software. Scanning electron microscope (SEM) images were obtained on a JSM-7001F SEM (JEOL, Japan) and were used to investigate the morphologies of the electrodes before and after cycling. 90 ° peel-off tests of electrode films were carried out on a MTS Tytron microforce tester (MTS, USA) to study the binders' adhesive properties., Sulfur-PTTG and Sulfur-PVDF cathodes were fabricated as per the method described below to carry out the peel-off testing; however rectangular sections of the film (ca. 5 cm x 2 cm) were cut and applied to an "L" shape aluminium alloy workpiece. Scotch tape was applied to the surface of the electrode film and was peeled perpendicularly to the film's surface at a speed of $0.1 \text{ mm}\cdot\text{s}^{-1}$ [27]. The experiment was repeated 7 times for each sample, with each replicate averaged to give the result.

3.4.3 Electrochemical Characterisation

Sulfur-PTTG electrodes were fabricated for electrochemical testing by mixing an electrode slurry consisting of elemental sulfur as the active material, carbon black as a conductive additive, and PTTG polymer as a binder in a weight ratio of 60:30:10 with 1-methyl-2-pyrrolidinone (NMP) as a solvent and was magnetically stirred until a homogeneous slurry was obtained. The solid to solvent ratio of the slurry was 1 mg:5 μL . After stirring, the slurry was cast onto C-coated Al foil using an adjustable blade with the gap set to 250 μm and then dried in a vacuum oven at 80 °C for 24 h. After drying, electrodes with a 13 mm ϕ (1.33 cm^2) were cut using a hole punch and stored in a glove box. The sulfur loading of the electrodes was approx. $1 \text{ mg}\cdot\text{cm}^{-2}$. As a reference, the above process was repeated, replacing the binder with

poly(vinylidene fluoride) (PVDF) (Mw 180,000) to form the Sulfur-PVDF electrodes. Half-cells were fabricated using either a Sulfur-PTTG or Sulfur-PVDF cathode, a lithium foil counter electrode, polypropylene (Celgard 2300) separator, and 1 M lithium bis(trifluoromethane)sulfonimide (LiTFSI) in 1,3-dioxolane/1,2-dimethoxyethane (1:1, v/v) with 0.2 M LiNO₃ as the electrolyte. Sulfur electrodes with an active material loading of approx. 4 mg·cm⁻² were also fabricated for areal capacity testing. The electrolyte/sulfur (E/S) ratio was constant at 20 μL of electrolyte per 1 mg of sulfur for all half-cells.

The half-cells underwent charge-discharge and rate performance testing on a Neware Battery Testing System (Neware, China) with a voltage window between 1.7 - 2.7 V in an oven set to 30 °C. All half-cells for the charge-discharge and rate performance tests were subjected to one activation cycle at 0.05 C (1 C = 1672 mAh·g⁻¹) before cycling at the specified rate, except for the cells subject to areal capacity testing, which were cycled directly at 0.25 mA·cm⁻². Electrochemical impedance spectroscopy (EIS) was carried out on a Biologic SP-200 (Biologic, France) with the AC set to 5 mV and a frequency range of 10 mHz to 100 kHz. Cyclic voltammetry (CV) was carried out on a CHI660D electrochemical station (CHI Instruments, USA) at 24 °C with a scan rate of 0.05 mV·s⁻¹ and a voltage window of 1.7 - 2.7 V.

3.4.4 Computational Details

The atomic configurations and adsorption energies between the polymer (PTTG/PVDF) and the lithium sulfide species (Li₂S/Li₂S₄) were calculated by using the plane-wave based density functional theory (DFT) method, as implemented in the Vienna ab initio Simulation Package (VASP) [28]. The Perdew-Burke-Ernzerh exchange-correlation functional was employed using generalized gradient approximation (GGA) parameterized by Perdew-Burke-Ernzerhof (PBE) [29]. The interaction potentials of the core electrons were replaced by Projector-augmented-wave (PAW) pseudopotentials [30]. All calculations employed a cutoff energy of 500 eV for the plane-wave basis set, while Brillouin-zone integrations were approximated by using 1×1×1 gamma-only k-points sampling. The energy difference and force required for convergence were set to 10⁻⁴ eV and 0.03 eV·Å⁻¹, respectively.

The vacuum between a polymer and its image is 30 Å, while the distance between the Li₂S/Li₂S₄ and its image is no less than 25 Å along the periodic directions. These systems were large enough to avoid any artificial interaction caused by periodicity. The binding energy, E_b , was defined as the energy difference between the Li₂S/Li₂S₄ adsorbed system

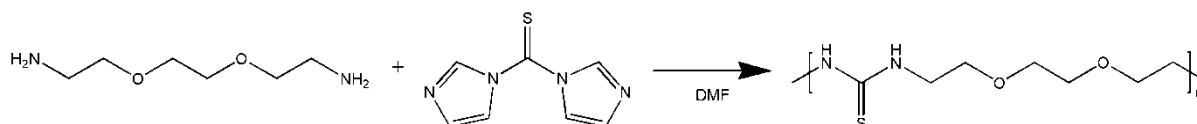
($E_{\text{polymer-xLi}_2\text{S/Li}_2\text{S}_4}$) and the summation of the pristine polymer (E_{polymer}) and isolated $\text{Li}_2\text{S/Li}_2\text{S}_4$ cluster, as shown in **Eqn. 3.1**.

$$E_b = (xE_{\text{Li}_2\text{S/Li}_2\text{S}_4} + E_{\text{polymer}}) - E_{\text{polymer-xLi}_2\text{S/Li}_2\text{S}_4} \quad (3.1)$$

With this definition, a positive binding energy indicated that the binding interaction was favoured. The three-dimensional visualization models were constructed using VESTA software.

3.5 Results and Discussion

The reaction scheme and chemical structure of the PTTG polymer are provided in **Scheme 3.1**. To confirm that the synthesis yielded the desired product, ^1H and ^{13}C NMR spectra were obtained (**Fig. 3.1a and b**, respectively), which match well with the previous report [26], suggesting that the PTTG polymer was successfully synthesised. By comparing the ratio of the integrated area of the primary end group amine hydrogen (2.76 ppm) and the thiourea hydrogen (7.51 ppm) within the polymer chain on the ^1H -NMR spectrum (**Fig. 3.1a**), the molecular weight of the PTTG polymer was approximated and found to be roughly 8800 a.m.u. The NMR characterization highlights the polymers' abundant functional groups, including lone pair rich thiourea and ether groups, which have been shown to reduce LiPS shuttling [31-33].



Scheme 3.1: The synthesis scheme and chemical structure of the PTTG polymer

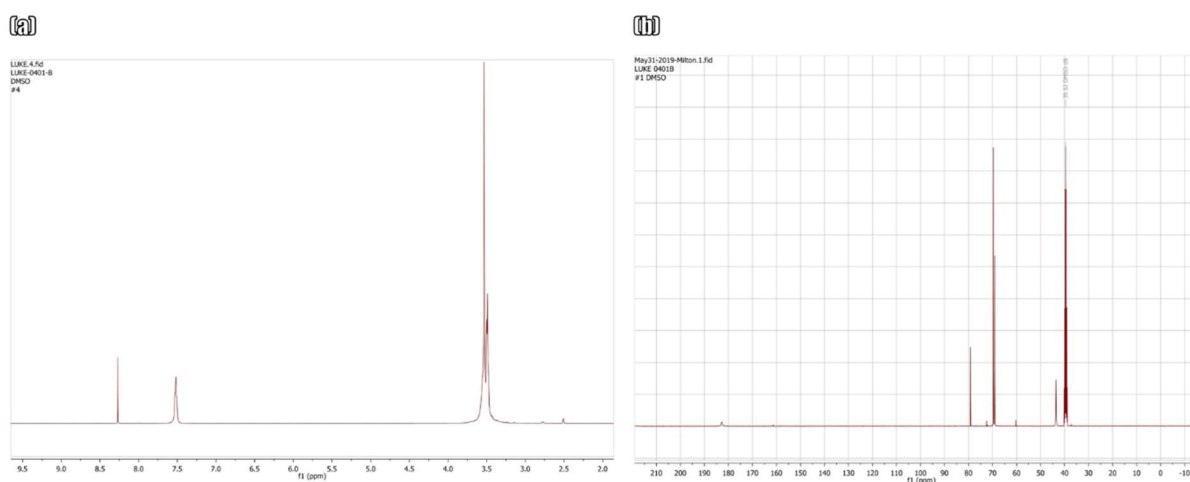


Figure 3.1: (a) ^1H -NMR spectra of the PTTG polymer and (b) ^{13}C -NMR spectra of the PTTG polymer

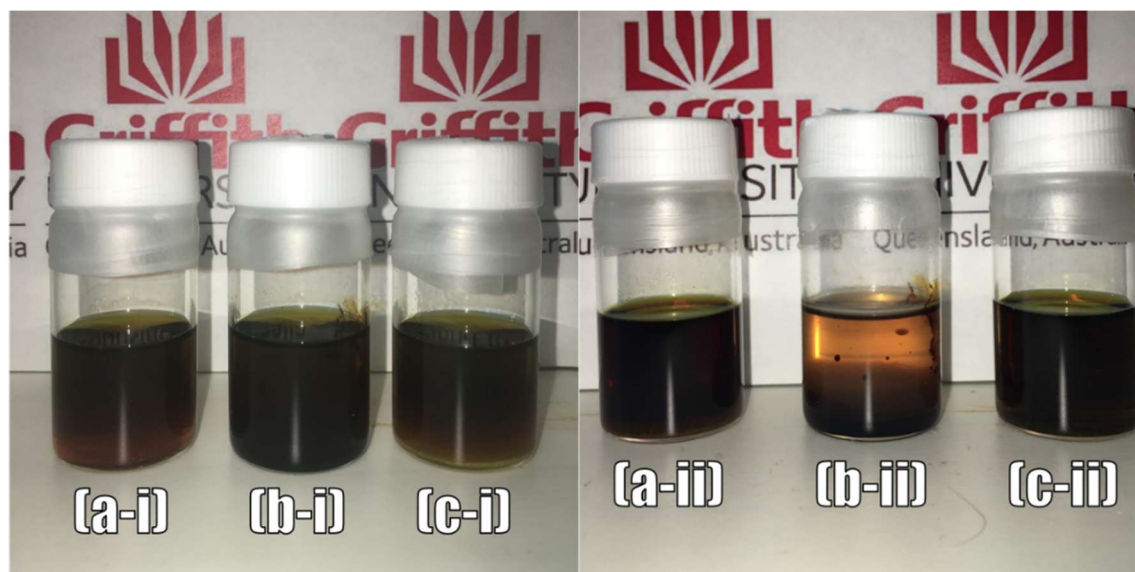
To experimentally verify whether or not the PTTG polymer could indeed interact with soluble LiPS, a simple adsorption test was carried out. A ca. 1 M solution of Li_2S_6 was exposed to 500 mg of PTTG and PVDF in separate vials and allowed to rest for 24 hours, as shown in **Fig. 3.2**. After exposure, it can be observed that the supernatant solution in the PTTG vial experienced a drastic colour change, unlike the solution exposed to PVDF. UV-Vis spectra were obtained from the supernatant solution (**Fig. 3.2d**), which corroborate the reduced concentration of LiPS present in the solution after PTTG exposure [34, 35]. Additionally, a milky white precipitate formed at the interface between the PTTG polymer and the LiPS solution. These preliminary results suggest that the PTTG polymer can chemically interact with soluble polysulfide species.

To further investigate the chemical adsorption of LiPS on PTTG polymer, Fourier transform infra-red (FTIR) investigation was carried out on both the pristine PTTG polymer and the sample of PTTG after LiPS exposure. The FTIR spectra are displayed in **Fig. 3.3**, with the critical peaks highlighted. The peaks at approx. 3290 and 1660 cm^{-1} correspond to the N–H stretching and bending vibration, respectively. The peaks at 3060 and 1545 cm^{-1} can be assigned to the thiourea moiety [26, 36], while the broad doublet peak at around 1090 cm^{-1} is assigned to the ether groups in the PTTG polymer. After exposure to the LiPS solution, the peak relating to N–H stretching increased and broadened, whereas the N–H bending peak sharply declined. The peaks assigned to both the thiourea and ether groups also declined after LiPS exposure. The changes in the peaks associated with electron-rich functional groups are attributed to coordinated bonds formed between the PTTG and the LiPS [37].

Additionally, the peak located at around 3060 cm^{-1} is of further interest in this work. This peak corresponds to the N–H deformation vibration of non-linearly H-bonded thiourea units and does not appear in semi-crystalline H-bonded urea-containing materials [26, 38]. This is particularly relevant in the LSB system because when employed as a binder, the H-bonding ability of the PTTG polymer could provide interfacial forces that could tightly adhere the electrode components [19, 20] without suffering the drawbacks of a crystalline and brittle H-bonded network inherent to standard binders such as carboxymethyl cellulose (CMC) [39].

Next, the XPS characterizations were conducted to confirm the chemical interaction between the PTTG polymer and soluble LiPS. 40 mg of the PTTG polymer was exposed to 40 mL 0.1 M Li_2S_4 solution for 2 h under magnetic stirring before the supernatant solution was removed, and the remaining solid was subjected to XPS analysis. As a reference, XPS spectra were also

obtained from the pure PTTG polymer. The resulting XPS survey spectra are shown in **Fig. 3.4**, with the corresponding high-resolution (HR) spectra shown in **Fig. 3.5**.



(d)

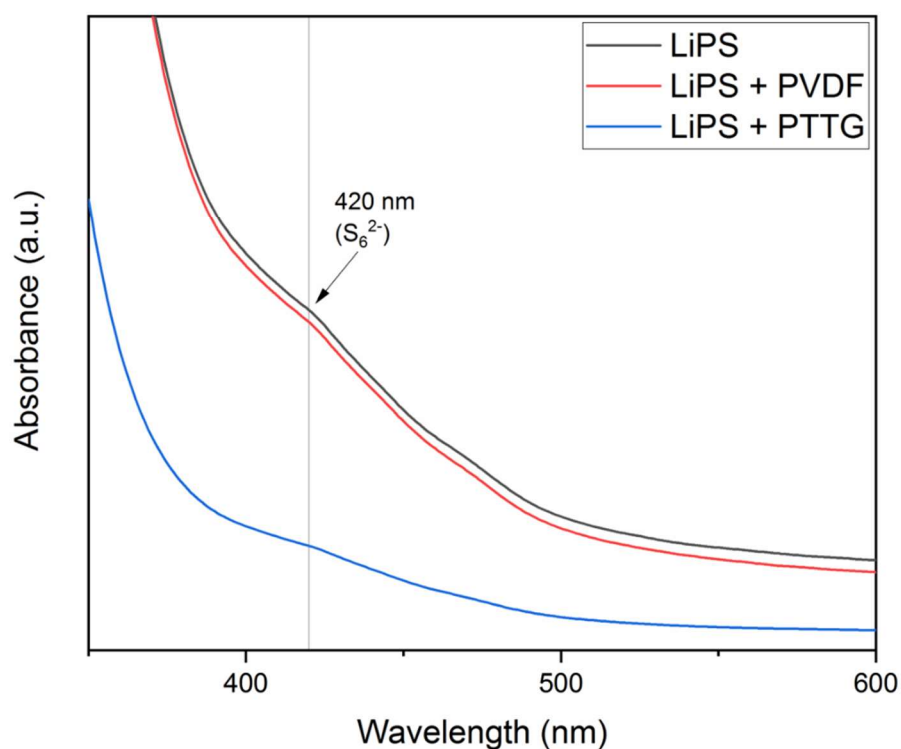


Figure 3.2: (a) Blank LiPS solution, (b) LiPS solution exposed to 500 mg PTTG, (c) LiPS solution exposed to 500 mg PVDF (i) before and (ii) after 24 h . (d) UV-Vis spectra of the supernatant lithium polysulfide (LiPS) solution after adsorption experiment

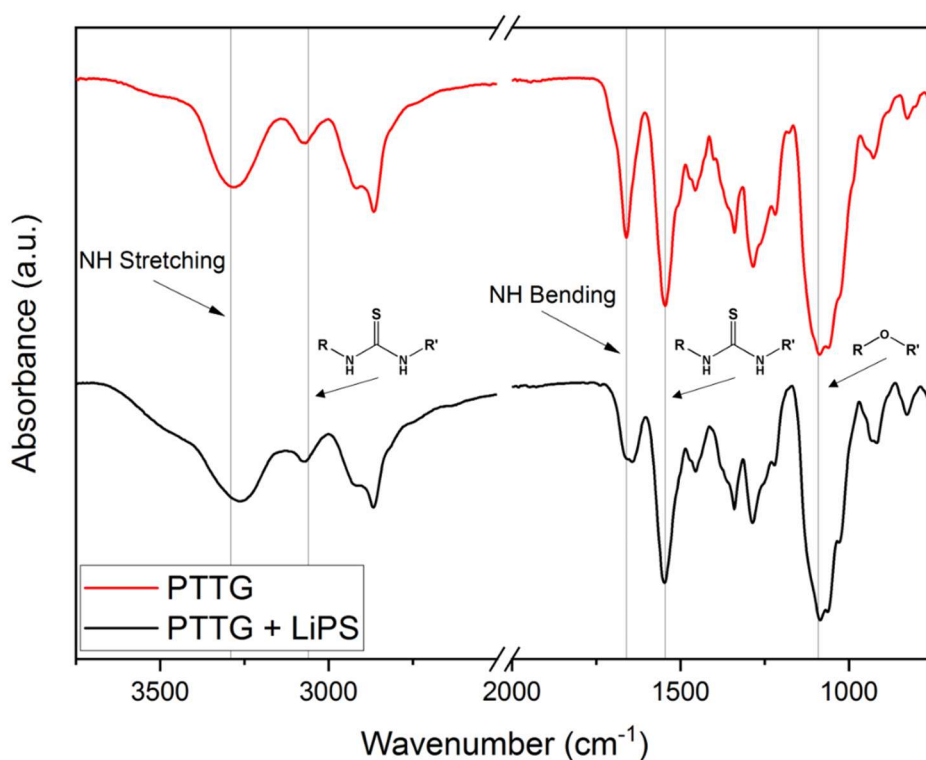


Figure 3.3: FTIR spectra of the PTTG polymer and the PTTG sample after LiPS exposure

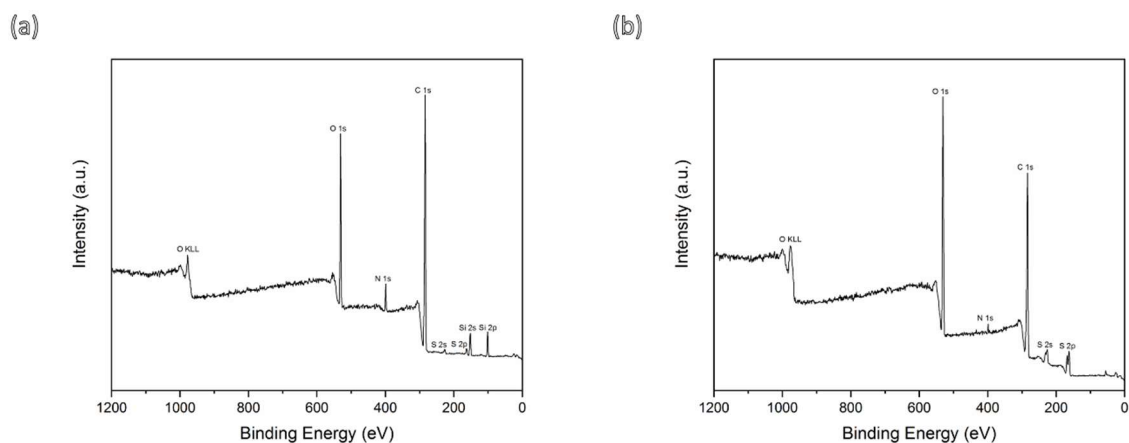


Figure 3.4: Survey XPS spectra of the (a) PTTG polymer and (b) PTTG polymer after Li_2S_4 exposure

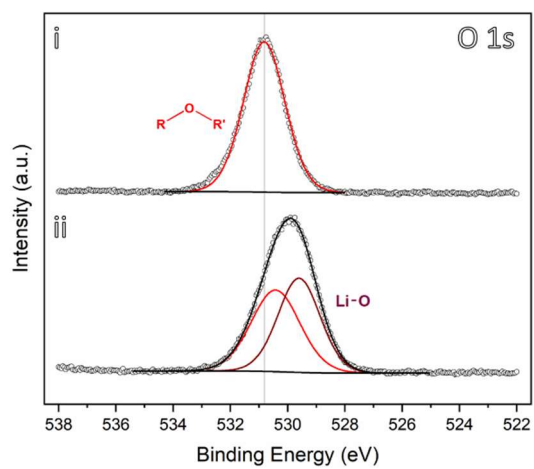
The HR spectra of the O 1s region for the PTTG polymer (**Fig. 3.5a-i**) displays a characteristic peak at 530.8 eV, typical for the ether group of polyethylene oxide [40]. After exposure to the Li_2S_4 solution, the O 1s signal shifts to a lower binding energy and can be expressed as two peaks relating to uncoordinated ether oxygen (530.4 eV) and the newly formed Li–O coordinate bond (529.6 eV), respectively (**Fig. 3.5a-ii**) [31]. Similarly, the N 1s peak at 399.1

eV displayed in **Fig. 3.5b-i**, which can be ascribed to the secondary amine within the thiourea moiety of the PTTG polymer [41], shifts to the lower binding energy of 398.2 eV with a new peak appearing at 397.5 eV due to the formation of the Li-N bond after Li₂S₄ exposure (**Fig. 3.5b-ii**) [42]. For the HR S 2p spectra, all signals were assigned as a doublet with a 2:1 area ratio and 1.18 eV peak separation, following the S 2p_{3/2}/S 2p_{1/2} spin doublet convention [43], with the S 2p_{3/2} portion represented by a solid line and the S 2p_{1/2} represented by a dashed line, and the quoted binding energies referencing the S2p_{3/2} section of the doublet. The thioketone group in the PTTG polymer is assigned to the major peak at 162.8 eV in **Fig. 3.5c-i** [44], with the minor satellite peaks assigned to SO₃²⁻ and S²⁻ [45]. After exposure to Li₂S₄, a downshift of the thioketone peak to 161.6 eV is observed, with an additional peak appearing at 160.9 eV due to the formation of the coordinated Li-S bond between the thioketone group and the lithium atom of the soluble LiPS. The reduction in the binding energies and the formation of new peaks attributed to coordinated Li bonds in the HR XPS spectra provides further evidence of PTTG's chemical interaction with soluble LiPSs.

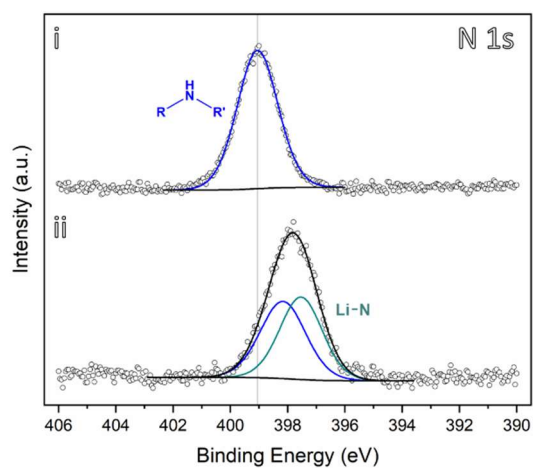
Following the LiPS adsorption experiments, DFT calculations were employed to provide a computational explanation of the obtained LiPS adsorption results. The calculation results are displayed in **Fig. 3.6 and 3.7**. **Fig. 3.6a** shows the relaxed PTTG structure used for calculations. It was found that Li₂S preferentially binds in one of two sites on the PTTG polymer structure, the thiourea site (**Fig. 3.6b-i and ii**) and the oxygen site (**Fig. 3.6c-i and ii**). The thiourea site can accommodate two Li₂S molecules at the sulfur and nitrogen atoms, respectively, providing a combined binding energy of 1.477 eV. In contrast, the oxygen site accommodates one Li₂S molecule with a binding energy of 0.821 eV, much higher than the binding energies calculated between Li₂S and PVDF (0.324 eV), as shown in **Fig 3.7a**.

To further confirm the formation of coordinated bonds between the PTTG polymer and soluble LiPSs, the binding energies of Li₂S₄ and PTTG were calculated. As shown in **Fig 3.7c and d**, the sulfur and oxygen site of the PTTG polymer coordinates with Li₂S₄ at a binding energy of 0.660 eV and 0.613 eV, respectively, again much higher than the binding energy calculated between PVDF and Li₂S₄ (0.256 eV). These DFT calculations support the earlier results obtained in the LiPS adsorption experiments [31, 46], all of which indicate an enhanced adsorption ability of PTTG towards LiPS, which means the LiPS shuttle phenomenon could be effectively inhibited when applied in LSBs.

(a)



(b)



(c)

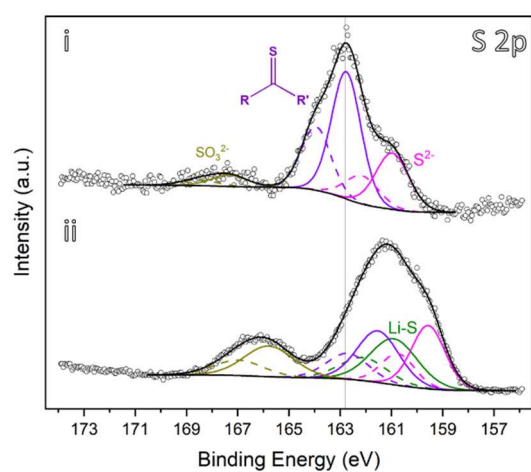


Figure 3.5: High-resolution XPS spectra of the (a) O 1s, (b) N 1s, and (c) S 2p regions for the PTTG polymer before (i) and after (ii) Li₂S₄ exposure

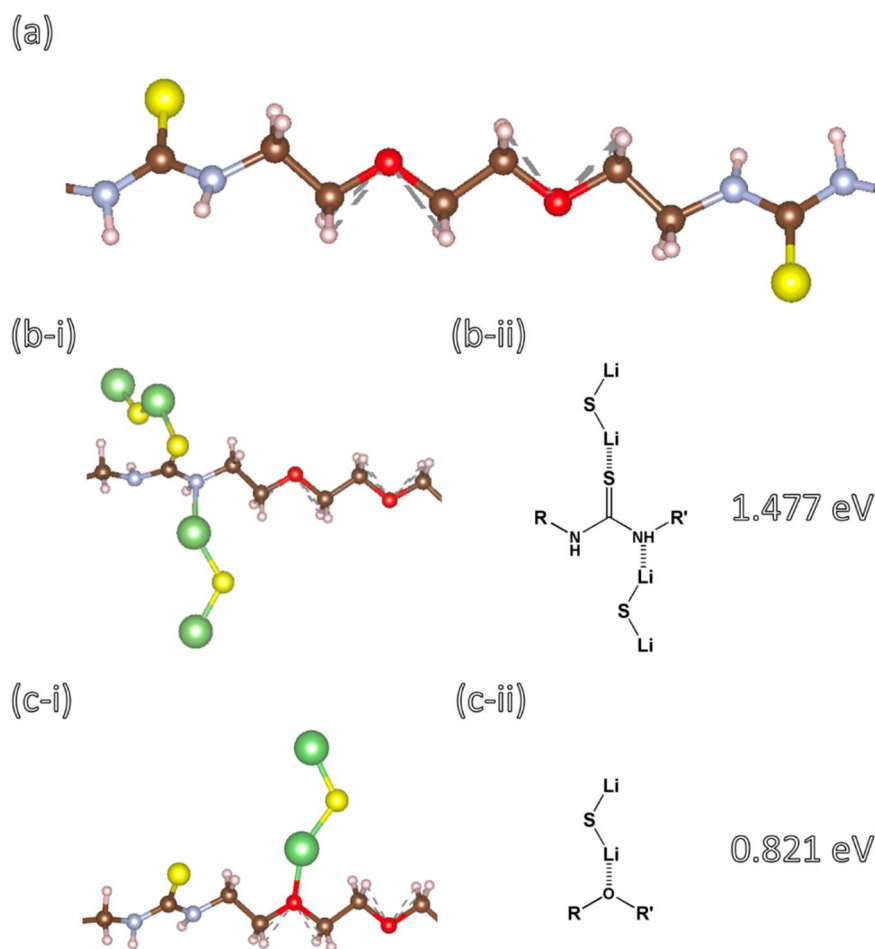


Figure 3.6: The DFT calculation of the binding energy between Li_2S and thiourea and ether sites (a) The relaxed structure of the PTTG polymer. (b-i and ii) The binding sites and binding energy between the thiourea sites and Li_2S . (c-i and ii) The binding site and binding energy between the ether sites and Li_2S . Yellow atom: sulfur, blue atom: nitrogen, red atom: oxygen, green atom: lithium, brown atom: carbon, pink atom: hydrogen

A thorough electrochemical investigation was carried out to determine whether the proposed benefits of the PTTG polymer enhance the performance of LSBs in practice. The cells were subject to charge-discharge testing at a rate of 0.2 C ($1 \text{ C} = 1672 \text{ mAh}\cdot\text{g}^{-1}$), with the voltage/capacity profile of the first cycle displayed in **Fig. 3.8a**. It is well-established that the discharge profile of the LSB can be separated into two distinct plateaus, with the first relating to the dissolution of solid sulfur to soluble LiPS intermediates and the second corresponding to the precipitation of the soluble species to form $\text{Li}_2\text{S}_2/\text{Li}_2\text{S}$, after which the discharge process is complete [5]. It can be observed that in both cells, a capacity of ca. $285 \text{ mAh}\cdot\text{g}^{-1}$ is obtained during the first discharge step, suggesting that in both cases, a roughly equivalent amount of solid sulfur has dissolved into soluble LiPS. However, upon complete discharge, the Sulfur-

PTTG cell delivers a capacity of $981 \text{ mAh}\cdot\text{g}^{-1}$ compared with $889 \text{ mAh}\cdot\text{g}^{-1}$ in the Sulfur-PVDF cell, suggesting that the PTTG binder enables more of the dissolved LiPSs to be completely reduced to Li_2S .

Additionally, the discharge plateaus in the Sulfur-PTTG cell display a higher reduction potential than the Sulfur-PVDF cell. In contrast, upon charging, the Sulfur-PTTG cell has a lower oxidation voltage than the Sulfur-PVDF cell, resulting in a reduced degree of polarization when PTTG is used as the binder. The discharge capacity and Coulombic efficiency (CE) over 80 cycles is displayed in **Fig. 3.8b**. The discharge capacity of the Sulfur-PTTG cell steadily decays to $825 \text{ mAh}\cdot\text{g}^{-1}$ after 80 cycles, corresponding to a capacity loss of 0.198 % per cycle over the tested range. On the other hand, the Sulfur-PVDF cell suffers from a more pronounced capacity fading of 0.426 % per cycle, resulting in a discharge capacity of $586 \text{ mAh}\cdot\text{g}^{-1}$ at the 80th cycle highlighting the ability of PTTG to reduce the capacity fading in LSBs. What's more, the CE of the Sulfur-PTTG cell is higher over the 80 cycles than that of the Sulfur-PVDF cell.

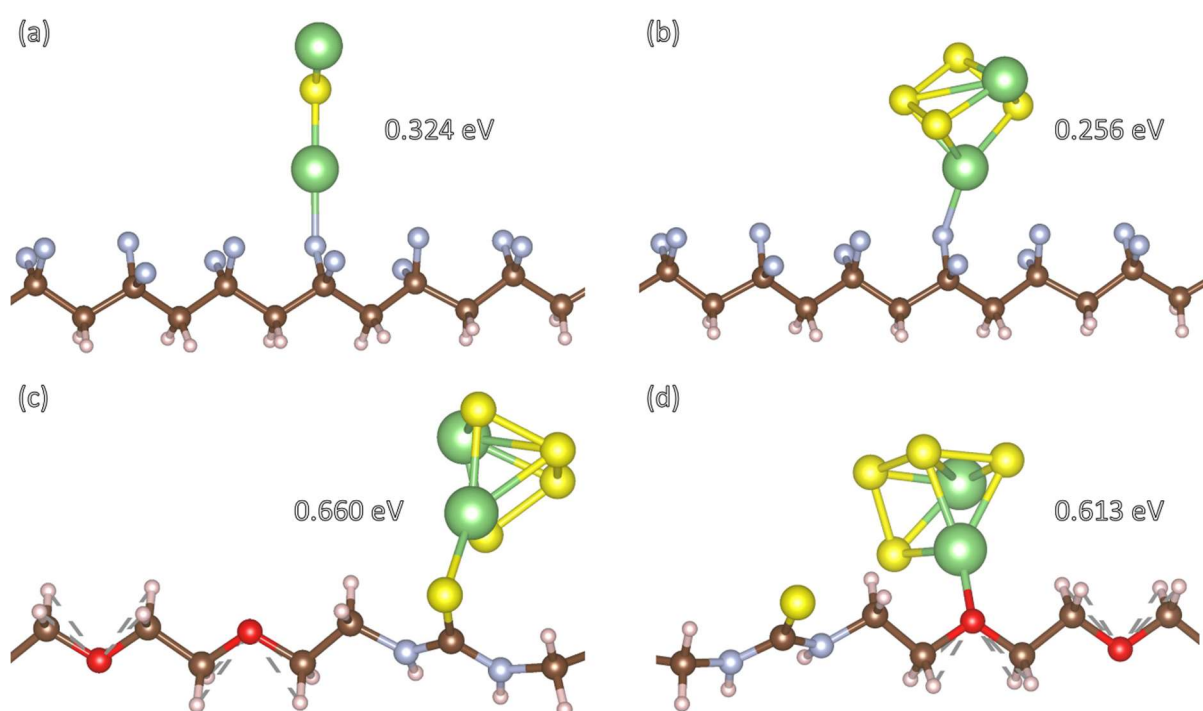


Figure 3.7: DTF model and binding energy of (a) PVDF and Li_2S , (b) PVDF and Li_2S_4 , (c) PTTG-Sulfur site and Li_2S_4 , and (d) PTTG-Oxygen site and Li_2S_4

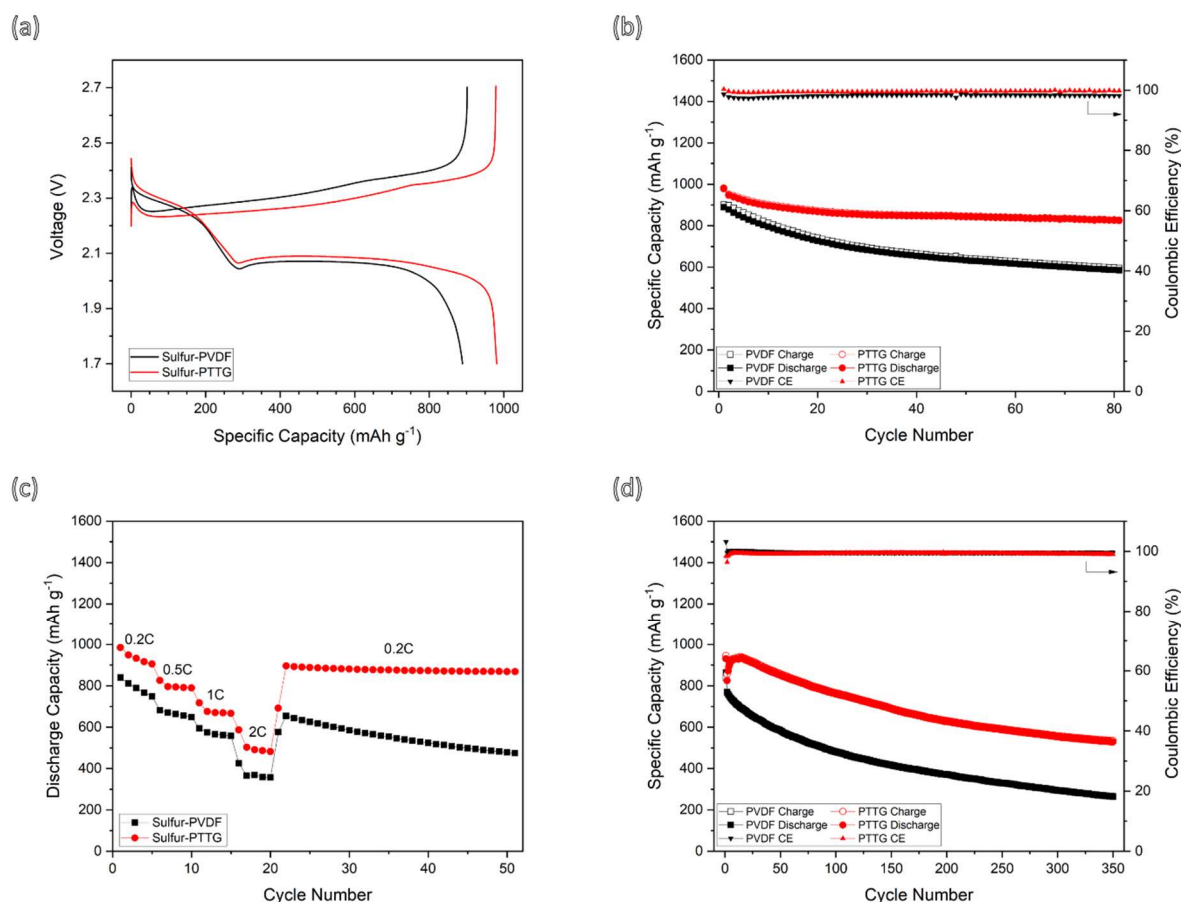


Figure 3.8: Electrochemical data of the Sulfur-PTTG (red) and Sulfur-PVDF (black) cells, including (a) first-discharge profile at 0.2 C ($1 \text{ C} = 1672 \text{ mAh g}^{-1}$), (b) charge-discharge capacity and coulombic efficiency at 0.2 C, (c) rate performance, and (d) charge-discharge capacity and coulombic efficiency at 0.5 C

In order to investigate the performance of the PTTG binder under different charge-discharge currents, rate performance testing was carried out, as shown in **Fig. 3.8c**. The cells were subjected to charge/discharge cycles at increasing C-rates before returning to the initial current density. The Sulfur-PTTG cell delivered capacities of 985, 826, 717, and 587 mAh g^{-1} at 0.2, 0.5, 1, and 2 C, respectively, whereas the Sulfur-PVDF cell delivered capacities of 840, 681, 595, and 426 mAh g^{-1} at the same current densities. These results demonstrate PTTG's ability to deliver a higher discharge capacity under increased charge/discharge rates, especially when cycled at 2 C. Additionally, upon returning to the original discharge rate of 0.2 C, the Sulfur-PTTG cell provides a higher discharge capacity from the 21st cycle onwards and suffers from a smaller capacity decay per cycle than the Sulfur-PVDF cell. Like before, the Sulfur-PTTG cell displayed a higher CE over the tested cycles and a much lower drop in efficiency when switching between discharge currents when compared with the Sulfur-PVDF cell (**Fig. 3.9**).

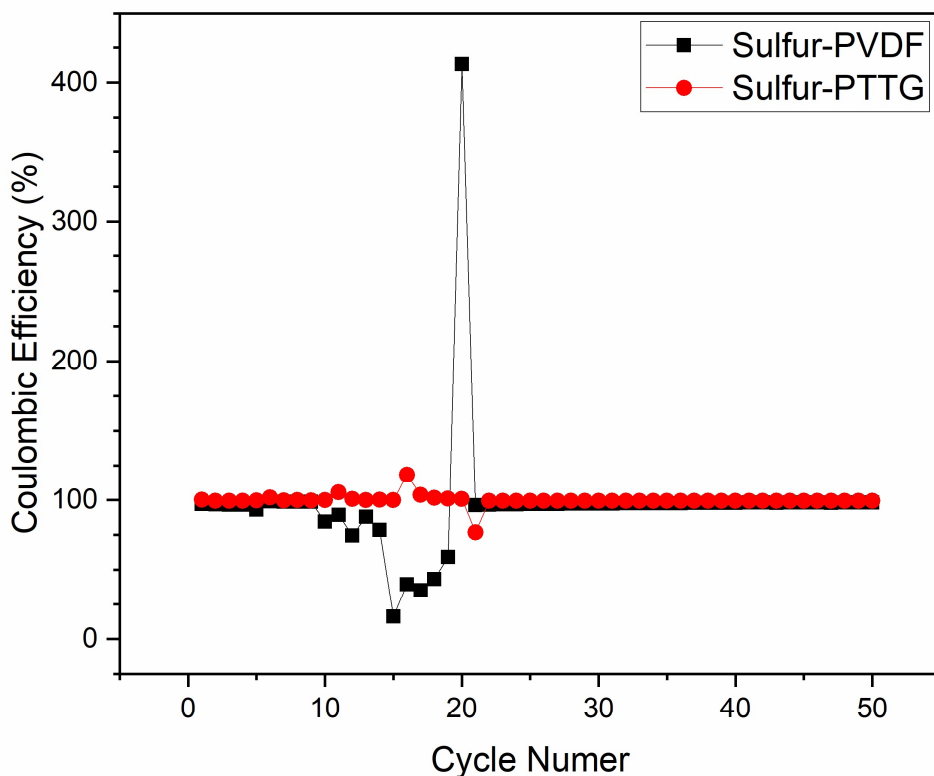


Figure 3.9: CE of the PTTG and PVDF-based cells during the rate performance experiment

The long term cycle performance was also examined in both the PTTG and PVDF-based cells, with the results shown in **Fig. 3.8d**. An activation process can be observed in the first few cycles for the PTTG-Sulfur cell, a common phenomenon [47]. After 350 cycles at 0.5 C, the PTTG-based cell delivers a discharge capacity of $529 \text{ mAh} \cdot \text{g}^{-1}$ compared with only $264 \text{ mAh} \cdot \text{g}^{-1}$ in the PVDF-based cell, corresponding to a capacity fading of 0.123 and 0.198 % per cycle for each cell, respectively, which again highlights the superior capacity retention displayed by the PTTG polymer. The areal capacity of the LSB is another critical parameter that must be improved before commercialisation [48]; thus the areal capacity obtained at 0.2 C with a sulfur loading of $1.0 \text{ mg} \cdot \text{cm}^{-2}$ is displayed in **Fig. 3.10a**. Following this, high loading cathodes ($\approx 4 \text{ mg cm}^{-2}$) were fabricated and cycled at 0.25 mA cm^{-2} to investigate the areal performance of the PTTG binder. As shown in **Fig. 3.10b**, the Sulfur-PTTG electrode delivers an areal capacity of about $2.5 \text{ mAh} \cdot \text{cm}^{-2}$ in the 5th cycle, much higher than the capacity of around $1.5 \text{ mAh} \cdot \text{cm}^{-2}$ delivered by the Sulfur-PVDF cathode at the same sulfur loading, which shows PTTG's ability to deliver better electrochemical performance, even at higher sulfur loading.

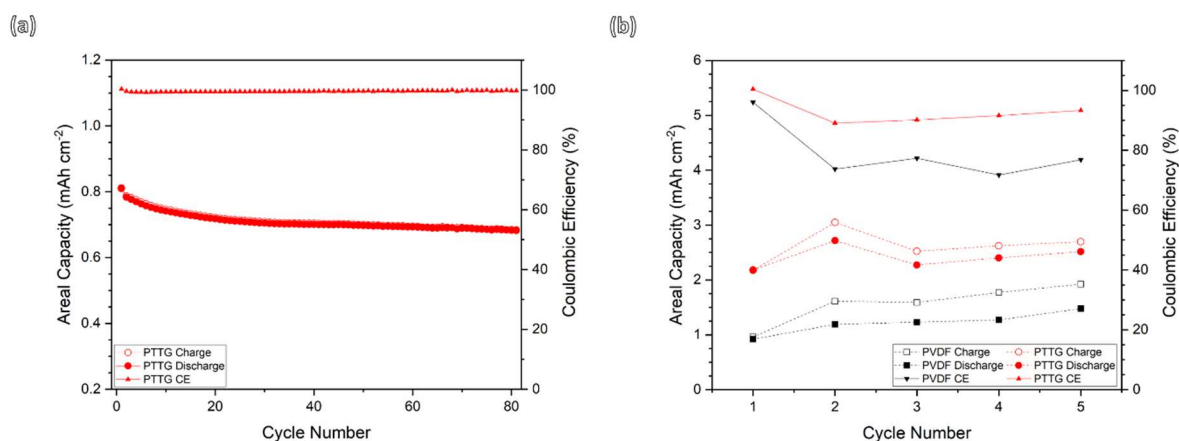
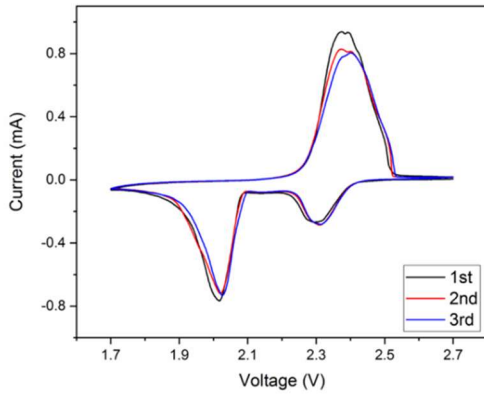


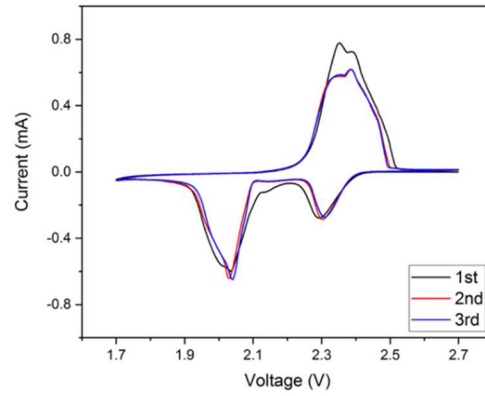
Figure 3.10: Areal capacity and Coulombic Efficiency of (a) the Sulfur-PTTG cathode over 80 cycles at 0.2 C and (b) the Sulfur-PTTG and Sulfur-PVDF cathodes over 5 cycles at 0.25 mA·cm⁻²

In order to deeply understand the mechanisms by which the PTTG binder enhances the electrochemical performance of LSBs, cyclic voltammetry testing was first carried out between the voltage window of 1.7 - 2.7 V at a scan rate of 0.05 mV·s⁻¹. As shown in **Fig. 3.11a**, the voltammogram of Sulfur-PTTG cell shows only a minor difference in the peak height and position between the first and second cycle, with almost no change between the second and third cycle. Compared with the CV curve for the Sulfur-PVDF battery (**Fig. 3.11b**), a less stable first cycle can be observed, with overlap between the first and second discharge peak. Additional differences in electrochemical performance between the cells can be noted by observing the peak current during discharge. The first discharge peak current in both the Sulfur-PTTG and Sulfur-PVDF cell is roughly equivalent (approx. -0.28 mA); however the peak current associated with soluble LiPS precipitation is higher in the Sulfur-PTTG cell compared with the Sulfur-PVDF cell (approx. -0.75 vs. -0.60 mA, respectively), highlighting the superior reaction kinetics of the cell when PTTG is used as a binder. These CV results indicate that the PTTG binder could effectively reduce the polarization of the sulfur cathode and accelerate the redox kinetics.

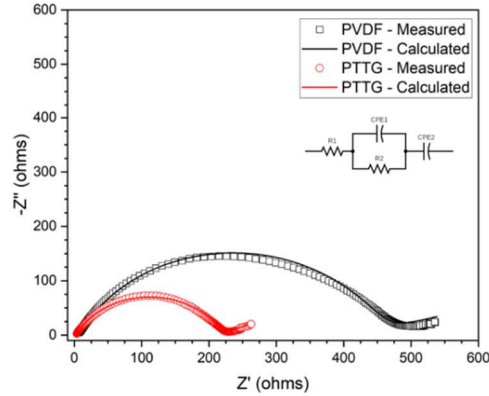
(a): Sulfur-PTTG



(b): Sulfur-PVDF



(c): Before Cycling



(d): After 50 Cycles

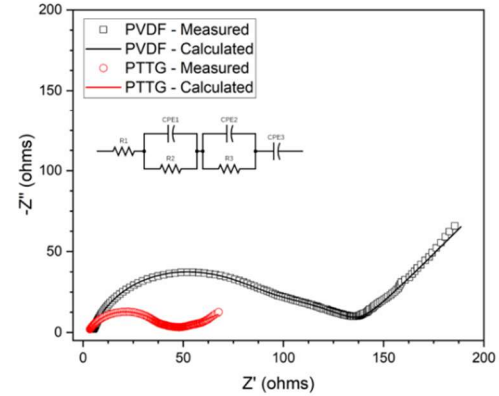


Figure 3.11: Cyclic voltammogram of the (a) Sulfur-PTTG and (b) Sulfur-PVDF cell for 3 cycles at $0.05 \text{ mV} \cdot \text{s}^{-1}$. EIS spectra of the Sulfur-PTTG and Sulfur-PVDF cathode (c) before and (d) after 50 cycles at 0.5 C

EIS was carried out on both the Sulfur-PTTG and Sulfur-PVDF cathodes before and after 50 cycles at 0.5 C . The resulting spectra were fit with an equivalent circuit, with the experimental and theoretical results displayed in **Fig. 3.11c and d** and **Table 3.1**, with the equivalent circuits displayed in the inset of the respective spectra.

Before cycling, the spectra can be modelled by the circuit displayed in **Fig. 3.11c** [49], with the impedance contributions attributed to the ohmic resistance (R_e), charge transfer resistance (R_{ct}), and Warburg impedance (W_0) in the cells, respectively. In the Sulfur-PTTG cell, an R_{ct} value of 212Ω is obtained, which is smaller than that of the Sulfur-PVDF cell (430Ω) (**Table 3.1**). After cycling, the cells can be modelled by the equivalent circuit shown in **Fig. 3.11d**, with the additional contribution to the impedance stemming from the interphase contact resistance in the electrode bulk (R_{int}) [50]. When the EIS results for the Sulfur-PTTG cell are fit to the equivalent circuit, the values of 31.6Ω and 14.3Ω are obtained for R_{ct} , and R_{int} ,

respectively, which are much lower than those in the Sulfur-PVDF cell (63.1 and 69.3 Ω) (**Table 3.1**). The lower R_{ct} and R_{int} values in the Sulfur-PTTG cell suggest quicker electron transportation, leading to lower polarization and faster redox kinetics.

Table 3.1: Resistance results from EIS fitting

	Before Cycling (Ω)	After Cycling (Ω)
PTTG	-	-
R_{ct}	212	31.6
R_{int}	N/A	14.3
PVDF	-	-
R_{ct}	430	63.1
R_{int}	N/A	69.3

$$D_{Li} = \frac{R^2 T^2}{2A^2 n^4 F^4 C^2 \sigma_w^2} \quad (3.2)$$

$$D_{Li} \propto \frac{1}{\sigma_w^2} \quad (3.3)$$

Qualitative lithium-ion diffusion information can also be obtained from the low-frequency region of the EIS results, which is attributed to W_o [51]. By graphing the real component of the complex impedance (Z') vs. the angular frequency ($\omega^{-0.5}$) in the low-frequency region of the EIS results after cycling, as shown in **Fig. 3.12**, a value for the Warburg factor (σ_W) can be obtained [52]. The trend in the lithium diffusion kinetics in both electrodes can be obtained through the inversely proportional relationship between the lithium-ion diffusion coefficient (D_{Li}) and σ_w , as shown in **Eqn. 3.2 and 3.3** [53]. Thus, as the Sulfur-PTTG cell displays a smaller σ_W compared with the Sulfur-PVDF cell (3.9691 vs. 13.651, respectively), improved lithium-ion diffusion kinetics can be inferred.

Secondly, the electrode morphological characterizations and peel tests were also carried out to explain the excellent mechanical properties that contribute to the improved electrochemical performance. To this end, SEM images were taken of the Sulfur-PTTG and Sulfur-PVDF cathodes before cycling and after 100 cycles at 0.5 C (**Fig. 3.13**). **Fig. 3.13a and c** show the surface of a pristine Sulfur-PTTG and Sulfur-PVDF cathode, respectively. The surface of the Sulfur-PTTG electrode shows good homogeneity with minimal pits and cracks in the electrode surface. In contrast, the surface of the Sulfur-PVDF electrode shows large surface cracks and

deep pits, while also displaying a reduced degree of homogeneity. These images suggest that the PTTG binder can help disperse the sulfur and carbon black throughout the electrode resulting in an even electrode surface, which supports the smaller R_{ct} obtained during EIS testing. Upon observing the SEM images of the electrodes after cycling, the differences between the electrodes using two different binders become even more pronounced. Although the Sulfur-PTTG electrode does display some small pits (**Fig. 3.13b**), the surface remains relatively smooth, homogeneous, and free from large cracks. In sharp contrast, the Sulfur-PVDF cathode's surface (**Fig. 3.13d**) shows large pits with an extremely rough surface, which could explain the higher R_{int} value obtained in the analysis of the Sulfur-PVDF cell. Additional morphological differences can be observed in the cross-sectional SEM images of the electrodes shown in the inset of **Fig. 3.13b and d**. Even after 100 cycles, the Sulfur-PTTG electrode film maintains tight adherence to the current collector, in contrast to the Sulfur-PVDF electrode film that detached from the current collector. The void between the electrode film and the current collector and the cracked surface of the electrode could result in regions of the Sulfur-PVDF cathode becoming inaccessible to the migrating electrons during charge/discharge, thereby reducing the electrochemical performance of the cell [49, 54]. As the Sulfur-PTTG cathode maintained its integrity during cycling, the electronic pathways throughout the electrode could have been preserved, which may contribute to the improved electrochemical performance and smaller R_{ct} mentioned earlier.

Finally, 90 ° peel-off testing was carried out to examine the mechanical adhesion of the PTTG and PVDF. According to the results shown in **Fig. 3.14**, the steep initial region of the line is more significant for the Sulfur-PTTG cathode, suggesting it requires more force to remove the Sulfur-PTTG film from the current collector compared to the Sulfur-PVDF film. Also, in the flatter horizontal region of the peel-off data, it can be observed that the line for the Sulfur-PVDF cathode is far more erratic compared with the Sulfur-PTTG cathode line, suggesting that the Sulfur-PTTG cathode has a more consistent and even adhesion to both the current collector and the components within the electrode film [35, 55, 56]. The higher adhesion and greater degree of consistency within the Sulfur-PTTG cathode can suggest why the morphology of Sulfur-PTTG cathode maintains its integrity and provides better electrochemical performance than the Sulfur-PVDF electrode.

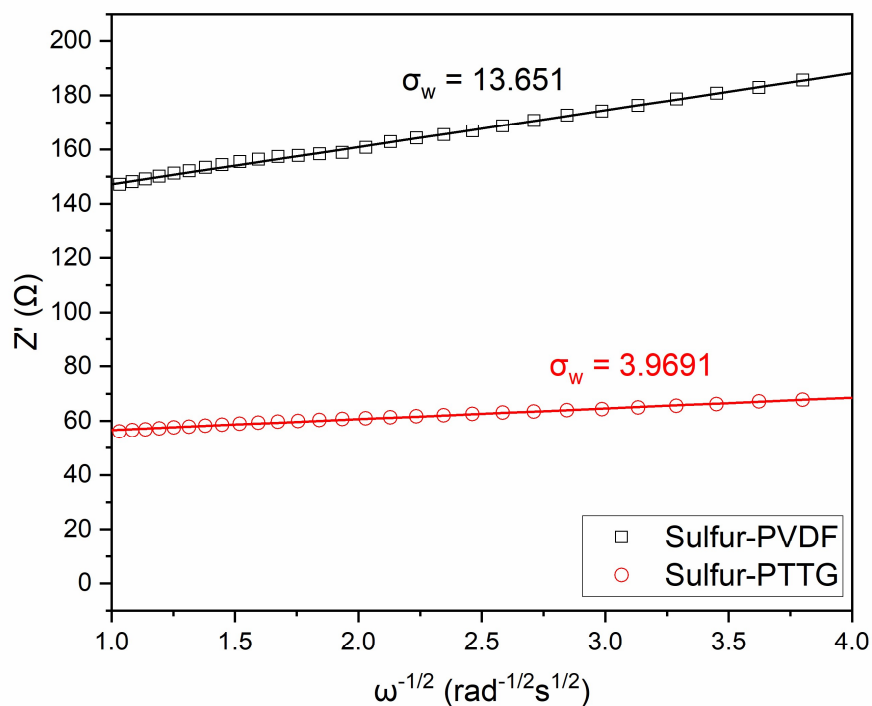


Figure 3.12: The real parts of the complex impedance (Z') vs. $\omega^{-1/2}$ for the Sulfur-PTTG and Sulfur-PVDF electrode

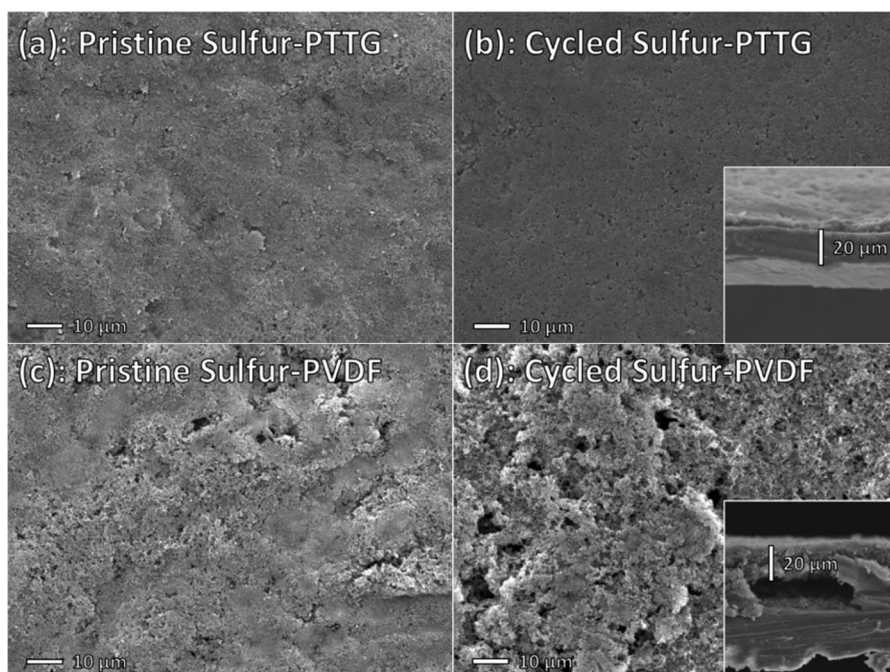


Figure 3.13: SEM images of the Sulfur-PTTG cathode (a) before cycling and (b) after 100 cycles with cross-section image inset, and the Sulfur-PVDF cathode (c) before cycling and (d) after 100 cycles with cross-section image inset

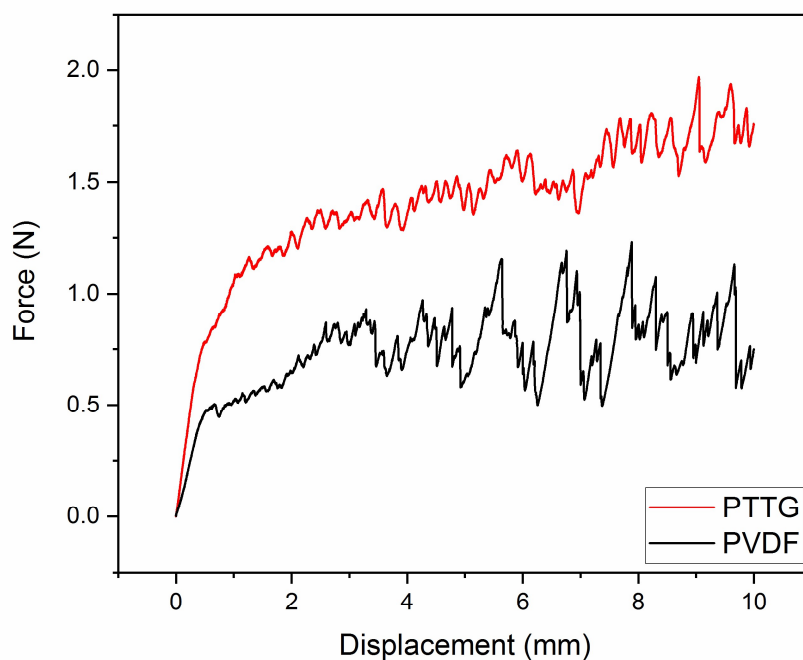


Figure 3.14: Mechanical peel tests of the Sulfur-PTTG (red) and the Sulfur-PVDF (black) cathodes

3.6 Conclusion

PTTG was successfully synthesized and applied as a multifunctional binder for the sulfur cathode in LSBs. Electrochemical investigation revealed that the Sulfur-PTTG cathode delivers a reduced capacity fading of 0.123 % per cycle at 0.5 C, a higher discharge capacity of 587 mAh·g⁻¹ at 2 C, and a higher areal capacity of 2.5 mAh·cm⁻² at 0.25 mA·cm⁻² compared to the Sulfur-PVDF cathode. Such excellent electrochemical performances obtained could be attributed to the multifunctional properties of PTTG:

- i) strong chemical adsorption of LiPS verified by both theoretical calculations and experiments;
- ii) good ionic/electronic conductivity of the Sulfur-PTTG electrode;
- iii) tight adherence to the current collector after cycling
- iv) superior ability to homogenise the electrode's surface

This work not only proves PTTG is a promising binder for LSBs but also guides the future synthesis of thiourea-containing binders for high-performance LSBs.

3.7 Acknowledgments

Luke Hencz would like to thank Dr Milton Kiefel, James Baxter, Darren Holland, and Jack Everson for helping with this paper's polymer synthesis and NMR analysis. The authors gratefully acknowledge financial support from the RTP and GUPRS scholarships and Australia Research Council Discovery Projects (DP160102627 and DP1701048343).

3.8 References

1. Fotouhi, A., et al., *A review on electric vehicle battery modelling: From Lithium-ion toward Lithium–Sulphur*. Renewable and Sustainable Energy Reviews, 2016. **56**: p. 1008-1021.
2. Wu, T., et al., *Controllable Chain-Length for Covalent Sulfur–Carbon Materials Enabling Stable and High-Capacity Sodium Storage*. Advanced Energy Materials, 2019. **9**(9): p. 1803478.
3. Manthiram, A., Y. Fu, and Y.-S. Su, *Challenges and Prospects of Lithium–Sulfur Batteries*. Accounts of Chemical Research, 2013. **46**(5): p. 1125-1134.
4. Ould Ely, T., et al., *Li–Sulfur Batteries: State of the Art and Future Directions*. ACS Applied Energy Materials, 2018.
5. Wang, Y., et al., *Sulfur Hosts against the Shuttle Effect*. Small Methods, 2018.
6. Gu, X., L. Hencz, and S. Zhang, *Recent development of carbonaceous materials for lithium–sulphur batteries*. Batteries, 2016. **2**(4): p. 33.
7. Manthiram, A., et al., *Rechargeable lithium–sulfur batteries*. Chemical reviews, 2014. **114**(23): p. 11751-11787.
8. Liu, B., et al., *Revisiting Scientific Issues for Industrial Applications of Lithium–Sulfur Batteries*. ENERGY & ENVIRONMENTAL MATERIALS, 2018. **1**(4): p. 196-208.
9. Nazar, L.F., M. Cuisinier, and Q. Pang, *Lithium-sulfur batteries*. MRS Bulletin, 2014. **39**(5): p. 436-442.
10. Cao, R., et al., *Anodes for Rechargeable Lithium-Sulfur Batteries*. Advanced Energy Materials, 2015. **5**(16): p. 1402273.
11. Zhang, J., et al., *Nanostructured Host Materials for Trapping Sulfur in Rechargeable Li–S Batteries: Structure Design and Interfacial Chemistry*. Small Methods, 2018. **2**(1): p. 1700279.
12. Liu, J., et al., *Progress and perspective of organosulfur polymers as cathode materials for advanced lithium-sulfur batteries*. Energy Storage Materials, 2018. **15**: p. 53-64.

13. Huang, J.-Q., Q. Zhang, and F. Wei, *Multi-functional separator/interlayer system for high-stable lithium-sulfur batteries: Progress and prospects*. Energy Storage Materials, 2015. **1**: p. 127-145.
14. Lin, D., Y. Liu, and Y. Cui, *Reviving the lithium metal anode for high-energy batteries*. Nature Nanotechnology, 2017. **12**: p. 194.
15. Scheers, J., S. Fantini, and P. Johansson, *A review of electrolytes for lithium–sulphur batteries*. Journal of Power Sources, 2014. **255**: p. 204-218.
16. Fang, R., et al., *Reaction Mechanism Optimization of Solid-State Li–S Batteries with a PEO-Based Electrolyte*. Advanced Functional Materials, 2021. **31**(2): p. 2001812.
17. Xu, L., et al., *Garnet Solid Electrolyte for Advanced All-Solid-State Li Batteries*. Advanced Energy Materials, 2021. **11**(2): p. 2000648.
18. Cleaver, T., et al., *Perspective—Commercializing Lithium Sulfur Batteries: Are We Doing the Right Research?* Journal of The Electrochemical Society, 2018. **165**(1): p. A6029-A6033.
19. Chen, H., et al., *Exploring Chemical, Mechanical, and Electrical Functionalities of Binders for Advanced Energy-Storage Devices*. Chemical Reviews, 2018.
20. Hencz, L., et al., *Housing Sulfur in Polymer Composite Frameworks for Li–S Batteries*. Nano-Micro Letters, 2019. **11**(1): p. 17.
21. Zhu, J., et al., *Recent progress in polymer materials for advanced lithium-sulfur batteries*. Progress in Polymer Science, 2018.
22. Liu, J., Q. Zhang, and Y.-K. Sun, *Recent progress of advanced binders for Li–S batteries*. Journal of Power Sources, 2018. **396**: p. 19-32.
23. Guo, Q. and Z. Zheng, *Rational Design of Binders for Stable Li–S and Na-S Batteries*. Advanced Functional Materials, 2019. **n/a**(n/a): p. 1907931.
24. Qi, Q., et al., *Multifunctional binder designs for lithium-sulfur batteries*. Journal of Energy Chemistry, 2019. **39**: p. 88-100.
25. Yuan, H., et al., *A Review of Functional Binders in Lithium–Sulfur Batteries*. Advanced Energy Materials, 2018. **8**(31): p. 1802107.

26. Yanagisawa, Y., et al., *Mechanically robust, readily repairable polymers via tailored noncovalent cross-linking*. Science, 2018. **359**(6371): p. 72-76.
27. Chen, S., et al., *Development of cross-linked dextrin as aqueous binders for silicon based anodes*. Journal of Power Sources, 2020. **450**: p. 227671.
28. Kresse, G. and J. Furthmüller, *Efficient iterative schemes for ab initio total-energy calculations using a plane-wave basis set*. Physical Review B, 1996. **54**(16): p. 11169-11186.
29. Perdew, J.P., K. Burke, and M. Ernzerhof, *Generalized Gradient Approximation Made Simple*. Physical Review Letters, 1996. **77**(18): p. 3865-3868.
30. Kresse, G. and D. Joubert, *From ultrasoft pseudopotentials to the projector augmented-wave method*. Physical Review B, 1999. **59**(3): p. 1758-1775.
31. Hou, T.-Z., et al., *Lithium Bond Chemistry in Lithium–Sulfur Batteries*. Angewandte Chemie International Edition, 2017. **56**(28): p. 8178-8182.
32. Lacey, M.J., et al., *Why PEO as a binder or polymer coating increases capacity in the Li–S system*. Chemical Communications, 2013. **49**(76): p. 8531-8533.
33. Cheon, S.-E., et al., *Structural factors of sulfur cathodes with poly (ethylene oxide) binder for performance of rechargeable lithium sulfur batteries*. Journal of the Electrochemical Society, 2002. **149**(11): p. A1437-A1441.
34. Ji, P., et al., *α -MoO₃ spheres as effective polysulfides adsorbent for high sulfur content cathode in lithium-sulfur batteries*. Journal of Power Sources, 2018. **400**: p. 572-579.
35. Yi, H., et al., *Aqueous-processable polymer binder with strong mechanical and polysulfide-trapping properties for high performance of lithium–sulfur batteries*. Journal of Materials Chemistry A, 2018. **6**(38): p. 18660-18668.
36. Rao, C.N.R. and R. Venkataraghavan, *The C=S stretching frequency and the “–N–C=S bands” in the infrared*. Spectrochimica Acta Part A: Molecular Spectroscopy, 1989. **45**: p. 299-305.
37. Li, G., et al., *The dual actions of modified polybenzimidazole in taming the polysulfide shuttle for long-life lithium–sulfur batteries*. NPG Asia Materials, 2016. **8**(10): p. e317-e317.
38. Custelcean, R., *Crystal engineering with urea and thiourea hydrogen-bonding groups*. Chemical Communications, 2008(3): p. 295-307.

39. Yoshio, M., R.J. Brodd, and A. Kozawa, *Lithium-ion batteries*. Vol. 1. 2009: Springer.
40. Louette, P., F. Bodino, and J.-J. Pireaux, *Poly (ethylene oxide)(PEO) XPS Reference Core Level and Energy Loss Spectra*. Surface Science Spectra, 2005. **12**(1): p. 59-63.
41. Martin, D.J., et al., *Highly Efficient Photocatalytic H₂ Evolution from Water using Visible Light and Structure-Controlled Graphitic Carbon Nitride*. Angewandte Chemie International Edition, 2014. **53**(35): p. 9240-9245.
42. Gu, X., et al., *From agaric hydrogel to nitrogen-doped 3D porous carbon for high-performance Li-S batteries*. Journal of Materials Science, 2020. **55**(3): p. 1136-1147.
43. Liang, X., et al., *A highly efficient polysulfide mediator for lithium-sulfur batteries*. Nature Communications, 2015. **6**(1): p. 5682.
44. Walton, R., *The x-ray photoelectron spectra of metal complexes of sulfur-containing ligands: sulfur 2p binding energies*. 1980.
45. Moulder, J.F., *Handbook of X-ray photoelectron spectroscopy*. Physical electronics, 1995: p. 230-232.
46. Seh, Z.W., et al., *Stable cycling of lithium sulfide cathodes through strong affinity with a bifunctional binder*. Chemical Science, 2013. **4**(9): p. 3673-3677.
47. Sun, K., H. Liu, and H. Gan, *Cathode Loading Effect on Sulfur Utilization in Lithium-Sulfur Battery*. Journal of Electrochemical Energy Conversion and Storage, 2016. **13**(2).
48. Peng, H.-J., et al., *Lithium-Sulfur Batteries: Review on High-Loading and High-Energy Lithium-Sulfur Batteries (Adv. Energy Mater. 24/2017)*. Advanced Energy Materials, 2017. **7**(24): p. 1770141.
49. Deng, Z., et al., *Electrochemical Impedance Spectroscopy Study of a Lithium/Sulfur Battery: Modeling and Analysis of Capacity Fading*. Journal of The Electrochemical Society, 2013. **160**(4): p. A553-A558.
50. Zhang, S.S., K. Xu, and T.R. Jow, *EIS study on the formation of solid electrolyte interface in Li-ion battery*. Electrochimica Acta, 2006. **51**(8): p. 1636-1640.

51. Wang, Y., et al., *Manipulation of Edge-Site Fe–N₂ Moiety on Holey Fe, N Codoped Graphene to Promote the Cycle Stability and Rate Capacity of Li–S Batteries*. *Advanced Functional Materials*, 2019. **29**(5): p. 1807485.
52. Li, B., et al., *Facile synthesis of Li₄Ti₅O₁₂/C composite with super rate performance*. *Energy & Environmental Science*, 2012. **5**(11): p. 9595-9602.
53. Takami, N., et al., *Structural and Kinetic Characterization of Lithium Intercalation into Carbon Anodes for Secondary Lithium Batteries*. *Journal of The Electrochemical Society*, 1995. **142**(2): p. 371-379.
54. Kim, H.M., et al., *Electrochemical properties of sulfurized-polyacrylonitrile cathode for lithium–sulfur batteries: effect of polyacrylic acid binder and fluoroethylene carbonate additive*. *The Journal of Physical Chemistry Letters*, 2017. **8**(21): p. 5331-5337.
55. Xu, G., et al., *Conductive graphene oxide-polyacrylic acid (GOPAA) binder for lithium-sulfur battery*. *Nano Energy*, 2017. **31**: p. 568-574.
56. Chen, W., et al., *A New Hydrophilic Binder Enabling Strongly Anchoring Polysulfides for High-Performance Sulfur Electrodes in Lithium-Sulfur Battery*. *Advanced Energy Materials*, 2018. **8**(12): p. 1702889.

Chapter 4:
Multifunctional Cation-Vacancy-Rich ZnCo_2O_4
Polysulfide-Blocking Layer for Ultrahigh-Loading
Li-S Battery

4.1 Abstract

The major hurdle in Li–S battery commercialization is the severe shuttle effect and sluggish reaction kinetics of polysulfide conversion during charge-discharge cycling. Herein, to overcome these barriers, we designed and synthesized Zn defective Zn/Co oxide (ZDZCO) nanosheets, a cation-vacancy-rich bimetallic oxide for constructing a multifunctional polysulfide-blocking layer. Both theoretical and experimental studies have comprehensively demonstrated that the ZDZCO shows robust binding capability towards polysulfides and a high catalytic ability for fast polysulfide conversion. Through a facile coating process, the multifunctional ZDZCO polysulfide-blocking layer is incorporated on a commercial polypropylene separator, forming a composite separator. The resultant separator facilitates an ultrahigh sulfur loading of $21.06 \text{ mg}\cdot\text{cm}^{-2}$ and an areal capacity as high as $24.25 \text{ mAh}\cdot\text{cm}^{-2}$. This study illuminates a promising and practical strategy to construct high-performance Li–S batteries with high sulfur loading.

Highlights

- Cation-vacancy-rich bimetallic oxide constructs a novel multifunctional polysulfide-blocking layer.
- Cation vacancies boost the catalytic performance of the multifunctional polysulfide-blocking layer.
- The Li–S battery achieves an ultrahigh loading of $21.06 \text{ mg}\cdot\text{cm}^{-2}$ and a prolonged lifespan of 60 cycles.

4.2 Introduction

Owing to the advantages of high energy density ($2600 \text{ Wh}\cdot\text{kg}^{-1}$), low cost, and eco-friendliness, the Li-S battery is considered one of the most promising energy storage devices for electric vehicles, hybrid electric vehicles, and smart power grids [1-3]. However, the electrochemical performance of Li-S batteries is severely restricted by the poor electronic conductivity of the active sulfur material and its discharge products ($\text{Li}_2\text{S}_2/\text{Li}_2\text{S}$), the large volume expansion associated with the conversion of sulfur to $\text{Li}_2\text{S}_2/\text{Li}_2\text{S}$, and the notorious shuttle effect of soluble polysulfides (Li_2S_x , $4 \leq x \leq 8$) [4, 5]. The intractable shuttle effect is especially troublesome, as it leads to fast active material loss, low Columbic efficiency, and severe corrosion and passivation of the Li anode, resulting in rapid electrochemical performance degradation [6-8].

Despite this, through the rational design of polysulfide host materials, high-performance Li-S batteries have been achieved. Various carbonaceous materials [9-11], functional polymers [12-15], and metal compounds [16-20] have been constructed and applied as host materials to improve the electrochemical performance of Li-S batteries. In addition to being applied to prepare S/host material composites, which are capable of immobilizing polysulfides in the cathode matrix, polysulfide-anchoring materials can also be applied in the construction of functional composite separators to effectively deliver a polysulfide shuttle barrier. Usually, when the anchoring materials are applied to modify the separator, rather than as cathodic polysulfide hosts, less inert anchoring materials are used, which improves the gravimetric energy density of the whole cell and aligns with the goal of a high-energy-density Li-S battery. Up to now, extensive efforts have been devoted to modifying commercial separators so that the cycling performance of Li-S batteries can be enhanced [21-32]. For example, an ion-selective Nafion-based layer modified Celgard separator was constructed to confine the polysulfide anions at the cathode side via the shielding effect [21, 22]. Alternatively, with the advantage of high electronic conductivity, a nonpolar super P-modified separator can function as both an upper current collector and a polysulfide-diffusion barrier by physical blocking [23, 26]. In contrast to physically blocking polysulfide migration, polar materials such as heteroatom-doped carbons, functional polymers, and metal compounds can immobilize polysulfides via strong chemical adsorption, which builds a more effective polysulfide-blocking layer on the separators [25, 27, 29, 31, 32].

Although Li-S batteries' cycling stability and discharge capacity have been significantly enhanced through the application of functional separators, most of the previous separator-

related research is based on batteries with low sulfur loading, which cannot satisfy the high energy density required for practical applications. Thus, it is crucial to fabricate high-loading Li-S batteries that can deliver a high areal capacity to obtain a sufficient energy density [33, 34]. It has been reported that a sulfur loading of $> 5 \text{ mg} \cdot \text{cm}^{-2}$ with a specific capacity of $1000 \text{ mAh} \cdot \text{g}^{-1}$, corresponding to an areal capacity of $5 \text{ mAh} \cdot \text{cm}^{-2}$, is required to achieve a satisfactorily high energy density Li-S battery [35]. However, as the sulfur loading increases, the increased severity of polysulfide dissolution and shuttling makes it very difficult to achieve a high-loading Li-S battery with high performance simultaneously. Even though strong-affinity materials applied on separators can effectively immobilize polysulfides, the sluggish reaction kinetics of polysulfide conversion results in the chronic occupation of the adsorption sites on the functional materials, leading to reduced polysulfide affinity after prolonged cycling. Recently, it has been demonstrated that introducing catalytic functionality into high-affinity functional materials is an efficient and promising strategy to achieve fast polysulfide conversion [36-41]. Extensive efforts have been devoted to constructing catalytic cathodes, while the development of catalytic separators is still in the early stage. Considering the reduced dosage of anchoring materials in functional separators, significantly enhanced catalytic properties are required if a high-performance Li-S battery is to be achieved, especially in the case of high sulfur loading. Therefore, the great challenge of designing robust-affinity and highly-catalytic functional material modified separators for high-loading Li-S batteries with high performance remains.

Constructing defects into functional materials has been demonstrated as a highly effective approach to boost the catalytic abilities and polysulfide affinity of functional materials for Li-S batteries [41, 42]. Amongst these, anion vacancies are usually constructed to achieve high-performance functional materials [43-45]. While, to the best of our knowledge, cation vacancies are rarely studied. Herein, a new anchoring functional material design strategy has been proposed via cation vacancies for high-loading Li-S batteries. Co_3O_4 , a strong-affinity host material for polysulfides [46], was chosen as a model to prove our new anchoring functional material design strategy. By partly replacing Co with Zn and in-situ etching, Zn defective ZnCo_2O_4 (ZDZCO) nanosheets were prepared to achieve the Zn vacancies. Both theoretical and experimental studies have demonstrated that the ZDZCO possesses robust binding capability towards polysulfides and a high catalytic ability for polysulfide conversion, resulting from the cation vacancies. As a result, when the ZDZCO was applied in the construction of a novel multifunctional polysulfide-blocking layer on a commercial separator,

Li-S battery with an ultrahigh loading of $21.06 \text{ mg} \cdot \text{cm}^{-2}$ can be achieved, which is stable over 60 cycles and delivers a high areal capacity of $13.95 \text{ mAh} \cdot \text{cm}^{-2}$. To the best of our knowledge, such a cycling lifespan of a Li-S battery with ultrahigh loading prepared via traditional electrode preparation technique has rarely been reported.

4.3 Experimental Section

4.3.1 *Synthesis of Zn defective ZnCo_2O_4 (ZDZCO) nanosheets*

All chemical reagents used in this study were analytical grade without any further purification. The Zn defective ZnCo_2O_4 (ZDZCO) nanosheets were synthesized by a facile hydrothermal method. Typically, 0.3 g $\text{Zn}(\text{NO}_3)_2 \cdot 6\text{H}_2\text{O}$, 0.575 g $\text{Co}(\text{NO}_3)_2 \cdot 6\text{H}_2\text{O}$, and 0.9 g urea were dissolved in a solvent containing 15 mL ethylene glycol (EG) and 15 mL deionized water with magnetic stirring for 5 min at room temperature. The obtained solution was transferred into a 50 mL Teflon-lined stainless steel autoclave and maintained at 180°C for 3 h in an oven. After cooling down to room temperature, ZDZCO precursor was obtained by centrifugation, washed several times with absolute ethyl alcohol, and dried at 80°C overnight in an oven. Finally, the precursor was annealed in air at 400°C for 2 h with a heating rate of $5^\circ\text{C} \cdot \text{min}^{-1}$. As a control, the Co_3O_4 nanosheets were synthesized through the same process without adding $\text{Zn}(\text{NO}_3)_2 \cdot 6\text{H}_2\text{O}$.

4.3.2 *Material characterization*

Scanning electron microscope (SEM) images were observed on a Hitachi S-8200 field emission scanning electron microscope, and elemental mapping was obtained on an EDAX Genesis energy dispersive X-ray fluorescence spectrometer. Transmission electron microscopy (TEM) images and selected area electron diffraction (SAED) patterns were obtained on a JEOL JEM-2100F transmission electron microscope. X-ray powder diffraction (XRD) measurements were carried out via a Bruker D8 Advance powder X-ray diffractometer with a scan speed of $5^\circ \cdot \text{min}^{-1}$ in the range of $10^\circ - 70^\circ$. X-ray photoelectron spectroscopy (XPS) spectra were obtained on a Thermo Scientific 250Xi X-ray photoelectron spectrometer. The content of Zn and Co was determined by inductively coupled plasma-optical emission spectrometer (ICP-OES) analysis (Agilent 730ES).

4.3.3 *Electrochemical Measurements*

For the ZDZCO-separator, the as-synthesized ZDZCO nanosheets, super P and polyvinylidene fluoride (PVDF) binder with a mass ratio of 6:3:1 were mixed in N-methyl-2-pyrrolidone

(NMP). Then the slurry was uniformly coated onto the commercial Celgard 2400 membrane and dried at 60 °C for 12h in a vacuum oven. The loading of the coating was about $0.28 \text{ mg} \cdot \text{cm}^{-2}$. In control experiments, the Co_3O_4 -separator (Co_3O_4 , super P, and PVDF with a mass ratio of 6:3:1) and super P-separator (super P and PVDF with a mass ratio of 9:1) were synthesized through the same procedure.

The sulfur powders (Aladdin) and super P with a mass ratio of 6:4 were mixed by grinding. The mixture was then transferred into a 50 mL Teflon-lined stainless steel autoclave and heated at 155 °C for 12 h to obtain the S/super P composite. For sulfur cathode, 80 wt% S/super P composite, 10 wt% Ketjen black (KB), 10 wt% PVDF binder were mixed in NMP. Then the slurry was uniformly coated on the carbon-coated Al foil using traditional blade coating technique and dried at 60 °C in a vacuum oven for 12 h. The mass loading of sulfur was about $0.6 \text{ mg} \cdot \text{cm}^{-2}$. The CR2016 coin cells were assembled in a glove box full of argon gas using the as-prepared sulfur cathodes, lithium foil anodes, and different separators. The electrolyte was 1 M LiTFSI in a mixed solvent of DOL and DME (1:1 v/v) with 2% LiNO_3 . Galvanostatic charge-discharge cycling tests were conducted on a LAND CT2001A battery tester at room temperature between 1.8 and 2.6 V. Cyclic voltammetry (CV) measurements and electrochemical impedance spectroscopy (EIS) tests were performed using a CHI660E electrochemical workstation. The scan rate of CV test is $0.1 \text{ mV} \cdot \text{s}^{-1}$ between 1.8 and 2.6 V. For the EIS test, the frequency range is from 10 mHz to 100 kHz with an amplitude of 5 mV.

S/super P composite with 80 wt% sulfur and 20 wt% super P were prepared and applied for high-loading Li-S battery. As the ordinary Al foil current collector will curl with high sulfur loading, the current collector was replaced with carbon paper for high-loading Li-S batteries ($5.59 - 21.06 \text{ mg} \cdot \text{cm}^{-2}$). The current density was $1.2 \text{ mA} \cdot \text{cm}^{-2}$ for Li-S battery with loading of $5.59 \text{ mg} \cdot \text{cm}^{-2}$ (the first cycle was $0.3 \text{ mA} \cdot \text{cm}^{-2}$); $0.4 \text{ mA} \cdot \text{cm}^{-2}$ for $11.57 \text{ mg} \cdot \text{cm}^{-2}$ and $21.06 \text{ mg} \cdot \text{cm}^{-2}$ (the first cycle was $0.2 \text{ mA} \cdot \text{cm}^{-2}$); $2.4 \text{ mA} \cdot \text{cm}^{-2}$ for $9.31 \text{ mg} \cdot \text{cm}^{-2}$ (the first cycle was $0.4 \text{ mA} \cdot \text{cm}^{-2}$ and the second cycle was $0.8 \text{ mA} \cdot \text{cm}^{-2}$).

4.3.4 Polysulfide adsorption and diffusion experiments

First, Li_2S and sulfur powders with a molar ratio of 1:5 were stirred in 6 mL DME at 65 °C for 48 h in the glove box to prepare a Li_2S_6 solution with an initial concentration of 0.1 M. Then the solution was diluted to 2 mM for the polysulfide adsorption. Furthermore, Li_2S and sulfur powders with a molar ratio of 1:5 were stirred in 6 mL tetrahydrofuran (THF) at 65 °C for 48

h in the glove box to prepare a Li_2S_6 solution with an initial concentration of 0.1 M. Then the solution was diluted to 4 mM for the polysulfide diffusion experiment.

For polysulfide adsorption tests, 80 mg ZDZCO, Co_3O_4 and super P were added into three glass bottles with 2 mM Li_2S_6 solutions, respectively. After standing for about 48 h, the supernatant liquid was injected into a quartz cuvette and sealed in the glove box. Then the Li_2S_6 solutions were tested by UV-visible absorption spectrophotometry (METASH UV8000) to quantitatively indicate the remnant Li_2S_6 in the solutions after adsorption tests. The ZDZCO after Li_2S_6 adsorption was used for the XPS test.

For the polysulfide diffusion experiment, H-shaped glass cells were set up. Half of the glass cell (left) was filled with 50 mL 4 mM Li_2S_6 solution, and the other half (right) was filled with 50 mL THF, separated by PP separator, super P-separator, Co_3O_4 -separator, and ZDZCO-separator, respectively. In order to protect the modified separator from abrasion, PP separators are added on both sides of the tested separator (PP separator, super P-separator, Co_3O_4 -separator, and ZDZCO-separator).

4.3.5 Symmetric cell tests and Li_2S nucleation experiments

Li_2S and sulfur powders with a molar ratio of 1:5 were stirred at 65 °C for 48h in a mixed solvent (DOL: DME = 1:1 v/v) to prepare a 0.1 M Li_2S_6 solution. 45 wt% ZDZCO, 45 wt% super P, and 10 wt% PVDF binder were mixed in NMP to obtain an uniform slurry. Then the slurry was cast on the carbon-coated Al foil and then dried at 60 °C for 12 h in a vacuum oven. The symmetric cells were assembled in a glove box using two same electrodes with the as-prepared Li_2S_6 solution (0.1 M). CV measurements were performed using a CHI660E electrochemical workstation with a scan rate of 10 $\text{mV}\cdot\text{s}^{-1}$ between -1.0 and 1.0 V. For comparison, super P-based electrode and Co_3O_4 -based electrode were also tested using the same process.

Li_2S and sulfur powders with a molar ratio of 1:7 were stirred at 65 °C for 48 h in tetraglyme to prepare a 0.2 M Li_2S_8 solution. 1.0 mg ZDZCO was dispersed on carbon paper and used as the cathode, while lithium foil was used as the counter electrode and Celgard 2400 as the separator to assemble a cell. 25 μL Li_2S_8 catholyte (0.2 M) was dropped on the cathode side and then 20 μL electrolyte (1 M LiTFSI in DOL and DME (1:1 v/v) with 2% LiNO_3) was dropped on the anode side. The cell was firstly galvanostatically discharged at 0.226 mA to

2.06 V and then kept at 2.05 V until the current was below 10^{-5} A for the nucleation of Li_2S . For comparison, the Co_3O_4 sample was also tested using the same process.

4.3.6 Theoretical study

Density functional theory (DFT) calculations were carried out using the Projector-Augmented Wave (PAW) method as implemented in the Vienna Ab Initio Simulation Package (VASP) [47]. For the exchange-correlation functional, we used the Perdew-Burke-Ernzerhof (PBE) [48] of Generalized-Gradient Approximation with the Hubbard U parameter proposed by Dudarev [49]. In this scheme, the effective value of U is described as: $U_{\text{eff}} = U - J$, where U and J represent the on-site coulomb and exchange interaction, respectively. In our calculations, the value of U_{eff} for Zn and Co were set to be 5.0 eV and 3.3 eV, respectively, which are similar to the values applied by Montoya et al. [50] and Huang et al. [51]. Long-range van der Waals interaction (dispersion forces) was also included using the D3 correction method of Grimme et al. [52]. The structure of ZnCo_2O_4 was modelled by replacing all the tetrahedral Co atoms by Zn in the Co_3O_4 structure [53]. A $2 \times 2 \times 2$ supercell and k -point mesh of $2 \times 2 \times 2$ were used for modeling Co_3O_4 , ZnCo_2O_4 , and $\text{Zn}_{0.875}\text{Co}_2\text{O}_4$ bulk systems. Using the fully optimized bulk structures, nonstoichiometric (100) surfaces with nine atomic layers ($\text{Co}_{28}\text{O}_{40}$, $\text{Zn}_8\text{Co}_{20}\text{O}_{40}$ and $\text{Zn}_7\text{Co}_{20}\text{O}_{40}$) were modelled. The (100) surface was considered because of its lowest surface energy among the low index planes $\gamma_{(100)} < \gamma_{(111)} < \gamma_{110}$ [54]. Two terminations were considered when $\text{ZnCo}_2\text{O}_4(100)$ surface was modeled: (A) Co and O atoms were presented on the termination layer while Zn atoms were in the sub-top layer; (B) Zn and O atoms were presented on the termination layer while Co atoms were in the sub-top layer. The surface free energy of $\text{ZnCo}_2\text{O}_4(100)$ surface with two terminations was compared as $\gamma_A < \gamma_B$. Therefore, $\text{ZnCo}_2\text{O}_4(100)$ surface with termination A was chosen in all the following surface calculations. One Zn vacancy was created by removing one Zn atom from the subsurface (second) layer. A vacuum size of 12 Å was applied to prevent the interaction between periodic images along the c direction. A k -point mesh of $2 \times 2 \times 1$ was used for surface calculations. An energy cutoff of 500 eV as well as an energy and a force convergence criterion of 0.0001 eV and $0.001 \text{ eV} \cdot \text{\AA}^{-1}$, respectively, were applied for both bulk and surface calculations.

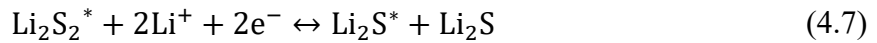
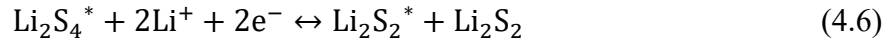
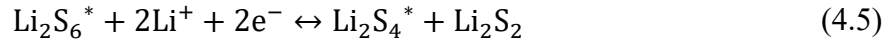
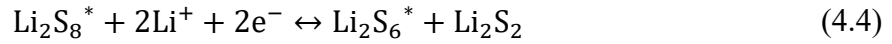
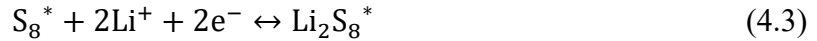
Test calculations were firstly performed with two different models: (i) a symmetric nonpolar surface with one fixed middle layer and termination A; and (ii) firstly, exchanging the Co and Zn atoms in the top and sub-top layer of model i. After fully optimizing the geometries, Co and Zn atoms were exchanged again and re-optimized. The calculated total energy of S_8 and Li_2S_x

($2 \leq x \leq 8$) adsorbed on $\text{ZnCo}_2\text{O}_4(100)$ with the model i was lower than with model ii. However, the total energy of Li_2S adsorbed on $\text{ZnCo}_2\text{O}_4(100)$ with model ii was lower than with model i. Considering the large supercomputer consuming, a simplified asymmetric nonpolar surface with three bottom layers fixed (model iii) was finally constructed for all calculations. The adsorption sites of S_8 and Li_2S_x on the surfaces in model iii are exactly the same as the most favorable structures from the test calculations. The BE between Li_2S_x and host materials (HM = $\text{Co}_3\text{O}_4/\text{ZnCo}_2\text{O}_4/\text{Zn}_{0.875}\text{Co}_2\text{O}_4$) is defined as:

$$E_b = E_{\text{HM}+\text{Li}_2\text{S}_x} - E_{\text{HM}} - E_{\text{Li}_2\text{S}_x} \quad (4.1)$$

Where $E_{\text{HM}+\text{Li}_2\text{S}_x}$, E_{HM} and $E_{\text{Li}_2\text{S}_x}$ are the total energy of Li_2S_x molecule adsorbed on host materials, bared host materials and Li_2S_x molecule, respectively.

To explore the catalytic effect of Co_3O_4 and $\text{Zn}_{0.875}\text{Co}_2\text{O}_4$, Gibbs free energy for S_8 , Li_2S_8 , Li_2S_6 , Li_2S_4 , Li_2S_2 , and Li_2S conversion is calculated with the following intermediate steps [55]:



The Gibbs free energy for the intermediate steps is defined as:

$$\Delta G = \Delta E_{\text{tot}} + \Delta \text{ZPE} + P\Delta V \quad (4.8)$$

Where ΔE_{tot} , ΔZPE , and ΔV are the changes in DFT total energies, zero-point energies, and volumes from the initial to the final states, respectively. The last term in **Eqn. 4.8** is very small and neglected.

4.4 Results and Discussion

Typically, in alkaline solutions at room temperature, Zn^{2+} in the solid-phase can react with OH^- to form soluble $\text{Zn}(\text{OH})_4^{2-}$, leading to Zn vacancies [56]. In contrast to the referenced work, this work partly replaces the Co in Co_3O_4 with Zn and etches the Zn in-situ in the presence of

urea during a facile hydrothermal method. The hydrolysis of urea offers mild alkaline conditions and active NH_3 ligands to react with Zn^{2+} and achieve Zn vacancies in ZnCo_2O_4 , resulting in the Zn-deficient Zn/Co oxide (ZDZCO). The as-prepared ZDZCO is large-area thin 2D nanosheets with some aggregation, as indicated by the SEM images in **Figs. 4.1a and b and 4.2c**. The XRD pattern of the obtained ZDZCO (**Fig. 4.1c**) shows diffraction peaks at $2\theta = 18.97^\circ, 31.26^\circ, 36.79^\circ, 38.51^\circ, 44.84^\circ, 55.54^\circ, 59.33^\circ$, and 65.20° , which are assigned to (111), (220), (311), (222), (400), (422), (511), and (440) crystal planes of spinel ZnCo_2O_4 phase (PDF No. 23-1390).

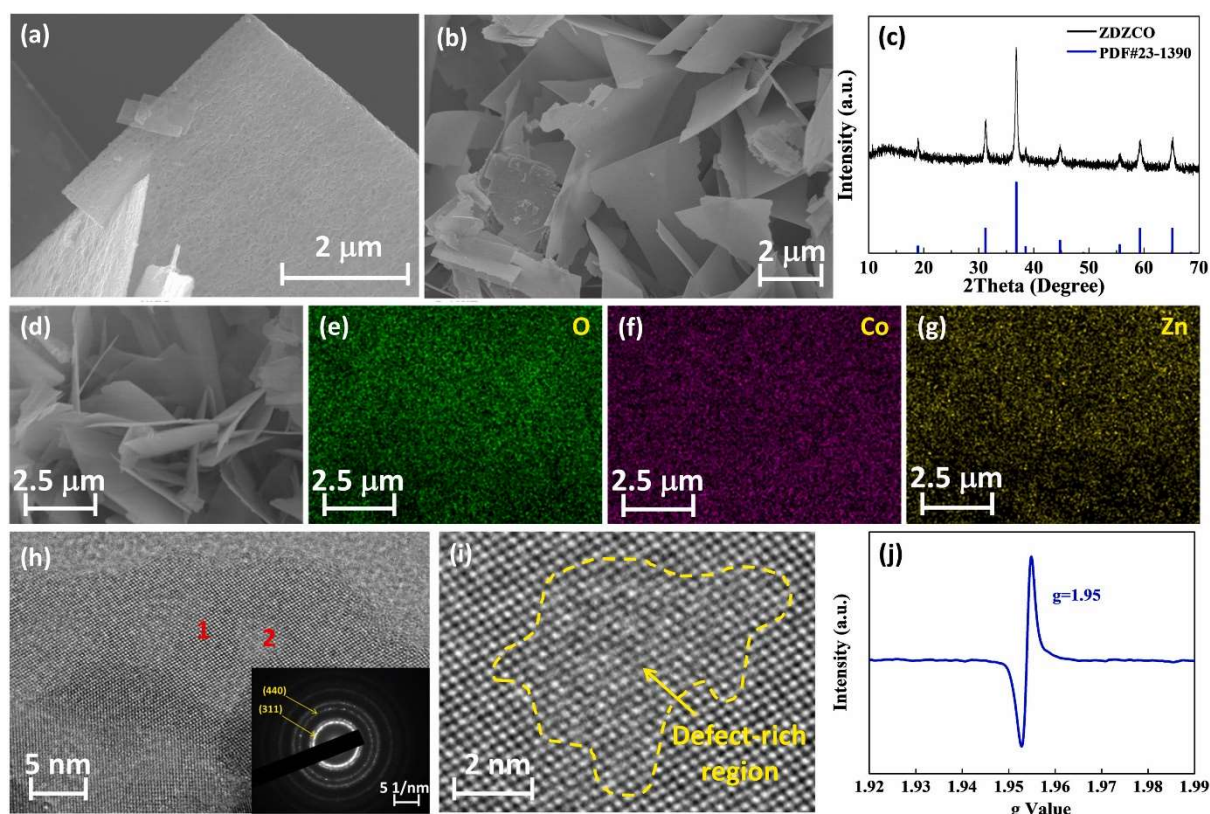


Figure 4.1: (a, b) SEM images and (c) XRD pattern of as-prepared ZDZCO; (e-g) O, Co, and Zn element distribution in the ZDZCO in (d); (h) TEM image of as-prepared ZDZCO and (i) corresponding enlarged view of Section 2; (j) EPR spectrum of as-prepared ZDZCO. The inset in (h) is the SAED pattern of as-prepared ZDZCO

The ratio of Zn and Co in the ZDZCO nanosheets, as determined by ICP-OES analysis, is 0.87:2, leading to a formula of $\text{Zn}_{0.87}\text{Co}_2\text{O}_4$. The element mappings (**Fig. 4.1e-g**) of the ZDZCO nanosheets in **Fig. 4.1d** demonstrate that the Co, Zn, and O elements are distributed uniformly. From the HRTEM images in **Fig. 4.2d** (enlarged view of Section 1 in **Fig. 4.1h**), one can observe an interplanar spacing of 0.27 nm, which is assigned to the (220) plane of ZnCo_2O_4 ,

with the selected area diffraction (SAED) pattern (inset in **Fig. 4.1h**) also showing the diffraction rings of (311) and (440) planes of ZnCo_2O_4 . In **Fig. 4.1i** (enlarged view of Section 2 in **Fig. 4.1h**), numerous small pits on the surface of the as-prepared ZDZCO can be observed, visually indicating the presence of defects in the ZDZCO nanosheets. Moreover, the as-prepared ZDZCO shows a strong EPR signal at $g = 1.95$ (**Fig. 4.1j**), indicating many Zn vacancies [57]. As a control, Co_3O_4 nanosheets were synthesized through the same process without adding $\text{Zn}(\text{NO}_3)_2 \cdot 6\text{H}_2\text{O}$ (**Fig. 4.2b**).

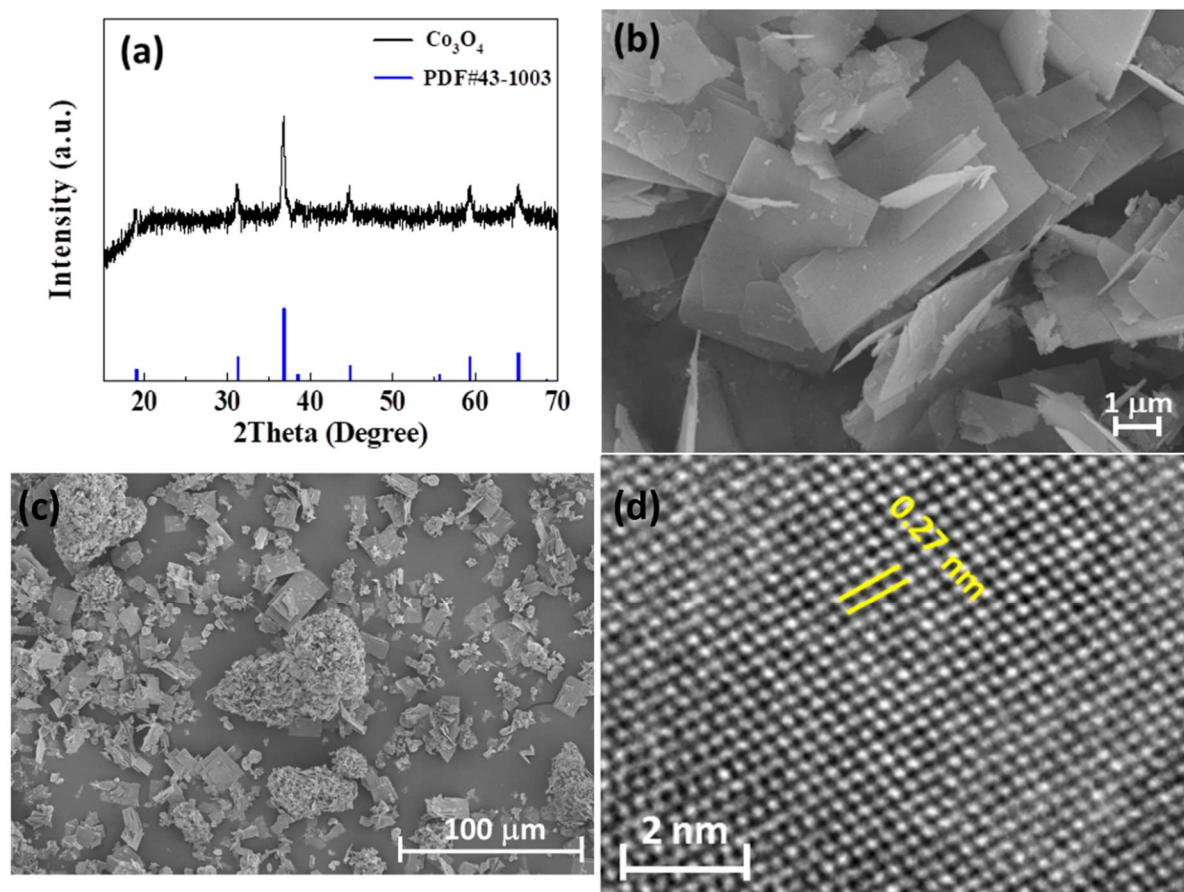


Figure 4.2: (a) XRD pattern and (b) SEM image of as-prepared Co_3O_4 . (c) Large-area SEM image of the as-prepared ZDZCO. (d) Enlarged HRTEM image of section 1 in Fig. 1h.

The ZDZCO-based composite is coated on a commercial PP separator using a blade coating method with ZDZCO nanosheets, super P, and PVDF binder in a mass ratio of 6:3:1 to prepare the ZDZCO polysulfide-blocking layer modified separator (ZDZCO-separator). The loading of the coating was controlled to be about $0.28 \text{ mg} \cdot \text{cm}^{-2}$. Super P was included in the ZDZCO-separator as a conductive additive to allow the modified separator to function as an upper current collector. The integrity of the as-prepared ZDZCO separator after folding, displayed in **Fig. 4.3a**, indicates good adhesion between the ZDZCO polysulfide-blocking layer and PP

separator. The thickness of the ZDZCO polysulfide-blocking layer is measured to be 2.4 μm , as shown in the cross-section SEM image of the ZDZCO-separator (**Fig. 4.3b**). For comparison, a super P-separator was also prepared with super P and PVDF binder in a mass ratio of 9:1. **Fig. 4.3c** shows that with the same mass loading level, the super P coating layer shows a much larger thickness (11.0 μm), almost 5 times thicker than the ZDZCO polysulfide-blocking layer. As a consequence, higher volumetric energy density can be achieved using ZDZCO-separator.

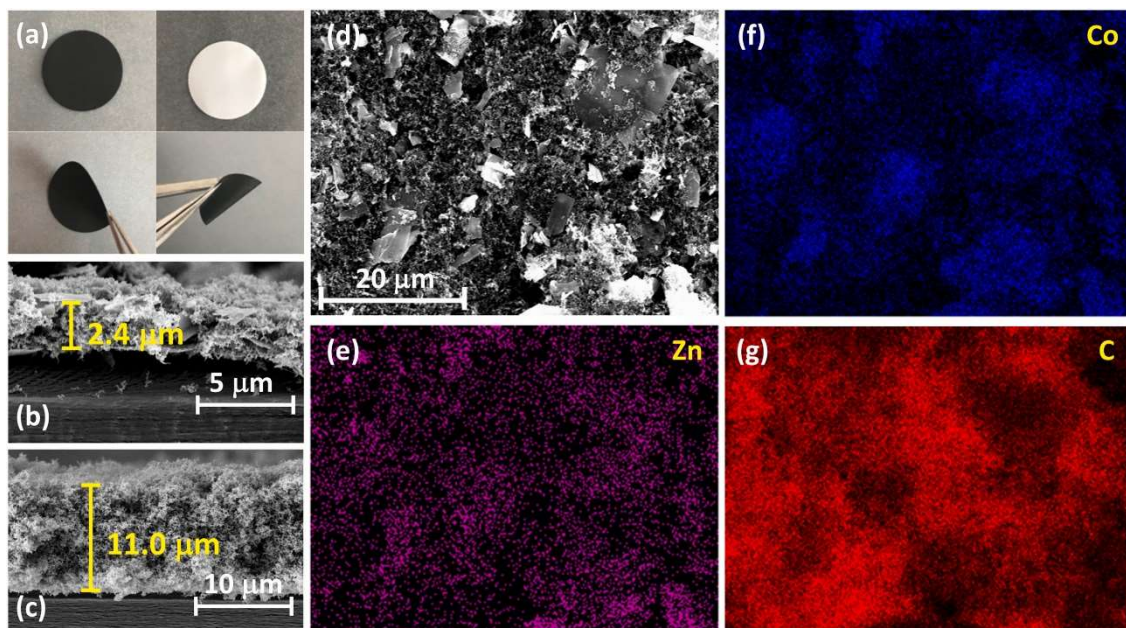


Figure 4.3: (a) Digital photos of as-prepared ZDZCO-separator; cross-section SEM images of (b) ZDZCO-separator and (c) super P-separator; (d) top-view SEM image and (e-g) element mappings of the ZDZCO-separator

By comparing the top-view SEM image of the ZDZCO-separator and super P-separator displayed in **Figs. 4.3d and 4.4**, one can observe that the ZDZCO nanosheets are uniformly embedded in the super P conductive carbon matrix. The element mappings (**Fig. 4.3e-g**) show that the Zn, Co, and C elements are dispersed over the separator. Consequently, it is expected that the ZDZCO-separator can not only effectively immobilize polysulfides but also act as an upper current collector for the continual conversion of polysulfides.

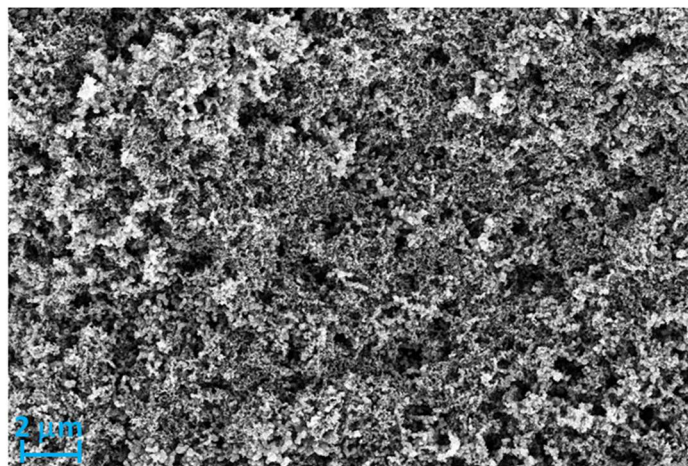


Figure 4.4: Top-view SEM image of the as-obtained super P-separator

Electrochemical tests were carried out at room temperature to evaluate the effect of the ZDZCO-separator on the cycling performance of Li-S batteries. Firstly, the electrochemical activity of ZDZCO between 1.8 and 2.6 V was studied through CV and charge-discharge cycling tests. As shown in **Fig. 4.5**, the ZDZCO is inactive and contributes negligible capacity between 1.8 and 2.6 V.

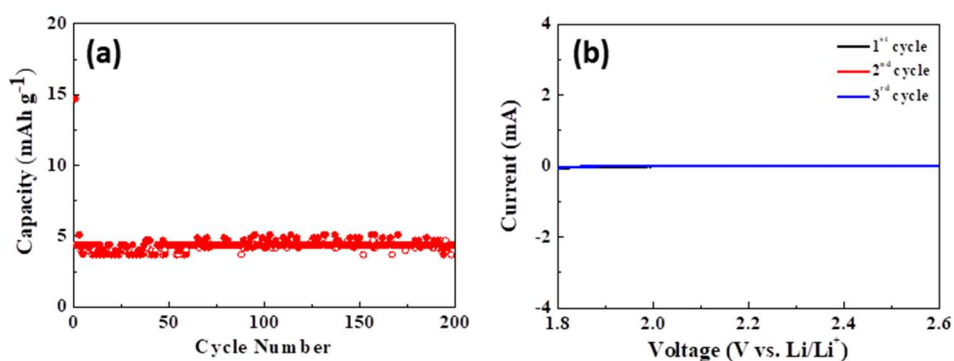


Figure 4.5: (a) The cycling performance and (b) the CV curves of ZDZCO electrode between 1.8 and 2.6 V.

The sulfur cathode was prepared with 80 wt% S/super P composite, 10 wt% Ketjen black (KB), and 10 wt% PVDF binder. It should be noted that in the sulfur cathode, there are no additional polysulfide hosts. **Fig. 4.6a** shows the typical charge-discharge behaviour of a Li-S battery, i.e., the formation of long-chain polysulfides (Li_2S_x , $4 \leq x \leq 8$) at 2.31 V and the conversion of Li_2S_x to $\text{Li}_2\text{S}_2/\text{Li}_2\text{S}$ at 2.03 V [58]. The charge-discharge curves (**Fig. 4.6b**) also display the typical two-platform discharge behaviour characteristic of the Li-S battery. The cycling

stability of the Li-S batteries with different separators at 0.5 C after an initial cycle at 0.2 C is compared in **Fig. 4.6c**. It indicates that the Li-S battery with ZDZCO-separator shows superior cycling stability with a high capacity of 857 mAh·g⁻¹ after 125 cycles, which is higher than that of Li-S battery with PP separator (547 mAh·g⁻¹), super P-separator (703 mAh·g⁻¹), and Co₃O₄-separator (771 mAh·g⁻¹).

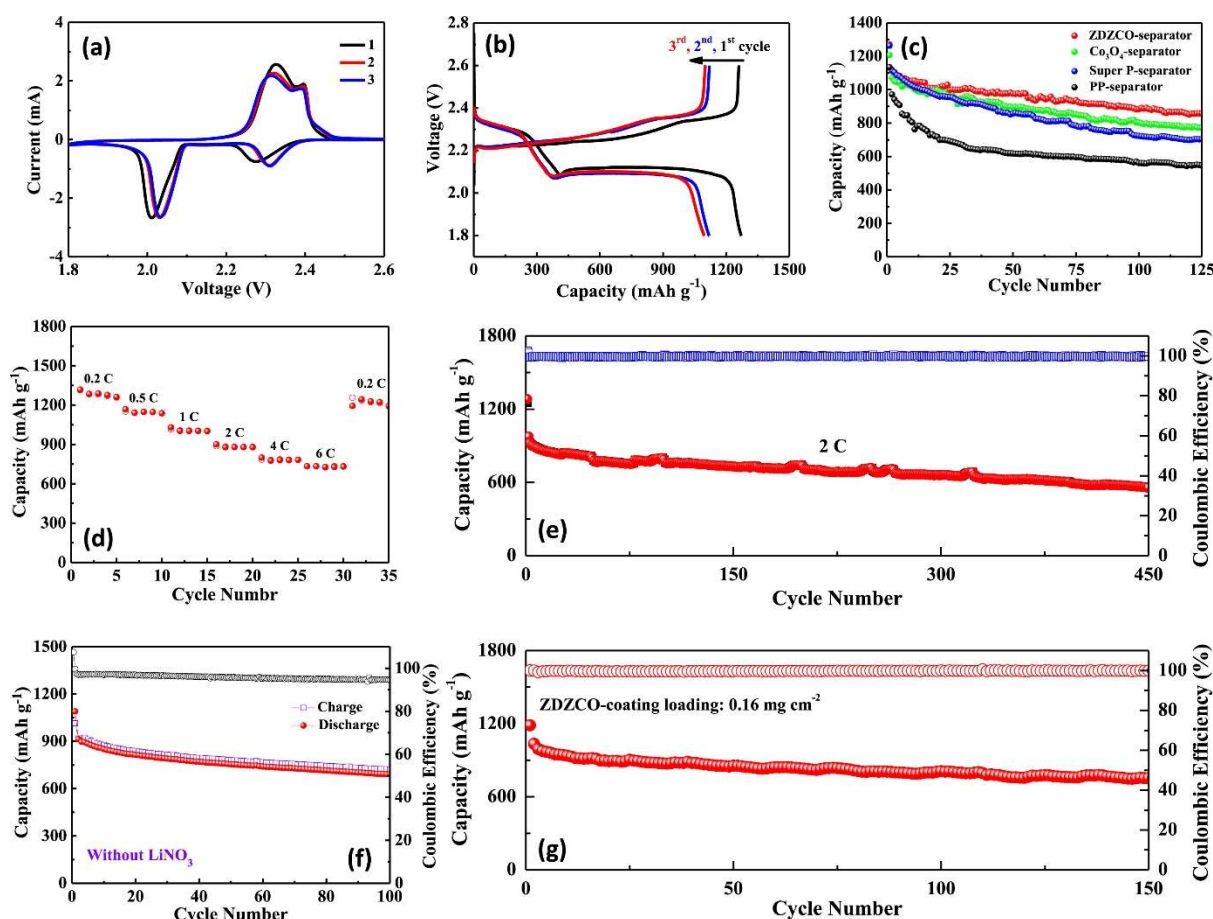


Figure 4.6: (a) CV curves and (b) charge-discharge curves of Li-S batteries with ZDZCO-separators; (c) comparison of cycling stability of Li-S batteries with different separators; (d) rate property and (e) long-term cycling performance at a high current density of 2 C of Li-S batteries with ZDZCO-separators; cycling performance of Li-S batteries with ZDZCO-separators (f) without LiNO₃ additive and (g) under a low ZDZCO-coating loading of 0.16 mg·cm⁻² with LiNO₃ additive

Moreover, the Li-S battery with the ZDZCO-separator also shows superior rate properties, delivering a high capacity of 731 mAh·g⁻¹ at 6.0 C, as shown in **Figs. 4.6d and 4.7**. The long-term cycling performance of the Li-S battery with the ZDZCO-separator at a high current density of 2.0 C is displayed in **Fig. 4.6e**. It shows that the Li-S battery can still deliver a capacity of 557 mAh·g⁻¹ after 450 cycles, indicating high long-term cycling stability.

Furthermore, the Li-S battery displays a high CE of 99.8 % after 450 cycles, suggesting suppressed shuttle effect. To further show the effectiveness of the ZDZCO-separator at suppressing the polysulfide shuttle, an electrolyte without the LiNO_3 additive is applied. A LiNO_3 additive promotes the formation of a stable passivation film on the Li anode, which can significantly suppress the polysulfide shuttle [59]; thus, by cycling a cell without the LiNO_3 additive, the role of the ZDZCO-separator is highlighted. As shown in **Fig. 4.6f**, the Li-S battery with the ZDZCO-separator can still give a stable and high capacity of $691 \text{ mAh}\cdot\text{g}^{-1}$ with a high CE of 95.8 % after 100 cycles even without the LiNO_3 additive. Even when the ZDZCO-coating loading is decreased to $0.16 \text{ mg}\cdot\text{cm}^{-2}$, the Li-S battery with the ZDZCO-separator shows high cycling stability with a capacity of $754 \text{ mAh}\cdot\text{g}^{-1}$ and CE of 99.9 % after 150 cycles (**Fig. 4.6g**). These excellent electrochemical performances have comprehensively demonstrated that the ZDZCO-separator possesses excellent application potential for high-performance Li-S batteries.

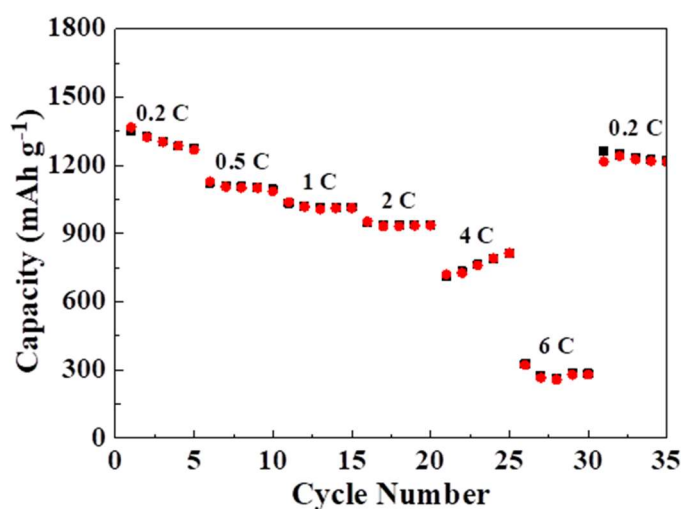


Figure 4.7: The rate properties of the Li-S battery with super-P separator.

A series of theoretical and experimental studies were carried out to deeply understand the reasoning behind the enhanced electrochemical performance of Li-S batteries with ZDZCO-separator. DFT calculations have proven themselves a powerful and widely applied way to study the binding energy (BE) of host materials with polysulfides, often to explain an enhanced electrochemical performance obtained experimentally. Herein, to analyse the anchoring capability of the functional material towards polysulfide molecules, we calculated the BE between polysulfide molecules and the (100) surface of Co_3O_4 , ZnCo_2O_4 , and $\text{Zn}_{0.875}\text{Co}_2\text{O}_4$. The most favourable atomic configurations of sulfur species (i.e., S_8 , Li_2S_8 , Li_2S_6 , Li_2S_4 , Li_2S_2 ,

and Li_2S) anchored on (100) surface of Co_3O_4 , ZnCo_2O_4 , and $\text{Zn}_{0.875}\text{Co}_2\text{O}_4$ and the calculated BEs are shown in **Fig. 4.8**.

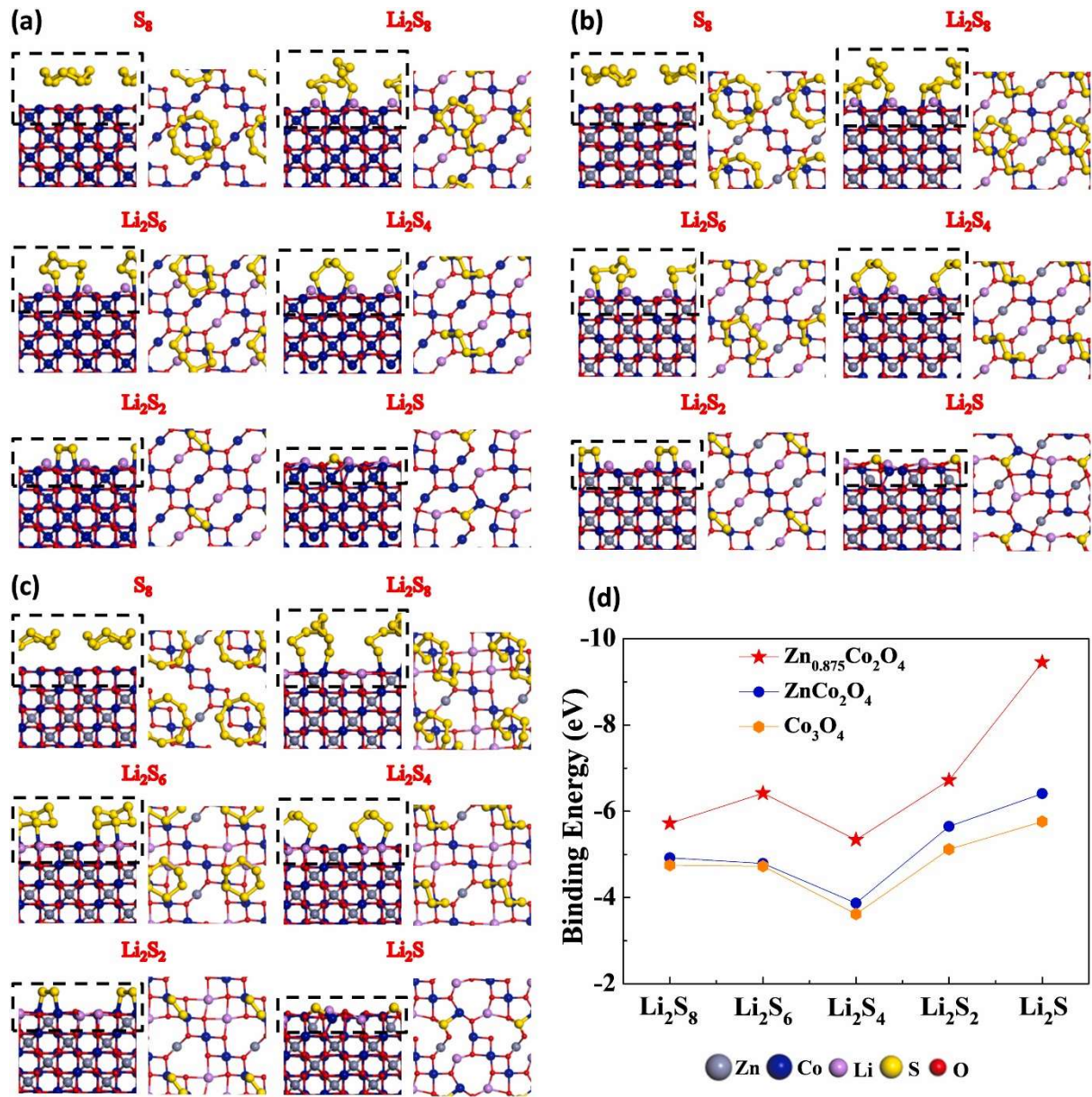


Figure 4.8: Atomic configurations for the sulfur species (i.e., S_8 , Li_2S_8 , Li_2S_6 , Li_2S_4 , Li_2S_2 , and Li_2S) adsorbed on the (100) surface of (a) Co_3O_4 , (b) ZnCo_2O_4 , and (c) $\text{Zn}_{0.875}\text{Co}_2\text{O}_4$; (d) the corresponding binding energies between the sulfur species and $\text{Co}_3\text{O}_4(100)$, $\text{ZnCo}_2\text{O}_4(100)$, and $\text{Zn}_{0.875}\text{Co}_2\text{O}_4(100)$

It is found that $\text{Zn}_{0.875}\text{Co}_2\text{O}_4$ offers the strongest BEs with Li_2S_x (-5.72, -6.42, -5.34, -6.72, and -9.45 eV for Li_2S_8 , Li_2S_6 , Li_2S_4 , Li_2S_2 , and Li_2S , respectively). Moreover, the BEs between ZnCo_2O_4 and Li_2S_x (-4.92, -4.79, -3.87, -5.65, and -6.41 eV for Li_2S_8 , Li_2S_6 , Li_2S_4 , Li_2S_2 , and Li_2S , respectively) are slightly more robust than those between Co_3O_4 and Li_2S_x (-4.75, -

4.73, - 3.62, - 5.12, and - 5.76 eV for Li_2S_8 , Li_2S_6 , Li_2S_4 , Li_2S_2 , and Li_2S , respectively). In our calculations, Van der Waals interactions were also considered to calculate the adsorption energy correctly. When the Li_2S_8 molecule is reduced to Li_2S_6 , the distance between the $\text{Zn}_{0.875}\text{Co}_2\text{O}_4$ surface and the respective polysulfide decreases, explaining the increased adsorption energy displayed between Li_2S_6 and $\text{Zn}_{0.875}\text{Co}_2\text{O}_4$, as shown in **Fig. 4.9**. In our calculations, Van der Waals interaction was also considered to correctly calculate the adsorption energy of Li_2S_x molecules on the surfaces of Co_3O_4 , ZnCo_2O_4 , and $\text{Zn}_{0.875}\text{Co}_2\text{O}_4$. As we know, the Van der Waals interaction is stronger when the distance between the molecule and the surface becomes reduces. The distances between the molecule and the surface of Co_3O_4 and ZnCo_2O_4 are increased when Li_2S_8 is reduced to Li_2S_6 , thus the corresponding Van der Waals interactions are decreased. However, the distance between Li_2S_6 molecule and $\text{Zn}_{0.875}\text{Co}_2\text{O}_4$ surface is smaller than the distance between Li_2S_8 molecule and $\text{Zn}_{0.875}\text{Co}_2\text{O}_4$ surface, so the Van der Waals interaction increases when Li_2S_8 is reduced to Li_2S_6 . Based on this, the adsorption energy of Li_2S_6 on the $\text{Zn}_{0.875}\text{Co}_2\text{O}_4$ surface may be increased compared to Li_2S_8 .

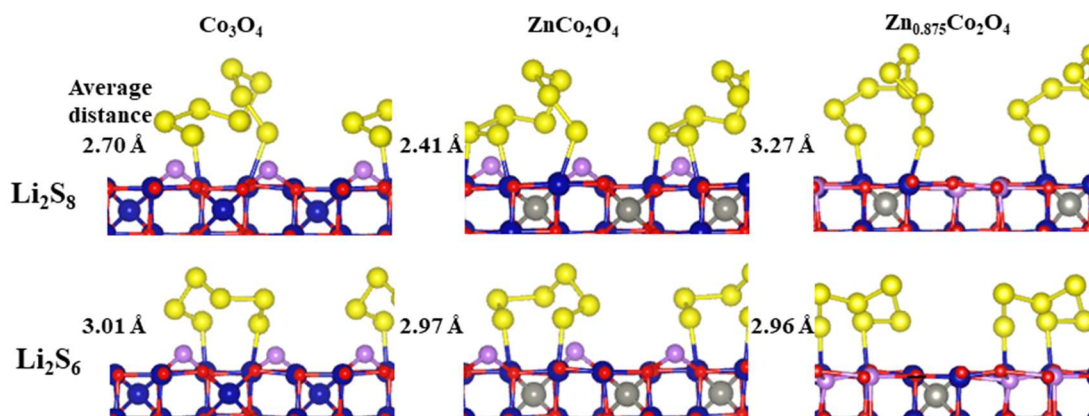


Figure 4.9: The side view of Li_2S_8 and Li_2S_6 molecules adsorbed on the (100) surfaces of Co_3O_4 , ZnCo_2O_4 , and $\text{Zn}_{0.875}\text{Co}_2\text{O}_4$ and the corresponding distances between the molecules and the surfaces (the atoms in plane perpendicular to the surface are excluded).

It is noteworthy that Li ions from Li_2S_x ($2 \leq x \leq 8$) prefer to bind to oxygen anions in the top layer of the surface. Simultaneously, polysulfide ions are bonded to two adjacent octahedral Co cations in the top layer of all three systems. Interestingly, a surface rearrangement arises when a Li_2S molecule adsorbs on all three systems' (100) surface. The Li_2S molecule inserts in the top layer of the surface structure and causes one Co atom to displace from the octahedral site. In this case, S^{2-} binds to two oxygen anions and one Co cation in the top layer, resulting

in a much stronger BE between Li_2S and the surfaces than other sulfur species. The significantly enhanced BEs between Li_2S_x and $\text{Zn}_{0.875}\text{Co}_2\text{O}_4$ is due to Li ions' insertion into the subsurface layers of the $\text{Zn}_{0.875}\text{Co}_2\text{O}_4$ surface. The Zn vacancy in the subsurface layer provides enough space for a Li-ion to penetrate the surface and bind more strongly to oxygen anions in the top layer. These DFT results suggest that constructing cation vacancies is an efficient and promising way to design strong-affinity anchoring functional materials for Li-S batteries.

Polysulfide adsorption tests were performed to indicate the strong affinity of ZDZCO towards polysulfides experimentally. Initially, the Li_2S_6 solution is deep yellow (inset in **Fig. 4.10a**); however, after adding ZDZCO nanosheets and standing for about 48 h, the solution becomes almost colourless, suggesting that most of the polysulfides are adsorbed on the ZDZCO surfaces. Conversely, the solutions with Co_3O_4 and super P still retain their yellow colour, suggesting that a large amount of free Li_2S_6 still exists. The UV-Vis absorption spectra in **Fig. 4.10a** quantitatively compare the Li_2S_6 remnant in the solutions after the adsorption tests. It shows that the ZDZCO has the strongest affinity towards polysulfides, as the remnant Li_2S_6 in the solution with ZDZCO is the lowest.

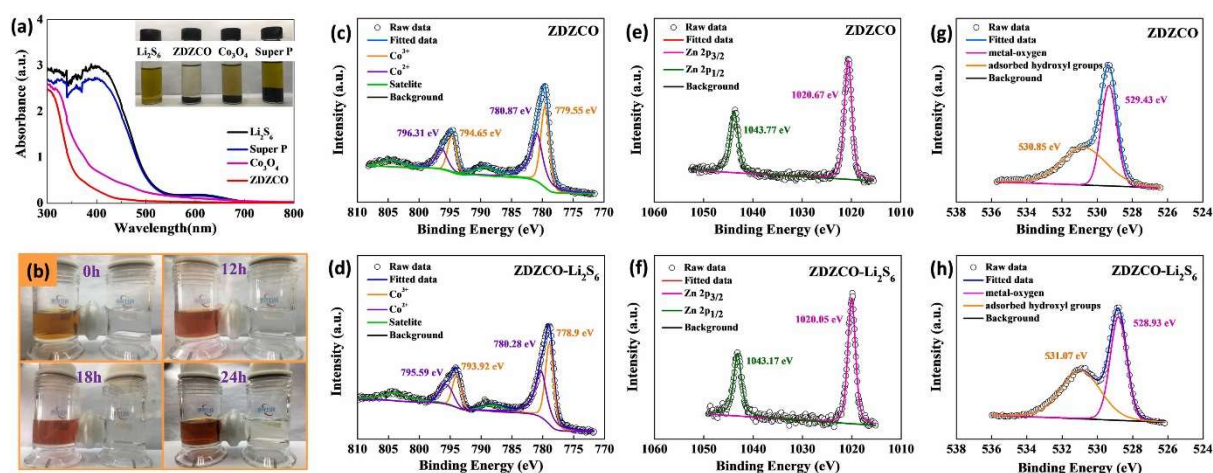


Figure 4.10: (a) UV-Vis spectra of the Li_2S_6 solution after polysulfide adsorption tests (inset is the photo of the Li_2S_6 solutions after polysulfide adsorption tests); (b) the photos of the polysulfide diffusion experiment using ZDZCO-separator; high-resolution XPS spectra of (c) Co 2p, (e) Zn 2p, and (g) O 1s for ZDZCO, and (d) Co 2p, (f) Zn 2p, and (h) O 1s for ZDZCO adsorbing Li_2S_6 , respectively

H-shaped glass cells are set up to show the polysulfide blocking capability of the ZDZCO-separator (**Figs. 4.10b and 4.11**). Half of the glass cell (left) was filled with 50 mL of 4 mM Li_2S_6 solution and the other half (right) was filled with 50 mL of tetrahydrofuran (THF), and

separated by a PP separator, super P-separator, Co_3O_4 -separator, and ZDZCO-separator, respectively. In **Fig. 4.11**, one can observe that the right chambers change to yellow after several hours, suggesting Li_2S_6 can diffuse across the PP separator, super P-separator, and Co_3O_4 -separator. Conversely, in the ZDZCO-separator cell, the polysulfides are contained in the left chamber, while the right chamber remains colourless (**Figs. 4.10b and 4.11**) owing to the strong polysulfide restriction ability of the ZDZCO. Consequently, the Li anode can retain a smooth morphology with almost no Li_2S deposition when the ZDZCO-separator is applied (**Fig. 4.12**) [39, 60].

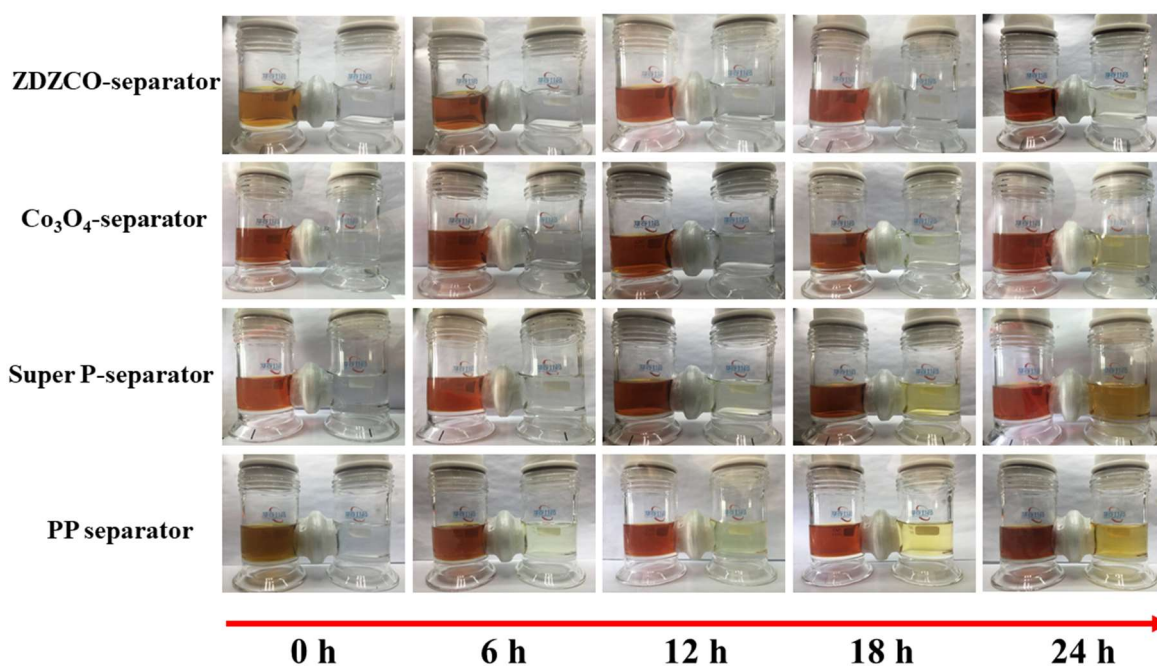


Figure 4.11: Polysulfide diffusion experiments using ZDZCO-separator, Co_3O_4 -separator, super P-separator, and PP separator

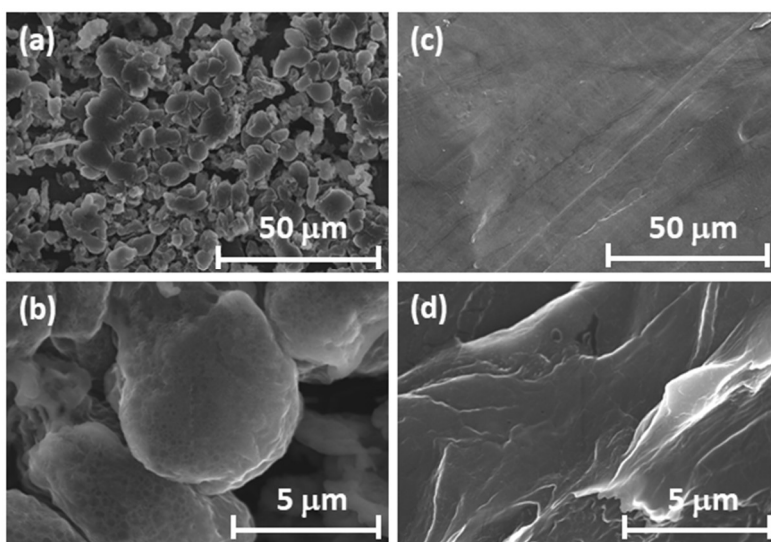


Figure 4.12: SEM images of Li anodes after 20 cycles (a, b) with PP separator and (c, d) with ZDZCO-separator

In order to further understand the chemical adsorption interaction between the ZDZCO and polysulfides, XPS spectra of the ZDZCO before and after adsorbing polysulfides (Li_2S_6) are compared. For the pristine ZDZCO, the high-resolution Co 2p spectrum in **Fig. 4.10c** displays peaks at the binding energies of 780.87 and 796.31 eV, which are associated with Co 2p_{3/2} and Co 2p_{1/2} of Co^{2+} , and peaks at 779.55 and 794.65 eV, which are associated to the Co 2p_{3/2} and Co 2p_{1/2} from Co^{3+} , suggesting the coexistence of Co(II) and Co(III) [61-63]. In the high-resolution Zn 2p spectrum (**Fig. 4.10e**), two peaks are located at binding energies of 1020.67 and 1043.77 eV, attributed to Zn 2p_{3/2} and Zn 2p_{1/2}, indicating the Zn(II) oxidation state. The O 1s XPS spectrum in **Fig. 4.10g** shows a peak at 529.43 eV that can be assigned to metal-oxygen bonding in ZDZCO, with the peak at 530.85 eV attributed to the oxygen of surface adsorbed hydroxyl groups [63]. After adsorbing Li_2S_6 , **Fig. 4.10d and f** display that, overall, the significant peaks corresponding to Co 2p and Zn 2p shift to lower binding energies, ascribed to the electron transfer from polysulfides to the metal atoms, indicating that a robust chemical interaction occurs [64, 65]. Similarly, the peak for metal-oxygen bonding in the O 1s spectrum (**Fig. 4.10h**) shifts to lower binding energy after interacting with Li_2S_6 , due to the strong chemisorption between the ZDZCO and Li_2S_6 . The above results comprehensively justify that the first mechanism by which the ZDZCO-separator improves the cycling performance of Li-S batteries is through its robust polysulfide affinity.

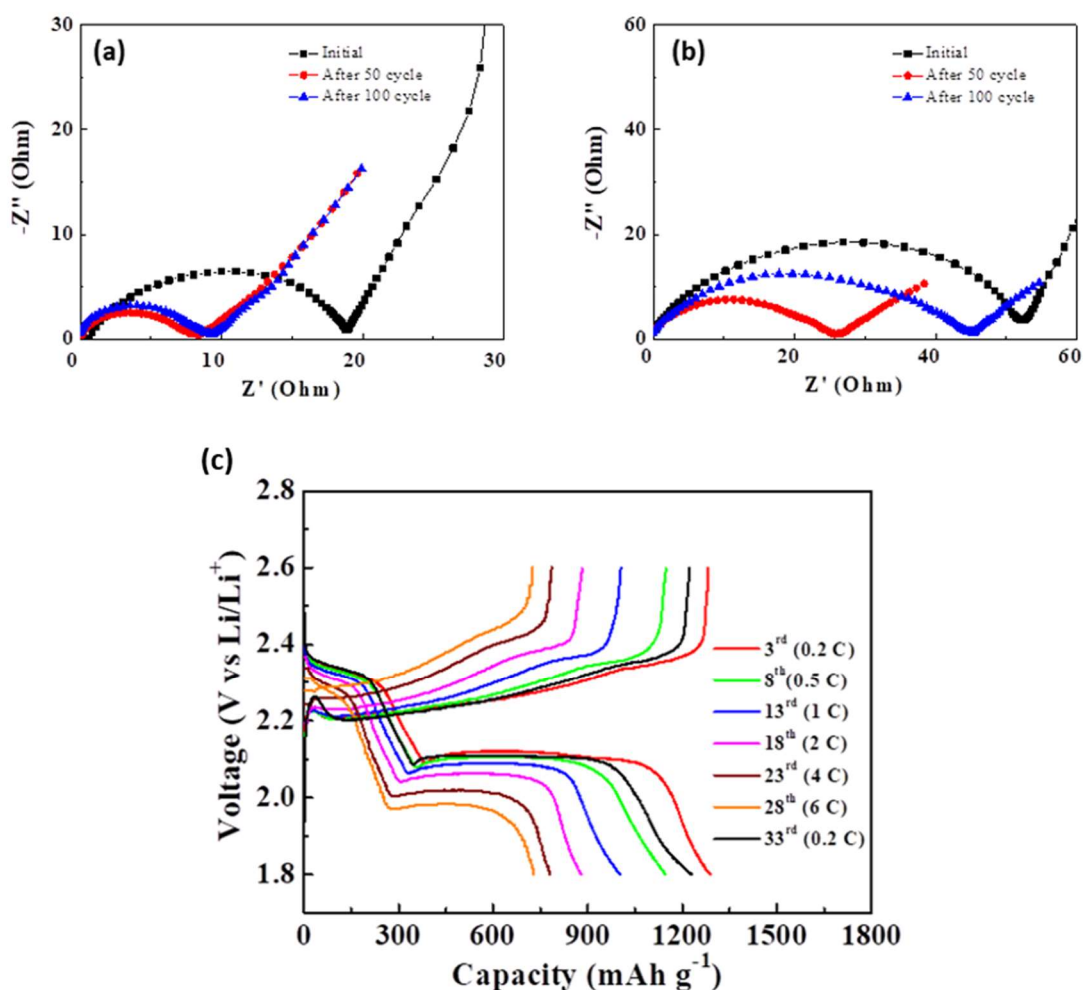


Figure 4.13: EIS tests of the Li-S batteries during cycling (a) with ZDZCO-separator and (b) with PP separator. (c) Charge-discharge curves of the Li-S battery with the ZDZCO-separator at different current densities

The second mechanism by which the ZDZCO-separator improves the performance is suspected to be through a catalytic effect for the continual conversion of polysulfides. The first evidence is the high discharge capacity at 6 C, as shown in **Fig. 4.6d**. To further expand on this, the charge-discharge profiles under various C-rates are displayed in **Fig. 4.13c**. Even at a high current density of 6 C, the Li-S battery with the ZDZCO-separator still shows two well-defined discharge plateaus, suggesting fast reaction kinetics. **Fig. 4.13a and b** show that a much smaller charge-transfer resistance for the Li-S battery with the ZDZCO-separator is obtained after cycling, indicating fast redox kinetics. To understand the reason for the improved reaction kinetics, the free energies involved in each sulfur reduction pathway on the surface of Co_3O_4 and $\text{Zn}_{0.875}\text{Co}_2\text{O}_4$, respectively, were calculated. As shown in **Fig. 4.14a**, the Gibbs free

energies for reducing S_8 to Li_2S_8 , Li_2S_8 to Li_2S_6 , and Li_2S_4 to Li_2S_2 on the surface of both Co_3O_4 and $Zn_{0.875}Co_2O_4$ are negative, signifying the fast kinetics. On both substrates, the step to form Li_2S_4 is endothermic, suggestive of the sluggish reaction kinetics. Fortunately, the Gibbs free energy is reduced from 0.4947 eV on the Co_3O_4 substrate to only 0.3593 eV on $Zn_{0.875}Co_2O_4$, indicating the superior catalytic ability of the $Zn_{0.875}Co_2O_4$. Notably, on the Co_3O_4 substrate, the reduction of Li_2S_2 to Li_2S is nearly thermoneutral, while on the $Zn_{0.875}Co_2O_4$ this step is exothermic with a significantly negative Gibbs free energy. CV measurements using symmetric cells with a Li_2S_6 electrolyte were conducted to study the polysulfide redox reactions' kinetics experimentally. Firstly, the negligible current density for the CV curve using ZDZCO-based electrode without Li_2S_6 in the electrolyte suggests that the ZDZCO is inactive between -1.0 and 1.0 V. As shown in **Fig. 4.14b**, the cell using ZDZCO-based electrode exhibits the highest current density, highlighting the significantly enhanced redox kinetics and facile polysulfide conversion on the ZDZCO surface [66, 67]. Theoretically, three-quarters of the capacity of a Li-S battery stems from the conversion of the Li_2S_4 intermediate to Li_2S . Therefore, it is essential to evaluate the catalytic capability of host materials in facilitating Li_2S electrodeposition [68]. **Fig. 4.14c and d** show the potentiostatic discharge curves at 2.05 V for the Li_2S precipitation experiments on the ZDZCO and Co_3O_4 samples, respectively, which follow the galvanostatic discharge at 0.226 mA to 2.06 V. As shown, the contributions of polysulfide (Li_2S_8/Li_2S_6) reduction and Li_2S precipitation are mathematically modelled and distinguished. The ZDZCO sample possesses a higher activity towards Li_2S precipitation with a higher peak current density (0.641 vs 0.469 mA). Also, the peak current for the Li_2S precipitation occurs much earlier for the ZDZCO sample (2600 s vs 3600 s), suggesting a higher Li_2S electrodeposition effective rate constant combining nucleation and growth rate constant [68, 69]. Calculated from the integral of the current, the capacity of Li_2S precipitation on the ZDZCO sample ($496.5 \text{ mAh}\cdot\text{g}^{-1}$) is also higher than that on the Co_3O_4 sample ($431.8 \text{ mAh}\cdot\text{g}^{-1}$), based on the weight of the sulfur in the catholyte.

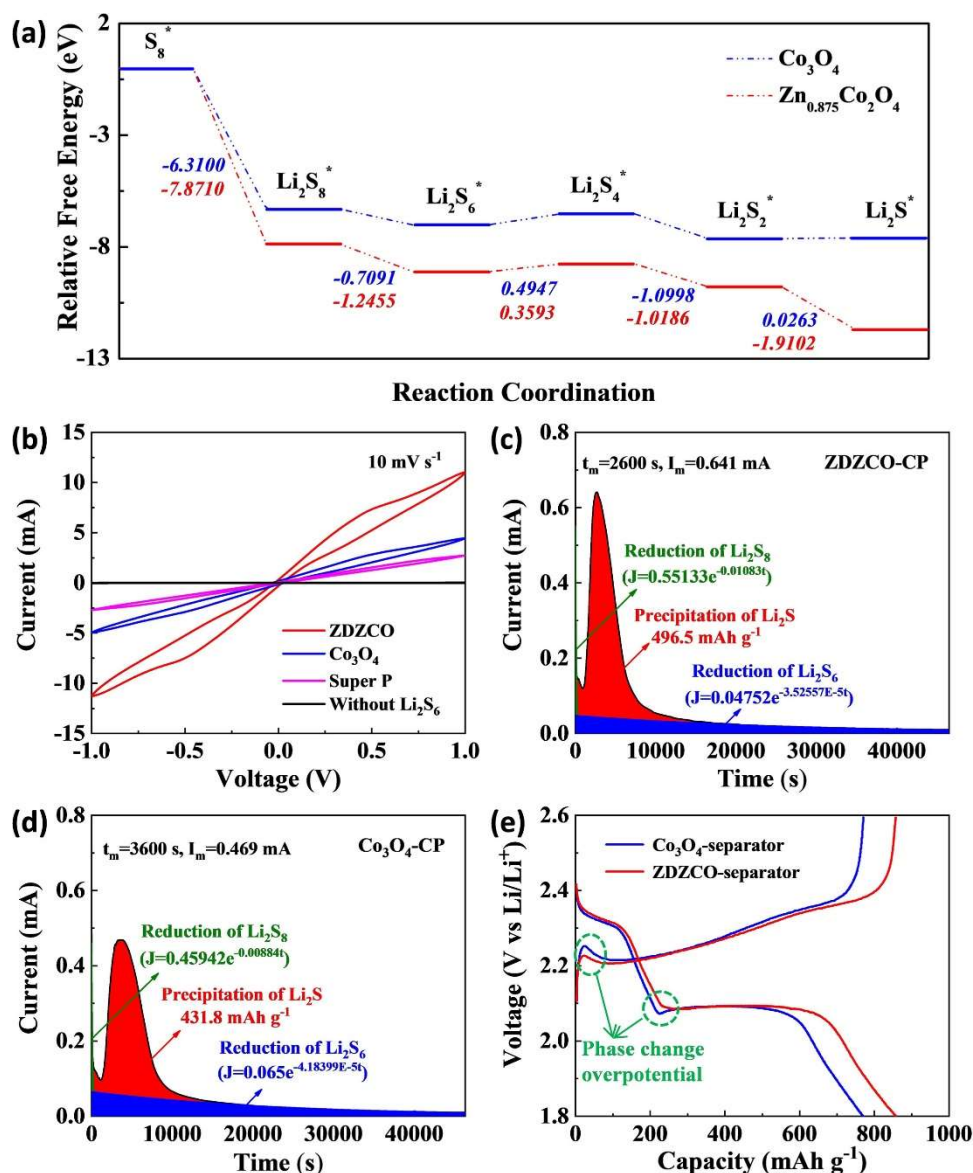


Figure 4.14: Catalytic effects of ZDZCO on polysulfide conversion: (a) The free energy diagrams for discharge process on the Co_3O_4 and $\text{Zn}_{0.875}\text{Co}_2\text{O}_4$ substrates, respectively; (b) CV curves of symmetric cells with ZDZCO, Co_3O_4 , and super P electrodes; potentiostatic discharge curves of Li_2S precipitation experiments of (c) ZDZCO and (d) Co_3O_4 samples; (e) charge-discharge curves at the 125th cycle of the Li-S batteries with ZDZCO-separator and Co_3O_4 -separator

Owing to the strong affinity and high catalytic effect, ZDZCO can induce a large amount of Li_2S to electrodeposit uniformly on the surface, as shown in **Fig. 4.15a**. **Fig. 4.15** also clearly shows that Li-O bonds and S-O bonds form, indicating a strong chemisorption effect between Li_2S and ZDZCO, which agrees with the theoretical calculation. As shown in the XPS survey (**Fig. 4.15b**), one can observe the presence of Li and S elements on the electrode. From the

high-resolution XPS spectra of Li 1s, the peak with the binding energy of 55.85 eV can be assigned to the Li–S bonds, and for the high-resolution XPS spectra of S 2p, the peaks at 162.42 and 163.64 eV can be attributed to the S 2p_{3/2} and S 2p_{1/2} contributions of the S–Li interactions in Li₂S. Moreover, owing to the strong chemisorption between Li₂S and ZDZCO, the peak at 56.55 eV can be assigned to Li–O interactions and the peak at 166.25 and 167.50 eV can be attributed to the S 2p_{3/2} and S 2p_{1/2} contributions of S–O bonds [70, 71]. These results have powerfully demonstrated that ZDZCO can significantly accelerate the polysulfide conversation. Consequently, the adsorbed polysulfides on ZDZCO can be rapidly converted and consumed, making the ZDZCO anchoring functional material work enduringly during prolonged cycling. The lower overpotential can indicate this during the phase change between the soluble polysulfides and insoluble Li₂S₂/Li₂S in the charge and discharge processes at the 125th cycle for Li–S battery with the ZDZCO-separator (**Fig. 4.14e**).

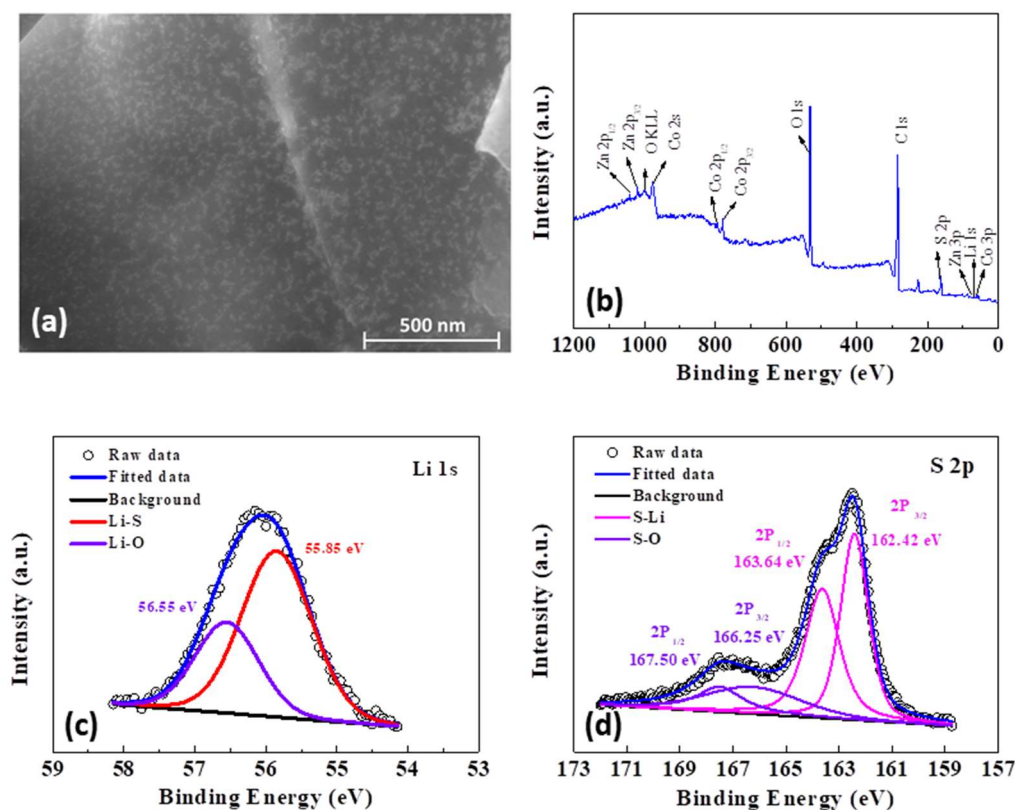


Figure 4.15: (a) SEM image of the ZDZCO nanosheet after Li₂S nucleation experiment, (b) XPS survey spectrum, high-resolution XPS spectra of (c) Li 1s, and (d) S 2p for the electrode after electrodeposition of Li₂S. Before the XPS test, the electrode was washed using DME to remove the soluble polysulfides

High-loading sulfur electrodes are of great importance to deliver high areal capacity [72, 73]. Herein, by simply using the as-prepared ZDZCO-separator, high-loading Li-S batteries were successfully achieved using the traditional blade coating technique. It should be mentioned that when the sulfur loading increases, the weight and thickness of the ZDZCO polysulfide-blocking layer are unaltered. As shown in **Fig. 4.16a**, when the sulfur loading increases to $5.59 \text{ mg} \cdot \text{cm}^{-2}$, the as-obtained high-loading Li-S battery still shows the typical electrochemical behaviour of Li-S systems. **Fig. 4.16b** displays that the high-loading Li-S battery can deliver an initial areal capacity of $6.47 \text{ mAh} \cdot \text{cm}^{-2}$ at $0.3 \text{ mA} \cdot \text{cm}^{-2}$, which remains at $3.52 \text{ mAh} \cdot \text{cm}^{-2}$ after 120 cycles at $1.2 \text{ mA} \cdot \text{cm}^{-2}$. It also should be noted that the high-loading battery possesses high CE (97.1 % on average) during cycling, suggesting the suppressed shuttle effect.

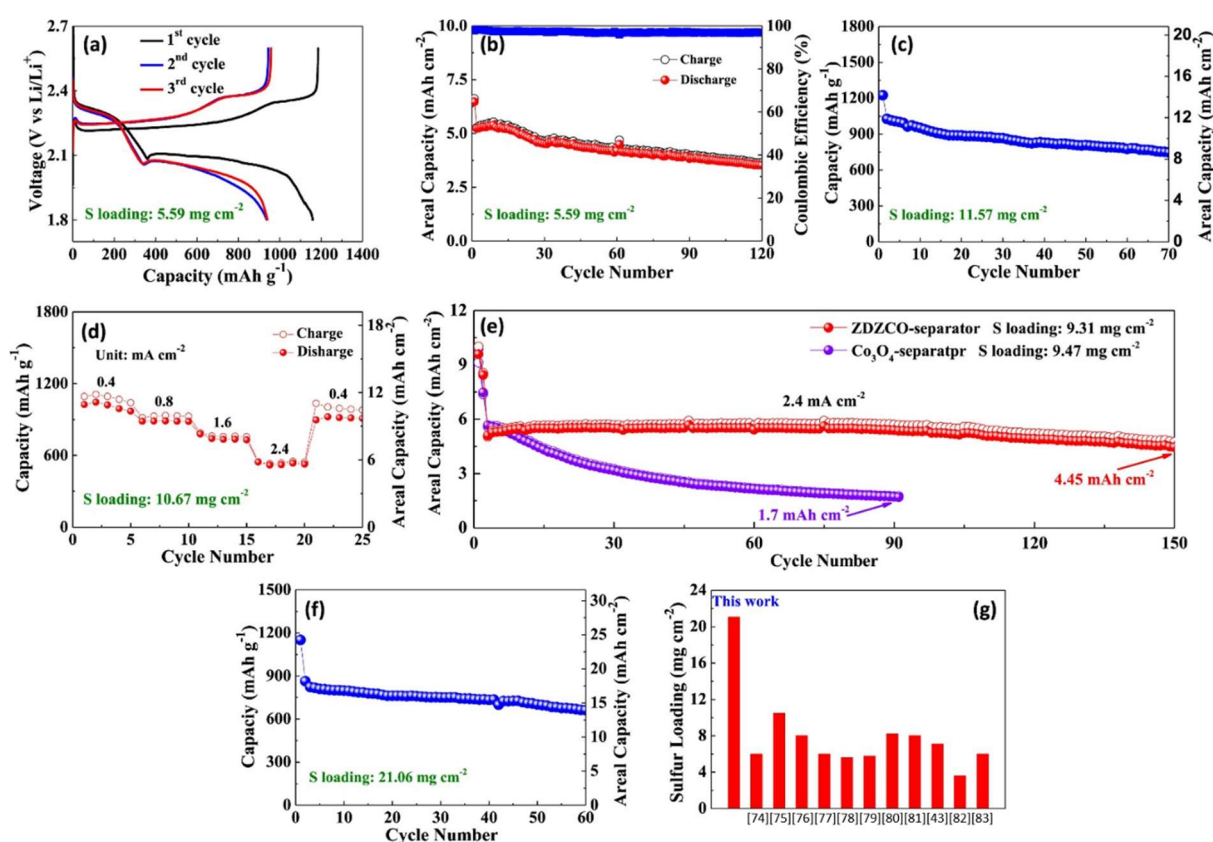


Figure 4.16: High loading Li-S batteries with ZDZCO-separator: (a) charge-discharge curves and (b) cycling performance with sulfur loading of $5.59 \text{ mg} \cdot \text{cm}^{-2}$; (c) cycling performance with sulfur loading of $11.57 \text{ mg} \cdot \text{cm}^{-2}$; (d) rate property with sulfur loading of $10.67 \text{ mg} \cdot \text{cm}^{-2}$; (e) long-term cycling performance at $2.4 \text{ mA} \cdot \text{cm}^{-2}$ with sulfur loading of $9.31 \text{ mg} \cdot \text{cm}^{-2}$; (f) cycling performance with sulfur loading of $21.06 \text{ mg} \cdot \text{cm}^{-2}$; (g) comparison of the sulfur loading with recently excellent separator-related literature [43, 74-83]

The sulfur loading is increased further to exceed the state-of-the-art Li-ion batteries. **Fig. 4.16c** shows that the Li-S battery with the loading of $11.57 \text{ mg} \cdot \text{cm}^{-2}$ can give a capacity of $749 \text{ mAh} \cdot \text{g}^{-1}$, corresponding to an areal capacity of $8.66 \text{ mAh} \cdot \text{cm}^{-2}$ after 70 cycles. **Figs. 4.16d and 4.17** indicate that the high-loading Li-S battery also shows excellent rate performance with a high capacity of $522 \text{ mAh} \cdot \text{g}^{-1}$, corresponding to $5.56 \text{ mAh} \cdot \text{cm}^{-2}$ at $2.4 \text{ mA} \cdot \text{cm}^{-2}$.

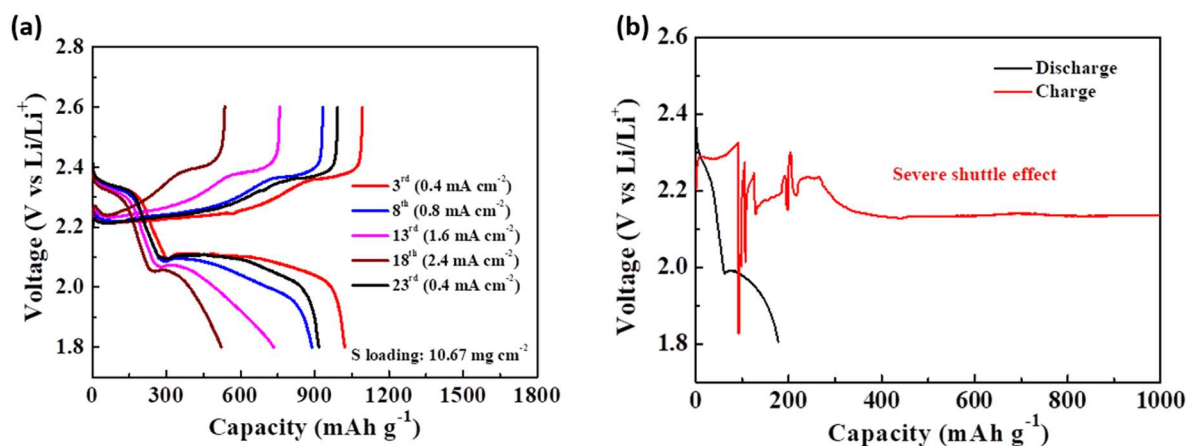


Figure 4.17: (a) Charge-discharge curves of high-loading Li-S battery at different current densities. (b) The charge-discharge curves of the Li-S battery with Co_3O_4 -separator under a sulfur loading of 9.47 mg cm^{-2} for the 92nd cycle

The long-term cycling test is also performed at a high current density of $2.4 \text{ mA} \cdot \text{cm}^{-2}$. It shows that the high-loading Li-S battery can stably cycle over 150 cycles with an areal capacity of $4.45 \text{ mAh} \cdot \text{cm}^{-2}$ (**Fig. 4.16e**). However, the Li-S battery with the Co_3O_4 -separator shows fast capacity fading with a low areal capacity of $1.7 \text{ mAh} \cdot \text{cm}^{-2}$ after only 91 cycles. Furthermore, as displayed in **Fig. 4.17b**, the Li-S battery with the Co_3O_4 -separator suffers severely from the shuttle effect due to the insufficient binding and catalytic ability of Co_3O_4 . In this study, Li-S batteries with a sulfur loading as high as $21.06 \text{ mg} \cdot \text{cm}^{-2}$ can be successfully achieved under a low E/S ratio of $\sim 12 \mu\text{L} \cdot \text{mg}^{-1}$, which delivers an initial capacity of $1152 \text{ mAh} \cdot \text{g}^{-1}$, corresponding to $24.25 \text{ mAh} \cdot \text{cm}^{-2}$, and maintains a capacity of $663 \text{ mAh} \cdot \text{g}^{-1}$, corresponding to $13.95 \text{ mAh} \cdot \text{cm}^{-2}$ after 60 cycles (**Fig. 4.16f**).

Table 4.1: Comparison of the sulfur loading in the recently published best-performing separator-related literature.

Ref. ^a	Separator	Sulfur Loading
This work	ZDZCO-separator	21.06 mg·cm⁻²
[74]	Ce-MOF-2/CNT-separator	6.0 mg·cm ⁻²
[75]	Cobalt-embedded N-doped porous carbon nanosheets and graphene-separator	10.5 mg·cm ⁻²
[76]	Ni ₃ (HITP) ₂ -separator	8.0 mg·cm ⁻²
[77]	NiCo ₂ O ₄ @rGO-separator	6.0 mg·cm ⁻²
[78]	Co ₉ S ₈ -separator	5.6 mg·cm ⁻²
[79]	Co/mSiO ₂ -NCNTs spider-web-like nanocomposite-separator	5.76 mg·cm ⁻²
[80]	Polymeric zwitterion -separator	8.2 mg·cm ⁻²
[81]	Graphene-supported Ni nanoparticles with a carbon coating-glass fiber membrane	8.0 mg·cm ⁻²
[43]	TiO ₂ nanosheets with oxygen vacancies-separator	7.1 mg·cm ⁻²
[82]	Atomic cobalt within mesoporous carbon-separator	3.6 mg·cm ⁻²
[83]	Single Ni atoms on N-doped graphene-separator	6.0 mg·cm ⁻²

Fig. 4.16g and Table 4.1 display that we successfully obtained an ultra-high sulfur loading compared with previous literature relating to Li-S separators. **Table 4.2** indicates that our Li-S batteries can be operated under a comparable current density with a significantly extended cycling lifespan compared with recently published literature using traditional electrode preparation techniques. To the best of our knowledge, such a cycling lifespan (over 210 days) of a Li-S battery with ultrahigh loading has rarely been reported.

Table 4.2: Comparison of the sulfur loading, operation current density, and cycling lifespan of this work with some recently published excellent literature using traditional electrode preparation technique.

Ref.	Approach	Sulfur		
		Loading (mg·cm ⁻²)	Current Density	Cycle Number
This work	ZDZCO-separator	9.31	2.4 mA·cm⁻² (~0.15 C)	150
[84]	Co ₉ S ₈ @MoS ₂ /CNF-interlayer	10.0	0.1 C	50
[85]	NiCo ₂ S ₄ host	8.9	0.1 C	70
[86]	Multifunctional zipper-like sulfur electrode	7.6	100 mA·g ⁻¹ (~0.06 C)	60
[80]	Polymeric zwitterion@PP separator	8.2	0.1 C	50
[87]	N doped CoSe ₂ host	10.2	0.2 C	70
[88]	All-fibrous cathode/separator based Li-S battery	9.28	0.2 C	100
[89]	CNF-gum arabic interlayer	12.0	0.1 C	30
[90]	VS ₄ @RGO host	10.0	0.2 C	100
[91]	Bi ₂ Te _{2.7} Se _{0.3} /PP separator	7.0	0.1 C	45
This work	ZDZCO-separator	21.06	0.4 mA·cm⁻² 0.05 C	60
[92]	VO ₂ -VN host	13.2	(1.1 mA·cm ⁻²)	20

Ref.	Approach	Sulfur		
		Loading (mg·cm ⁻²)	Current Density	Cycle Number
[93]	A comprehensive approach coupling			
	hierarchically structured sulfur composite with cross-linked binder	14.9	1.0 mA·cm ⁻²	10
[33]	N-GG-XG binder	19.8	0.8 mA·cm ⁻²	6

However, as shown in **Fig. 4.18a and b**, large cracks occur in the thick sulfur electrode due to the poor mechanical properties of the PVDF binder. We believe that in future studies, through combining binders, unique electrode configurations, high-performance anodes and electrolytes [33, 73-76], our high-loading Li-S battery using ZDZCO-separator possesses significant practical application potential. To visually demonstrate the high energy density of the as-prepared high-loading Li-S cells, we used a Li-S cell to power 12 LED lights. As displayed in **Fig. 4.18c**, after 2 h the LED lights are still sparkling, suggesting high energy density. Therefore, owing to the cation vacancies, the ZDZCO-separator can effectively anchor polysulfides and accelerate the redox kinetics, which significantly suppresses the shuttle effect and improves the electrochemical performance of high-loading Li-S battery for practical applications.

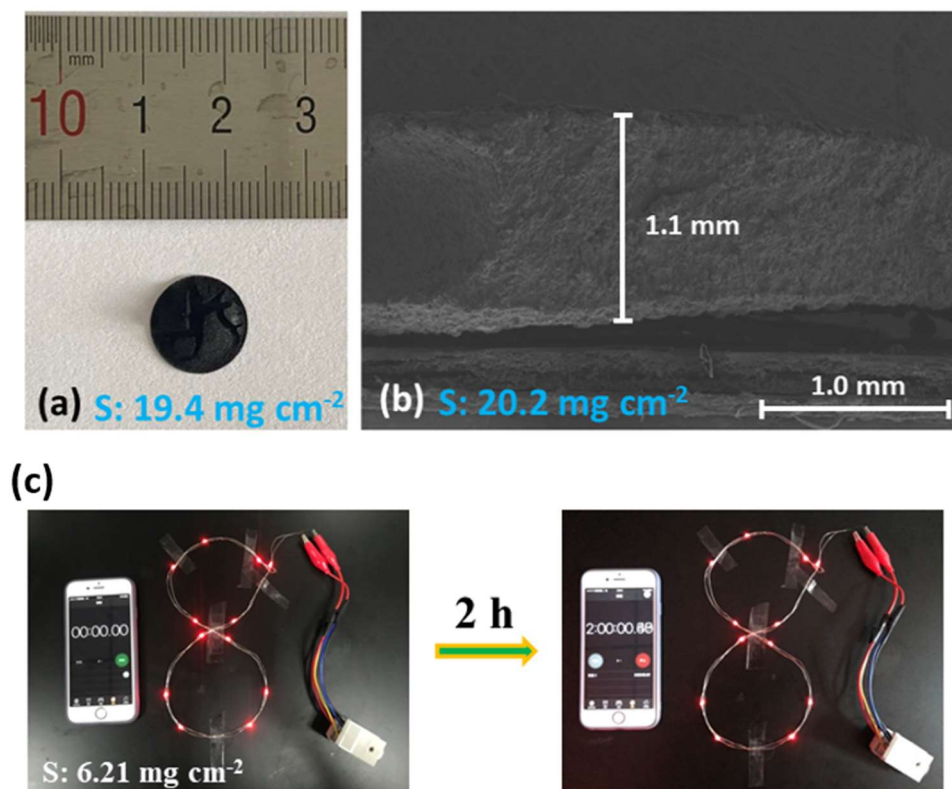


Figure 4.18: (a) Photo and (b) cross-section SEM image of ultrahigh-loading sulfur electrodes. (c) Photos of a Li-S cell with high loading of 6.21 mg·cm⁻², showing high energy density to power 12 LED lights for 2 h

4.5 Conclusion

A bimetallic oxide with abundant cation vacancies has been prepared and applied to construct a multifunctional polysulfide-blocking layer on a separator for high-performance Li-S batteries. The cation vacancies can effectively boost the anchoring and catalytic effects of the multifunctional polysulfide-blocking layer, which have been powerfully proven via theoretical and experimental studies. As a result, the multifunctional polysulfide-blocking layer on the separator can function as an upper current collector, polysulfide anchor, and catalytic reactor to significantly suppress the shuttle effect. Therefore, high-loading Li-S batteries can be successfully achieved by using the multifunctional polysulfide-blocking layer modified separator. Most notably, a Li-S battery with an ultrahigh loading of 21.06 mg·cm⁻² can be achieved, which can stably cycle over 60 cycles with a high areal capacity of 13.95 mAh·cm⁻². This study offers an effective and promising strategy to construct high-energy-density Li-S batteries with high loading.

4.6 References

1. Jiang, M., et al., *Polymer electrolytes for Li–S batteries: Polymeric fundamentals and performance optimization*. Journal of Energy Chemistry, 2021. **58**: p. 300-317.
2. Li, Z., et al., *Cationic-Polymer-Functionalized Separator As a High-Efficiency Polysulfide Shuttle Barrier for Long-Life Li–S Battery*. ACS Applied Energy Materials, 2021. **4**(3): p. 2914-2921.
3. Du, H., et al., *Stable cycling of lithium-sulfur battery enabled by a reliable gel polymer electrolyte rich in ester groups*. Journal of Membrane Science, 2018. **550**: p. 399-406.
4. Liu, J., et al., *A robust network binder with dual functions of Cu²⁺ ions as ionic crosslinking and chemical binding agents for highly stable Li–S batteries*. Journal of Materials Chemistry A, 2018. **6**(17): p. 7382-7388.
5. Hu, G., et al., *3D Graphene-Foam–Reduced-Graphene-Oxide Hybrid Nested Hierarchical Networks for High-Performance Li–S Batteries*. Advanced Materials, 2016. **28**(8): p. 1603-1609.
6. Qu, H., et al., *Inorganic separators enable significantly suppressed polysulfide shuttling in high-performance lithium–sulfur batteries*. Journal of Materials Chemistry A, 2018. **6**(46): p. 23720-23729.
7. Hou, T.-Z., et al., *Lithium Bond Chemistry in Lithium–Sulfur Batteries*. Angewandte Chemie International Edition, 2017. **56**(28): p. 8178-8182.
8. Zhang, S.S. and J.A. Read, *A new direction for the performance improvement of rechargeable lithium/sulfur batteries*. Journal of Power Sources, 2012. **200**: p. 77-82.
9. Liang, J., et al., *Carbon materials for Li–S batteries: Functional evolution and performance improvement*. Energy Storage Materials, 2016. **2**: p. 76-106.
10. Du, H., et al., *A Delicately Designed Sulfide Graphdiyne Compatible Cathode for High-Performance Lithium/Magnesium–Sulfur Batteries*. Small, 2017. **13**(44): p. 1702277.
11. Ma, L., et al., *Enhanced Li–S Batteries Using Amine-Functionalized Carbon Nanotubes in the Cathode*. ACS Nano, 2016. **10**(1): p. 1050-1059.

12. Park, K., et al., *Trapping lithium polysulfides of a Li–S battery by forming lithium bonds in a polymer matrix*. Energy & Environmental Science, 2015. **8**(8): p. 2389-2395.
13. Chen, W., et al., *A new type of multifunctional polar binder: toward practical application of high energy lithium sulfur batteries*. Advanced Materials, 2017. **29**(12): p. 1605160.
14. Liu, J., et al., *Multifunctional Cellulose Nanocrystals as a High-Efficient Polysulfide Stopper for Practical Li–S Batteries*. ACS Applied Materials & Interfaces, 2020. **12**(15): p. 17592-17601.
15. Yang, H., et al., *Dense and high loading sulfurized pyrolyzed poly (acrylonitrile)(S@pPAN) cathode for rechargeable lithium batteries*. Energy Storage Materials, 2020. **31**: p. 187-194.
16. Tian, Y., et al., *Low-Bandgap Se-Deficient Antimony Selenide as a Multifunctional Polysulfide Barrier toward High-Performance Lithium–Sulfur Batteries*. Advanced Materials, 2020. **32**(4): p. 1904876.
17. Liang, X. and L.F. Nazar, *In Situ Reactive Assembly of Scalable Core–Shell Sulfur–MnO₂ Composite Cathodes*. ACS Nano, 2016. **10**(4): p. 4192-4198.
18. Xi, K., et al., *Enhanced Sulfur Transformation by Multifunctional FeS₂/FeS/S Composites for High-Volumetric Capacity Cathodes in Lithium–Sulfur Batteries*. Advanced Science, 2019. **6**(6): p. 1800815.
19. Sun, Q., et al., *Nitrogen-Doped Graphene-Supported Mixed Transition-Metal Oxide Porous Particles to Confine Polysulfides for Lithium–Sulfur Batteries*. Advanced Energy Materials, 2018. **8**(22): p. 1800595.
20. Guo, D., et al., *MXene based self-assembled cathode and antifouling separator for high-rate and dendrite-inhibited Li–S battery*. Nano Energy, 2019. **61**: p. 478-485.
21. Huang, J.-Q., et al., *Ionic shield for polysulfides towards highly-stable lithium–sulfur batteries*. Energy & Environmental Science, 2014. **7**(1): p. 347-353.
22. Bauer, I., et al., *Reduced polysulfide shuttle in lithium–sulfur batteries using Nafion-based separators*. Journal of Power Sources, 2014. **251**: p. 417-422.

23. Chung, S.-H. and A. Manthiram, *Bifunctional Separator with a Light-Weight Carbon-Coating for Dynamically and Statically Stable Lithium-Sulfur Batteries*. *Advanced Functional Materials*, 2014. **24**(33): p. 5299-5306.
24. Huang, J.-Q., Q. Zhang, and F. Wei, *Multi-functional separator/interlayer system for high-stable lithium-sulfur batteries: Progress and prospects*. *Energy Storage Materials*, 2015. **1**: p. 127-145.
25. Chen, C., et al., *Ni/SiO₂/Graphene-modified separator as a multifunctional polysulfide barrier for advanced lithium-sulfur batteries*. *Nano Energy*, 2020. **76**: p. 105033.
26. Yao, H., et al., *Improved lithium-sulfur batteries with a conductive coating on the separator to prevent the accumulation of inactive S-related species at the cathode-separator interface*. *Energy & Environmental Science*, 2014. **7**(10): p. 3381-3390.
27. Gu, X., et al., *A porous nitrogen and phosphorous dual doped graphene blocking layer for high performance Li-S batteries*. *Journal of Materials Chemistry A*, 2015. **3**(32): p. 16670-16678.
28. Hu, Y., X. Zhu, and L. Wang, *Two-Dimensional Material-Functionalized Separators for High-Energy-Density Metal-Sulfur and Metal-Based Batteries*. *ChemSusChem*, 2020. **13**(6): p. 1366-1378.
29. Bai, S., et al., *Metal-organic framework-based separator for lithium-sulfur batteries*. *Nature Energy*, 2016. **1**(7): p. 16094.
30. Mo, Y.-X., et al., *Core-Shell Structured S@Co(OH)₂ with a Carbon-Nanofiber Interlayer: A Conductive Cathode with Suppressed Shuttling Effect for High-Performance Lithium-Sulfur Batteries*. *ACS Applied Materials & Interfaces*, 2019. **11**(4): p. 4065-4073.
31. Lei, T., et al., *Inhibiting Polysulfide Shuttling with a Graphene Composite Separator for Highly Robust Lithium-Sulfur Batteries*. *Joule*, 2018. **2**(10): p. 2091-2104.
32. Ghazi, Z.A., et al., *MoS₂/Celgard Separator as Efficient Polysulfide Barrier for Long-Life Lithium-Sulfur Batteries*. *Advanced Materials*, 2017. **29**(21): p. 1606817.
33. Liu, J., et al., *Exploiting a robust biopolymer network binder for an ultrahigh-areal-capacity Li-S battery*. *Energy & Environmental Science*, 2017. **10**(3): p. 750-755.

34. Wang, X., et al., *Stabilizing high sulfur loading Li–S batteries by chemisorption of polysulfide on three-dimensional current collector*. Nano Energy, 2016. **30**: p. 700-708.
35. Hu, Y., et al., *Strategies toward High-Loading Lithium–Sulfur Battery*. Advanced Energy Materials, 2020. **10**(17): p. 2000082.
36. Zhou, G., et al., *Theoretical Calculation Guided Design of Single-Atom Catalysts toward Fast Kinetic and Long-Life Li–S Batteries*. Nano Letters, 2020. **20**(2): p. 1252-1261.
37. Song, Y., et al., *Rationalizing Electrocatalysis of Li–S Chemistry by Mediator Design: Progress and Prospects*. Advanced Energy Materials, 2020. **10**(11): p. 1901075.
38. Du, Z., et al., *Cobalt in Nitrogen-Doped Graphene as Single-Atom Catalyst for High-Sulfur Content Lithium–Sulfur Batteries*. Journal of the American Chemical Society, 2019. **141**(9): p. 3977-3985.
39. Liu, D., et al., *Catalytic Effects in Lithium–Sulfur Batteries: Promoted Sulfur Transformation and Reduced Shuttle Effect*. Advanced Science, 2018. **5**(1): p. 1700270.
40. Yu, M., et al., *Accelerating polysulfide redox conversion on bifunctional electrocatalytic electrode for stable Li–S batteries*. Energy Storage Materials, 2019. **20**: p. 98-107.
41. Luo, D., et al., *Synergistic Engineering of Defects and Architecture in Binary Metal Chalcogenide toward Fast and Reliable Lithium–Sulfur Batteries*. Advanced Energy Materials, 2019. **9**(18): p. 1900228.
42. Wang, W., et al., *Defect-Rich Multishelled Fe-Doped Co₃O₄ Hollow Microspheres with Multiple Spatial Confinements to Facilitate Catalytic Conversion of Polysulfides for High-Performance Li–S Batteries*. ACS Applied Materials & Interfaces, 2020. **12**(11): p. 12763-12773.
43. Li, Z., et al., *Engineering Oxygen Vacancies in a Polysulfide-Blocking Layer with Enhanced Catalytic Ability*. Advanced Materials, 2020. **32**(10): p. 1907444.
44. Wu, H., et al., *Cobalt nitride nanoparticle coated hollow carbon spheres with nitrogen vacancies as an electrocatalyst for lithium–sulfur batteries*. Journal of Materials Chemistry A, 2020. **8**(29): p. 14498-14505.

45. Li, Y., et al., *β -FeOOH Interlayer With Abundant Oxygen Vacancy Toward Boosting Catalytic Effect for Lithium Sulfur Batteries*. *Frontiers in Chemistry*, 2020. **8**(309).
46. Chang, Z., et al., *Co₃O₄ nanoneedle arrays as a multifunctional “super-reservoir” electrode for long cycle life Li–S batteries*. *Journal of Materials Chemistry A*, 2017. **5**(1): p. 250-257.
47. Blöchl, P.E., *Projector augmented-wave method*. *Physical Review B*, 1994. **50**(24): p. 17953-17979.
48. Perdew, J.P., K. Burke, and M. Ernzerhof, *Generalized Gradient Approximation Made Simple*. *Physical Review Letters*, 1996. **77**(18): p. 3865-3868.
49. Dudarev, S.L., et al., *Electron-energy-loss spectra and the structural stability of nickel oxide: An LSDA+U study*. *Physical Review B*, 1998. **57**(3): p. 1505-1509.
50. Montoya, A. and B.S. Haynes, *Periodic density functional study of Co₃O₄ surfaces*. *Chemical Physics Letters*, 2011. **502**(1): p. 63-68.
51. Huang, G.-Y., C.-Y. Wang, and J.-T. Wang, *Detailed check of the LDA+U and GGA+U corrected method for defect calculations in wurtzite ZnO*. *Computer Physics Communications*, 2012. **183**(8): p. 1749-1752.
52. Grimme, S., et al., *A consistent and accurate ab initio parametrization of density functional dispersion correction (DFT-D) for the 94 elements H–Pu*. *The Journal of Chemical Physics*, 2010. **132**(15): p. 154104.
53. Zhang, D., et al., *Self-assembly of mesoporous ZnCo₂O₄ nanomaterials: density functional theory calculation and flexible all-solid-state energy storage*. *Journal of Materials Chemistry A*, 2016. **4**(2): p. 568-577.
54. Zasada, F., et al., *Periodic DFT and HR-STEM Studies of Surface Structure and Morphology of Cobalt Spinel Nanocrystals. Retrieving 3D Shapes from 2D Images*. *The Journal of Physical Chemistry C*, 2011. **115**(14): p. 6423-6432.
55. Assary, R.S., L.A. Curtiss, and J.S. Moore, *Toward a Molecular Understanding of Energetics in Li–S Batteries Using Nonaqueous Electrolytes: A High-Level Quantum Chemical Study*. *The Journal of Physical Chemistry C*, 2014. **118**(22): p. 11545-11558.

56. Carbone, M., *Zn defective ZnCo₂O₄ nanorods as high capacity anode for lithium ion batteries*. Journal of Electroanalytical Chemistry, 2018. **815**: p. 151-157.
57. Kaftelen, H., et al., *EPR and photoluminescence spectroscopy studies on the defect structure of ZnO nanocrystals*. Physical Review B, 2012. **86**(1): p. 014113.
58. Xu, J., et al., *MOF-derived porous N-Co₃O₄@N-C nanododecahedra wrapped with reduced graphene oxide as a high capacity cathode for lithium-sulfur batteries*. Journal of Materials Chemistry A, 2018. **6**(6): p. 2797-2807.
59. Zhang, S.S., *Role of LiNO₃ in rechargeable lithium/sulfur battery*. Electrochimica Acta, 2012. **70**: p. 344-348.
60. Ni, X., et al., *High Lithium Ion Conductivity LiF/GO Solid Electrolyte Interphase Inhibiting the Shuttle of Lithium Polysulfides in Long-Life Li-S Batteries*. Advanced Functional Materials, 2018. **28**(13): p. 1706513.
61. Cheng, H., et al., *Interacting ZnCo₂O₄ and Au nanodots on carbon nanotubes as highly efficient water oxidation electrocatalyst*. Journal of Power Sources, 2017. **357**: p. 1-10.
62. Huang, G., et al., *Defective ZnCo₂O₄ with Zn vacancies: Synthesis, property and electrochemical application*. Journal of Alloys and Compounds, 2017. **724**: p. 1149-1156.
63. Joshi, N., et al., *Yolk-shelled ZnCo₂O₄ microspheres: Surface properties and gas sensing application*. Sensors and Actuators B: Chemical, 2018. **257**: p. 906-915.
64. Liu, B., et al., *Bifunctional NiCo₂S₄ catalysts supported on a carbon textile interlayer for ultra-stable Li-S battery*. Journal of Materials Chemistry A, 2019. **7**(13): p. 7604-7613.
65. Ye, Z., et al., *Exceptional adsorption and catalysis effects of hollow polyhedra/carbon nanotube confined CoP nanoparticles superstructures for enhanced lithium-sulfur batteries*. Nano Energy, 2019. **64**: p. 103965.
66. Shi, K., et al., *LiNi_{0.8}Co_{0.15}Al_{0.05}O₂ as both a trapper and accelerator of polysulfides for lithium-sulfur batteries*. Energy Storage Materials, 2019. **17**: p. 111-117.
67. An, D., et al., *An ultrathin and continuous Li₄Ti₅O₁₂ coated carbon nanofiber interlayer for high rate lithium sulfur battery*. Journal of Energy Chemistry, 2019. **31**: p. 19-26.

68. Wu, Q., et al., *Adenine Derivative Host with Interlaced 2D Structure and Dual Lithiophilic–Sulphilic Sites to Enable High-Loading Li–S Batteries*. ACS Nano, 2019. **13**(8): p. 9520-9532.
69. Fan, F.Y., W.C. Carter, and Y.-M. Chiang, *Mechanism and Kinetics of Li₂S Precipitation in Lithium–Sulfur Batteries*. Advanced Materials, 2015. **27**(35): p. 5203-5209.
70. Chen, Y., et al., *3D graphene framework supported Li₂S coated with ultra-thin Al₂O₃ films: binder-free cathodes for high-performance lithium sulfur batteries*. Journal of Materials Chemistry A, 2017. **5**(1): p. 102-112.
71. Chen, L., et al., *A Ni(OH)₂–CoS₂ hybrid nanowire array: a superior non-noble-metal catalyst toward the hydrogen evolution reaction in alkaline media*. Nanoscale, 2017. **9**(43): p. 16632-16637.
72. Wang, L., et al., *Ultra-small self-discharge and stable lithium-sulfur batteries achieved by synergetic effects of multicomponent sandwich-type composite interlayer*. Nano Energy, 2018. **50**: p. 367-375.
73. Liu, T., et al., *Interweaving 3D Network Binder for High-Areal-Capacity Si Anode through Combined Hard and Soft Polymers*. Advanced Energy Materials, 2019. **9**(3): p. 1802645.
74. Hong, X.-J., et al., *Cerium Based Metal–Organic Frameworks as an Efficient Separator Coating Catalyzing the Conversion of Polysulfides for High Performance Lithium–Sulfur Batteries*. ACS Nano, 2019. **13**(2): p. 1923-1931.
75. Cheng, Z., et al., *Separator Modified by Cobalt-Embedded Carbon Nanosheets Enabling Chemisorption and Catalytic Effects of Polysulfides for High-Energy-Density Lithium-Sulfur Batteries*. Advanced Energy Materials, 2019. **9**(32): p. 1901609.
76. Zang, Y., et al., *Large-Area Preparation of Crack-Free Crystalline Microporous Conductive Membrane to Upgrade High Energy Lithium–Sulfur Batteries*. Advanced Energy Materials, 2018. **8**(31): p. 1802052.
77. Lv, X., et al., *An Efficient Separator with Low Li-Ion Diffusion Energy Barrier Resolving Feeble Conductivity for Practical Lithium–Sulfur Batteries*. Advanced Energy Materials, 2019. **9**(40): p. 1901800.

78. He, J., Y. Chen, and A. Manthiram, *Vertical Co₉S₈ hollow nanowall arrays grown on a Celgard separator as a multifunctional polysulfide barrier for high-performance Li–S batteries*. Energy & Environmental Science, 2018. **11**(9): p. 2560-2568.
79. Fang, D., et al., *Spider-Web-Inspired Nanocomposite-Modified Separator: Structural and Chemical Cooperativity Inhibiting the Shuttle Effect in Li–S Batteries*. ACS Nano, 2019. **13**(2): p. 1563-1573.
80. Li, G., et al., *Polysulfide Regulation by the Zwitterionic Barrier toward Durable Lithium–Sulfur Batteries*. Journal of the American Chemical Society, 2020. **142**(7): p. 3583-3592.
81. Yu, Z., et al., *Boosting Polysulfide Redox Kinetics by Graphene-Supported Ni Nanoparticles with Carbon Coating*. Advanced Energy Materials, 2020. **10**(25): p. 2000907.
82. Xie, J., et al., *Implanting Atomic Cobalt within Mesoporous Carbon toward Highly Stable Lithium–Sulfur Batteries*. Advanced Materials, 2019. **31**(43): p. 1903813.
83. Zhang, L., et al., *Single Nickel Atoms on Nitrogen-Doped Graphene Enabling Enhanced Kinetics of Lithium–Sulfur Batteries*. Advanced Materials, 2019. **31**(40): p. 1903955.
84. Li, B., et al., *Tuning the Band Structure of MoS₂ via Co₉S₈@MoS₂ Core–Shell Structure to Boost Catalytic Activity for Lithium–Sulfur Batteries*. ACS Nano, 2020. **14**(12): p. 17285-17294.
85. Li, S., et al., *Propelling polysulfide conversion for high-loading lithium–sulfur batteries through highly sulfiphilic NiCo₂S₄ nanotubes*. Energy Storage Materials, 2020. **27**: p. 51-60.
86. Zeng, F.-L., et al., *A multifunctional zipper-like sulfur electrode enables the stable operation of lithium-sulfur battery through self-healing chemistry*. Energy Storage Materials, 2021. **34**: p. 755-767.
87. Wang, M., et al., *Nitrogen-Doped CoSe₂ as a Bifunctional Catalyst for High Areal Capacity and Lean Electrolyte of Li–S Battery*. ACS Energy Letters, 2020. **5**(9): p. 3041-3050.

88. Kim, J.-H., et al., *Nanomat Li–S batteries based on all-fibrous cathode/separator assemblies and reinforced Li metal anodes: towards ultrahigh energy density and flexibility*. Energy & Environmental Science, 2019. **12**(1): p. 177-186.
89. Tu, S., et al., *A Polysulfide-Immobilizing Polymer Retards the Shuttling of Polysulfide Intermediates in Lithium–Sulfur Batteries*. Advanced Materials, 2018. **30**(45): p. 1804581.
90. Luo, L., et al., *In-Situ Assembled VS₄ as a Polysulfide Mediator for High-Loading Lithium–Sulfur Batteries*. ACS Energy Letters, 2020. **5**(4): p. 1177-1185.
91. He, D., et al., *Ultrathin Conductive Interlayer with High-Density Antisite Defects for Advanced Lithium–Sulfur Batteries*. Advanced Functional Materials, 2021. **31**(2): p. 2001201.
92. Song, Y., et al., *Synchronous immobilization and conversion of polysulfides on a VO₂–VN binary host targeting high sulfur load Li–S batteries*. Energy & Environmental Science, 2018. **11**(9): p. 2620-2630.
93. Pang, Q., et al., *A Comprehensive Approach toward Stable Lithium–Sulfur Batteries with High Volumetric Energy Density*. Advanced Energy Materials, 2017. **7**(6): p. 1601630.

Chapter 5:
Environmentally Benign and Highly-Branched
Amylopectin (HBA) Binder for Enhanced
Longevity in Sulfur Cathodes

5.1 Abstract

Lithium-sulfur (Li-S) batteries are a promising next-generation energy storage technology due to the low-cost, high-energy-density, and environmentally benign sulfur cathode material. However, Li-S batteries have inherent problems, including rapid capacity fading and short circuits, which researchers aim to address. One method to alleviate these concerns is through the application of multifunctional binders. Multifunctional binders derived from natural sources are particularly appealing as they align with the goals of low-cost and environmentally friendly batteries. This work uses a low-cost and environmentally friendly binder extracted from sticky rice to fabricate cathodes for Li-S batteries. The cells fabricated using the highly-branched amylopectin (HBA) binder deliver better discharge capacity, lower capacity fading per cycle, and better reaction kinetics than cells based on the traditional PVDF binder. The HBA-based cells also outperform batteries based on a lowly-branched polysaccharide (LBP) obtained from potatoes. The improved electrochemical performance in the BAP-based cell is explained via two mechanisms. Firstly, the HBA shows enhanced polysulfide retention due to the polymer's abundant lone-pair rich hydroxyl groups. Secondly, the branched structure of the HBA provides enhanced mechanical and adhesive properties, which allow for a robust electronic and ionic conductive framework to be maintained throughout the cathode after extended cycling. The improved mechanical properties and polysulfide anchoring allow the HBA-based Li-S battery to deliver a long-cycle life of 500 cycles at 2 C while only displaying a capacity fading of 0.104 % per cycle.

Keywords

Lithium-Sulfur battery, highly-branched amylopectin, lowly-branched polysaccharides, binders

Highlights

- Environmentally benign extraction method produces highly-branched amylopectin (HBA) as a binder for sulfur cathodes
- The lone-pair rich hydroxyl groups and the formation of C–S bonds between the HBA and polysulfides prohibits the shuttle effect of polysulfides
- The HBA binder delivers enhanced mechanical and adhesive properties to maintain a robust network in the sulfur cathode
- HBA binder delivers enhanced electrochemical performance over the traditional PVDF binder and a lowly-branched polysaccharide (LBP) obtained from potatoes

5.2 Introduction

As continual global population and economic growth increase society's demand for energy, the environmental consequences of energy production become more apparent [1]. Since energy production is one of the major driving forces of carbon emissions and climate change [2] and the majority of energy from non-renewable resources [3], the requirement for clean and renewable energy is urgent than ever [4]. Wind and solar-based renewable energy have made significant inroads into energy grids across the world [5], but their implementation is hindered by their variable power supply [6], reaping up to 20% variability for wind energy [7]. Therefore, energy storage systems such as rechargeable batteries are being implemented to supplement renewable energy generators [8, 9].

Rechargeable batteries are also gaining traction in electric vehicles, which benefit from reducing CO₂ emissions produced by internal combustion engines [10]. However, rechargeable batteries are limited by their cost, energy density, and toxic components [11]. As a result, novel battery chemistries are being investigated so that these shortfalls can be avoided. Lithium-Sulfur (Li-S) batteries are promising next-generation battery chemistry that possesses a greater energy density than state-of-the-art Lithium-ion batteries (LIBs), without the use of toxic transition metals in the cathode [12]. However, they are limited in their commercial application due to some intractable technical issues.

The single greatest challenge hindering the practical application of the Li-S battery is the polysulfide shuttle phenomenon (or effect), which arises from the fact that the lithium polysulfide reaction intermediates formed during cycling are readily soluble in the ether-based electrolytes used in Li-S cells [13-16]. This dissolution of the active materials at the cathode forms a concentration gradient, which causes the soluble species to migrate towards the anode, where they can be further reduced and damage the anode [17]. These reactions cause a severe loss in Coulombic efficiency and rapid capacity fading [18]. Additionally, the insulating nature of elemental sulfur (S₈) as well as the solid discharge product in the Li-S cell (Li₂S₂/Li₂S) causes poor active material utilisation and sluggish reaction kinetics, resulting in insufficient discharge capacity and poor performance at high C-rates, respectively [19, 20]. The conversion from sulfur to Li₂S is also accompanied by an $\approx 80\%$ increase in volume, which causes damage to the electronic conducting network and electrode delamination from the current collector, again reducing the electrochemical performance in Li-S cells [21, 22]. Finally, the use of the

metallic lithium anode can cause dendrite formation, which may pierce the separator and causes operation safety concerns [23].

Researchers in the field have directed their attention to the cathode [24], anode [25], electrolyte [26], and separator [27] of the Li-S cell in order to improve the electrochemical performance. Of these, the cathode of the Li-S cell has received particular attention through the development and successful application of multifunctional sulfur hosts [11]. When appropriately designed, sulfur hosts in Li-S batteries can simultaneously mitigate multiple challenges within the Li-S cell. For example, sulfur hosts with ample void structures, such as hierarchical porous carbons [28], can provide the necessary volume to accommodate a sufficiently large sulfur loading in the cathode while also providing abundant channels for electrolyte penetration during cycling [29]. Sulfur hosts with inherent electronic conductivity can improve active material utilisation and facilitate rapid charging/discharging [30]. Heteroatom [31], transition metal oxide [32], or transition metal sulfide-doped [33] sulfur hosts can provide soluble polysulfide anchoring points to reduce the shuttle effect and catalyse the electrochemical reaction, improving the discharge capacity, reducing the capacity fading, and improving the kinetics at high C-rates. Well-designed sulfur hosts can incorporate many of these features at once.

Although remarkably effective at alleviating the aforementioned challenges, sulfur hosts can do little in the way of maintaining the intimate contact between the components of the composite sulfur cathode [34]. Thus, researchers have turned their attention to the binders in the Li-S cathode so that the structural damage and electrode delamination can be addressed [35]. By utilising binders with superior adhesive properties, a robust cathode composite can be maintained throughout extended cycles [36]. However, adhesion between electrode components is not the only role that a binder can play in a Li-S cathode, as demonstrated through the use of multifunctional binders. These binders go beyond simply providing improved adhesive properties by filling some of the roles traditionally left to the sulfur host, including providing chemical polysulfide anchoring via their functional groups or improving the electronic conductivity of the composite cathode [37]. Amongst these multifunctional binders, bio-derived binders have been widely applied in Li-S cells due to their inherent mechanical properties, cost, chemical functionality, and environmental benignity [38-40].

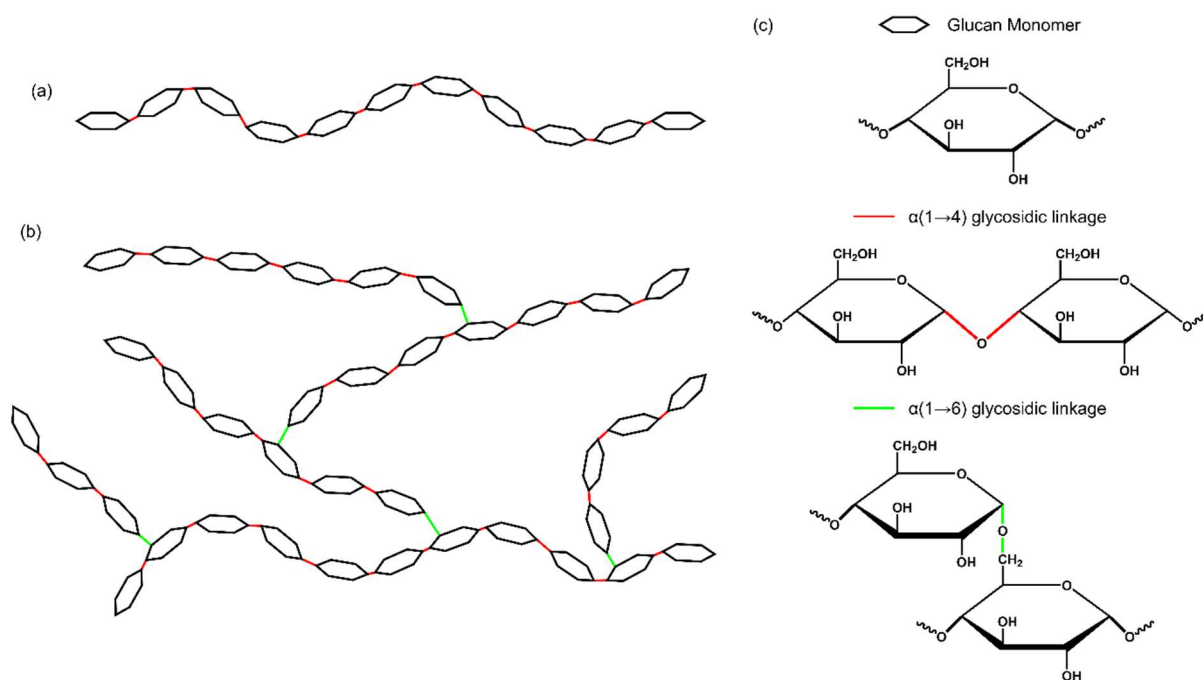


Figure 5.1: Representation of the (a) lowly-branched polysaccharide (LBP) and (b) highly-branched amylopectin (HBA) binders. (c) Chemical structure of the glucan monomer, $\alpha(1\rightarrow4)$ glycosidic linkage (red), and $\alpha(1\rightarrow6)$ glycosidic linkages (green)

Starch, mainly composed of the two polysaccharides, amylopectin and amylose (**Fig. 5.1**) [41], is primarily used as food but has also found uses in textile, chemical production, paper binders, and adhesive applications [42]. Both amylopectin and amylose consist of repeating glucose units but differ in their structural configurations [43]. Amylose is an essentially linear chain polymer, with $\alpha(1\rightarrow4)$ glycosidic bonds and a typical molecular weight around $10^6 \text{ g}\cdot\text{mol}^{-1}$, whereas amylopectin displays both $\alpha(1\rightarrow4)$ and $\alpha(1\rightarrow6)$ linkages resulting in a highly branched structure and an increased molecular weight of approx. $10^8 \text{ g}\cdot\text{mol}^{-1}$ [42, 44]. The different conformations of the two polysaccharides affect the resulting physical and chemical properties. Initially, starch is insoluble in water, but upon heating, amylose forms a non-viscous solution, whereas amylopectin remains insoluble and forms a viscous gel [45]. The physical structure of the starch is also related to its digestibility, with starches ranging from rapidly digestible to resistant [46].

Sticky (or glutinous) rice is a valuable starch source and has favourable adhesive properties due to its high amylopectin content. Sticky rice has been used as a mortar ingredient in ancient China for over 3000 years [47] and has been applied in constructing tombs, roads, cities, and even in the Great Wall of China [48]. Starch has already been applied in LIBs with varying success [49-52] and is beginning to emerge in Li-S applications [53]. However, little attention

has been paid to the highly branched amylopectin polysaccharide found in starch. With its highly branched structure, the starch extracted from sticky rice is expected to deliver an improved electrochemical performance in Li-S cells compared to previous works that haven't considered the degree of branching in the starch.

As shown by the PTTG polymer developed in Chapter 3 of this thesis, lone-pair-rich polymers display an outstanding ability to mitigate the polysulfide shuttle effect in Li-S batteries and can reduce the capacity fading that plagues LSBs. Chapter 3 also demonstrated the critical importance of robust mechanical and adhesive properties that multifunctional Li-S binders require. Thus, a multifunctional polymer that displays chemical polysulfide retention and superb adhesive properties is required for high performance LSBs.

To expand upon the work shown in Chapter 3, this Chapter applies highly-branched amylopectin (HBA) binder as a low-cost and environmentally benign Li-S cathode binder, which is expected to have similar functionality to the PTTG polymer developed previously due to its lone-pair-rich chemical moieties and excellent mechanical properties. However, in contrast to the PTTG polymer from Chapter 3, the HBA binder is produced from sustainable source materials and processes, without relying on complicated chemical synthesis and reagents.

The HBA binder displays improved mechanical properties and adhesion compared with the traditional Li-S binder (PVDF) and a mixed lowly-branched polysaccharide (LBP) binder. Experiments demonstrate that the HBA binder also displays the ability to chemically retard soluble lithium polysulfides due to its lone-pair rich hydroxyl groups and C-S bond formation. These features allow the HBA-based binder to deliver enhanced electrochemical performance in Li-S cells compared to cells based on PVDF and LBP binders. The HBA-based cell delivers a capacity fading as low as 0.104 % over 500 cycles at a 2 C rate, superior rate kinetics, and better Li⁺ diffusion throughout the cathode. This improvement is particularly appealing as the HBA is derived from both an environmentally friendly source and extraction method, which could reduce the environmental impact of the Li-S cell.

5.3 Experimental Section

5.3.1 *Highly-Branched Amylopectin (HBA) Extraction*

Sticky (glutinous) rice was obtained from the local Asian supermarket. The sticky rice was soaked in deionised (DI) water at room temperature for 24 h before refluxing at 80 °C for 4 h

under magnetic stirring. The mixture was then cooled to RT and centrifuged. After centrifuging, the mixture contained a solid lower layer, a highly viscous gelatinous middle layer, and a low viscosity upper layer. The middle layer was separated, centrifuged again, and collected before being freeze-dried. The collected extract is referred to as the highly-branched amylopectin (HBA) binder hereafter.

5.3.2 Materials Characterisation

Elemental Sulfur, Carbon Black (CB), lowly-branched polysaccharide (LBP), Poly(vinylidene fluoride) (PVDF), 1,3-dioxolane (DOL), 1,2-dimethoxyethane (DME), bis(trifluoromethane)sulfonimide (LiTFSI), lithium nitrate (LiNO_3), lithium sulfide (Li_2S), and 1-methyl-2-pyrrolidinone (NMP) were obtained from Sigma-Aldrich and used directly without any further purification. Thermogravimetric analysis (TGA) was carried out on a Netzsch STA 449 F3 Jupiter (Netzsch, Germany) at a temperature ranging from RT to 650 °C at a heating rate of 15 °C·min⁻¹ under an argon atmosphere. X-ray diffraction (XRD) patterns were conducted in a Model LabX-6000 diffractometer (Shimadzu, Japan) using Cu K α radiation ($\lambda = 1.54 \text{ \AA}$) at 40 kV and 40 mA between the 2θ range of 10 - 80 °. For the polysulfide adsorption experiment, a 0.01 M Li_2S_6 solution was prepared by adding Li_2S and elemental sulfur in a 1:5 molar ratio to a solvent of DOL:DME (1:1 v/v) in an argon-filled glovebox, before being magnetically stirred at 70 °C for 24 h. 100 mg of PVDF, LBP, and HBA were exposed to 20 mL of 0.01 M Li_2S_6 solution for 4 h. Then, an aliquot of the supernatant solution was taken and UV-Vis spectroscopy was carried out on a Cary Series UV-Vis-NIR Spectrophotometer (Agilent Technologies, USA). Fourier transform infrared (FTIR) spectroscopy was carried out on a Bruker Alpha (Bruker, USA) in absorbance mode to compare the spectra of the PVDF, LBP, and HBA samples before and after Li_2S_6 exposure. Scanning electron microscope (SEM) images and Energy-dispersive X-ray spectroscopy (EDS) data were obtained on a JSM-7001F SEM (JEOL, Japan) and was used to investigate the morphologies and elemental distributions of the S/PVDF, S/LBP, and S/HBA electrodes before and after cycling.

5.3.3 Mechanical Characterisation

The peeling tests were carried out on the three electrodes at a constant speed of 1 mm·s⁻¹ on an MTS Tytron microforce tester (MTS, USA). The peeling test samples were fixed on aluminium substrates, and the electrode materials were peeled off from current collectors using Scotch Sticky Tape (12 mm in width). The nano-indentation, nano-scratching, and morphology mapping were performed using Hysitron TI 950 nano-indentation system (Hysitron, USA). The

reduced modulus and hardness were obtained by the nano-indentation with a Berkovich indenter. The force for nano-indentation was kept at 2000 μN , and the holding time was set to 10 s. The conical indenter with a tip 1 μm in diameter was used to perform scratching on the surface of the electrodes and the morphology mapping after scratching.

5.3.4 Electrochemical Characterisation

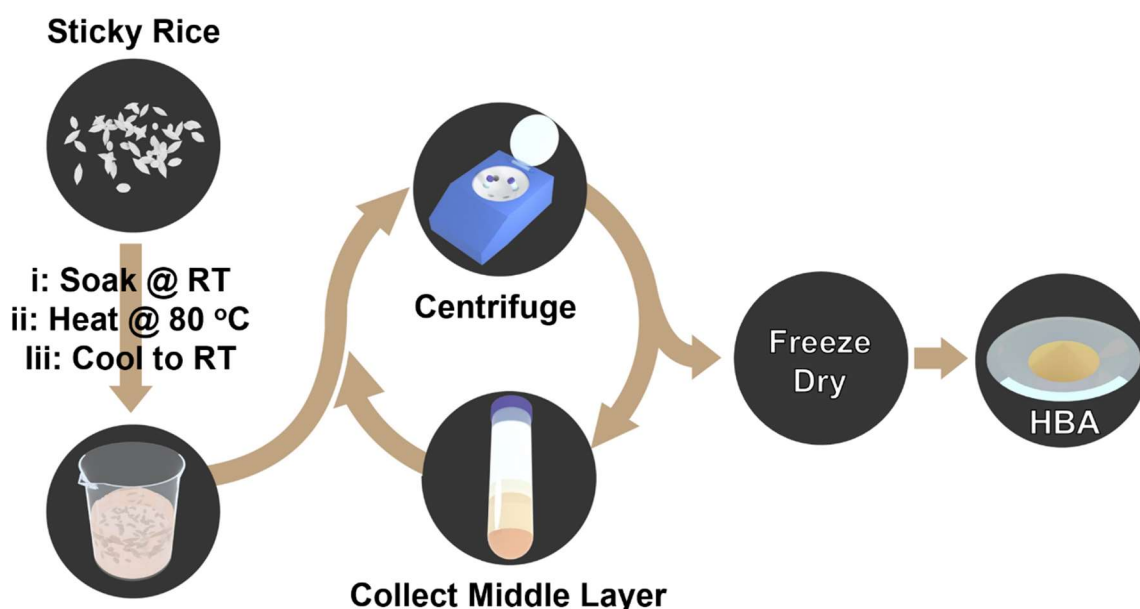
For electrochemical testing, sulfur cathodes using PVDF, LBP, or HBA as a binder were fabricated with elemental sulfur, carbon black, and binder in a mass ratio of 60:30:10 and were denoted S/PVDF, S/LBP, and S/HBA, respectively. The electrode components were ground in a mortar and pestle before being made into an electrode slurry using NMP as the solvent. The slurry was cast using a gapped blade on carbon-coated aluminium foil before being dried in a vacuum oven at 60 $^{\circ}\text{C}$ for 24 h and cut into disks with a diameter of 13 mm. The active material loading in the electrodes was approx. 0.5 $\text{mg}\cdot\text{cm}^{-2}$. Electrodes with a sulfur loading of $\approx 2 \text{ mg}\cdot\text{cm}^{-2}$ were also fabricated for high sulfur load testing. Electrodes fabricated from 80% carbon black and 20% HBA were also fabricated for electrolyte stability testing. Half-cells were fabricated in an argon-filled glovebox using either an S/PVDF, S/LBP, or S/HBA cathode, a lithium foil counter electrode, polypropylene (Celgard 2300) separator, and 1 M LiTFSI in DOL/DME (1:1, v/v) with 0.2 M LiNO_3 as the electrolyte. The electrolyte/sulfur (E/S) ratio was kept constant at 1 mg :20 μL for all half-cells. The half-cells underwent galvanostatic charge/discharge testing on a Neware Battery Testing System (Neware, China) with a 1.7 - 2.7 V voltage window in an oven set to 30 $^{\circ}\text{C}$. For the 0.5 C (1 C = 1672 $\text{mAh}\cdot\text{g}^{-1}$) and high-loading 0.2 C testing, an electrochemical sulfur infiltration pre-cycle of 0.05 C was performed before cycling at the specified rate. For the 2 C testing, a 0.2 C pre-cycle was utilised. Electrochemical impedance spectroscopy (EIS) was carried out on a Biologic SP-200 (Biologic, France) with the AC set to 5 mV and a frequency range of 10 mHz to 100 kHz. Cyclic voltammetry (CV) testing was also carried out on the Biologic SP-200.

5.4 Results and Discussion

The extraction of sticky rice binder is outlined in **Scheme 1**. After processing and centrifuging, the upper-most low viscosity layer and the lower insoluble pellet were separated from the highly viscous central supernatant layer to obtain the highly-branched amylopectin (HBA) binder. The HBA was expected to have a high amylopectin content due to the relative viscosities of amylopectin and amylose solutions, which were exploited during processing [54].

As a result, a simple separation is achieved by simply extracting the HBA in water, and a highly-branched and environmentally benign binder is obtained.

Following the extraction and freeze-drying of the HBA, thermogravimetric analysis (TGA) was carried out to observe the amylopectin content in the HBA qualitatively. The TGA results for the LBP and HBA samples are displayed in **Fig. 5.2a** and show that both samples experience a mass loss up to a temperature of about 150 °C, which can be attributed to water incorporated into the starch matrix. By observing the temperature at 50 % mass loss, the amount of branching in the starch can be estimated, with a higher degree of branching giving a higher temperature at 50 % mass loss [55]. Thus, upon observing the temperature at 50 % mass loss for both samples, it can be inferred that the HBA sample has a higher degree of branching when compared to the LBP sample.



Scheme 1: Extraction and purification of the highly-branched amylopectin (HBA) binder from sticky rice

X-ray diffraction (XRD) analysis was also carried out to observe the crystal structure of the three samples, with the diffraction patterns presented in **Fig. 5.2b**. The PVDF sample displays diffraction peaks at 18.33, 19.89, and 26.23 °, confirming the presence of α -phase PVDF [56], which is non-polar and semi-crystalline [57]. The diffraction pattern of the LBP displays both crystalline and amorphous regions, with the amylose fraction of the LBP responsible for the crystalline phase, while the amorphous phase can be attributed to the amylopectin within the

LBP [58]. In contrast, the HBA diffraction pattern is entirely amorphous, confirming the high amylopectin content suggested by the TGA.

To investigate the mechanical and adhesive properties of the samples, 90° peel-off, nano-scratch, and nano-indentation testing were carried out on the S/PVDF, S/LB, and S/HBA electrodes. The mechanical peel test results in **Fig. 5.2c** show that the S/PVDF and S/LBP samples initially display a roughly equivalent resistance to peeling, with the S/LBP sample providing slightly better adhesion as the peel distance increases. In sharp contrast, the S/HBA sample displays a much larger initial resistance to the pulling force, shown at low displacement values, and a dramatically increased adhesion force towards the end of the peel test. These results clearly show that the S/HBA displays much better adhesion than both S/PVDF and the S/LBP samples [59]. The hardness of the three electrodes was also evaluated by nano-indentation testing. A shallower indentation at the same load suggests a more rigid material. The results in **Fig. 5.2d** show that the indentation depth at a load of 2000 μN for the S/HBA, S/LBP and S/PVDF samples was 1.53, 2.91 and 5.32 μm , respectively, which displays the rigid and robust nature of the S/HBA electrode [60].

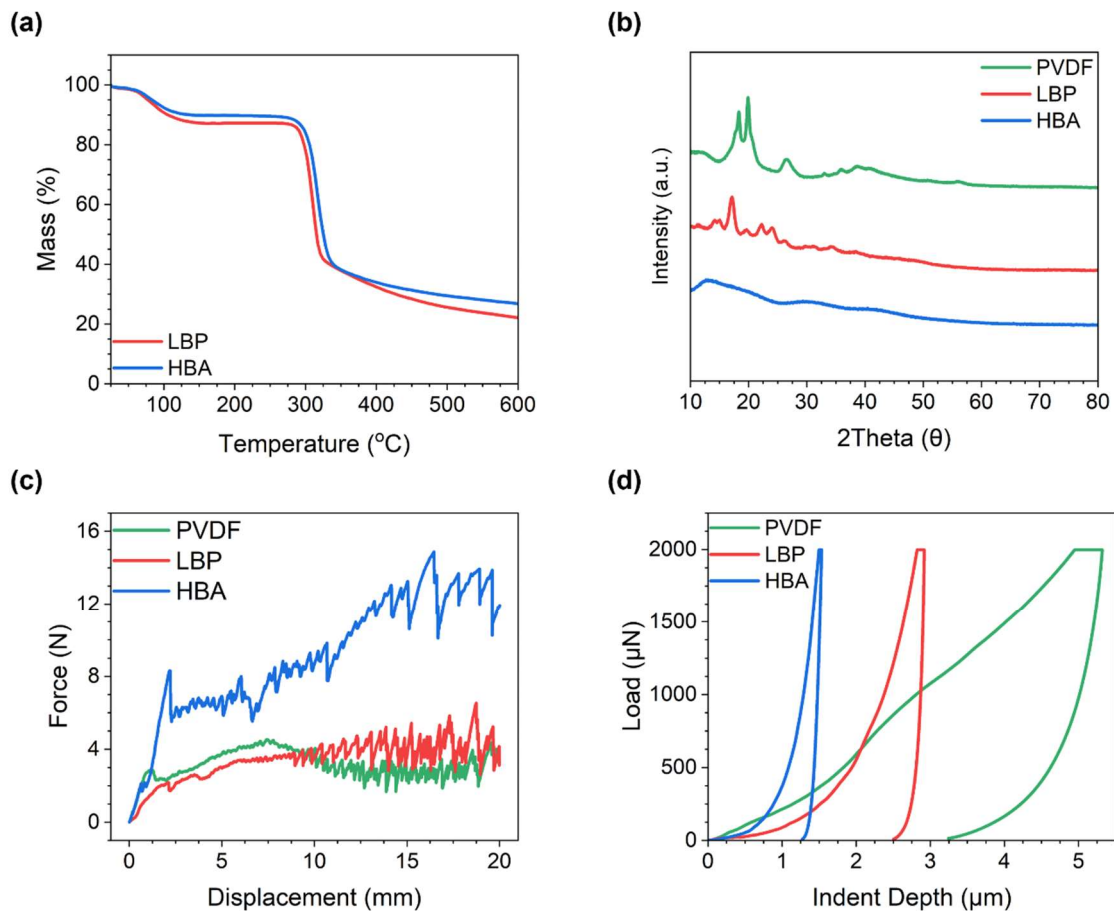


Figure 5.2: (a) TGA spectra of the LBP and HBA samples. (b) XRD patterns of PVDF, LBP, and HBA. Results from the (c) 90 ° mechanical peel and (d) nano-indentation tests

Nano-scratch testing was also carried out to evaluate the adhesive properties and homogeneity of the S/PVDF, S/LBP, and S/HBA electrodes. As the results in **Fig. 5.3a** show, both the S/HBA and S/LBP samples display smoother profiles than the S/PVDF sample, suggesting a better homogeneity of these electrodes. What's more, the average friction coefficients for the S/HBA, S/LBP, and S/PVDF samples are 1.04, 0.99, and 0.84, respectively. The higher friction coefficient in the nano-scratch test suggests a higher adhesion in the electrodes [38]. Overall, the results in **Fig. 5.2 and 5.3** show that the HBA has a highly branched structure and low crystallinity, while the S/HBA possesses better adhesion, more homogeneity, and increased hardness than the S/LBP and S/PVDF samples.

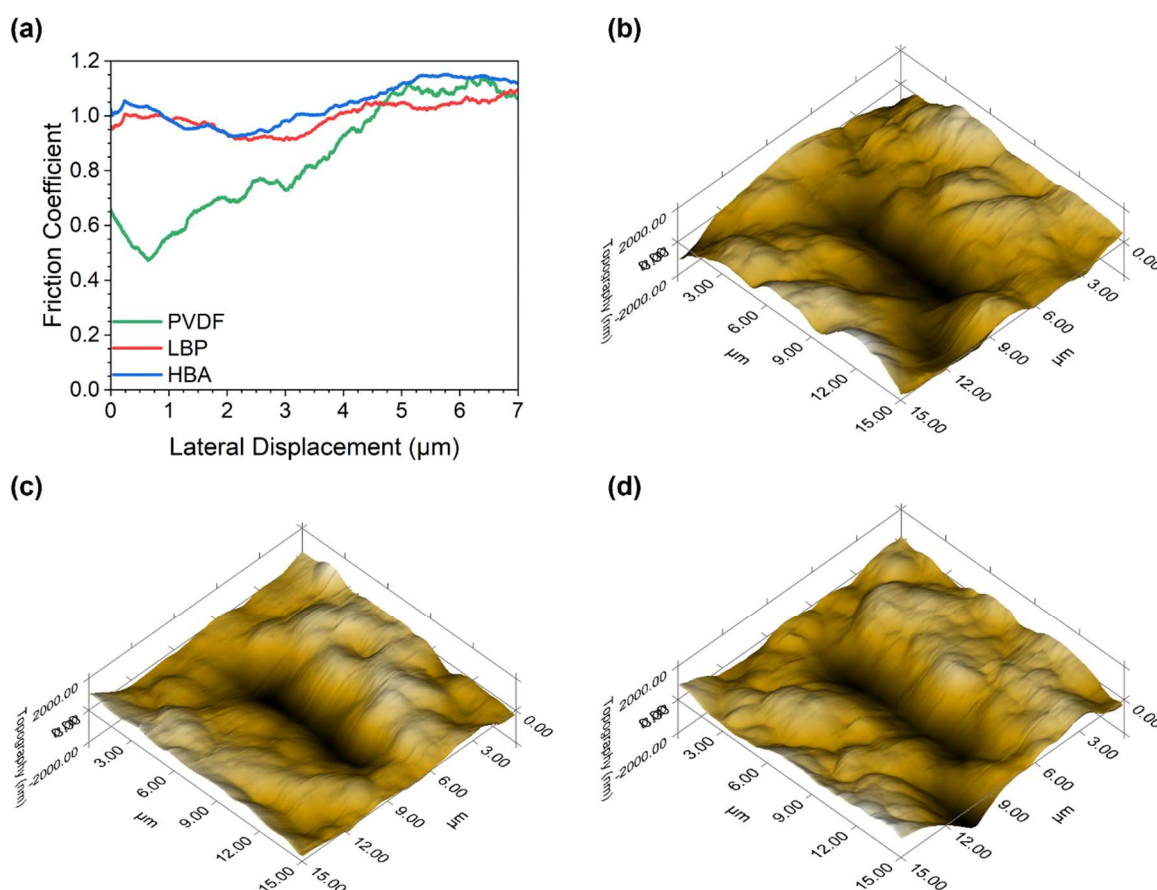


Figure 5.3: (a) Nano-scratch test results for the S/PVDF, S/LBP, and S/HBA samples. (b-d) Scanning probe microscopy (SPM) images of the S/PVDF, S/LBP, and S/HBA samples, respectively

A simple adsorption experiment was conducted to demonstrate whether the HBA could retain soluble polysulfides. 100 mg of either the PVDF, LBP, or HBA samples were exposed to a 0.01 M solution of Li_2S_6 in DOL:DME for 4 h, after which the supernatant solution was studied using UV-Vis spectroscopy (**Fig. 5.4a**). The spectra from the solution of Li_2S_6 contain a broad absorbance peak around 250 - 280 nm, which is characteristic of the S_6^{2-} anion [61]. The spectra from the supernatant solutions clearly show that the PVDF has no interaction with the polysulfides as the peak height remains unchanged. Conversely, both the LBP and HBA display some ability to adsorb soluble polysulfides as the S_6^{2-} peak height has reduced in both cases. As the HBA displays the smallest peak ascribed to S_6^{2-} , it is inferred it possesses the best polysulfide anchoring ability. These results could visually be confirmed by the digital photographs attached in the inset of **Fig. 5.4a**, which shows the Li_2S_6 solution that was exposed to the PVDF experienced no colour fading, the solution exposed to the LBP showed minimal colour fading to light yellow, and the solution exposed to the HBA sample experienced a significant colour fading from dark brown to almost colourless.

Fig. 5.4b-d present the FTIR spectra of the PVDF, LBP, and HBA before and after Li_2S_6 exposure. The magnified regions of the peaks associated with the O–H and C–S stretching in the HBA samples are provided in **Fig. 5.4e and f**. The peak located at around 3300 cm^{-1} in the HBA sample is assigned to the O–H stretching vibration (**Fig. 5.4e**) [62, 63]. After Li_2S_6 exposure, it can be observed that the O–H stretching vibration peak experiences a downshift from 3296 to 3233 cm^{-1} while also becoming broader. The downshift could signify a coordination interaction between the lone-pair rich hydroxyl groups and the Li^+ from Li_2S_6 [64].

Furthermore, the appearance of the new peak at 670 cm^{-1} (**Fig. 5.4f**) can be assigned to the formation of the C–S bond after the HBA was exposed to Li_2S_6 [38, 65]. These two interactions suggest the possible mechanism of the polysulfide adsorption delivered by the HBA. When compared to the LBP sample, it can be observed that the O–H stretching peak only experiences a downshift of about 13 cm^{-1} and does not display a new peak associated with the C–S bond, which provides evidence as to why the LBP only displays mild interactions with the Li_2S_6 solution.

Before electrochemical testing, electrodes consisting of 80 % carbon black and 20 % HBA were fabricated and assembled into half-cells. These cells were then subjected to cyclic voltammetry at $0.05\text{ mV}\cdot\text{s}^{-1}$ to investigate the stability of the HBA in the electrolyte, with the

voltammogram shown in **Fig. 5.5a**. As there is no electrochemical peak during the anodic or cathodic scans, it can be inferred that the HBA is stable in the electrolyte during charge/discharge and does not contribute electrochemically to the reaction.

Next, electrochemical evaluation was carried out to determine if the polysulfide anchoring ability and superior mechanical properties of the HBA actualised an enhanced electrochemical performance. Sulfur cathodes using the HBA, LBP, and PVDF binders were used to fabricate sulfur composite electrodes and are denoted as S/HBA, S/LBP, and S/PVDF, respectively. First, galvanostatic charge-discharge testing at various current densities was carried out on the S/PVDF, S/LBP, and S/HBA batteries. **Fig. 5.5b** shows the cells' discharge capacity and Coulombic efficiency at 0.5 C ($1\text{ C} = 1,672\text{ mAh}\cdot\text{g}^{-1}$). The discharge capacity in the initial cycle for the S/PVDF, S/LBP, and S/HBA-based cells are 751, 817, and 866 $\text{mAh}\cdot\text{g}^{-1}$, respectively. After 500 cycles, the S/PVDF, S/LBP, and S/HBA cells deliver a capacity of 285, 354, and 392 $\text{mAh}\cdot\text{g}^{-1}$, corresponding to a 0.124, 0.113, and 0.109 % capacity fade per cycle, respectively. In **Fig. 5.5c**, the current density increases to 2 C, with the cells again being subjected to 500 charge/discharge cycles, after which the superior capacity retention of the S/HBA-based cell is highlighted. The S/PVDF and S/LBP cells again deliver similar initial performances, with the S/HBA cell suffering from a higher capacity fade per cycle in the initial 3 cycles. Despite this, the S/HBA cell suffers the smallest capacity fade from the 4th cycle onwards and delivers the highest discharge capacity of 328 $\text{mAh}\cdot\text{g}^{-1}$ at the 500th cycle. The capacity fade per cycle during testing is 0.124, 0.137, and 0.104 % for the S/PVDF, S/LBP, and S/HBA cells, with the fade per cycle for the S/HBA cell dropping to 0.0845 % when calculated from the 4th cycle onwards.

The amount of active materials at the cathode is also crucial for Li-S battery commercialisation [34]. Therefore, S/PVDF, S/LBP, and S/HBA electrodes were fabricated with a sulfur loading of roughly $2\text{ mg}\cdot\text{cm}^{-2}$ and subjected to charge/discharge testing at 0.2 C, with the results shown in **Fig. 5.5d**. Even at a higher material loading, the S/HBA electrode delivers a higher initial capacity of 978 $\text{mAh}\cdot\text{g}^{-1}$, a reversible capacity of 842 $\text{mAh}\cdot\text{g}^{-1}$ at the 50th cycle, and a capacity fading of 0.278% per cycle over the tested range, again outperforming both the S/LBP and S/PVDF batteries. Thus, galvanostatic charge/discharge testing reveals that the S/HBA cell delivers a higher reversible capacity and lower capacity fading per cycle at various current densities and sulfur loadings compared with cells fabricated using either PVDF or LBP binders.

Rate performance is another critical parameter for electrochemical cells because charging/discharging in real situations is rarely galvanostatic. Thus, to evaluate the performance under differing current densities, rate performance testing was carried out with the results shown in **Fig. 5.6**. The cells were charged and discharged at progressively larger current densities (**Fig. 5.6a-i, b-i, c-i**) before being subjected to a final cycle at 0.2 C to observe the electrochemical performance after high rate testing, with the charge/discharge profile of the two 0.2 C cycles shown in **Fig. 5.6a-ii, b-ii, c-ii**. The S/HBA cell delivers a higher discharge capacity and lower overpotential at all current densities than both the S/LBP and S/PVDF cells, reflecting the galvanostatic charge/discharge results shown in **Fig. 5.5**. Additionally, when observing the charge curve at 2 C, the S/HBA cell is smooth with no irregularities (**Fig. 5.6c-i**), whereas the same curve in the S/PVDF cell shows inhomogeneity (**Fig. 5.6a-i**).

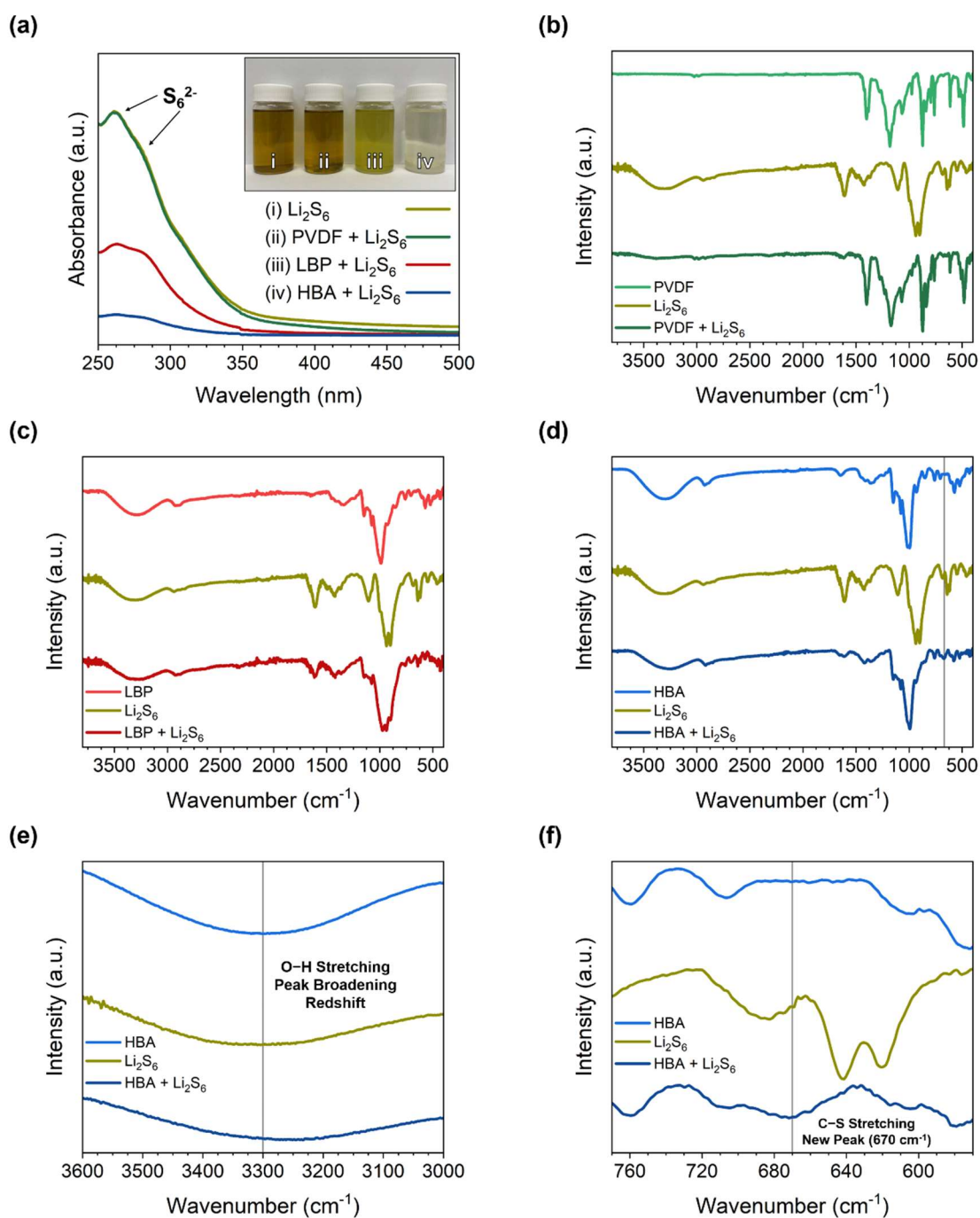


Figure 5.4: (a) UV-Vis spectra of the Li_2S_6 , $\text{Li}_2\text{S}_6 + \text{PVDF}$, $\text{Li}_2\text{S}_6 + \text{LBP}$, and $\text{Li}_2\text{S}_6 + \text{HBA}$ solutions with digital photographs of the respective solutions (inset). (b) FTIR spectra of PVDF , Li_2S_6 , and $\text{PVDF} + \text{Li}_2\text{S}_6$ samples. (c) FTIR spectra of LBP , Li_2S_6 , and $\text{LBP} + \text{Li}_2\text{S}_6$ samples. (d) FTIR spectra of HBA , Li_2S_6 , and $\text{HBA} + \text{Li}_2\text{S}_6$ samples. Magnified regions of the HBA , Li_2S_6 , and $\text{HBA} + \text{Li}_2\text{S}_6$ FTIR spectra showing the (e) O–H stretching and (f) C–S stretching regions

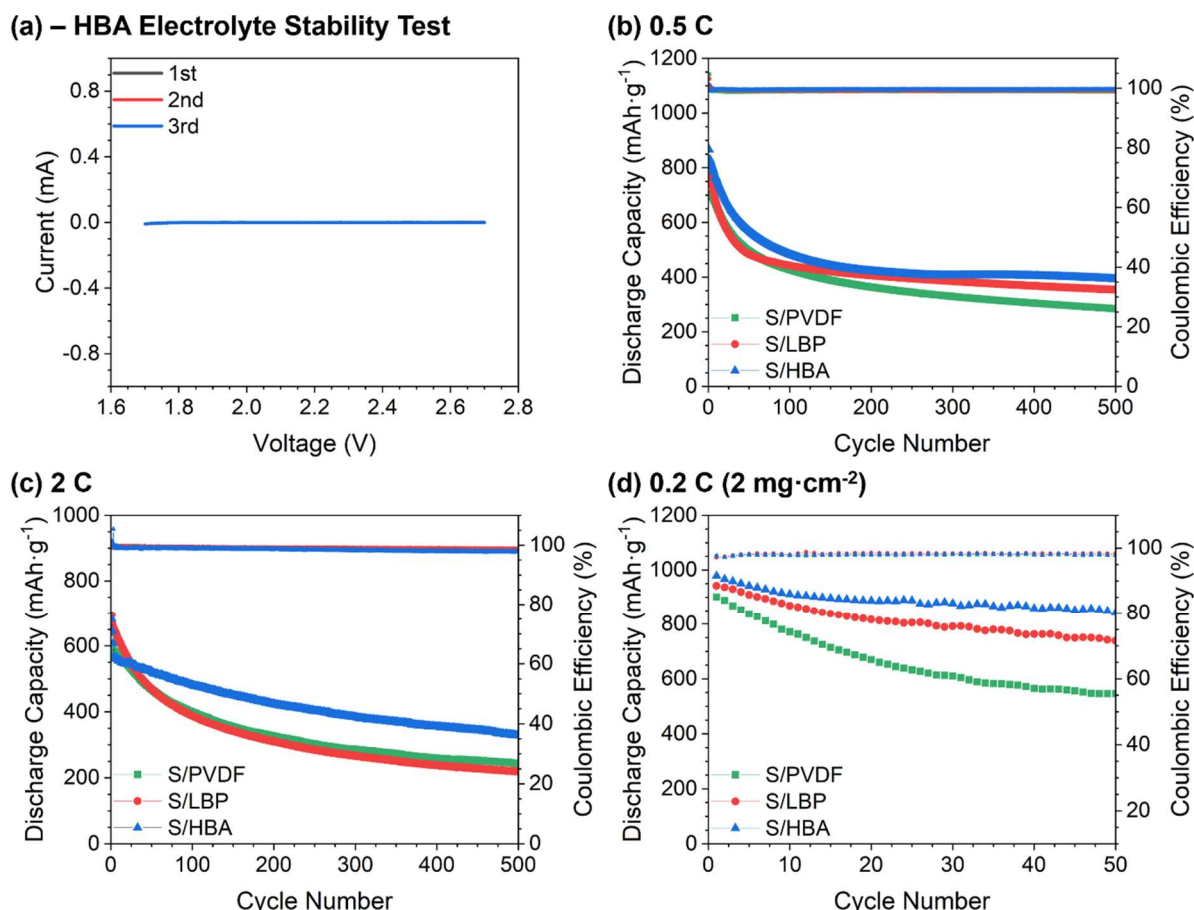


Figure 5.5: (a) Cyclic voltammogram of the CB:HBA (80:20) electrode for electrolyte stability testing. Cycle performance of the S/PVDF, S/LBP, and S/HBA electrodes at (b) 0.5 C, (c) 2 C, and (d) 0.2 C

Furthermore, it can be observed that even at 2 C, the S/HBA cell exhibits the two clear characteristic discharge plateaus associated with the Li–S battery, whereas the plateaus in both the S/PVDF and S/LBP curves become less pronounced, which may explain the enhanced performance of the S/HBA cell at higher current densities. Upon observing the charge/discharge profile of the 0.2 C cycle before and after rate testing, it is clear that the S/HBA cell delivers a higher initial discharge capacity and a higher discharge capacity after cycling at high rates. The discharge capacity retention after rate performance testing was found to be 86.3, 81.7, and 94.6 % retention for the S/PVDF, S/LBP, and S/HBA-based cells, respectively. The rate performance results demonstrate that the S/HBA cell delivers higher discharge capacities at high current densities and retains more capacity when reverting to lower current density cycling than both the S/LBP and S/PVDF cells.

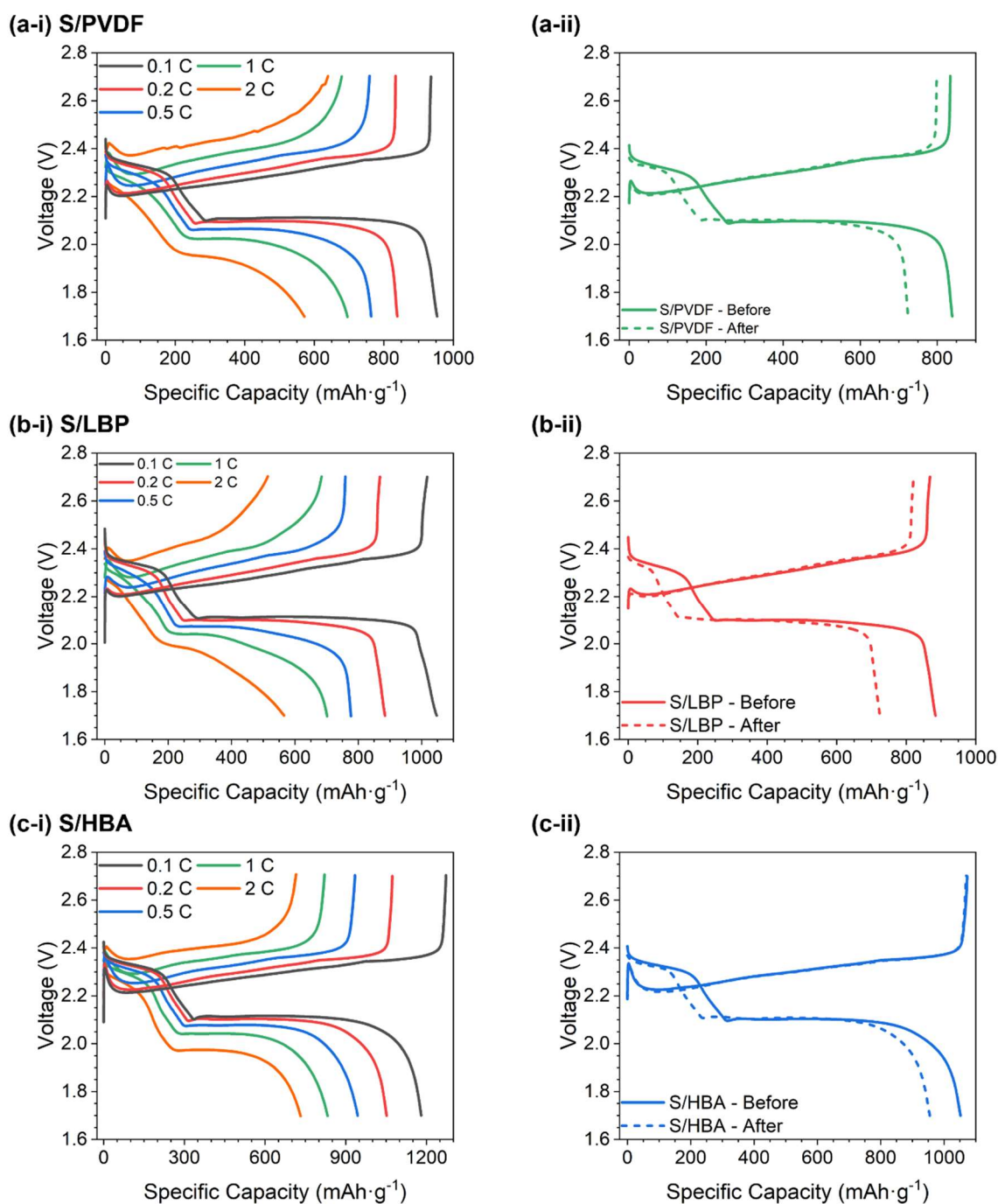


Figure 5.6: Capacity/Voltage profile of the (a) S/PVDF, (b) S/LBP, and (c) S/HBA cells (i) during rate capability testing and (ii) for the two 0.2 C cycles

To investigate the reaction kinetics in the S/PVDF, S/LBP and S/HBA cells, cyclic voltammetry at varying scan rates was carried out so that the lithium-ion diffusion (D_{Li}) properties could be evaluated (**Fig. 5.7**) [66]. The cells display similar electrochemical reaction voltages; however, the S/HBA cell displays much higher peak currents at all reaction steps than the S/PVDF cell. Compared with the S/LBP cell, the S/HBA cell displays a similar peak current

in the anodic scan but a much higher peak current in the cathodic scan, suggesting much faster reaction kinetics.

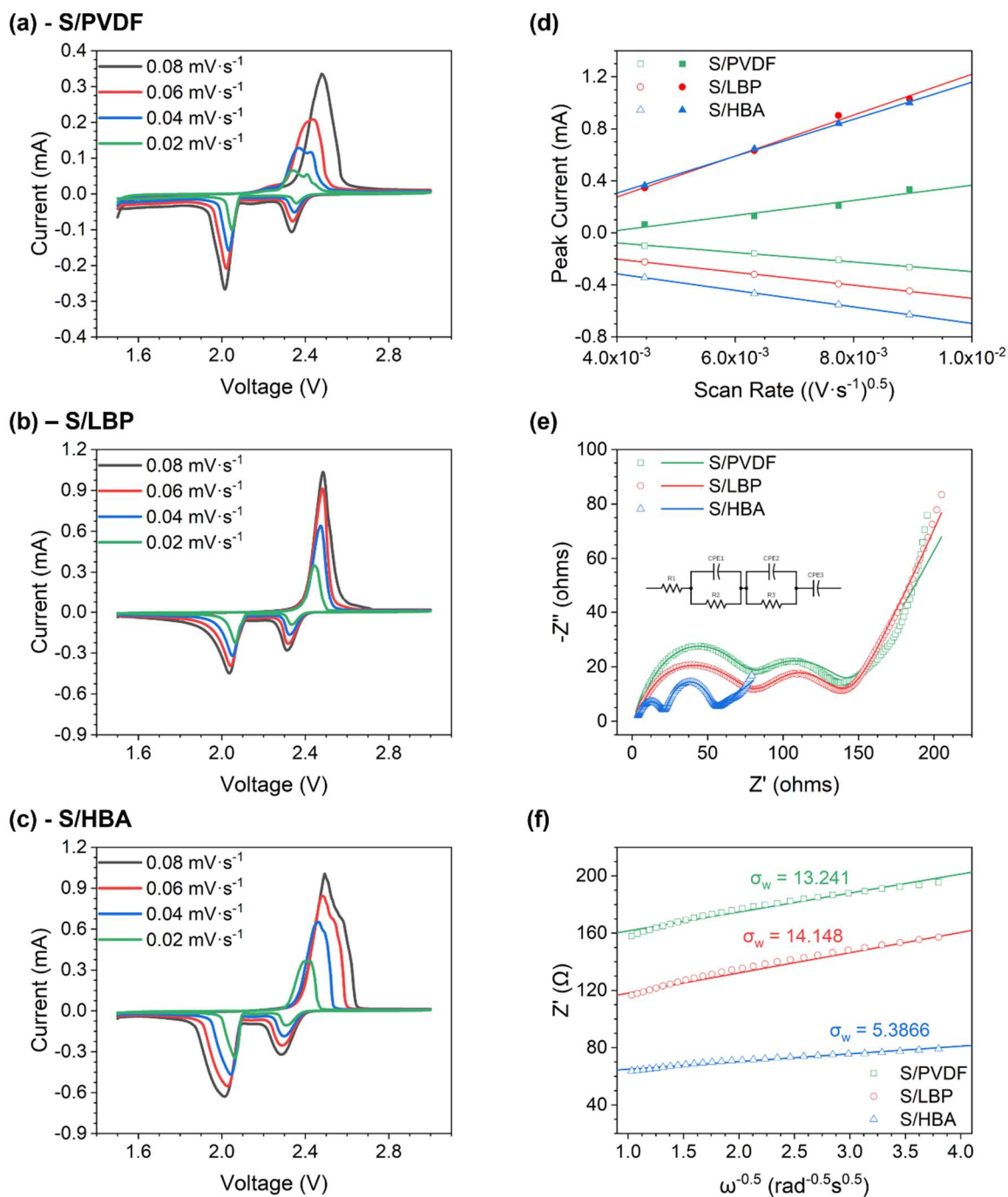


Figure 5.7: Cyclic Voltammograms (CV) of the (a) S/PVDF, (b) S/LBP, and (c) S/HBA electrodes. (d) Peak current (I_p) vs. the square root of the scan rate. (e) EIS spectra of the S/PVDF, S/LBP, and S/HBA electrodes after 20 cycles at 0.2C with the equivalent circuit using for EIS fitting (inset). (f) Z' vs. $\omega^{-1/2}$ showing the Warburg factor (σ_w)

After plotting the peak current (I_p) against the square of the scan rate ($v^{0.5}$) (**Fig. 5.7d**), a linear relationship is observed, indicating a diffusion-controlled process [67]. Thus, according to the Randles-Sevcik equation (**Eqn. 5.1**), a steeper gradient in **Fig. 5.7d** can be related to a higher D_{Li} [68]. As a result, the S/HBA cell displays better Li^+ diffusion when compared to the S/PVDF and S/LBP cells. This phenomenon may explain the enhanced performance, especially at the higher current rate of 2 C.

$$I_p = 2.686 \cdot 10^5 n^{\frac{3}{2}} A D^{\frac{1}{2}} C v^{\frac{1}{2}} \quad (5.1)$$

$$|Z'| = R_{ct} + R_{int} + \sigma_W \omega^{-0.5} \quad (5.2)$$

$$D_{Li} = \frac{R^2 T^2}{2 A^2 n^4 F^4 C^2 \sigma_W^2} \quad (5.3)$$

To further investigate the electrochemical performance, the S/PVDF, S/LBP, and S/HBA cells were also subjected to electrochemical impedance spectroscopy (EIS) analysis after 20 cycles at 0.2 C with the experimental and fitting results shown in **Fig. 5.7e**. The equivalent circuits used for fitting are shown in the inset of **Fig. 5.7e**. Depressed semi-circles in the high to medium frequency region of the spectra can be observed, which can be attributed to the electrolyte resistance (R_e), charge transfer resistance (R_{ct}), and interface/solid electrolyte interface resistance (R_{int}), respectively [69]. As the S/HBA cell displays lower resistances in all cases (**Table 5.1**), it can be inferred that the HBA better maintains the conductive carbon network after cycling compared to when PVDF or LBP is used as a binder. The linear portion of the curve in the low-frequency region of **Fig. 5.7e** can be attributed to the Warburg (W_o) impedance in the cells [70]. By graphing the real portion of the impedance (Z') in the linear region of the EIS spectra and $\omega^{-1/2}$ (**Fig. 5.7f**), the Warburg factor (σ_W) can be calculated through the equation shown in **Eqn. 5.2** [71]. The Warburg factor is inversely proportional to D_{Li} , as shown in **Eqn. 5.3** [72]. As the S/HBA cell displays the smallest σ_W , it is inferred that the S/HBA cell displays the best lithium ion diffusion throughout the electrode matrix, again supporting the enhanced electrochemical performance at the high discharge rate of 2 C.

Table 5.1: Fitting results from EIS analysis

	S/PVDF	S/LBP	S/HBA
R_e	3.12 Ω	1.93 Ω	2.62 Ω
R_{ct}	73.12 Ω	58.85 Ω	17.71 Ω
R_{int}	63.72 Ω	37.71 Ω	27.51 Ω

To further explain the enhanced performance of the S/HBA battery, post-mortem SEM and EDS analysis was carried out before and after the high-loading S/HBA, S/LBP, and S/PVDF cells were subjected to 20 cycles at 0.2 C. **Fig. 5.8** shows the morphology of the S/PVDF (**Fig. 5.8a**), S/LBP (**Fig. 5.8b**), and S/HBA (**Fig. 5.8c**) electrode's (i) surface before cycling, (ii) surface after cycling, and (iii) cross-section after cycling. Before cycling, the S/PVDF, S/LBP, and S/HBA electrodes display relatively comparable morphologies. However, after cycling, the difference between the electrodes becomes pronounced. **Fig. 5.8c-ii** shows that the S/HBA electrode maintains a relatively homogeneous surface with minimal large pits, with no observable $\text{Li}_2\text{S}/\text{Li}_2\text{S}_2$ formation remaining on the electrode surface. The S/LBP electrode displays a similar morphology to the S/HBA electrode, albeit with slightly more surface irregularities (**Fig. 5.8b-ii**). In contrast, **Fig. 5.8a-ii** shows that after cycling, the S/PVDF electrode displays large pits and evident precipitation of the active materials, which is highlighted in yellow.

Cross-sectional images of the high-loading electrodes were also taken to observe the lateral homogeneity of the three electrodes. As shown in **Fig. 5.8a-iii**, the S/PVDF electrode is roughly 50 μm thick and highlights that the extremely rough surface morphology persists throughout the whole depth of the electrode. The evident electroactive material precipitation is also highlighted in the cross-sectional view. Conversely, the two starch-based electrodes display a more compact cross-section with depths of roughly 30 μm , as shown in **Fig. 5.8b-iii and c-iii**. The HBA-based cross-section displays the electrodes' dense and homogeneous morphology, reflecting the surface morphology SEM images discussed previously and is attributed to the HBA-binder's outstanding mechanical and adhesive properties.

To examine the elemental distributions and homogeneity of the three electrodes, energy-dispersive X-ray spectroscopic (EDS) analysis was carried out on the cycled electrodes, with the results shown in **Fig. 5.9**. The EDS results demonstrate that the S/HBA electrode was the most homogeneous after cycling, with the S/PVDF being the least. Overall, the smooth and homogenous electrode morphology, achieved through the enhanced mechanical and adhesive properties of the HBA, suggests the maintenance of a robust electronically conductive network. This feature, combined with the polysulfide anchoring ability of the HBA, can explain the enhanced capacity retention during charge/discharge testing and the enhanced reaction kinetics observed in the CV and EIS testing.

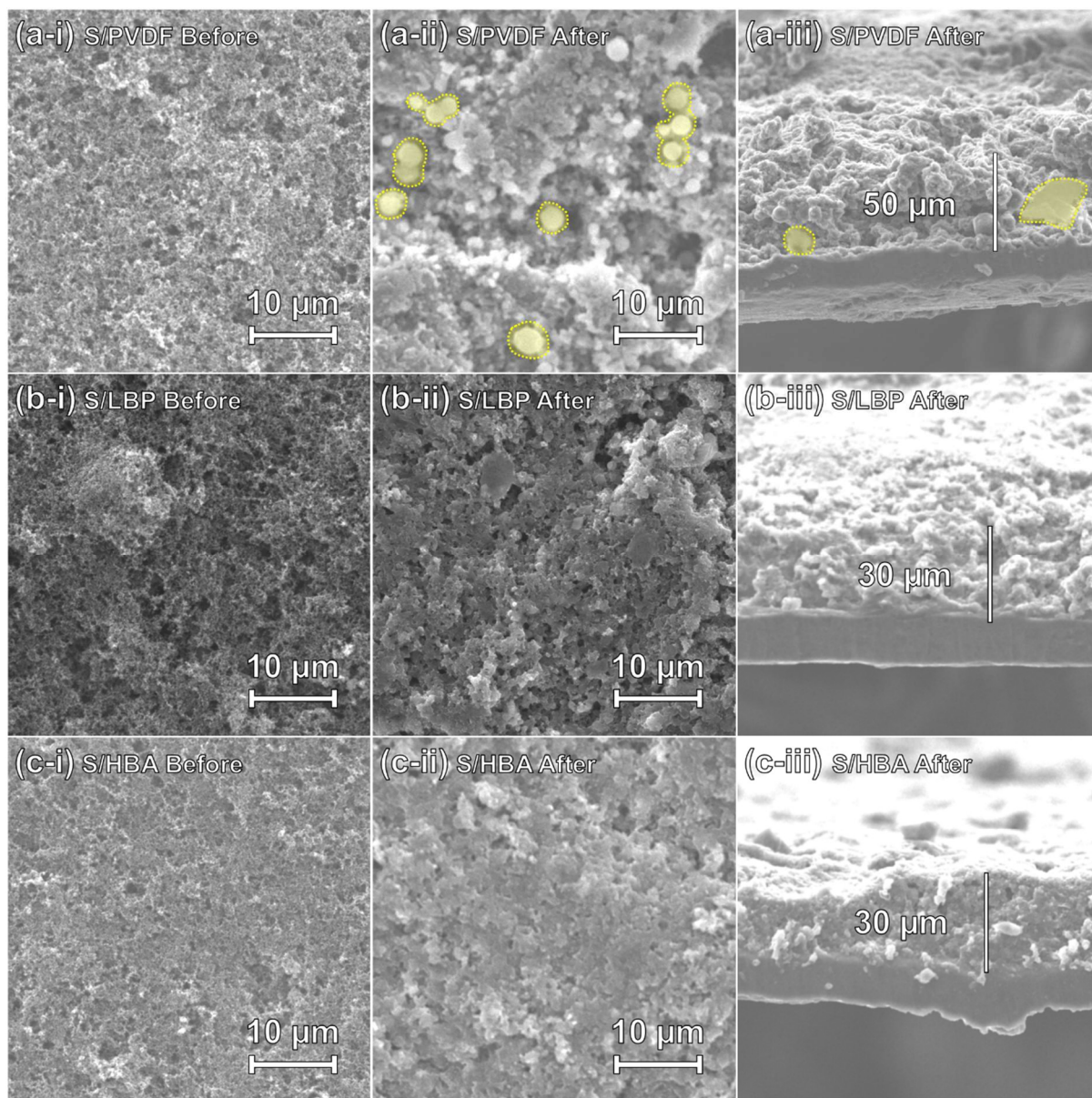


Figure 5.8: SEM images of the (a) S/PVDF, (b) S/LBP, and (c) S/HBA electrode's (i) surface before cycling (ii) surface after cycling, and (iii) cross-section after cycling

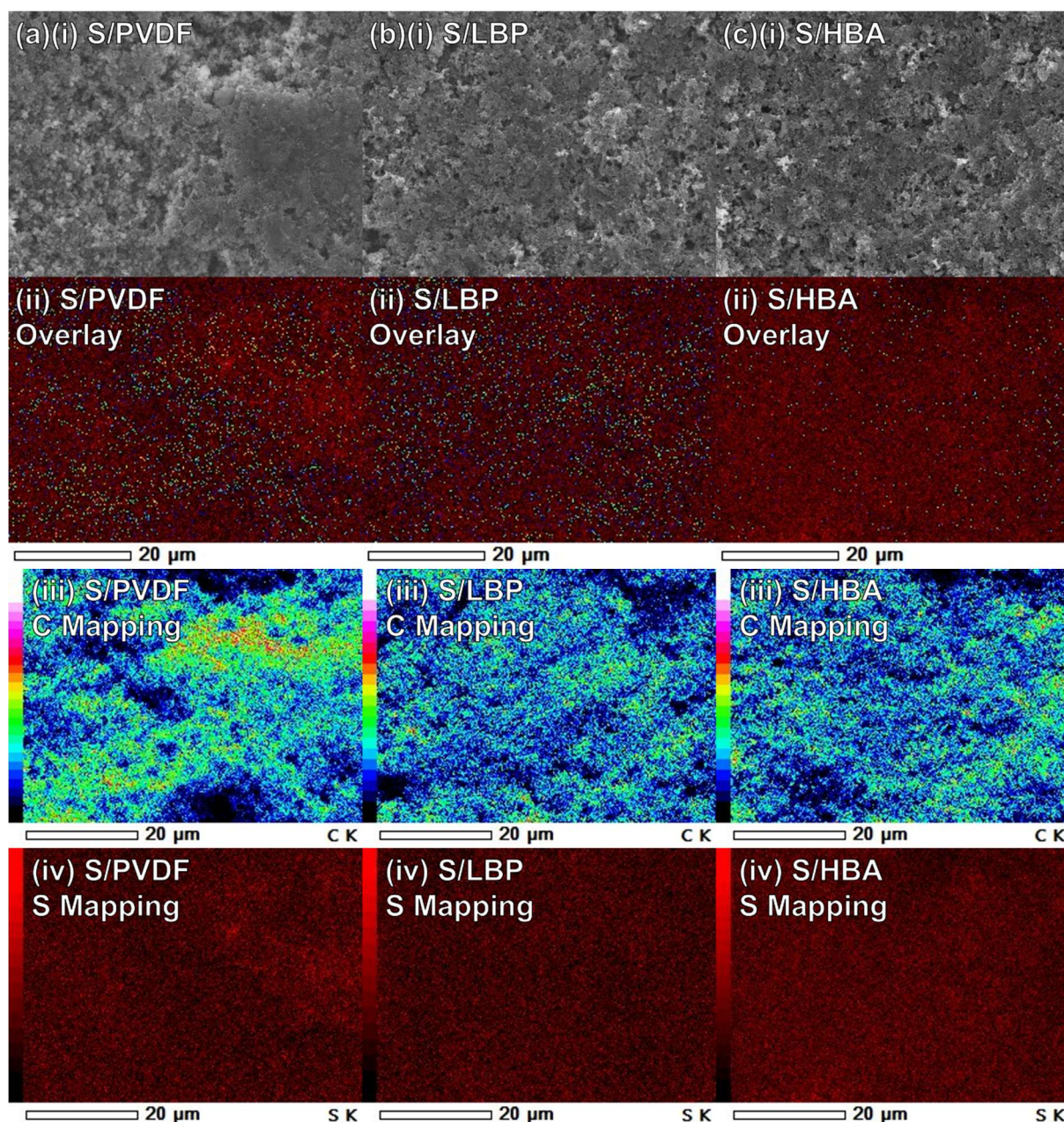


Figure 5.9: Energy-dispersive X-ray spectroscopy (EDS) results showing the (i) SEM image, (ii) elemental mapping overlay, (iii) carbon distribution, and (iv) sulfur distribution for the (a) S/PVDF, (b) S/LBP, and (c) S/HBA electrode after cycling

5.5 Conclusion

Natural polysaccharides binders, including highly-branched amylopectin (HBA) and lowly-branched polysaccharide (LBP) binders, were successfully extracted, characterised, and applied during the fabrication of sulfur cathodes (i.e., the S/HBA and S/LBP electrodes) for Li–S batteries. The S/HBA cathode significantly outperforms the conventional S/ PVDF and S/LBP cathodes due to the highly-branched structure and abundant hydroxyl functional groups

of the HBA. After 500 cycles, the S/HBA cathode could still deliver a reversible capacity of $396 \text{ mAh}\cdot\text{g}^{-1}$ (0.101 % fading per cycle) at 0.5 C and 328 (0.104 % fading per cycle) at 2 C, which is remarkable in comparison to both the S/LBP and S/PVDF cathodes. Such an enhanced performance of the S/HBA cells can be explained through two mechanisms. Firstly, the HBA possesses the ability to chemically retain soluble polysulfide molecules at the cathode as it possesses abundant lone-pair rich hydroxyl groups along with the ability to form the C–S bonds with soluble polysulfides. Secondly, HBA displays outstanding mechanical properties that can help maintain a robust conductive network after extended cycling, facilitating the rapid electrochemical reaction kinetics of the charge and discharge processes and evidenced by the EIS and CV characterisations. Furthermore, HBA could be readily obtained from the environment, representing a low-cost, non-toxic, and sustainable natural product. Therefore, this work inspires the modern battery industry to develop towards high performance and low cost and towards environmentally-friendly trends and sustainability.

5.6 References

1. Dincer, I., *Renewable energy and sustainable development: a crucial review*. Renewable and Sustainable Energy Reviews, 2000. **4**(2): p. 157-175.
2. Owusu, P.A. and S. Asumadu-Sarkodie, *A review of renewable energy sources, sustainability issues and climate change mitigation*. Cogent Engineering, 2016. **3**(1): p. 1167990.
3. Solaun, K. and E. Cerdá, *Climate change impacts on renewable energy generation. A review of quantitative projections*. Renewable and Sustainable Energy Reviews, 2019. **116**: p. 109415.
4. Shafiullah, G.M., et al., *Prospects of renewable energy – a feasibility study in the Australian context*. Renewable Energy, 2012. **39**(1): p. 183-197.
5. Zahedi, A., *Australian renewable energy progress*. Renewable and Sustainable Energy Reviews, 2010. **14**(8): p. 2208-2213.
6. Denholm, P., et al., *Role of energy storage with renewable electricity generation*. 2010, National Renewable Energy Lab.(NREL), Golden, CO (United States).
7. Castillo, A. and D.F. Gayme, *Grid-scale energy storage applications in renewable energy integration: A survey*. Energy Conversion and Management, 2014. **87**: p. 885-894.
8. Olabi, A.G., *Renewable energy and energy storage systems*. Energy, 2017. **136**: p. 1-6.
9. Yang, Z., et al., *Electrochemical Energy Storage for Green Grid*. Chemical Reviews, 2011. **111**(5): p. 3577-3613.
10. Fotouhi, A., et al., *A review on electric vehicle battery modelling: From Lithium-ion toward Lithium–Sulphur*. Renewable and Sustainable Energy Reviews, 2016. **56**: p. 1008-1021.
11. Wang, Y., et al., *Sulfur Hosts against the Shuttle Effect*. Small Methods, 2018.
12. Huang, S., et al., *Recent Advances in Heterostructure Engineering for Lithium–Sulfur Batteries*. Advanced Energy Materials, 2021. **11**(10): p. 2003689.
13. Hofmann, A.F., D.N. Fronczek, and W.G. Bessler, *Mechanistic modeling of polysulfide shuttle and capacity loss in lithium–sulfur batteries*. Journal of Power Sources, 2014. **259**: p. 300-310.
14. Cheon, S.-E., et al., *Rechargeable Lithium Sulfur Battery*. Journal of The Electrochemical Society, 2003. **150**(6): p. A800.
15. Peled, E., et al., *Lithium-Sulfur Battery: Evaluation of Dioxolane-Based Electrolytes*. Journal of The Electrochemical Society, 1989. **136**(6): p. 1621-1625.

16. Mikhaylik, Y.V. and J.R. Akridge, *Polysulfide Shuttle Study in the Li/S Battery System*. Journal of The Electrochemical Society, 2004. **151**(11): p. A1969.
17. Mistry, A.N. and P.P. Mukherjee, “*Shuttle*” in *Polysulfide Shuttle: Friend or Foe?* The Journal of Physical Chemistry C, 2018. **122**(42): p. 23845-23851.
18. Moy, D., A. Manivannan, and S.R. Narayanan, *Direct Measurement of Polysulfide Shuttle Current: A Window into Understanding the Performance of Lithium-Sulfur Cells*. Journal of The Electrochemical Society, 2014. **162**(1): p. A1-A7.
19. Zhou, G., et al., *Catalytic oxidation of Li₂S on the surface of metal sulfides for Li–S batteries*. Proceedings of the National Academy of Sciences, 2017. **114**(5): p. 840-845.
20. Liu, B., et al., *Revisiting Scientific Issues for Industrial Applications of Lithium–Sulfur Batteries*. ENERGY & ENVIRONMENTAL MATERIALS, 2018. **1**(4): p. 196-208.
21. Barai, P., A. Mistry, and P.P. Mukherjee, *Poromechanical effect in the lithium–sulfur battery cathode*. Extreme Mechanics Letters, 2016. **9**: p. 359-370.
22. He, G., et al., *Tailoring Porosity in Carbon Nanospheres for Lithium–Sulfur Battery Cathodes*. ACS Nano, 2013. **7**(12): p. 10920-10930.
23. Dörfler, S., et al., *Recent Progress and Emerging Application Areas for Lithium–Sulfur Battery Technology*. Energy Technology, 2021. **9**(1): p. 2000694.
24. Deng, R., et al., *Recent Advances and Applications Towards Emerging Lithium-Sulfur Batteries: Working Principles and Opportunities*. ENERGY & ENVIRONMENTAL MATERIALS, 2021. **n/a**(n/a).
25. Zhao, H., et al., *A review on anode for lithium-sulfur batteries: Progress and prospects*. Chemical Engineering Journal, 2018. **347**: p. 343-365.
26. Lin, Y., et al., *Organic liquid electrolytes in Li–S batteries: actualities and perspectives*. Energy Storage Materials, 2021. **34**: p. 128-147.
27. Ponnada, S., et al., *Insight into Lithium–Sulfur Batteries with Novel Modified Separators: Recent Progress and Perspectives*. Energy & Fuels, 2021. **35**(14): p. 11089-11117.
28. Wei, S., et al., *Pig bone derived hierarchical porous carbon and its enhanced cycling performance of lithium–sulfur batteries*. Energy & Environmental Science, 2011. **4**(3): p. 736-740.
29. Wang, M., et al., *Porous Carbon Hosts for Lithium–Sulfur Batteries*. Chemistry – A European Journal, 2019. **25**(15): p. 3710-3725.
30. Jiang, G., et al., *Mesoporous, conductive molybdenum nitride as efficient sulfur hosts for high-performance lithium-sulfur batteries*. Journal of Power Sources, 2018. **395**: p. 77-84.

31. Hou, T.-Z., et al., *Design Principles for Heteroatom-Doped Nanocarbon to Achieve Strong Anchoring of Polysulfides for Lithium–Sulfur Batteries*. Small, 2016. **12**(24): p. 3283-3291.
32. Liang, X., et al., *Tuning Transition Metal Oxide–Sulfur Interactions for Long Life Lithium Sulfur Batteries: The “Goldilocks” Principle*. Advanced Energy Materials, 2016. **6**(6): p. 1501636.
33. Chen, L., X. Li, and Y. Xu, *Recent Advances of Polar Transition-Metal Sulfides Host Materials for Advanced Lithium–Sulfur Batteries*, in *Functional Materials for Next-Generation Rechargeable Batteries*. 2020, WORLD SCIENTIFIC. p. 47-64.
34. Hencz, L., et al., *Housing Sulfur in Polymer Composite Frameworks for Li–S Batteries*. Nano-Micro Letters, 2019. **11**(1): p. 17.
35. Cleaver, T., et al., *Perspective—Commercializing Lithium Sulfur Batteries: Are We Doing the Right Research?* Journal of The Electrochemical Society, 2018. **165**(1): p. A6029-A6033.
36. Chen, H., et al., *Exploring Chemical, Mechanical, and Electrical Functionalities of Binders for Advanced Energy-Storage Devices*. Chemical Reviews, 2018.
37. Yuan, H., et al., *A Review of Functional Binders in Lithium–Sulfur Batteries*. Advanced Energy Materials, 2018. **8**(31): p. 1802107.
38. Li, G., et al., *Acacia Senegal–inspired bifunctional binder for longevity of lithium–sulfur batteries*. Advanced Energy Materials, 2015. **5**(21).
39. Jeon, J., et al., *Natural-Wood-Derived Lignosulfonate Ionomer as Multifunctional Binder for High-Performance Lithium–Sulfur Battery*. ACS Sustainable Chemistry & Engineering, 2019. **7**(21): p. 17580-17586.
40. Chen, L., et al., *Highly stabilized sulfur cathode with natural fenugreek gum as binder*. Chemical Engineering Journal, 2020: p. 127769.
41. Jane, J., *Starch Properties, Modifications, and Applications*. Journal of Macromolecular Science, Part A, 1995. **32**(4): p. 751-757.
42. Ogunsona, E., E. Ojogbo, and T. Mekonnen, *Advanced material applications of starch and its derivatives*. European Polymer Journal, 2018. **108**: p. 570-581.
43. Zou, W., et al., *Effects of amylose/amylopectin ratio on starch-based superabsorbent polymers*. Carbohydrate Polymers, 2012. **87**(2): p. 1583-1588.
44. Jane, J., et al., *Effects of Amylopectin Branch Chain Length and Amylose Content on the Gelatinization and Pasting Properties of Starch*. Cereal Chemistry, 1999. **76**(5): p. 629-637.

45. Mukherjee, P.K., *Chapter 7 - Bioactive Phytochemicals and Their Analysis*, in *Quality Control and Evaluation of Herbal Drugs*, P.K. Mukherjee, Editor. 2019, Elsevier. p. 237-328.
46. Chung, H.-J., et al., *Relationship between the structure, physicochemical properties and in vitro digestibility of rice starches with different amylose contents*. Food Hydrocolloids, 2011. **25**(5): p. 968-975.
47. Luo, Y.-B. and Y.-J. Zhang, *Investigation of sticky-rice lime mortar of the Horse Stopped Wall in Jiange*. Heritage Science, 2013. **1**(1): p. 26.
48. Yang, F., et al., *Traditional mortar represented by sticky rice lime mortar—One of the great inventions in ancient China*. Science in China Series E: Technological Sciences, 2009. **52**(6): p. 1641-1647.
49. Hapuarachchi, S.N.S., et al., *Mechanically Robust Tapioca Starch Composite Binder with Improved Ionic Conductivity for Sustainable Lithium-Ion Batteries*. ACS Sustainable Chemistry & Engineering, 2020. **8**(26): p. 9857-9865.
50. Bie, Y., et al., *Oxidized starch as a superior binder for silicon anodes in lithium-ion batteries*. RSC Advances, 2016. **6**(99): p. 97084-97088.
51. Jin, B., et al., *Biomass-derived fluorinated corn starch emulsion as binder for silicon and silicon oxide based anodes in lithium-ion batteries*. Electrochimica Acta, 2021. **365**: p. 137359.
52. Rohan, R., et al., *Low-cost and sustainable corn starch as a high-performance aqueous binder in silicon anodes via in situ cross-linking*. Journal of Power Sources, 2018. **396**: p. 459-466.
53. Duan, X., et al., *Improved capacity retention of low cost sulfur cathodes enabled by a novel starch binder derived from food*. Rsc Advances, 2014. **4**(105): p. 60995-61000.
54. Juhász, R. and A. Salgó, *Pasting Behavior of Amylose, Amylopectin and Their Mixtures as Determined by RVA Curves and First Derivatives*. Starch - Stärke, 2008. **60**(2): p. 70-78.
55. Liu, X., et al., *Thermal Decomposition of Corn Starch with Different Amylose/Amylopectin Ratios in Open and Sealed Systems*. Cereal Chemistry, 2009. **86**(4): p. 383-385.
56. Nishiyama, T., et al., *Crystalline structure control of poly(vinylidene fluoride) films with the antisolvent addition method*. Polymer Journal, 2016. **48**(10): p. 1035-1038.
57. Barrau, S., et al., *Nanoscale Investigations of α - and γ -Crystal Phases in PVDF-Based Nanocomposites*. ACS Applied Materials & Interfaces, 2018. **10**(15): p. 13092-13099.

58. Todica, M., et al., *XRD Investigation of Some Thermal Degraded Starch Based Materials*. Journal of Spectroscopy, 2016. **2016**: p. 9605312.
59. Chen, S., et al., *Development of cross-linked dextrin as aqueous binders for silicon based anodes*. Journal of Power Sources, 2020. **450**: p. 227671.
60. Ling, M., et al., *Multifunctional SA-PProDOT Binder for Lithium Ion Batteries*. Nano Letters, 2015. **15**(7): p. 4440-4447.
61. Zhou, G., et al., *Free-standing TiO₂ nanowire-embedded graphene hybrid membrane for advanced Li/dissolved polysulfide batteries*. Nano Energy, 2015. **12**: p. 240-249.
62. Ma, Y., et al., *Assessment of Polysaccharides from Mycelia of genus Ganoderma by Mid-Infrared and Near-Infrared Spectroscopy*. Scientific Reports, 2018. **8**(1): p. 10.
63. Warren, F.J., M.J. Gidley, and B.M. Flanagan, *Infrared spectroscopy as a tool to characterise starch ordered structure—a joint FTIR–ATR, NMR, XRD and DSC study*. Carbohydrate Polymers, 2016. **139**: p. 35-42.
64. Ling, H.Y., et al., *Sustainable okra gum for silicon anode in lithium-ion batteries*. Sustainable Materials and Technologies, 2021. **28**: p. e00283.
65. Qian, W. and S. Krimm, *Conformation dependence of the SH and CS stretch frequencies of the cysteine residue*. Biopolymers, 1992. **32**(11): p. 1503-1518.
66. Gao, X., et al., *Strong charge polarization effect enabled by surface oxidized titanium nitride for lithium-sulfur batteries*. Communications Chemistry, 2019. **2**(1): p. 66.
67. Zhou, G., et al., *Catalytic oxidation of Li₂S on the surface of metal sulfides for Li–S batteries*. Proceedings of the National Academy of Sciences, 2017. **114**(5): p. 840-845.
68. Tao, X., et al., *Balancing surface adsorption and diffusion of lithium-polysulfides on nonconductive oxides for lithium–sulfur battery design*. Nature Communications, 2016. **7**(1): p. 11203.
69. Geng, X., et al., *Water Reducer: A Highly Dispersing Binder for High-Performance Lithium-Sulfur Batteries†*. Chinese Journal of Chemistry, 2021. **39**(6): p. 1523-1530.
70. Jing, H.-K., et al., *Protected lithium anode with porous Al₂O₃ layer for lithium–sulfur battery*. Journal of Materials Chemistry A, 2015. **3**(23): p. 12213-12219.
71. Wang, Y., et al., *Manipulation of Edge-Site Fe–N₂ Moiety on Holey Fe, N Codoped Graphene to Promote the Cycle Stability and Rate Capacity of Li–S Batteries*. Advanced Functional Materials, 2019. **29**(5): p. 1807485.
72. Li, B., et al., *Facile synthesis of Li₄Ti₅O₁₂/C composite with super rate performance*. Energy & Environmental Science, 2012. **5**(11): p. 9595-9602.

Chapter 6:
Oxygen-Rich Hierarchical Porous Carbon Host
(HPCH) for Li–S Cathodes

6.1 Abstract

Lithium-sulfur (Li-S) batteries could usurp the dominant current generation LIBs due to their superior theoretical capacity and energy density. However, the Li-S cell suffers from rapid capacity fading due to polysulfide dissolution and shuttling, low active material loading in the cathode, and sluggish reaction kinetics. These shortfalls can be combatted by applying sulfur hosts, which can provide ample void structure, maintain electronic and ionic pathways, and retain soluble polysulfides at the cathode. This work aims to produce a hierarchical porous carbon via an environmentally friendly method and directly applies it into the sulfur composite cathode, forgoing a traditional sulfur impregnation at elevated temperature. The hierarchical porous carbon host (HPC) is shown to have an outstanding specific surface area of $1540 \text{ m}^2 \cdot \text{g}^{-1}$ with a favourable pore size distribution due to the unique solvent/porogen system employed during synthesis. The porous matrix can adsorb the polysulfides at the cathode through two mechanisms. Firstly, the polysulfides can be physically adsorbed in the porous structure of the HPC. Secondly, the polysulfides can be chemically retained by the hydroxyl and carbonyl groups located at the material's surface. The dual-action adsorption is shown to have a positive effect on the capacity retention of the as-fabricated cells.

Further electrochemical investigation reveals that the HPC enhances both the ionic and electronic conductivity of the S/HPC batteries. This two-fold mechanism allows a reversible capacity of nearly $500 \text{ mAh} \cdot \text{g}^{-1}$ to be obtained after 500 cycles at 0.5 C and enhanced performance at high C-rates. Overall, this work shows that a high-performance Li-S battery can be fabricated using the HPC synthesised through an environmentally friendly synthesis method.

Keywords

Hierarchical porous carbon, sulfur host, shuttle effect, polysulfide anchoring

Highlights

- Hierarchical porous carbon host (HPCH) is produced via an environmentally friendly method and applied as a sulfur host for Li–S battery cathodes
- A large surface area of $1540 \text{ m}^2 \cdot \text{g}^{-1}$ is achieved due to the homogeneous distribution of the KOH porogen through the novel synthesis method
- The HPCH adsorbs soluble polysulfides through two mechanisms, physically trapping in the nanopores and chemical adsorption at surface carbonyl and hydroxyl groups
- The HPCH increases both electronic conductivity and ion transfer in the sulfur composite cathode improving reaction kinetics
- The resulting S/HPCH Li–S cells deliver superior cycle life and rate performance while reducing the environmental impact of Li–S batteries

6.2 Introduction

The global climate crisis, primarily driven by CO₂ emissions arising from energy generation and transportation, threatens human society at large [1]. Fossil fuel-based energy generation and transportation must be phased out, favouring less environmentally damaging methods so that a lower emissions future can be realised and a climate catastrophe can be avoided [2]. Wind and solar have the substantial appeal of CO₂ emission-free energy production; however, they are limited in their uptake due to sporadic energy generation. Therefore, grid-scale energy storage systems are being considered [3]. Electric vehicles are also increasing their market share, displacing traditional internal combustion engine-based vehicles [4]. Secondary (or rechargeable) batteries, particularly lithium-ion batteries, have been crucial for the success of grid-scale energy storage systems and electric vehicles thus far [5, 6]. Despite this, the shortfalls of current generation lithium-ion batteries are becoming apparent, especially in fast charge/discharge settings [7] and in long-range electronic vehicles [8]. As such, researchers are currently investigating alternative battery chemistry options to ease the transition into a more sustainable energy future, with one such example being the lithium-sulfur (Li-S) battery [9].

Li-S batteries are a promising next-generation energy storage candidate due to their extremely high theoretical capacity (1672 mAh·g⁻¹) and energy density (ca. 2600 Wh·kg⁻¹) and may be particularly suitable for long-distance electric vehicle applications [10]. However, as with most emerging technologies, Li-S batteries suffer from inherent shortfalls. The most problematic being the low electronic conductivity of sulfur and its discharge products, the significant volumetric expansion of the active materials upon cycling, and the notorious shuttle effect [11]. Researchers have investigated many aspects of the Li-S cell to improve overall electrochemical performance, with one popular approach being the implementation of nanostructured and conductive sulfur hosts [12]. Cathodic sulfur hosts work to improve the electrochemical performance of Li-S batteries by improving conductivity, providing sufficient space to withstand active material volume expansion, and trapping the soluble polysulfides at the cathode through two mechanisms, physical trapping in nanopores and chemical adsorption through surface functionality [13]. Carbon hosts based upon hierarchical porous carbon, that is carbon-containing micro ($\varnothing \leq 2$ nm), meso ($2 \text{ nm} \leq \varnothing \leq 50$ nm), and macro ($\varnothing \geq 50$ nm) pores, are an appealing choice as their morphology allows for sufficient sulfur loadings, physical retention of polysulfides, electrolyte infiltration, and the ability to withstand volume expansion of the active materials [14-16].

Bottom-up synthesis methods for hierarchical porous carbons allow for a high degree of customisation. However, they are usually carried out on small scales and require templating with SiO₂ followed by HF etching [17], carbonisation of MOF frameworks [18], or complex multi-step organic synthesis [19]. Such complicated and expensive synthesis methods tend to produce the tailored materials on the scale of milligrams, which is far away from the kilogram scale required for the commercial application of host-based sulfur cathodes [20-22]. Furthermore, although remarkably effective, traditional sulfur hosts usually require a heat treatment process so that the sulfur can infiltrate the host matrix, which adds a step during electrode manufacturing. However, the heat-treatment step can be avoided by using an electrochemical infiltration cycle, and the manufacturing process can be simplified.

To this end, this work produces a hierarchical porous carbon host (HPCH) with a high surface area and chemical functionality due to the unique solvent/porogen system in the environmentally-friendly method without relying on hard-templating methods. The HPCH is then directly applied in the cathode without the sulfur infiltration step for Li-S batteries. The HPCH's porous carbon skeleton is expected to provide a large pore volume to trap soluble polysulfides physically, chemically trap polysulfides via abundant lone-pair rich carbonyl and hydroxyl groups, and improve both the electronic and ionic conductivity throughout the composite carbon cathode to bi-functionally enhance the electrochemical performance in Li-S cells. The resulting S/HPCH cells deliver a low capacity fading of 0.102 % per cycle after 500 cycles and superior electrochemical performance at a high C-rate of 2 C.

6.3 Experimental Section

6.3.1 Hierarchical Porous Carbon Host (HPCH) Synthesis

All reagents were obtained from Sigma-Aldrich and used without further purification. 1 g of D-(+)-glucose and 5 g NaCl were added to 25 mL of deionised (DI) water under magnetic stirring and freeze-dried for 24 h. The freeze-dried solution was annealed in a tubular furnace at 600 °C for 1 h with a heating rate of 5 °C·min⁻¹ under flowing argon. Subsequently, the NaCl pore template was removed by thorough washing with DI and ethanol before being dried in an air oven for 4h. The product was then added to an ethanol solution containing KOH so that the mass ratio between the KOH and carbon was 3:1, before being dried in an air oven again and annealed in the tube furnace at 900 °C (2 h, 5 °C·min⁻¹). The product was then washed with DI water and ethanol via vacuum filtration and dried in an air oven to obtain the hierarchical porous carbon host (HPCH).

6.3.2 Electrochemical Characterisation

Composite sulfur cathodes with the HPCH (S/HPCH) were fabricated using elemental sulfur, HPCH, carbon black (CB), and poly(vinylidene fluoride) (PVDF) in a mass ratio of 6:2:1:1. For electrochemical comparison, sulfur cathodes using only CB (S/CB) were fabricated in a mass ratio of 6:3:1. The solid electrode components were thoroughly ground with a mortar and pestle before an electrode slurry was formed using 1-methyl-2-pyrrolidinone (NMP) as the solvent. The slurry was cast on C-coated aluminium foil with a gapped blade and dried in a vacuum oven at 60 °C overnight before being cut into electrode disks 13 mm in diameter. The active material loading in the electrodes was approx. $0.5 \text{ mg}\cdot\text{cm}^{-2}$. Electrodes with a sulfur loading of $\approx 2 \text{ mg}\cdot\text{cm}^{-2}$ were also fabricated for testing at higher sulfur loading. Half-cells were fabricated in an argon-filled glovebox using the prepared cathodes, a lithium foil counter electrode, polypropylene (Celgard 2300) separator, and 1 M lithium bis(trifluoromethane)sulfonimide (LiTFSI) in 1,3-dioxolane/1,2-dimethoxyethane (1:1, v/v) with 0.2 M LiNO_3 as the electrolyte. The electrolyte:sulfur ratio was kept constant at 1 mg:20 μL for all half-cells. The half-cells underwent galvanostatic charge/discharge testing on a Neware Battery Testing System (Neware, China) with a 1.7 - 2.7 V voltage window in an oven set to 30 °C. For the 0.5 C (1 C = 1672 mAh/g) and high-loading 0.2 C testing, an electrochemical sulfur infiltration pre-cycle of 0.05 C was performed before cycling at the specified rate. For the 2 C testing, a 0.2 C pre-cycle was utilised. Electrochemical impedance spectroscopy (EIS) was carried out on a Biologic SP-200 (Biologic, France) with the AC set to 5 mV and a frequency range of 10 mHz to 100 kHz. Cyclic voltammetry (CV) testing was also carried out on the Biologic SP-200.

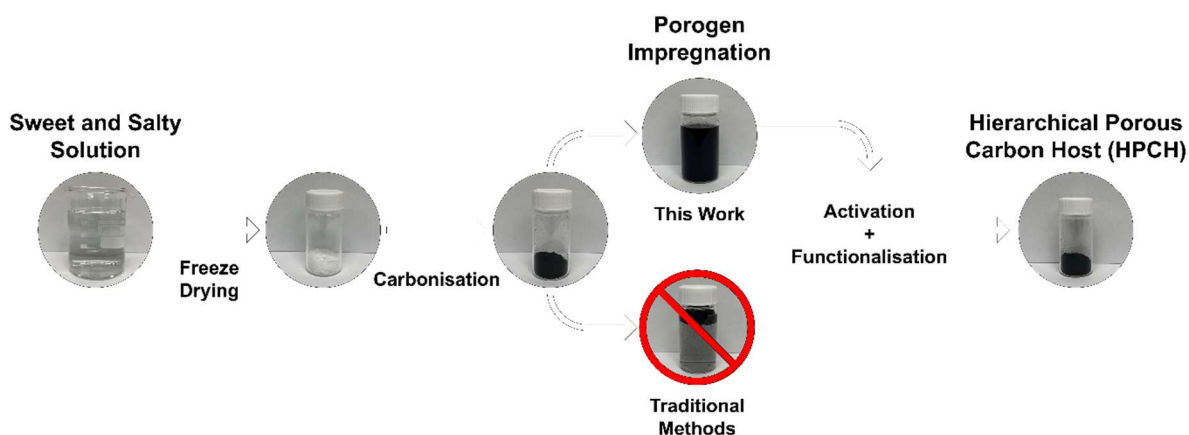
6.3.3 Materials Characterisation

Scanning electron microscope (SEM) images and Energy Dispersive X-ray Spectroscopy (EDS) elemental mappings were obtained on a JSM-7001F SEM (JEOL, Japan) and were used to investigate the morphologies of the HPCH material as well as the S/HPCH and S/CB electrodes before and after cycling. X-ray diffraction (XRD) patterns were obtained on a Model LabX-6000 diffractometer (Shimadzu, Japan) using $\text{Cu K}\alpha$ radiation ($\lambda = 1.54 \text{ \AA}$) at 40 kV and 40 mA between the 2θ range of 5 - 80 °. Raman spectroscopy was carried out on a Renishaw 100 (Renishaw, United Kingdom) using a 632.8 nm He-Ne laser. The specific surface area of the HPCH and CB was measured by N_2 adsorption/desorption at 77 K on an Autosorb iQ (Anton Paar, Austria). The pore size distribution plot was obtained through the NLDFT equilibrium model. For the polysulfide adsorption experiment, a 0.01 M solution of Li_2S_6 was

prepared by mixing Li_2S and elemental sulfur in a 1:5 molar ratio in an argon-filled glovebox before the mixture was added DOL:DME (1:1 v/v) solvent. The solution was heated to 70 °C and magnetically stirred for 24 h. To conduct the adsorption experiment, 50 mg of HPCH and CB were exposed to 20 mL of the Li_2S_6 solution and allowed to rest for 4 h before the Li_2S_6 , $\text{Li}_2\text{S}_6 + \text{CB}$, and $\text{Li}_2\text{S}_6 + \text{HCPH}$ solutions were subjected to UV-Vis analysis on a Cary Series UV-Vis-NIR Spectrophotometer (Agilent Technologies, USA). XPS analysis of the HPCH before and after Li_2S_6 exposure was carried out on a Kratos Axis ULTRA X-ray Photoelectron Spectrometer incorporating a 165 mm hemispherical electron energy analyser. The incident radiation was Monochromatic $\text{Al K}\alpha$ X-rays (1486.6 eV) at 225 W (15 kV, 15 mA). Survey (wide) scans were taken at an analyser pass energy of 160 eV and multiplex (narrow) high-resolution scans at 40 eV. Survey scans were carried out over 1200 - 0 eV binding energy range with 1.0 eV steps and a dwell time of 100 ms. Narrow high-resolution scans were run with 0.05 eV steps and 250 ms dwell time. The base pressure in the analysis chamber was 1.0×10^{-9} torr and 1.0×10^{-8} torr during sample analysis. Peak fitting of the high-resolution data was carried out using the CasaXPS software.

6.4 Results and Discussion

This work aimed to develop a ground-up synthesis method which utilised environmentally benign reagents and processes to increase the likelihood of lab based functional materials making their way into practical and industrial applications. Thus, the “sweet and salty” synthesis method, outlined in **Scheme 1**, was specifically designed to produce a conductive, hierarchically porous, and surface-functionalised sulfur host for applications for Li–S batteries.



Scheme 1: Schematic representation of the Hierarchical Porous Carbon Host (HPCH) synthesis

The starting reagents include glucose as a carbon source, sodium chloride as a mesopore/macropore template, and potassium hydroxide as a porogen. The use of NaCl as a pore template for functional carbons has been demonstrated by our group previously [23], wherein we found that the ratio between NaCl and the carbon source successfully tailored the meso/macroporous structure of the product. This work uses the NaCl pore template approach as shown previously and expands upon the synthesis through a subsequent KOH activation step to enhance the material's pore structure and produce oxygen-rich functional groups at the material's surface.

KOH was chosen as the porogen in the synthesis for two reasons. Firstly, KOH produces abundant micropores throughout the carbon through the multi-step mechanisms shown in **Eqn. 6.1-6.6** [24-26]. Secondly, the activation of the carbon with KOH will produce abundant lone-pair rich moieties, including carbonyl, hydroxyl, and carboxylic groups at the carbon's surface [27]. The presence of a microporous structure and lone-pair rich functional groups have been previously demonstrated as desirable traits in sulfur hosts [28].



Using KOH as a porogen to increase the surface area of carbon materials is not a new phenomenon [15, 29, 30], but in most cases, the KOH is usually mixed with the carbon either as a solid or in an aqueous solution. However, due to the low wettability of carbonised materials in aqueous KOH solutions, a homogeneous distribution of the KOH porogen through the carbon matrix is difficult to achieve (**Fig. 6.1a**). This work uses an ethanoic KOH solution to achieve a homogeneous distribution of the KOH porogen due to the enhanced wettability of carbon products in ethanol (**Fig. 6.1b**). The even distribution of the KOH porogen is expected to produce a hierarchical porous carbon host (HPCH) material with abundant pore volume and homogeneous morphology.

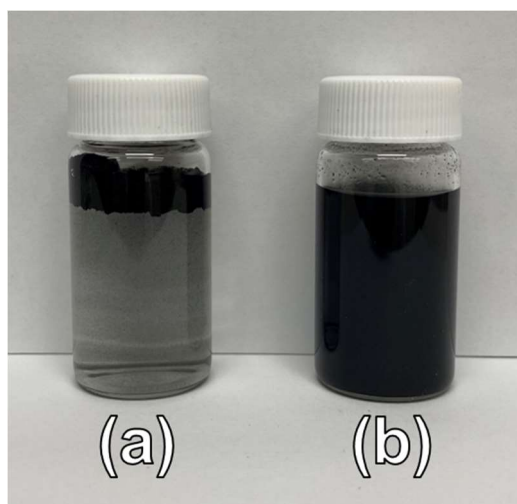


Figure 6.1: Dispersion of carbon materials in aqueous (a) and ethanoic (b) KOH solutions

Materials characterisation was carried out after synthesis to evaluate the efficacy of the “sweet and salty” synthesis method and observe in detail the parameters of the HPCH. Firstly, scanning electron microscopy (SEM) was carried out to observe the morphology of the product. **Fig. 6.2a** shows the product at a magnification of 1000x and reveals a homogeneous morphology. Upon further magnification at 10000x (**Fig. 6.2b**), the macroporous morphology of the product is shown.

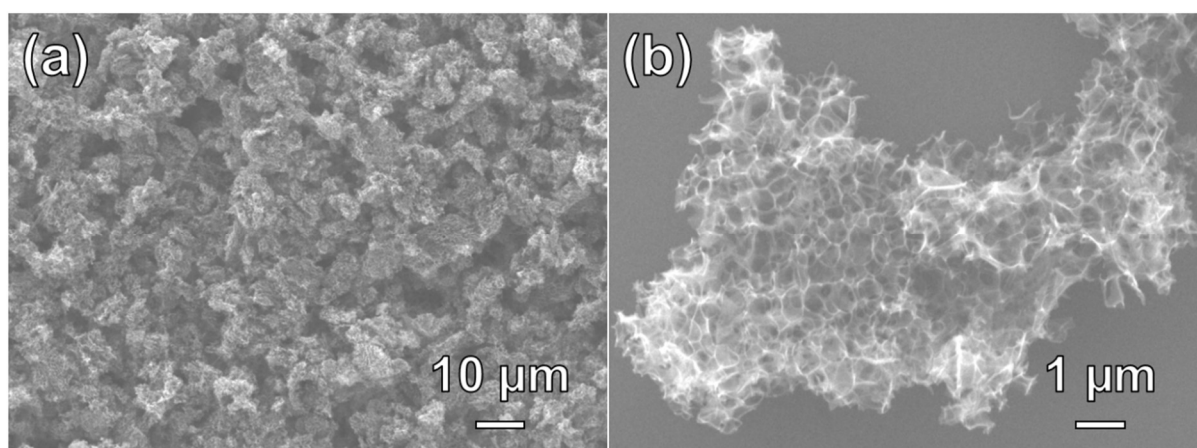


Figure 6.2: Scanning electron microscope (SEM) images of the HPCH material at (a) 1000x and (b) 10000x magnification

Next, so that the pore structure of the HPCH could be characterised, an N₂ adsorption/desorption analysis was carried out and compared to the results from a CB sample. The adsorption/desorption isotherm is displayed in **Fig. 6.3a-i and b-i** for the CB and HPCH samples, respectively. Upon observing the N₂ adsorption/desorption isotherm obtained for the CB sample (**Fig. 6.3a-i**), it can be clearly observed that an insignificant amount of surface area

is present. The total specific surface area for the CB sample was found to be only $69.043 \text{ m}^2 \cdot \text{g}^{-1}$ via the Brunauer, Emmett, and Teller (BET) equation [31]. The pore size distribution (PSD) was calculated through the NLDFT equilibrium model to quantify the nature of the porous morphology within the carbon black [32], which shows no appreciable pore volume associated with the micropores or mesopores range (**Fig. 6.3a-ii**)

For the N_2 adsorption/desorption isotherm obtained for the HPC sample (**Fig. 6.3b-i**), a type I isotherm is observed in the low-pressure region ($P/P_0 < 0.1$) which verifies the existence of micropores in the material [33]. On the other hand, a type II isotherm is observed at high pressure [34]. The gentle slope of P/P_0 between 0.1 and 0.9 suggests the pore volume associated with mesopores, while present, is limited and may also suggest why only a small amount of hysteresis is observed [35]. For the HPCH sample, the total specific surface area was found to be about $1540 \text{ m}^2 \cdot \text{g}^{-1}$.

The PSD was also calculated for the HPCH sample, with the results shown in **Fig 6.3b-ii**, and show a considerable amount of pore volume is obtained across the entire 0.5 to 2 nm range, which is considered the microporous region. Additional pore volume is obtained from the pores falling in the 2 to 4 nm range (the mesoporous region), albeit at a lower total volume arising from the microporous contribution [36]. Thus, the pore size distribution results show that the HPCH contains abundant micropores and a considerable amount of mesopores. Therefore, it is confirmed that the HPCH displays micro and mesoporosity. While also considering the macroporous structure revealed by SEM investigation, a hierarchical porous structure is revealed, and the material can reasonably be referred to as a hierarchical porous carbon host (HPCH).

Carbonaceous materials are expected to display amorphous characteristics after KOH activation at high temperatures [29] due to the pore formation resulting in the graphitic layers being ‘opened’ to produce a disordered carbon material [37]., X-ray diffraction (XRD) analysis was carried out on the CB and HPCH samples to verify that this phenomenon occurred, with the diffraction pattern shown in **Fig. 6.4a-i and b-i**, respectively. The XRD diffraction pattern for the CB material reveals its crystalline nature via the characteristic peaks at 25.28, 43.16, and 51.56 degrees, corresponding to the (002), (101), (004) planes of graphite [38]. Conversely, the amorphous nature of the HPCH sample was revealed by the absence of a sharp peak at around 25 degrees and the presence of a broad peak between 40 and 50 degrees (**Fig. 6.4b-i**) [39].

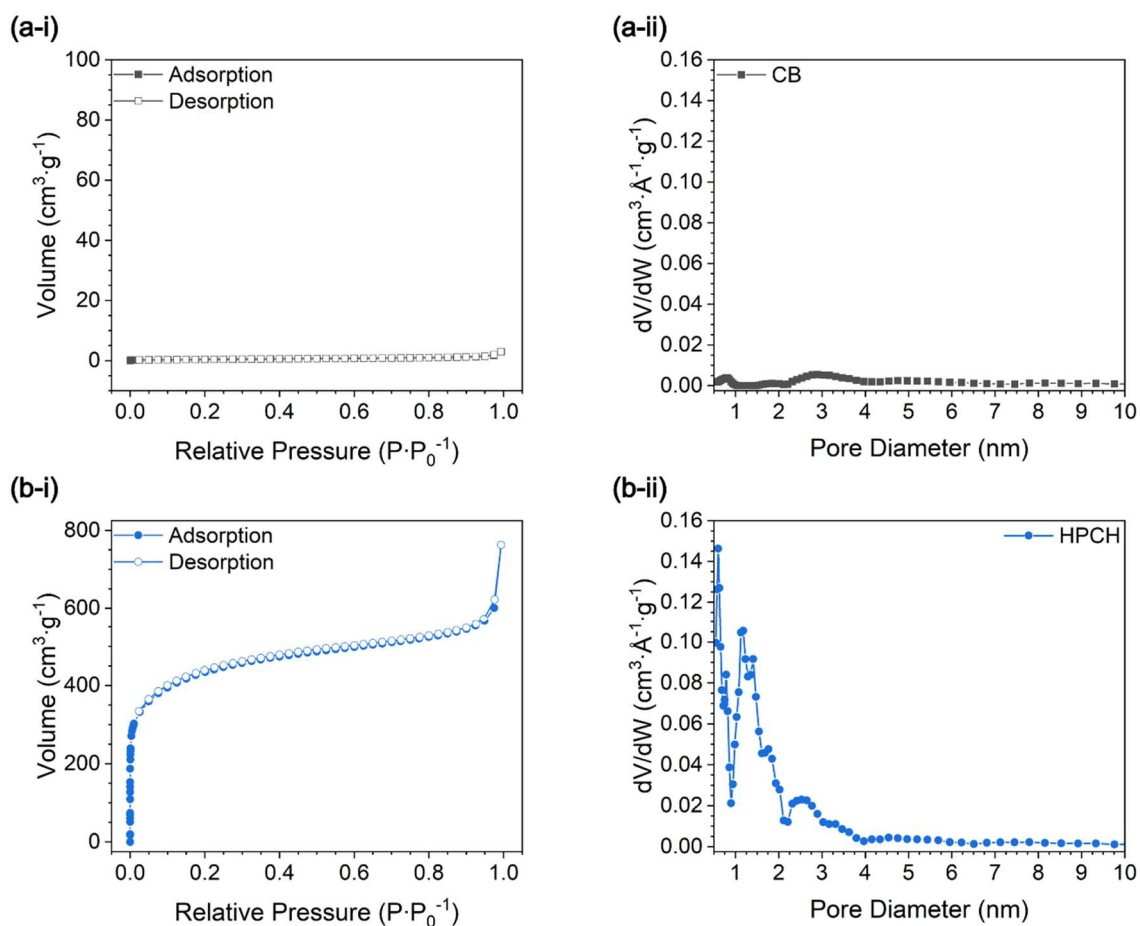


Figure 6.3: (a) N₂ adsorption/desorption isotherm and (b) pore size distribution from the (i) CB and (ii) HPCH samples

RAMAN spectroscopy was carried out to further investigate graphitisation in the CB and HPCH samples, with the spectra provided in **Fig. 6.4a-ii and b-ii**, respectively. The spectra of both the CB and HPCH materials have characteristic D (≈ 1320 cm⁻¹) and G (≈ 1595 cm⁻¹) bands corresponding to disordered and sp^2 hybridised carbon, respectively [40]. The I_D/I_G ratio can be calculated by observing the intensity between the D and G band and was found to be 1.44 and 1.38 for the CB and HPCH, respectively [41]. The results reinforce that the HPCH is a disordered carbon material.

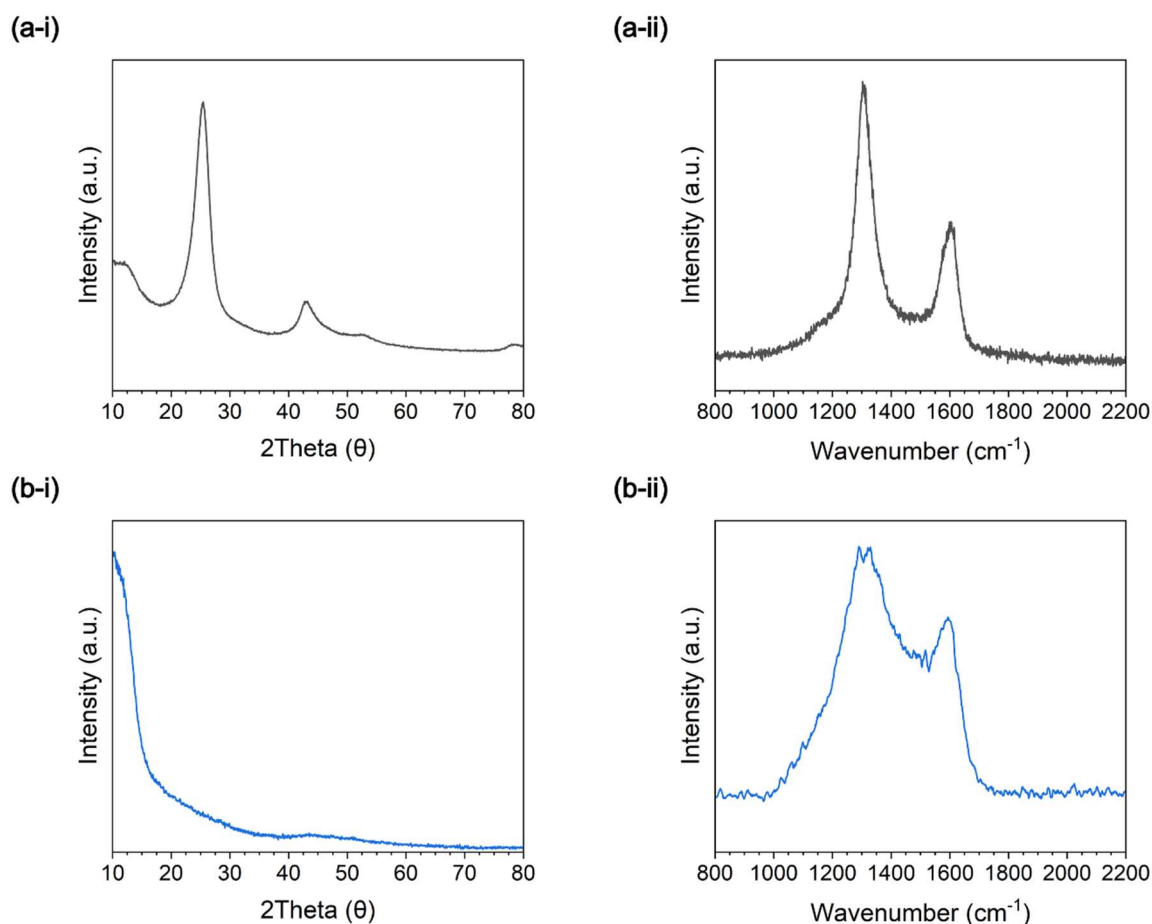


Figure 6.4: (a) X-ray diffraction (XRD) pattern and (b) RAMAN spectra from the (i) CB and (ii) HPCH samples

After the morphological characterisations were complete, a simple polysulfide adsorption experiment was conducted to verify whether the HPCH could adsorb soluble polysulfides. 50 mg of CB or HPCH were exposed to 20 mL of a 0.01 M Li_2S_6 solution and allowed to stand for 4 h. The digital photograph in the inset of **Fig. 6.5** shows that the vial containing the HPCH becomes almost colourless after exposure, in contrast to the vial containing CB, which displays no colour change., UV-Vis spectroscopy was carried out on aliquots of the supernatant solutions after exposure to the respective carbon sample to investigate further. The spectra displayed in **Fig. 6.5** display the characteristic peaks between 250 - 280 nm, which can be ascribed to the S_6^{2-} anion [42]. As expected, the solution exposed to CB shows almost no change compared with the spectra of the pure Li_2S_6 solution, confirming that the CB shows no activity towards the soluble polysulfides. Conversely, the S_6^{2-} peak for the solution exposed to the HPC significantly diminished, reflecting the colour change observed in the digital photographs. The test confirms that the HPCH can adsorb the soluble polysulfides.

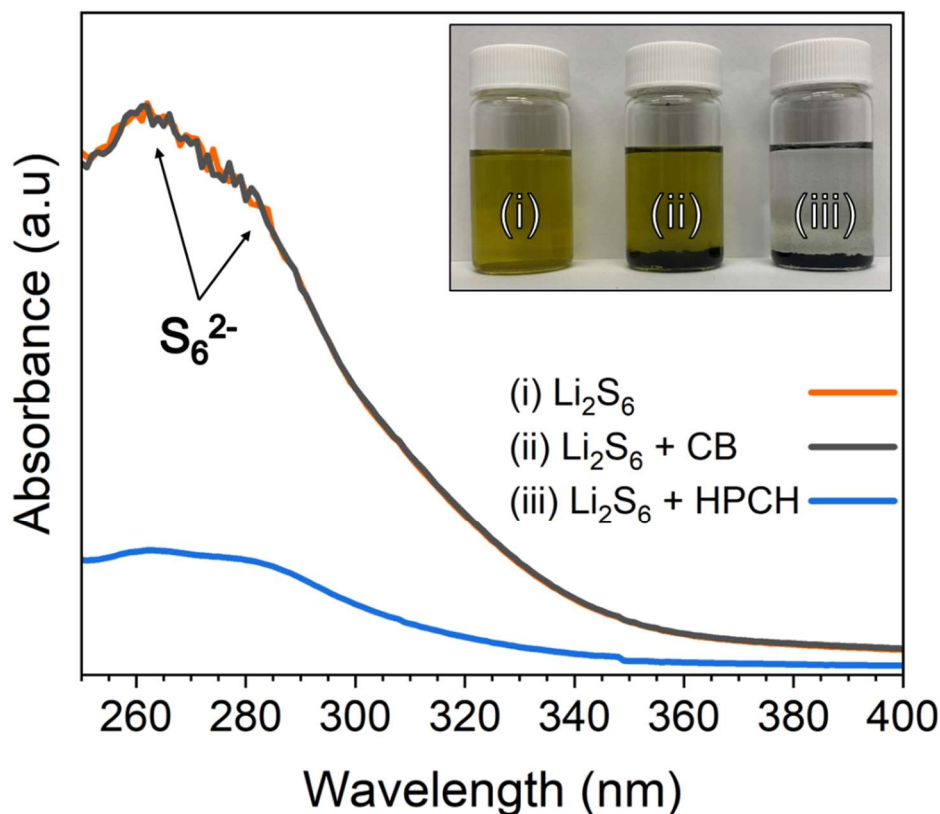


Figure 6.5: UV-Vis spectra of the Li_2S_6 , $\text{Li}_2\text{S}_6 + \text{CB}$, and $\text{Li}_2\text{S}_6 + \text{HPCH}$ solutions; (inset) Digital photograph of the (i) Li_2S_6 , (ii) CB, and (iii) HPCH samples after 4 h.

XPS analysis was carried out to observe whether the KOH activation successfully achieved chemical functionality on the surface of the HPCH and investigate the nature of the interaction between the soluble polysulfides and the HPCH. KOH activation of carbon materials is expected to produce abundant lone-pair rich carbonyl and hydroxyl groups at the carbon's surface. Thus, the high-resolution C 1s and O 1s regions of the XPS spectra of the HPCH material are provided in **Fig. 6.6a-i and b-i**, respectively. The convoluted C1s HR spectrum can be attributed to contributions from the C–C, C–O, and C=O at the binding energies of 284.335, 285.214, and 289.088 eV, respectively [43]. The presence of the C=O and C–O bonds are reflected in the O 1s HR spectrum, with contributions arising from the C=O and C–O bonds at 530.668 and 531.965 eV, respectively [44]. These results suggest that the KOH activation successfully endowed the HPCH's surface with abundant lone-pair rich carbonyl and hydroxyl groups. After Li_2S_6 exposure, it can be observed that the C–O and C=O intensities increase relative to the C–C bond peak before the HPCH was exposed to Li_2S_6 . Furthermore, in the HR

O1s region, the newly formed Li–O bond can be observed, which may explain the activity of the HPCH towards the soluble polysulfides.

Due to the fact that the shuttling of polysulfides in the LSBs is such a critical shortfall of the battery, the mechanism the polysulfide adsorption is well-researched. Broadly speaking, the soluble polysulfides can be retained at the sulfur cathode via two mechanisms, namely physical polysulfide confinement and chemical anchoring [45].

Typically, physical polysulfide retention is achieved through non-polar and porous carbon materials [46]. Micropore retention is thought to be achieved by restricting the size of the polysulfides to favour shorter chain polysulfides [47, 48], which can help trap the reaction intermediates at the cathode. Chemical retention, on the other hand, relies on polar functional groups at the material's surface to interact with the polar and soluble polysulfides [49]. DFT calculations have shown that the partially positive lithium atom in the soluble polysulfides favourably binds to the lone-pair-rich functional groups on a materials [50]. The lithium-bond in Li-S batteries is now a well-researched phenomenon, and is crucial for restricting soluble polysulfides to reduce the shuttle effect [28]. Therefore, the high surface area with abundant micropores as well as polar surface functionality of the HPCH can explain the strong activity towards the soluble polysulfides in the adsorption experiment, UV-Vis analysis, and XPS investigation.

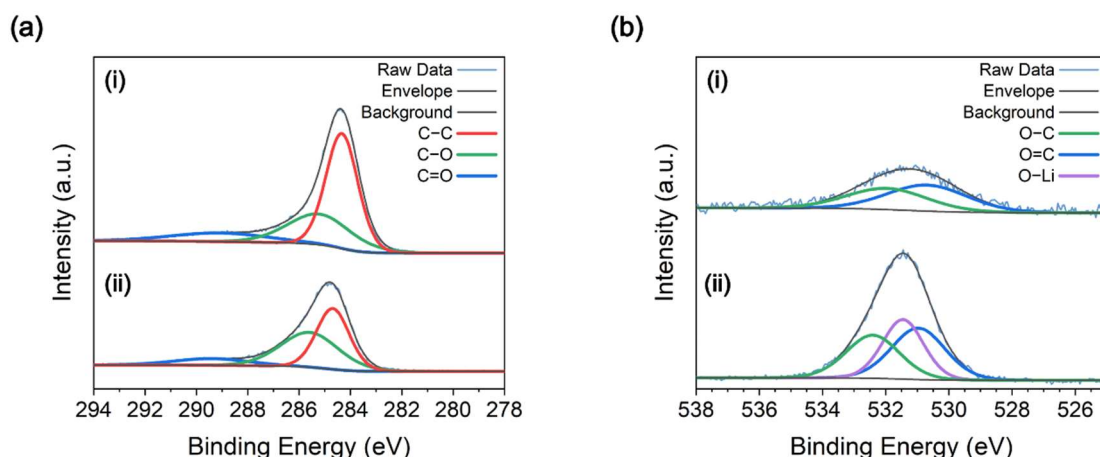


Figure 6.6: High-resolution spectra from the (a) C 1s and (b) O 1s region of the HPCH material before (i) and after (ii) exposure to Li_2S_6

Subsequently, electrochemical characterisation was carried out to evaluate the electrochemical performance of the HPCH in Li–S batteries. Li–S batteries were fabricated using HPCH as a bi-functional sulfur host in the cathode of the cells, with reference cells fabricated using CB.

The cells are referred to as S/HPCH and S/CB, respectively. **Fig. 6.7** shows the electrochemical performance of the S/CB and S/HPCH cells under galvanostatic charge/discharge testing at various current densities and sulfur loadings. **Fig. 6.7a and b** show the long-term electrochemical performance of the cells when cycled at 0.5 and 2 C (1 C = 1,672 mAh/g), respectively. In the first cycle at 0.5 C, the S/HPCH cell delivers a discharge capacity of 999 mAh/g, compared to only 751 mAh/g delivered by the S/CB electrode. After 500 cycles, the difference between the two cells is much more pronounced, with the S/HPCH cell delivering a reversible capacity of 490 mAh·g⁻¹, corresponding to a capacity fading of 0.102 % per cycle.

Conversely, the S/CB cell delivers only 285 mAh/g after cycling, which results in a higher capacity fading per cycle of 0.124 %. This trend continues when the cells are cycled at a higher C-rate of 2 C, as shown in **Fig. 6.7b**. The initial discharge capacities are 786 and 639 mAh/g, the reversible discharge capacities are 363 and 242 mAh/g after 500 cycles, and the capacity fading is 0.107 and 0.124 % per cycle for the S/HPCH and S/CB cells, respectively. The galvanostatic charge/discharge testing reveals that the cells fabricated using the HPCH host material display a higher initial capacity, a higher reversible capacity after 500 cycles, and a lower capacity fading per cycle compared with cells using only carbon black. Following this, S/HPCH and S/CB electrodes with sulfur loading of $\approx 2 \text{ mg}\cdot\text{cm}^{-2}$ were tested at 0.2 C, with the results shown in **Fig. 6.7c**. As shown previously, the S/HPCH cells deliver a higher initial capacity of 1072 mAh·g⁻¹, a higher reversible discharge capacity of 875 mAh·g⁻¹, and a smaller capacity fading per cycle of 0.368 % when compared with the S/CB cells, which delivered 901 mAh/g, 546 mAh/g, and 0.788 %, respectively. The improved capacity retention and lower capacity fading per cycle in the S/HPCH cell may be attributed to the adsorption of the soluble polysulfides in the porous structure and at the surface functional groups of the HPCH as demonstrated in the polysulfide adsorption experiment and XPS analysis.

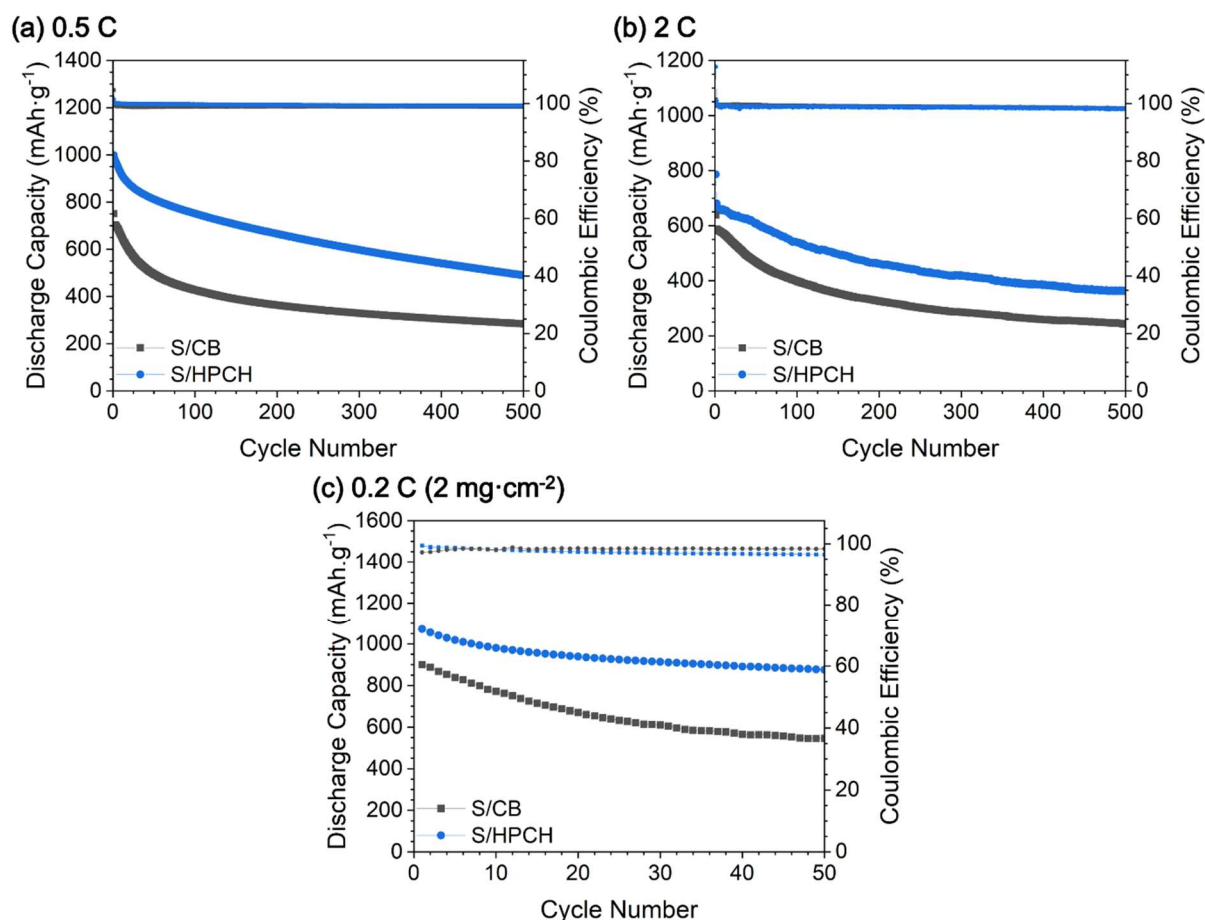


Figure 6.7: Cycle performance of the S/CB and S/HPCH electrodes at (a) 0.5 C, (b) 2 C, and (c) 0.2 C.

In addition to long-term cycling at a single C-rate, Li-S batteries should be able to withstand cycling at varying current densities [51]. Therefore the voltage/capacity profiles of the S/CB (**Fig. 6.8a-i**) and S/HPCH (**Fig. 6.8b-i**) cells at increasing current densities are provided. The discharge capacity obtained for the S/HPCH cell is 1376, 1229, 1117, 1030, and 890 $\text{mAh}\cdot\text{g}^{-1}$ at 0.1, 0.2, 0.5, 1, and 2 C, compared to only 1017, 868, 759, 684, and 514 $\text{mAh}\cdot\text{g}^{-1}$ for the S/CB cell at the same C-rates, respectively. A significant difference between the discharge curves at 2 C can be observed between the cells, in that the second discharge plateau is almost non-existent for the S/CB cell, which may explain why the S/HPCH cell delivers better performance at higher C-rates. Overall, the profiles from the S/HPCH cell display a higher discharge capacity and lower over-potential at all current densities when compared to the profiles of the S/CB cell. After the cycle at the high rate of 2 C, the cells were subject to an additional cycle at 0.2 C, with the charge/discharge profile before and after rate capability testing shown in **Fig. 6.8a-ii and b-ii** for the S/CB and S/HPCH cells, respectively. After testing at high C-rates, the S/HPCH cell delivers a capacity of 1220 mAh/g at 0.2 C, which

results in a 99.3 % capacity retention compared to the initial 0.2 C cycle. In comparison, the S/CB cell delivers 821 mAh/g after rate capability testing, resulting in a 94.5% capacity retention. The results clearly show that the S/HPCH-based cell delivers a higher discharge capacity at high C-rates and enhanced capacity retention when returning to lower C-rates after the rate capability testing.

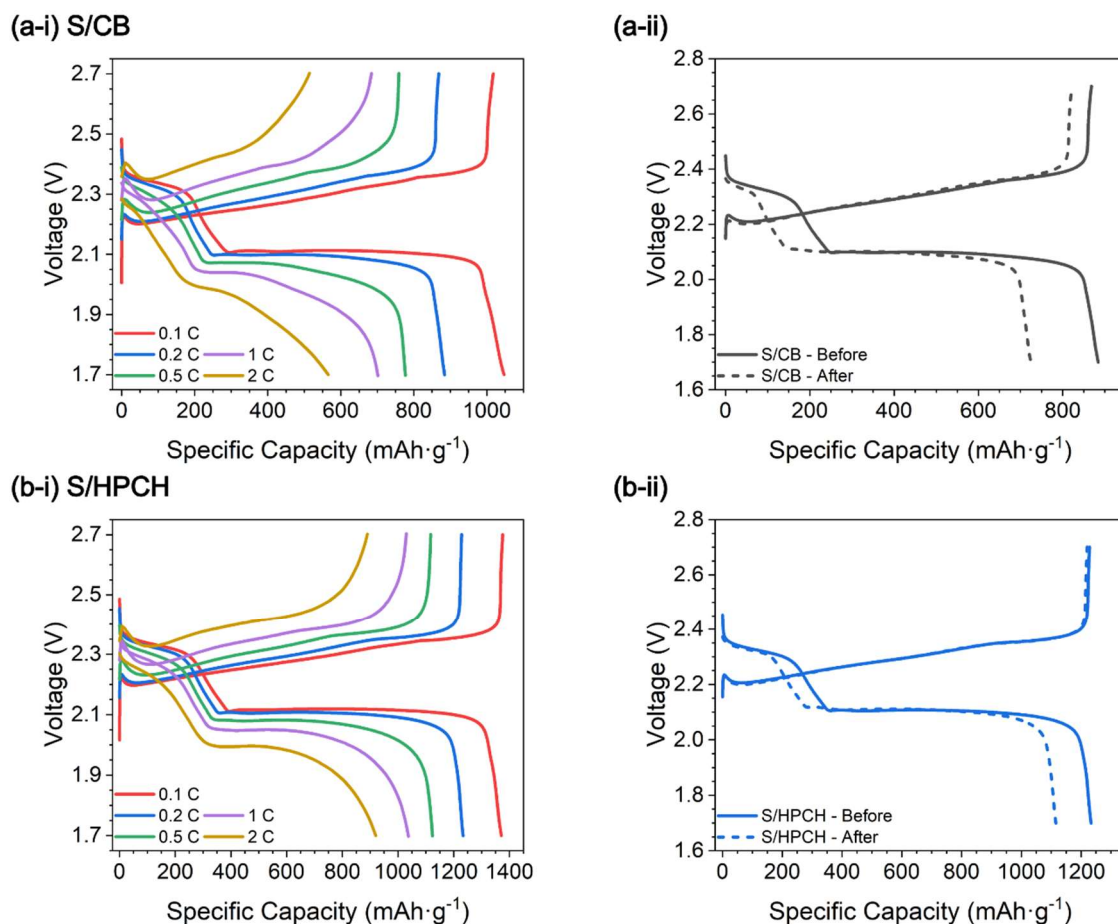


Figure 6.8: Capacity/Voltage profile of the (a) S/CB and (c) S/HPCH cells (i) during rate capability testing and (ii) for the two 0.2 C cycles

Cyclic voltammetry (CV) was carried out at increasing scan rates to investigate the electrochemical kinetics in the S/CB and S/HPCH cells, with the results shown in **Fig. 6.9a and b**. The S/HPCH cell shows much higher peak currents in the anodic and cathodic peaks than the S/CB voltammogram, suggesting much faster kinetics in the S/HPCH cell. Additionally, in the S/HPCH cell, the peaks occur at higher potentials upon discharge and a lower potential on charging, reflecting a lower over-potential and agreeing with the voltage/capacity profile obtained in the rate capability testing.

Information about both electrodes' lithium-ion diffusion coefficient (D_{Li}) can be obtained via the relationship shown in **Eqn. 6.7** [52]. When the peak current (I_p) is plotted against the square root of the scan rate, as shown in **Fig. 6.9c and d**, information about D_{Li} can be obtained [53]. A linear relationship in the anodic and cathodic scans for both the S/CB and S/HPCH cells indicate diffusion-controlled processes in all cases [54]. As the slope gradient in **Fig. 6.9c and d** is proportional to D_{Li} , it can be inferred that the S/HPCH cell displays faster Li^+ ion migration in both the anodic and cathodic processes compared to the S/CB cell [55]. The enhanced diffusion properties in the S/HPCH cell may explain the enhanced electrochemical performance at high C-rates.

$$I_p = 2.686 \cdot 10^5 n^{1.5} A D^{0.5} C v^{0.5} \quad (6.7)$$

$$|Z'| = R_{ct} + R_{int} + \sigma_w \omega^{-0.5} \quad (6.8)$$

$$D_{Li} = \frac{R^2 T^2}{2 A^2 n^4 F^4 C^2 \sigma_w^2} \quad (6.9)$$

Further electrochemical characterisation of the S/HPCH and S/CB cells was carried out through electrochemical impedance spectroscopy (EIS). The cells were subjected to 20 charge/discharge cycles at 0.2 C before EIS spectra were obtained, as shown in **Fig. 6.9e**. In the EIS spectra, inverted semi-circles in the high/medium frequency region and a sloped line in the low-frequency region can be observed, relating to internal cell resistances and Warburg diffusion, respectively [56]. It is clear that the semi-circles in the spectra for the S/HPCH cell are smaller and more obviously defined than those in the S/CB cell, relating to reduced Ohmic resistance of the electrolyte and cell components in the S/HPCH electrode [57]. The results were fit with an equivalent circuit (**Fig. 6.9e inset**) to quantify the different resistances in the cells, which clearly show the lower resistances of all components in the S/HPCH cell, as tabulated in **Table 6.1**.

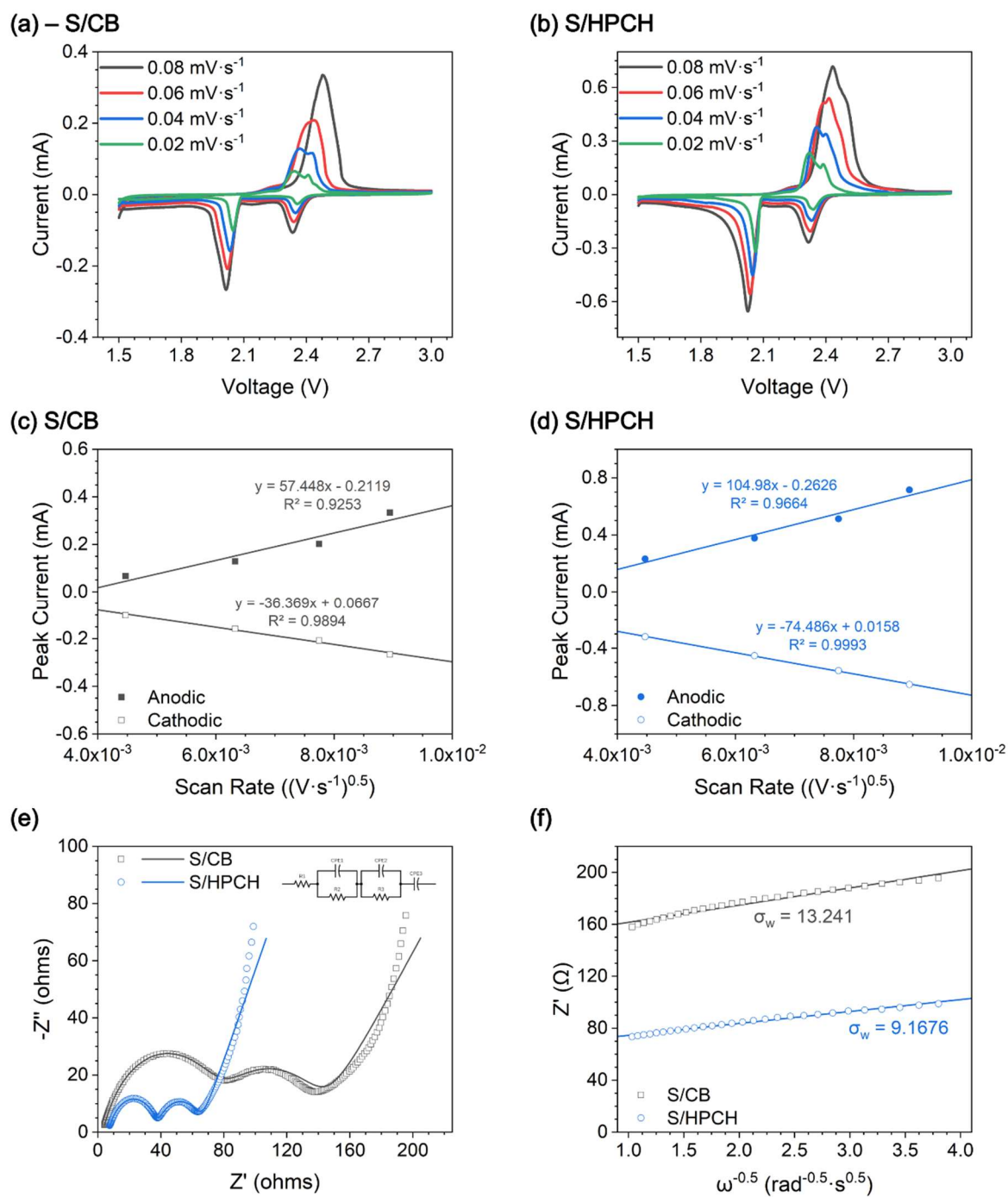


Figure 6.9: Cyclic Voltammograms (CV) of the (a) S/CB electrode and (b) S/HPCH electrode. Peak current (I_p) vs. the square root of the scan rate of the (c) S/CB electrode and (d) S/HPCH electrode. (e) EIS spectra of the S/CB and S/HPCH electrodes after 20 cycles at 0.2C. (f) Z' vs. $\omega^{-0.5}$ showing (σ_w)

Table 6.1: Fitting results from EIS analysis

	S/CB	S/HPCH
R_e	3.12 Ω	6.76 Ω
R_{ct}	73.12 Ω	26.54 Ω
R_{int}	63.72 Ω	31.19 Ω

Further information relating to the diffusion properties of both electrodes can be extracted from the linear section of the low-frequency region in the EIS spectra via **Eqn. 6.8 and 6.9** [58]. The gradient of the line that is obtained when Z' is plot against $\omega^{-0.5}$ relates to the Warburg factor (σ_W), which in turn is inversely proportional to D_{Li} . Thus, as the gradient obtained from the S/HPCH data is smaller than that from S/CB (**Fig. 6.9f**), it can be inferred that the diffusion properties in the S/HPCH electrode are enhanced, which mirrors the diffusion properties found during the CV investigation above. After all, the EIS investigation reveals that the S/HPCH electrode displays lower internal resistances and better Li^+ diffusion properties when compared with the S/CB cell, further justifying the enhanced electrochemical performance at high C-rates when using the HPCH material.

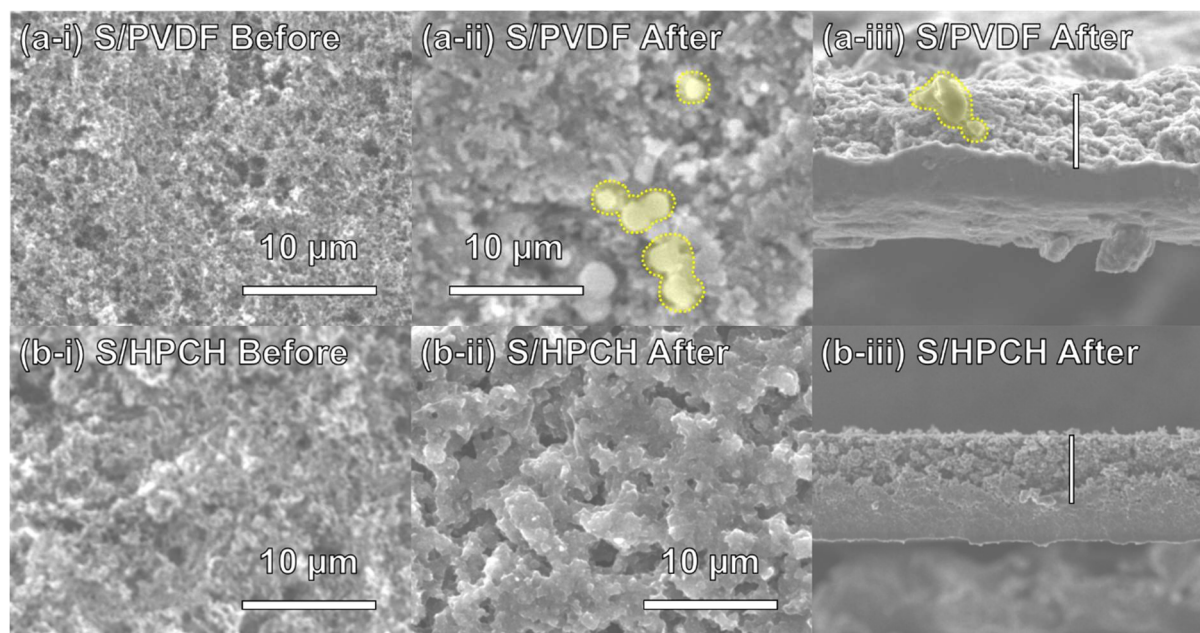


Figure 6.10: SEM of the (a) S/CB and (b) S/HPCH electrode surface (i) before cycling, (ii) after cycling, and (iii) cross section after cycling (scale bar: 30 μm)

Following the electrochemical investigation of the S/HPCH cells, post-mortem SEM analysis was carried out to investigate the source of the obtained enhanced performance. The SEM

images of the S/HPCH and S/CB electrodes before and after 20 cycles at 0.2 C are shown in **Fig. 6.10**. Before cycling, both the S/HPCH and S/CB electrodes display relatively similar morphologies; however, the differences become apparent after cycling. The S/HPCH electrode has a relatively dense and homogeneous surface in contrast to the S/CB electrode surface, which is inhomogeneous and has evident precipitation of active materials (yellow highlights, **Fig. 6.10a-ii**). The precipitation of the active materials can cause “dead” areas of the electrode in which the active material cannot undergo electrochemical reactions. Alternatively, as the HPCH material has a large pore structure, the expanding active material can easily be contained within the carbon matrix, severely limiting any large “dead” areas of the electrode and maximising the active material’s participation in the electrochemical reaction [59]. The precipitation of the active materials on the S/CB electrode can also be observed in the cross-sectional images of the high-loading sulfur cathodes after cycling (**Fig. 6.10a-iii**). Conversely, the high-loading S/HPCH electrode displays an extremely dense and homogeneous morphology due to the porous void structure provided by the HPCH (**Fig. 6.10b-iii**).

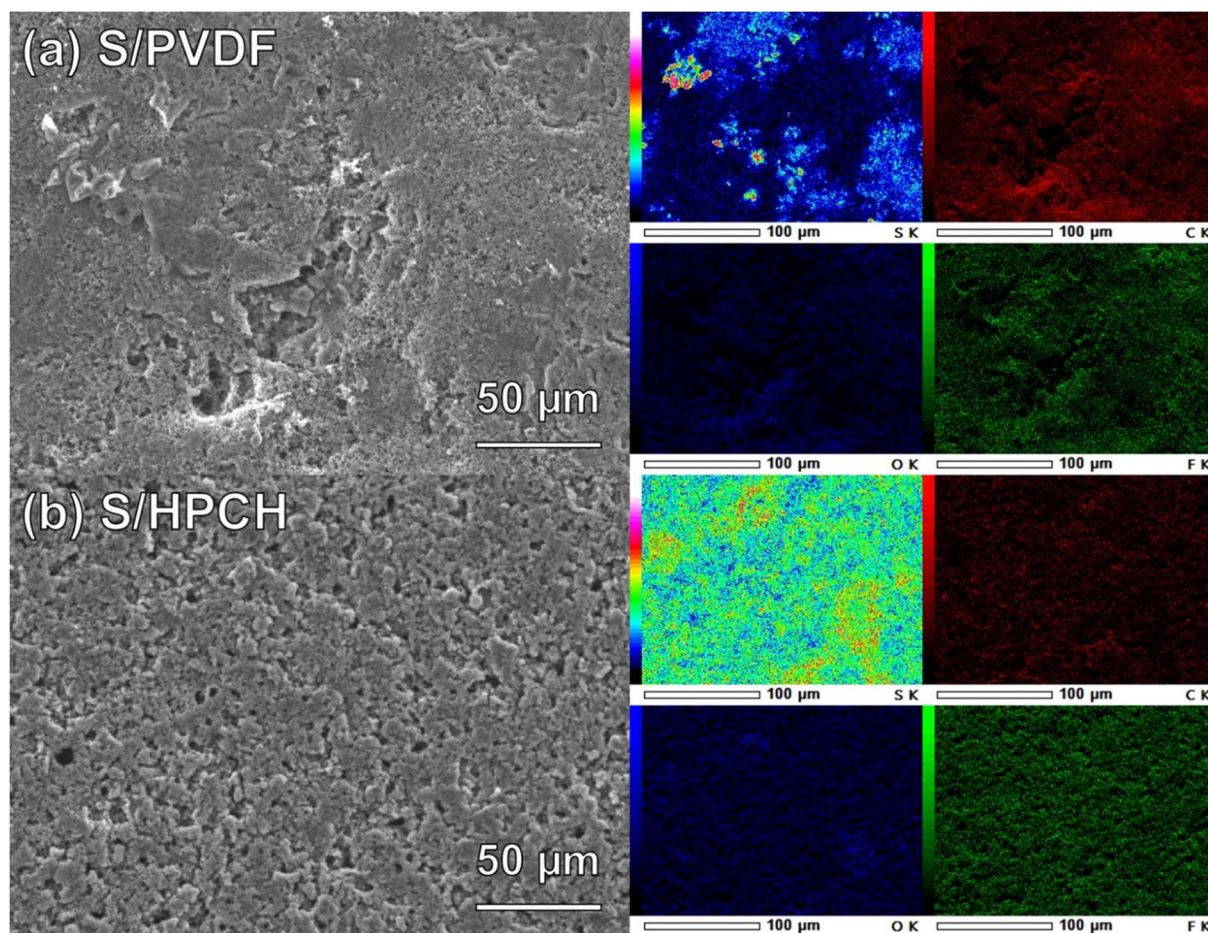


Figure 6.11: SEM images and Energy Dispersive X-ray Spectroscopic (EDS) mapping of the high-loading (a) S/CB and (b) S/HPCH electrodes

Post-mortem SEM and EDS analysis were carried out on the high-loading electrodes after cycling, with the results shown in **Fig. 6.11**. The dense and homogeneous morphology of the S/HPCH electrode is again revealed by the SEM image (**Fig. 6.11b**). In comparison, the inhomogeneous S/CB electrode (**Fig. 6.11a**) shows evident precipitation of the active materials. The elemental mappings revealed through EDS analysis confirms that the S/CB electrode inhomogeneity is the active sulfur materials precipitated on the electrode surface. On the other hand, the EDS mapping reveals that the S/HPCH-based electrode displays superior homogeneity and distribution of the electrode composite materials.

6.5 Conclusion

The “sweet and salty” synthesis of a hierarchical porous carbon host (HPCH) was successfully applied to produce a high-performance sulfur host for Li–S batteries. The HPCH displayed a hierarchical porous structure with a high specific surface area of $1540 \text{ m}^2 \cdot \text{g}^{-1}$ and a favourable pore size distribution which were shown to trap polysulfides via physical and chemical means. After being assembled into Li–S cells, the S/HPCH electrode delivered a low capacity fading of 0.102 % per cycle over 500 cycles, a discharge capacity of $890 \text{ mAh} \cdot \text{g}^{-1}$ at 2 C, and an initial capacity of $1072 \text{ mAh} \cdot \text{g}^{-1}$ at a sulfur loading of $2 \text{ mg} \cdot \text{cm}^2$. The S/HPCH also displayed enhanced kinetic and diffusion properties compared with the S/CB cell, as evidenced by EIS and CV analysis. Post-mortem SEM analysis reveals that the S/HPCH displays no precipitation of the sulfur or its discharge products after cycling, owing to the large pore surface area of the HPCH material. Overall, the “sweet and salty” synthesis method efficiently produced a hierarchical porous carbon in an environmentally benign method, and helps to provide excellent electrochemical performance when applied as a sulfur host in Li–S battery cathodes.

6.6 References

1. Leggett, L.M.W. and D.A. Ball, *The implication for climate change and peak fossil fuel of the continuation of the current trend in wind and solar energy production*. Energy Policy, 2012. **41**: p. 610-617.
2. Leonard, M.D., E.E. Michaelides, and D.N. Michaelides, *Energy storage needs for the substitution of fossil fuel power plants with renewables*. Renewable Energy, 2020. **145**: p. 951-962.
3. Yang, Z., et al., *Electrochemical Energy Storage for Green Grid*. Chemical Reviews, 2011. **111**(5): p. 3577-3613.
4. Pollet, B.G., I. Staffell, and J.L. Shang, *Current status of hybrid, battery and fuel cell electric vehicles: From electrochemistry to market prospects*. Electrochimica Acta, 2012. **84**: p. 235-249.
5. Braun, P.V., et al., *High power rechargeable batteries*. Current Opinion in Solid State and Materials Science, 2012. **16**(4): p. 186-198.
6. Jiang, F. and P. Peng, *Elucidating the Performance Limitations of Lithium-ion Batteries due to Species and Charge Transport through Five Characteristic Parameters*. Scientific Reports, 2016. **6**(1): p. 32639.
7. Lain, M.J. and E. Kendrick, *Understanding the limitations of lithium ion batteries at high rates*. Journal of Power Sources, 2021. **493**: p. 229690.
8. Thackeray, M.M., C. Wolverton, and E.D. Isaacs, *Electrical energy storage for transportation—approaching the limits of, and going beyond, lithium-ion batteries*. Energy & Environmental Science, 2012. **5**(7): p. 7854-7863.
9. Zhang, S.S., *Liquid electrolyte lithium/sulfur battery: Fundamental chemistry, problems, and solutions*. Journal of Power Sources, 2013. **231**: p. 153-162.
10. Rana, M., et al., *Review on areal capacities and long-term cycling performances of lithium sulfur battery at high sulfur loading*. Energy Storage Materials, 2019. **18**: p. 289-310.
11. Li, T., et al., *A Comprehensive Understanding of Lithium–Sulfur Battery Technology*. Advanced Functional Materials, 2019. **29**(32): p. 1901730.
12. Wang, Y., et al., *Sulfur Hosts against the Shuttle Effect*. Small Methods, 2018.
13. Wang, M., et al., *Porous Carbon Hosts for Lithium–Sulfur Batteries*. Chemistry – A European Journal, 2019. **25**(15): p. 3710-3725.

14. Jung, D.S., et al., *Hierarchical Porous Carbon by Ultrasonic Spray Pyrolysis Yields Stable Cycling in Lithium–Sulfur Battery*. Nano Letters, 2014. **14**(8): p. 4418-4425.
15. Wei, S., et al., *Pig bone derived hierarchical porous carbon and its enhanced cycling performance of lithium–sulfur batteries*. Energy & Environmental Science, 2011. **4**(3): p. 736-740.
16. Ren, G., et al., *Soybean-derived hierarchical porous carbon with large sulfur loading and sulfur content for high-performance lithium–sulfur batteries*. Journal of Materials Chemistry A, 2016. **4**(42): p. 16507-16515.
17. Li, S., et al., *Hollow carbon spheres, synthesis and applications – a review*. Journal of Materials Chemistry A, 2016. **4**(33): p. 12686-12713.
18. Yang, S.J., et al., *MOF-Derived Hierarchically Porous Carbon with Exceptional Porosity and Hydrogen Storage Capacity*. Chemistry of Materials, 2012. **24**(3): p. 464-470.
19. Du, Y., et al., *Template-Free Preparation of Hierarchical Porous Carbon Nanosheets for Lithium–Sulfur Battery*. Langmuir, 2020. **36**(48): p. 14507-14513.
20. Xiao, Q., et al., *Biomass-derived nitrogen-doped hierarchical porous carbon as efficient sulfur host for lithium–sulfur batteries*. Journal of Energy Chemistry, 2020. **44**: p. 61-67.
21. Xue, M., et al., *A novel mangosteen peels derived hierarchical porous carbon for lithium sulfur battery*. Materials Letters, 2017. **209**: p. 594-597.
22. You, X.-l., et al., *Novel biomass derived hierarchical porous carbon for lithium sulfur batteries*. Materials Letters, 2018. **217**: p. 167-170.
23. Su, Z., et al., *Honeycomb-like carbon materials derived from coffee extract via a “salty” thermal treatment for high-performance Li-I2 batteries*. Carbon Energy, 2020. **n/a**(n/a).
24. Ahmadvpour, A. and D.D. Do, *The preparation of active carbons from coal by chemical and physical activation*. Carbon, 1996. **34**(4): p. 471-479.
25. Yang, T. and A.C. Lua, *Characteristics of activated carbons prepared from pistachio-nut shells by potassium hydroxide activation*. Microporous and Mesoporous Materials, 2003. **63**(1): p. 113-124.
26. El-Hendawy, A.-N.A., *An insight into the KOH activation mechanism through the production of microporous activated carbon for the removal of Pb²⁺ cations*. Applied Surface Science, 2009. **255**(6): p. 3723-3730.

27. Otowa, T., Y. Nojima, and T. Miyazaki, *Development of KOH activated high surface area carbon and its application to drinking water purification*. Carbon, 1997. **35**(9): p. 1315-1319.
28. Hou, T.-Z., et al., *Lithium Bond Chemistry in Lithium–Sulfur Batteries*. Angewandte Chemie International Edition, 2017. **56**(28): p. 8178-8182.
29. Wang, J. and S. Kaskel, *KOH activation of carbon-based materials for energy storage*. Journal of Materials Chemistry, 2012. **22**(45): p. 23710-23725.
30. Zhang, J., et al., *Biomass derived activated carbon with 3D connected architecture for rechargeable lithium–sulfur batteries*. Electrochimica Acta, 2014. **116**: p. 146-151.
31. Ladavos, A.K., et al., *The BET equation, the inflection points of N₂ adsorption isotherms and the estimation of specific surface area of porous solids*. Microporous and Mesoporous Materials, 2012. **151**: p. 126-133.
32. Ravikovitch, P.I., G.L. Haller, and A.V. Neimark, *Density functional theory model for calculating pore size distributions: pore structure of nanoporous catalysts*. Advances in Colloid and Interface Science, 1998. **76-77**: p. 203-226.
33. Xu, G., et al., *Hierarchically Porous Carbon Encapsulating Sulfur as a Superior Cathode Material for High Performance Lithium–Sulfur Batteries*. ACS Applied Materials & Interfaces, 2014. **6**(1): p. 194-199.
34. Pognon, G., T. Brousse, and D. Bélanger, *Effect of molecular grafting on the pore size distribution and the double layer capacitance of activated carbon for electrochemical double layer capacitors*. Carbon, 2011. **49**(4): p. 1340-1348.
35. Su, Y.-S. and A. Manthiram, *Lithium–sulphur batteries with a microporous carbon paper as a bifunctional interlayer*. Nature Communications, 2012. **3**(1): p. 1166.
36. Gu, X., L. Hencz, and S. Zhang, *Recent development of carbonaceous materials for lithium–sulphur batteries*. Batteries, 2016. **2**(4): p. 33.
37. Gu, X., et al., *Microporous bamboo biochar for lithium-sulfur batteries*. Nano Research, 2015. **8**(1): p. 129-139.
38. Liu, N., et al., *One-Step Ionic-Liquid-Assisted Electrochemical Synthesis of Ionic-Liquid-Functionalized Graphene Sheets Directly from Graphite*. Advanced Functional Materials, 2008. **18**(10): p. 1518-1525.
39. Zhao, S., et al., *A novel porous nanocomposite of sulfur/carbon obtained from fish scales for lithium–sulfur batteries*. Journal of Materials Chemistry A, 2013. **1**(10): p. 3334-3339.

40. Chen, Y., et al., *Novel Ag@Nitrogen-doped Porous Carbon Composite with High Electrochemical Performance as Anode Materials for Lithium-ion Batteries*. Nano-Micro Letters, 2017. **9**(3): p. 32.
41. Gu, X., et al., *Highly Reversible Li–Se Batteries with Ultra-Lightweight N,S-Codoped Graphene Blocking Layer*. Nano-Micro Letters, 2018. **10**(4): p. 59.
42. Han, K., et al., *Free-Standing Nitrogen-doped Graphene Paper as Electrodes for High-Performance Lithium/Dissolved Polysulfide Batteries*. ChemSusChem, 2014. **7**(9): p. 2545-2553.
43. Petridis, C., et al., *Post-fabrication, in situ laser reduction of graphene oxide devices*. Applied Physics Letters, 2013. **102**(9): p. 093115.
44. Shim, S.H., et al., *Facile Method to Functionalize Graphene Oxide and Its Application to Poly(ethylene terephthalate)/Graphene Composite*. ACS Applied Materials & Interfaces, 2012. **4**(8): p. 4184-4191.
45. Yan, R., M. Oschatz, and F. Wu, *Towards stable lithium-sulfur battery cathodes by combining physical and chemical confinement of polysulfides in core-shell structured nitrogen-doped carbons*. Carbon, 2020. **161**: p. 162-168.
46. Xu, Y., et al., *Confined Sulfur in Microporous Carbon Renders Superior Cycling Stability in Li/S Batteries*. Advanced Functional Materials, 2015. **25**(27): p. 4312-4320.
47. Zhang, B., et al., *Enhancement of long stability of sulfur cathode by encapsulating sulfur into micropores of carbon spheres*. Energy & Environmental Science, 2010. **3**(10): p. 1531-1537.
48. Xin, S., et al., *Smaller Sulfur Molecules Promise Better Lithium–Sulfur Batteries*. Journal of the American Chemical Society, 2012. **134**(45): p. 18510-18513.
49. Peng, H.-J. and Q. Zhang, *Designing Host Materials for Sulfur Cathodes: From Physical Confinement to Surface Chemistry*. Angewandte Chemie International Edition, 2015. **54**(38): p. 11018-11020.
50. Seh, Z.W., et al., *Stable cycling of lithium sulfide cathodes through strong affinity with a bifunctional binder*. Chemical Science, 2013. **4**(9): p. 3673-3677.
51. Chung, S.H., C.H. Chang, and A. Manthiram, *Progress on the Critical Parameters for Lithium–Sulfur Batteries to be Practically Viable*. Advanced Functional Materials, 2018: p. 1801188.
52. Li, P., et al., *Lithium sodium vanadium phosphate and its phase transition as cathode material for lithium ion batteries*. Electrochimica Acta, 2015. **180**: p. 120-128.

53. Rui, X.H., et al., *Analysis of the chemical diffusion coefficient of lithium ions in $\text{Li}_3\text{V}_2(\text{PO}_4)_3$ cathode material*. *Electrochimica Acta*, 2010. **55**(7): p. 2384-2390.
54. González-Meza, O.A., et al., *Development of a Randles-Ševčík-like equation to predict the peak current of cyclic voltammetry for solid metal hexacyanoferrates*. *Journal of Solid State Electrochemistry*, 2019. **23**(11): p. 3123-3133.
55. Vujković, M., et al., *Gel-combustion synthesis of LiFePO_4/C composite with improved capacity retention in aerated aqueous electrolyte solution*. *Electrochimica Acta*, 2013. **92**: p. 248-256.
56. Yuan, L., et al., *New insight into the discharge process of sulfur cathode by electrochemical impedance spectroscopy*. *Journal of Power Sources*, 2009. **189**(1): p. 127-132.
57. Sun, J., et al., *Entrapment of Polysulfides by a Black-Phosphorus-Modified Separator for Lithium–Sulfur Batteries*. *Advanced Materials*, 2016. **28**(44): p. 9797-9803.
58. Takami, N., et al., *Structural and Kinetic Characterization of Lithium Intercalation into Carbon Anodes for Secondary Lithium Batteries*. *Journal of The Electrochemical Society*, 1995. **142**(2): p. 371-379.
59. Hencz, L., et al., *Highly porous nitrogen-doped seaweed carbon for high-performance lithium–sulfur batteries*. *Journal of Materials Science*, 2017. **52**(20): p. 12336-12347.

Chapter 7:

Conclusion and Future Work

7.1 General Conclusions

This thesis aims to address the challenges hindering broader Li-S development and application in the real world. Rapid capacity fading due to the polysulfide shuttle phenomenon and binder failure remains the most troublesome challenges in Li-S development. Other tangential problems relate to the sluggish reaction kinetics, which prevents fast charging/discharging of the Li-S cell, insufficient sulfur loading in the cathode, and costly and pollution-inducing chemical synthesis methods and materials associated with Li-S cell fabrication. Each experimental chapter alleviates at least one of these concerns in some capacity. As a result, the research objectives of this thesis are successfully met. A summary of significant findings and achievements of the experimental chapters are emphasised as follows;

Chapter 3 focuses on synthesising and applying the multifunctional polymer poly(thiourea triethylene glycol) (PTTG) as a binder in Li-S composite cathodes. The abundant electron-rich functional groups in the PTTG polymer backbone enabled the electrochemical performance of the Li-S cell to be enhanced in two primary ways. Firstly, the superior mechanical properties of the PTTG polymer enabled the Sulfur-PTTG composite cathode to withstand the volume expansion and contraction associated with repeated charge/discharge cycles in the cell. Even after cycling, the enhanced mechanical properties of the Sulfur-PTTG composite allowed for a robust and well-connected electron-conducting network to persist. In comparison, the Sulfur-PVDF cathode displayed severe morphological damage and delamination, showing one method by which the electrochemical performance in the Sulfur-PTTG cell was improved. Secondly, the electron-rich functional groups in the PTTG polymer allowed for co-ordination between the cathode composite and the soluble polysulfides, thereby reducing the effects of the polysulfide shuttle phenomenon and allowing a longer cycle life to be achieved. This work helps to highlight to researchers in the field the viability of the lone-pair rich thiourea functional group, an unexplored chemical moiety, towards chemically trapping soluble polysulfides at the sulfur cathode's surface.

Chapter 4 applied a conductive Zn Defective Zinc Cobalt Oxide (ZDZCO) composite at the Li-S surface through a multifunctional interlayer. The ZDZCO composite provided a multifaceted boost to the electrochemical performance in Li-S cells. Firstly, the ZDZCO was shown both through calculation and experiment to have a superior polysulfide anchoring ability than both the non-defective ZnCo_2O_4 and Co_3O_4 , which after electrochemical testing revealed a reduced polysulfide shuttle and enhanced cycle life in the fabricated cells. The ZDZCO also

displayed superior catalytic properties, which enabled the ZDZCO-based cell to deliver a much higher capacity at the high current density of 6 C when compared to the CB-based composite. To highlight the real-world ramifications of this work, sulfur cathodes with ultra-high sulfur loading of $21.06 \text{ mg}\cdot\text{cm}^{-2}$ were constructed using the ZDZCO-based composite separator, which delivered an areal capacity of $13.95 \text{ mA}\cdot\text{cm}^{-2}$. Overall, the multifunctional ZDZCO composite reduced the polysulfide shuttle, enhanced the electrochemical reaction kinetics, and allowed for increased sulfur loading far surpassing the requirements for commercialisation ($> 5 \text{ mg}\cdot\text{cm}^{-2}$). This chapter helped to highlight the role that cation defective bi-metallic oxides can play in the chemical retention of soluble polysulfides to help mitigate the polysulfide shuttle in Li-S batteries.

Chapter 5 utilised ancient insight into the adhesive properties of sticky rice to extract and purify an environmentally friendly highly-branched amylopectin (HBA) binder to construct S/HBA electrodes for Li-S batteries. The green synthesis method used only water and mild conditions to produce a highly-branched starch extract from the widely available sticky rice starting material. The HBA enhanced the electrochemical performance of Li-S batteries through two mechanisms. Firstly, soluble polysulfides were retained at the surface of the cathode via coordination and C-S bonds. As a result, the capacity fading from the polysulfide shuttle effect was reduced, as evidenced by the polysulfide adsorption experiment and FTIR investigation. Secondly, the HBA possessed better mechanical and adhesive properties than PVDF and lowly-branched polysaccharide (LBP). Experiments revealed that the enhanced properties of the HBA arise from its branched structure, which allowed for better adhesion throughout the S/HBA composite. The strong adhesion maintained the electronic and ionic conductive network throughout the composite cathode, which improved electrochemical performance in the S/HBA cell. The environmentally friendly extraction method of the binder could reduce the reliance on chemical synthesis methods and materials currently used in Li-S cell fabrication. The work displayed in Chapter 5 can be thought of as an extension to the work of Chapter 3. Chapter 3 shows that by applying mechanically robust adhesive polymers with lone-pair-rich functionality as the Li-S cathode binder, excellent electrochemical performance can be obtained. The HBA binder used in Chapter 5 also displays robust adhesion and lone-pair-rich moieties, and shows that the binder can indeed improve the electrochemical performance of the cell. However, in contrast to the traditional chemical synthesis employed in Chapter 3's experiment, this work highlights the importance of naturally occurring and environmentally

benign multifunctional polymers and shows their potential to help combat the technical limitations hindering Li-S battery commercialisation.

Similar to Chapter 5's experiment, Chapter 6 investigated green synthesis methods for Li-S composite cathode components. The work in Chapter 6 can be considered as an extension of Chapter 4, where the initial experiment investigates materials synthesised from more traditional chemical processes to observe the improved electrochemical performance of the material and is expanded upon by applying those principles to more environmentally friendly and sustainable battery components. The "sweet and salty" synthesis method produced a hierarchical porous carbon host (HPCH) and applied it as a bi-functional sulfur host in composite sulfur cathodes. The HPCH can be easily incorporated into traditional slurry-casting electrode fabrication techniques without requiring any sulfur-infiltration step while still significantly improving the electrochemical performance of the Li-S cell. The conductive pore structure of the HPCH allowed provided physical polysulfide retention, and the lone-pair rich surface hydroxyl and carbonyl groups on the material's surface provided chemical polysulfide retention, which both reduced the shuttle phenomenon and improved the cycle life of the S/HPCH cells. The HPCH also enabled an enhanced electronic and ionic conductivity compared with composite cathodes using only CB additives. As the synthesis only uses water and ethanol solvents, the environmental impacts of the fabrication of Li-S cells can be reduced while still delivering enhanced performance, which can help guide researchers towards more and environmentally benign synthesis methods in the future.

In summary, this thesis successfully showed that the chemical retention of soluble polysulfides at the cathode's surface is viable to deliver improved electrochemical performance in Li-S cells. Each work in this thesis also investigated additional methods to improve the performance and fabrication of the Li-S battery, either through enhanced catalytic conversion as shown in Chapter 4, or through the environmentally friendly methods shown in Chapters 5 and 6. By applying enhanced Li-S batteries commercially, EVs that can travel as far as combustion-based vehicles in a single charge could be realised. Robust electrochemical energy storage systems could also bolster the applicability of renewable energy technologies. If these goals are realised, a reduction in CO₂ emissions is feasible and would help achieve a carbon-neutral future.

7.2 Future Work

Although great strides have been achieved towards improving the commercial viability of the Li-S cell, there remains a significant amount of work. A few research directions are provided below;

- The experiments in chapters 3 and 4 utilized DFT to explain some mechanisms of polysulfide adsorption and conversion. However, applying DFT thusly only scratches the surface of the potential applications of the technique. DFT calculations can also be utilised to calculate Li^+ diffusion pathways, further explaining the Li^+ diffusion results obtained through experimental electrochemical means. Furthermore, the typical reaction pathways for lithium polysulfide conversion, which is typically provided in Li-S battery research, are only general, as shown in chapters 2 and 4. DFT calculations could be used to elucidate the complicated reaction pathways of sulfur dissolution and conversion. Future research could incorporate more DFT calculations to provide a better fundamental understanding of the Li-S system's chemistry.
- Li-S battery research relies on intensive characterisation techniques to explain the electrochemical results. However, in most cases, these techniques are limited to investigating materials and electrodes before cycling or through post-mortem disassembly of the cells after cycling and may not give the best insight into the reaction mechanisms and processes. For instance, post-mortem SEM analysis of the electrodes utilised in each experimental chapter of this thesis relies on cell disassembly after cycling. Even if this procedure is done in the glovebox, contamination with oxygen can occur when transferring the sample to the SEM, which can cause oxidation of the air-sensitive components of the electrode, changing the surface chemistry. In-situ/operando analysis techniques could be employed to obtain a deeper insight into the electrochemical processes during cycling without

sample contamination. For example, in-situ XRD can be used to observe the changes in the crystal structure of the electrode materials during cycling, in-situ XAS can be applied to observe changes in the oxidation states of electrode components, and in-situ X-ray image can be used to observe changes in the material's morphology during discharge. These in-situ techniques can also give more profound insight into the complicated cell mechanics during cycling.

- The scaling-up of the material synthesis is another avenue open to researchers going forward. Typically, due to the limitations of cost and available plant put on university researchers, much of the materials synthesis and electrochemical testing conducted at universities is limited to lab-scale experiments on coin cells. Small-scale experiments are undoubtedly helpful to elucidate electrochemical mechanisms or ideas, but researchers must also think of the potential of their material in the future. Care can be taken to focus on methods that may be scaled-up in the future, even if the researcher cannot achieve so at present. For instance, complicated synthesis methods such as hydrothermal methods/hard-templating approaches can produce exciting materials but are not feasible for larger-scale applications. Hydrothermal methods can produce wildly different morphologies of the final product even if small experimental parameters are changed, such as the reaction vessel volume. Hard-templating approaches produce a large amount of chemical waste compared to the small amount of product. Researchers can focus on scalable and environmentally friendly synthesis methods to help address the scaling-up of the Li-S cell in the future.
- Finally, researchers can look towards larger-scale electrochemical testing in the hopes of commercialising the Li-S battery. As mentioned, much of the electrochemical research is done on coin cells, which is helpful for small-scale and exploratory battery research but is far from the analysis needed for commercialisation. Even if the

researcher only has coin-cell assembly facilities, care can still be taken to make their electrochemical data as commercially valuable as possible. For instance, statistical analysis on the electrochemical performance of coin cells is rarely conducted, with almost all of the literature reporting data on single electrochemical cells. Obviously, for commercial viability, the performance of electrochemical cells over many devices can be measured to obtain more robust and significant data. Researchers must also carefully control the electrochemical experimental parameters, as the majority of the literature has at least some of the experimental parameters, such as electrode diameter, electrolyte content, material loading, sulfur loading, etc., missing. In addition, there are no standards of measurements during electrochemical testing, with most papers reporting a different number of cycles and charge/discharge currents. Both of these procedures make it challenging to compare electrochemical data across different manuscripts. In doing so, even if larger-scale experiments such as pouch cell testing is not available to the researcher, their data is still as accurate and statistically significant as possible, which may help to bridge the gap between the electrochemical performances obtained experimentally in labs and the electrochemical performance of pouch cells in commercial applications.